

KINETICS OF TiB FORMATION

by

GEORGE C. WALTHER, JR.

A DISSERTATION PRESENTED TO THE GRADUATE COUNCIL OF
THE UNIVERSITY OF FLORIDA
IN PARTIAL FULFILLMENT OF THE REQUIREMENTS FOR THE
DEGREE OF DOCTOR OF PHILOSOPHY

UNIVERSITY OF FLORIDA

1976

ACKNOWLEDGMENTS

The author wishes to thank each of his supervisory committee members for their advice and counsel during the course of this work. They have contributed solutions to a variety of problems encountered during this research.

Thanks are due Dr. Frank Gotsama of Union Carbide Corporation for his gift of ZrO_2 fibers.

Financial support provided by Dr. L. L. Hench, the Department of Materials Science and Engineering, and the National Science Foundation is also acknowledged.

And, I would like to thank my wife for her enduring and endearing during these past several years.

TABLE OF CONTENTS

	<u>Page</u>
ACKNOWLEDGMENTS.....	ii
LIST OF TABLES.....	v
LIST OF FIGURES.....	vi
ABSTRACT.....	ix
 SECTION	
I	
INTRODUCTION.....	1
Statement of Problem.....	1
Ti-B System: Phase Relations.....	2
Ti-B System; Chemical Reactions.....	14
Quantitative Microscopy.....	23
Kinetic Models.....	32
II	
EXPERIMENTAL PROCEDURE.....	45
Sample Preparation.....	46
Quantitative Microscopy Measurements.....	52
Quantitative X-Ray Analysis.....	70
III	
RESULTS AND DISCUSSION.....	75
Metallographic Examination.....	75
Transport Experiment Results.....	84
Quantitative Microscopy Results.....	89
Quantitative X-Ray Results.....	137
IV	
MODEL ANALYSES.....	158
V	
CONCLUSIONS.....	195
Recommendations on Use of Quantitative Microscopy.....	196
General Recommendations for Future Work.....	198

Table of Contents - continued.

	<u>Page</u>
APPENDIX	
1	Comparison of the X-Ray Lines of Orthorhombic TiB, Ti ₂ B, and Ti Superlattice.....200
2	List of Qualitative Microstructural Features for a Four Phase System.....202
3	Calculation of Statistical Parameters for a Random Sample of Size n.....204
4	Computer Programs.....206
5	Glossary of Computer Variables.....212 Quantitative Microscopy Results for 1200 - 1500°C.....214
6	Results of Archimedian Porosity.....222
7	Selected X-Ray Data.....223
8	X-Ray Data.....224 X-Ray Standards Data.....224 X-Ray Sample Data.....225
9	Results of Sasaki Model.....227
10	Quantitative Microscopy Model Calculations.....229
11	Quantitative X-Ray Model Calculations.....231
12	Quantitative Microscopy Slope Data: TiB ₂233
13	Velocity and Curvature Results.....234
BIBLIOGRAPHY.....235	
BIOGRAPHICAL SKETCH.....245	

LIST OF TABLES

<u>Table</u>	<u>Page</u>
1 Powder Compact Kinetic Models.....	34
2 Summary of m Values for Nucleation and Growth Models.....	39
3 Results of Electrostaining.....	54
4 Data for TiB Standard Material.....	104
5 Quantitative Microscopy Data for Starting Material Compact.....	134
6 Variability in Quantimet Operating Technique.....	135
7 X-ray Error Determinations.....	138
8 X-ray Absorption for TiB and TiB ₂	152
9 Ti Peak Shift Data.....	156
A1-A4 Quantitative Microscopy Results for 1200°C - 1500°C.....	214- 221
A5 Results of Archimedean Porosity.....	222
A6 X-ray Standards Data.....	224
A7 X-ray Sample Data.....	225
A8 Results of Sasaki Model.....	227
A9 Quantitative Microscopy Model Calculations.....	229
A10 Quantitative X-ray Model Calculations.....	231
A11 Quantitative Microscopy Slope Data: TiB ₂	233
A12 Velocity and Curvature Results.....	234

LIST OF FIGURES

<u>Figure</u>		<u>Page</u>
1	Phase diagram of the Ti-B system after Palty et al.....	6
2	Phase diagram of the Ti-B system after Rudy and St. Windisch.....	9
3	Crystal structures of TiB_2 and TiB.....	13
4	Grid of length L placed on a section showing particles of A in a matrix of B.....	26
5	Model geometries.....	36
6	Particle size distribution of reactant powders.....	47
7	Micrograph of Ti particles.....	48
8	Micrographs of TiB_2 particles.....	49
9	Centorr furnace.....	51
10	Schematic of electrostaining apparatus.....	53
11	The Quantimet 720 image analyzing computer.....	56
12	Effect of nonideal signal on detected image.....	57
13	Effect of sizer on detected image.....	59
14	Effect of nonuniform background level on detected image.....	59
15	Quantimet display.....	60
16	Images detected by Quantimet.....	62
17	Schematic of transport experiments.....	66
18	Diffusion couple markers.....	69

List of Figures - continued.

<u>Figure</u>		<u>Page</u>
19	X-ray equipment.....	71
20	Sequence of reaction.....	78
21	Large Ti grain and surrounding porosity.....	81
22	Polished and electrostained surface.....	81
23	Micrographs of fracture surfaces.....	82
24	Result for surface diffusion transport experiment.....	86
25	Diffusion couple interfaces.....	87
26-29	Quantitative Microscopy volume fraction results for 1200°C - 1500°C.....	91- 94
30	Porosity determined by Quantitative Microscopy.....	96
31	Porosity determined by immersion displacement.....	97
32-35	Quantitative Microscopy mole fraction results for 1200°C - 1500°C.....	99- 102
36-39	Quantitative Microscopy surface area per volume for 1200°C - 1500°C.....	106- 109
40-43	Quantitative Microscopy specific interface area for 1200°C - 1500°C.....	111- 114
44	The proximity parameter.....	116
45-48	Quantitative Microscopy total curvature results for 1200°C.....	117- 120

List of Figures - continued.

<u>Figure</u>		<u>Page</u>
49-52	The $\bar{\lambda}$ parameters for 1200°C - 1500°C.....	122- 125
53-56	The \bar{H} parameters for 1200°C - 1500°C.....	127- 130
57	Qualitative x-ray strip chart patterns.....	140
58	Internal standard calibration curves.....	142
59-62	Quantitative x-ray volume fraction results for 1100°C - 1400°C.....	144- 147
63	Pulverized x-ray sample.....	149
64	Direct comparison calibration curves.....	150
65	Peak shift for Ti (011) line.....	154
66	Valensi-Carter model as a function of extent of reaction.....	163
67	Standard curve for Sasaki model.....	164
68	Extent of reaction for Quantitative Microscopy data.....	165
69	Extent of reaction for quantitative x-ray data.....	166
70-79	Model results for Quantitative Microscopy data.....	168- 177
80-87	Model results for quantitative x-ray data.....	179- 186
88	Average interface velocity results.....	191
89	Modified average interface velocity results.....	193

Abstract of Dissertation Presented to the
Graduate Council of the University of Florida in Partial
Fulfillment of the Requirements for the
Degree of Doctor of Philosophy

KINETICS OF TiB FORMATION

by

George C. Walther, Jr.

August, 1976

Chairman: Ronald E. Loehman
Major Department: Materials Science and Engineering

The kinetics of forming TiB from Ti and TiB₂ was studied using pressed powder compact and diffusion couple geometries. Powder samples were heated in an Ar atmosphere at 1100 - 1500°C for 0 - 120 min. Metallographic examination showed the reaction initiates at the contact points between Ti and TiB₂ and proceeds rapidly due to surface diffusion of Ti coating the TiB₂ particles. Weight loss experiments showed negligible vapor transport of Ti or B occurs. A Kirkendall shift observed on a Ti-TiB₂ diffusion couple indicates Ti is the major diffusing element; some counter diffusion of B also occurs. Analyses by Quantitative Microscopy and quantitative x-ray diffraction suggest the initial reaction is controlled by the rate of Ti diffusion through the TiB. During the

later stages, the reaction rate changes to an inverse time dependence due to reduced availability of Ti. The Quantitative Microscopy measurements provided volume fraction, surface area, and total curvature data for the microstructural features. An average velocity for the reacting interface was obtained from this data. Evidence to exclude rate control by nucleation and growth or interface reaction mechanisms is presented. The curvature of the TiB-TiB₂ interface does not significantly influence the reaction.

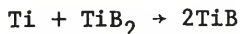
A 10 - 15 volume % expansion of the powder compact was observed due to the volume increase of TiB₂ transforming to TiB. Competing densification from sintering of TiB or TiB₂ is negligible. Fabrication of TiB articles by sinter-reacting powders thus results in weaker products.

This study shows the importance of microstructural geometry on reaction kinetics in powder compacts.

SECTION I INTRODUCTION

Statement of the Problem

The object of this study is to examine the mechanisms of transforming TiB_2 and Ti to TiB in a mixed powder compact. Titanium diboride is a hard brittle refractory material with a high strength to weight ratio at high temperatures which exhibits good resistance to corrosion, oxidation, and attack by some liquid metals. It shows promise for use in crucibles, electrodes, hard facing, and a variety of cermet or alloy applications. The high strength and light weight, corrosion resistance, and refractoriness of Ti are also well-known. However, during an x-ray investigation of the reaction between mixed Ti and $B_{12}C_3$ powders,¹ rapid formation of TiB as one of the major products was observed, rather than the expected TiB_2 . These results suggested the less stable monoboride was favored kinetically and implied a potential limitation on the use of Ti or TiB_2 in some applications. Therefore, a study of the kinetics of forming TiB by the simpler reaction



was begun to determine the mechanism for the rapid TiB

formation. Since x-ray evidence alone was not sufficient, it was decided to follow the evolution of the reaction using Quantitative Microscopy to see what influence the powder compact structure had on the reaction rate. It appears that the use of Quantitative Microscopy for this purpose has never been reported.

Ti-B System: Phase Relations

Understanding of the phase relations in the Ti-B system has been hindered by the refractory nature of the titanium borides, problems with impurities, limitations of early x-ray techniques, and difficulties of metallographically preparing these hard materials. The borides that have so far been proposed for this system include Ti_2B , TiB (cubic or orthorhombic forms), Ti_3B_4 , TiB_2 , Ti_2B_5 , and TiB_x ($x \approx 10$). The most reliable evidence supports only TiB_2 and orthorhombic TiB as stable equilibrium phases, although uncertainty concerning the nature of Ti_3B_4 is not completely resolved at this time. The development of current understanding is presented below.

The preparation of TiB_2 was first reported by Andrieux,² utilizing electrolysis of TiO_2 dissolved in a fused boric acid - metal fluoride bath. The product was not very pure. Agte and Moers³ produced purer TiB_2 by

vapor deposition reaction of TiCl_4 and BBr_3 on a heated W filament. Ehrlich⁴ performed the first systematic study of the Ti-B system by x-ray investigation of sinter-reacted Ti and B powders. He reported finding the compounds TiB (zinc blend structure) and TiB_2 (hexagonal AlB_2 type). The Ti lattice parameters increased with B additions up to 44 atomic % without an observed phase break. This suggested a large solubility of B in Ti and that no phases intermediate in B between Ti and TiB existed. From samples at both the Ti-rich and B-rich end of his compositional range, Ehrlich obtained additional x-ray lines that could not be indexed. From this evidence he proposed a Ti superlattice and a boride phase higher in B than TiB_2 . Norton et al.⁵ and Zachariassen⁶ confirmed Ehrlich's structural interpretation of TiB_2 . Most of Ehrlich's other results were contradicted by later workers, who cited the presence of impurities, non-equilibrium conditions, and inadequate x-ray sensitivity as reasons for the discrepancies.

Except for TiB_2 , the evidence reported by other early workers provided little clarification of Ehrlich's results. From considerations of B atomic radii, Andersson and Kiessling⁷ suggested that TiB is fcc (NaCl type), stable only at high temperatures, and that it decomposes

to α -Ti and TiB_2 at lower temperatures. Brewer et al.⁸ did a study on sinter-reacted Ti and B powders similar to Ehrlich's. They were confident only of the existence of TiB_2 (with a narrow homogeneity range) and found no evidence for higher B phases. The additional weak lines of a fcc phase were explained as TiN due to N contamination rather than TiB. Although they also found a continuous increase in Ti lattice parameters with B additions up to 50 atomic %, in agreement with Ehrlich, the presence of more lines than required made a Ti superlattice interpretation difficult. Greenhouse et al.⁹ were the only workers to claim the existence of a TiB_x ($x \approx 10$) phase as one of the products of reaction between TiC and $B_{12}C_3$. Ogden and Jaffee¹⁰ arc melted pure Ti and B powders to produce Ti-rich alloys for x-ray analysis; they found no shift in the α -Ti lines, but did observe definite lines from a second phase, corresponding to Ehrlich's Ti superlattice. Following a suggestion of Hansen,¹¹ they proposed these were due to a Ti_2B hexagonal phase almost identical in structure to α -Ti. Utilizing hot pressing techniques on Ti and B powders, Glaser¹² and Post and Glaser¹³ reported several new phases: a tetragonal Ti_2B , a hexagonal Ti_2B_5 , and a fcc TiB that was stable at low temperatures. They admitted equilibrium conditions were

not always achieved during their experiments, but felt their results were stable phases because chemical analyses showed very low C and N contents in their samples. They determined the melting point of TiB_2 to be $2790^\circ C$, but later reported a value of $2920^\circ C$ (Post et al.¹⁴).

The first Ti-B phase diagram was presented by Palty et al.¹⁵ (Figure 1). Their results were not definitive since they noted that three or more phases often coexisted and hence equilibrium was not always attained. Their powder samples were arc melted and heat treated and then examined with metallographic, x-ray, and melting point techniques. They noted that etching was required to distinguish boride phases and Ti_2B detected by x-ray was not always seen metallographically. After elimination of the x-ray lines for Ti, TiB, and TiB_2 presented by Ehrlich,⁴ the remainder was assumed to be the pattern for Ti_2B . However, they interpreted their x-ray results for Ti_2B and TiB as being in better agreement with the results of Glaser.¹² No evidence for Ti_2B_5 was given since the compositional range they studied did not extend to that B level. In spite of problems achieving equilibrium, discrepancies between x-ray and metallographic detection, and questions concerning interpretation of x-ray data based on the combined Ehrlich⁴-Glaser¹² patterns, this

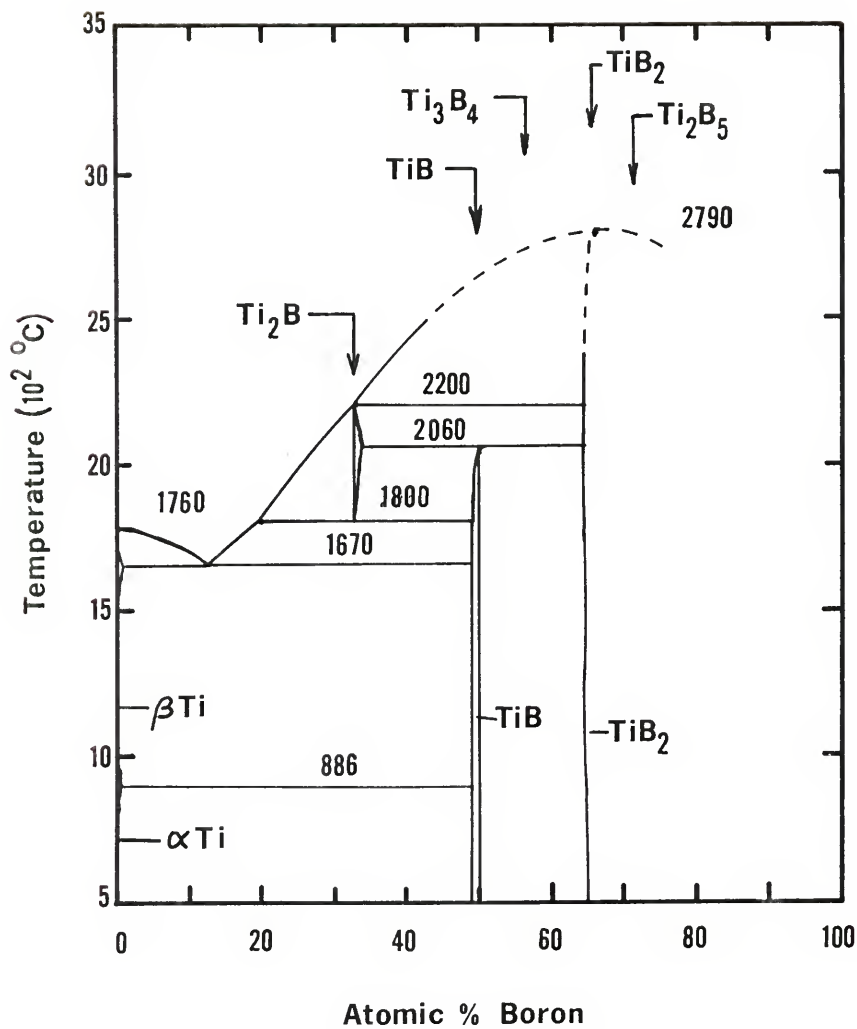


Figure 1. Phase diagram of the Ti-B system after Palty et al.¹⁵

diagram due to Palty et al.¹⁵ was accepted in later work by Samsonov and Umanskiy¹⁶ and by Hansen.¹⁷

Subsequent investigations began to clarify the questions of extended solubility, presence or absence of Ti superlattice, Ti_2B and TiB structures, and the existence of high B phases. The early studies did not produce any doubts about the existence or structural interpretation of TiB_2 . Metallographic results of Craighead et al.¹⁸ showed the B solubility in Ti to be much lower than previously thought (less than 0.43 atomic %). Decker and Kasper¹⁹ obtained single crystal needles of TiB (1 mm long and 0.1 mm diameter) by arc melting a 23 atomic % B alloy and dissolving the excess Ti with acid. From the results of their x-ray analysis, they described an orthorhombic FeB type crystal structure based on B chains with the b axis as the needle axis. Although this structural interpretation of TiB was initially resisted by Samsonov and Umanskiy¹⁶ in favor of the results of Post and Glaser,¹³ it gained greater acceptance when Aronsson²⁰ pointed out that the " Ti_2B " x-ray data of Palty et al.¹⁵ were essentially equivalent to the orthorhombic TiB data of Decker and Kasper.¹⁹ A comparison of these two patterns is given in Appendix 1. In addition, Aronsson²⁰ felt the cubic form of TiB resulted from a ternary solid solution

with O, N or C since three coexisting phases had been reported,^{4,15} and smaller O or N atoms replacing B would explain the smaller lattice parameter of cubic TiB compared with TiC. Although Nowotny²¹ reported cubic and orthorhombic TiB phases coexisting in a study of silicide and boride cermets, he and his coworkers (Nowotny et al.²² and Wittmann et al.²³) later agreed with Aronsson²⁰ that cubic TiB was not a stable phase in the binary Ti-B system. These same workers²¹⁻²³ also found no evidence for the existence of Ti_2B_5 . Seybolt²⁴ restricted his investigation to the high B alloys and found only TiB_2 - no Ti_2B_5 was seen. Thus, these several workers showed that only orthorhombic TiB and TiB_2 are recognized as stable equilibrium phases and that Ti_2B , cubic TiB, and Ti_2B_5 were due to previous experimental artifacts.

These features were all confirmed by Rudy and St. Windisch.²⁵ They re-examined the Ti-B binary phase diagram to reconcile their results for several boride ternary systems with previously reported data. Using high purity Ti and B powders and sinter-reacting, hot pressing, or arc melting their samples, they examined them using melting point determinations, x-ray diffraction, metallography, and high temperature DTA. Their resultant diagram is shown in Figure 2. As can be seen, they found no evi-

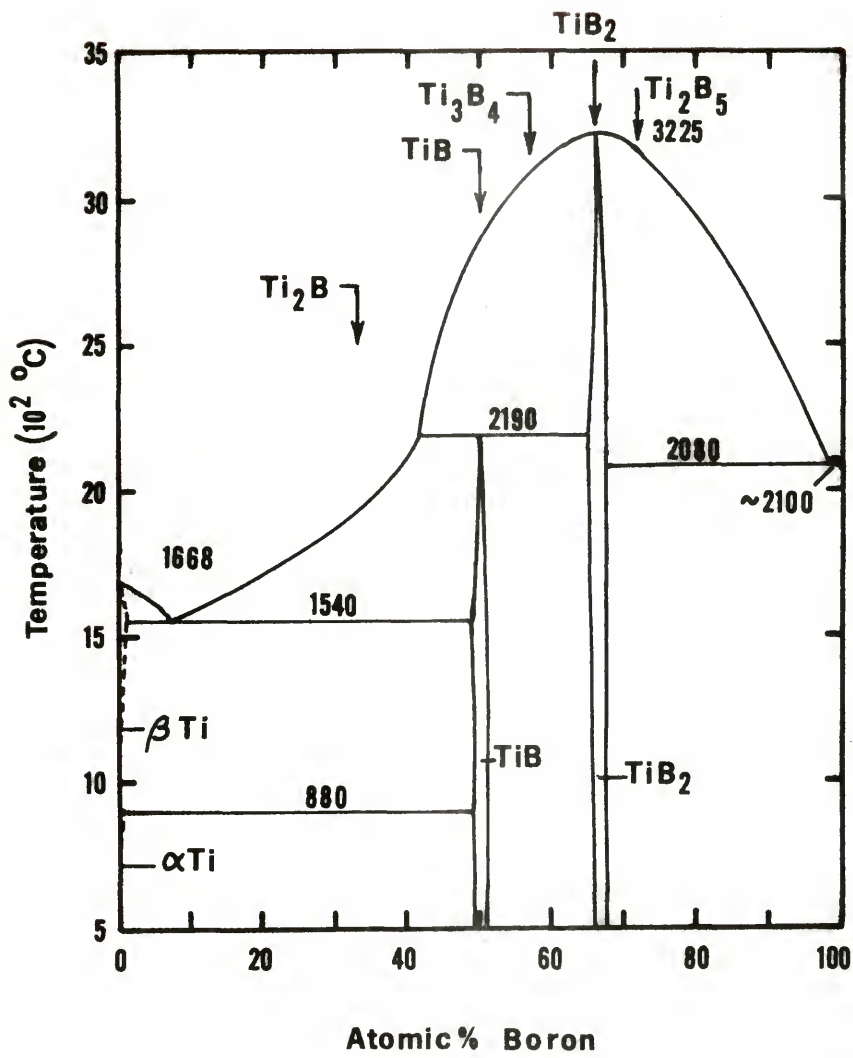


Figure 2. Phase diagram of the Ti-B system after Rudy and St. Windisch.²⁵

dence for Ti_2B , cubic TiB , or Ti_2B_5 ; only orthorhombic TiB and TiB_2 were observed. These two phases are present with narrow homogeneity ranges. They also remarked on the different etching characteristics of TiB on each side of the peritectic composition (42 atomic % B), which could explain the metallographic observance of " Ti_2B " by earlier workers. Two features of Figure 1 may be compared with the more recent results of Figure 2. The TiB eutectic temperature ($1670^\circ C$) shown by Palty et al.¹⁵ is almost identical to the melting point of Ti ($1668^\circ C$), shown on the diagram of Rudy and St. Windisch.²⁵ The peritectic reaction temperature of " Ti_2B " ($2200^\circ C$) in Figure 1 is also very close to the peritectic reaction temperature of orthorhombic TiB ($2190^\circ C$) in Figure 2. This suggests the experimental results obtained in developing both versions of the diagram were similar, but that the interpretation of metallographic observations made by Palty et al.¹⁵ was incorrect. The TiB eutectic temperature ($1540^\circ C$) of Figure 2 is also confirmed by Garfinkle and Davis,²⁶ who observed the contact reaction between liquid Ti and TiB_2 to be a eutectic reaction at $1550^\circ C$. Rudy and St. Windisch²⁵ also determined the melting point of TiB_2 to be $3225^\circ C$, in contrast to the earlier results of Post et al.¹⁴ ($2920^\circ C$) or Latva²⁷ ($2980^\circ C$), and suggest this discrepancy is due to C contamination.

In a theoretical consideration of electron concentrations in alloys, Engel²⁸ hypothesized that a stable configuration for a Ti_3B_4 phase existed. Later, Fenish²⁹ reported fabricating an orthorhombic Ti_3B_4 compound by sinter-reacting mixed Ti and B powders in a 3:4 stoichiometric ratio. It required several cycles of crushing, re-mixing, and reheating this product in a TiB_2 crucible (at 2020°C for 16 - 20 hrs.) to obtain near completion of the reaction.³⁰ Residual TiB was removed by dissolving in hydrofluoric and sulfuric acids. The resultant material was claimed to be structurally related by several M_3B_4 borides²⁹ and to undergo a peritectic reaction at 2010°C.³⁰ Although Rudy and St. Windisch²⁵ reported no evidence of another phase intermediate in B between TiB and TiB_2 , Walther and Whitney¹ found x-ray lines fitting the Ti_3B_4 pattern of Fenish in their preliminary study of Ti and $B_{12}C_3$. Walther also obtained strong Ti_3B_4 x-ray intensities (in addition to TiB and TiB_2) from Ti and B powders mixed in a 3:4 molar ratio and hot pressed at 1600 - 1800°C for several hours in BN-lined graphite dies. Fenish believed his use of very pure starting materials (Ti:99.98%; B:99.8%³⁰) explained his observation of Ti_3B_4 , in contrast to the work of Rudy and St. Windisch,²⁵ who used materials of lesser purity ($\approx 99.7\%$). Although it is

possible Finnish experienced contamination of his samples from the TiB_2 crucible or from the grinding apparatus during crushing, Walther obtained his results with material whose purity is comparable to that of Rudy and St. Windisch.²⁵ The question of the existence and nature of Ti_3B_4 as a stable, metastable, or impurity-stabilized phase in the Ti-B system is not yet resolved.

The above series of investigations have clarified the phase relations in the binary Ti-B system. The TiB_2 and orthorhombic TiB phases are the only stable borides presently established with reasonable certainty. The possibility that Ti_3B_4 is also a stable equilibrium compound is not yet firmly established. The suggestion of a Ti superlattice made by Ehrlich⁴ was the result of a misinterpretation of his x-ray data because of insufficient number of lines detected. The pattern for " Ti_2B " was shown to be identical to that of orthorhombic TiB. The cubic TiB, Ti_2B_5 , and TiB_x phases were not found by later investigations and appear to have been present in earlier studies because of contamination. The comparison of features between Figures 1 and 2 shows that incorrect interpretation of metallographic results led to further misunderstandings concerning the true phase relationships. The crystal structures of TiB_2 and TiB are shown in Figure 3.

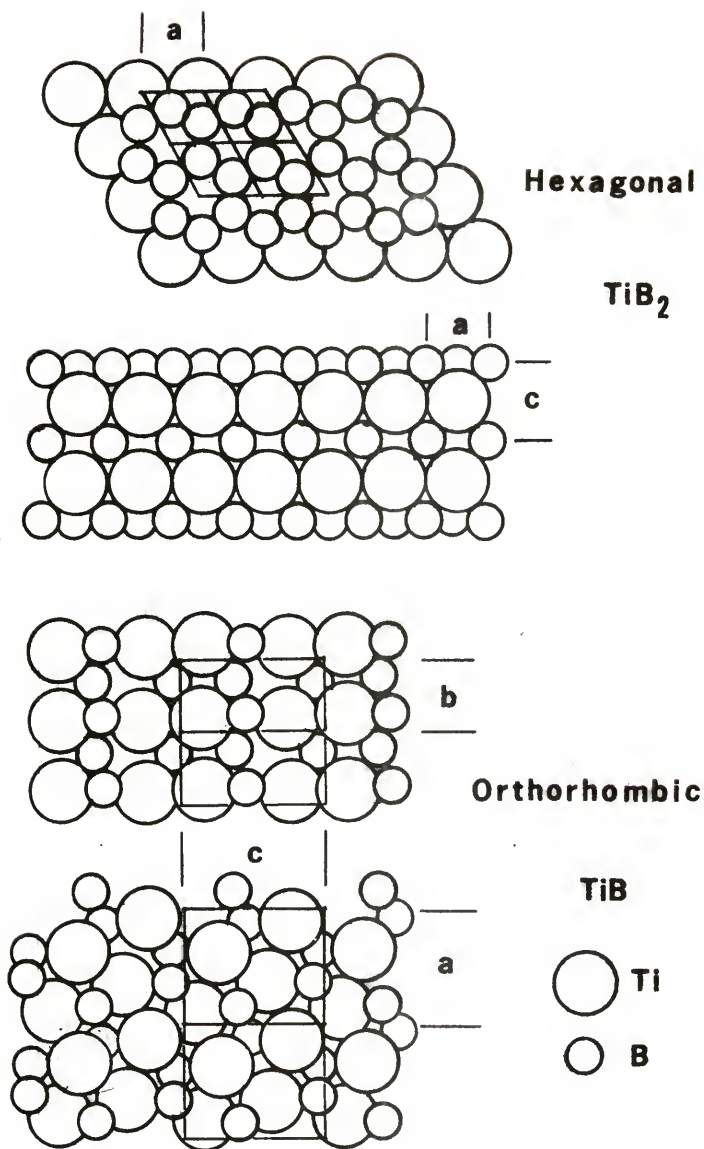


Figure 3. Crystal structures of TiB₂ and TiB.

Ti-B System: Chemical Reactions

The problems in understanding the phase relations in the Ti-B system have also contributed to difficulties interpreting some results of chemical reactivity in this system. Studies of the reaction between Ti and TiB_2 and between Ti and B have been reported.

In studying the chemical stability of dispersed boride compounds, Antony and Cummings³¹ heated 2-4 μm TiB_2 particles in an excess Ti powder matrix for 2 hours at 1000°C. X-ray and metallographic examination showed a product ring of TiB around the TiB_2 particles. However, their conclusion that the diffusion of B into the matrix material is rate-controlling is not firmly established by this simple observation. Strashinskaya and Stepanchuk³² studied the interaction between TiB_2 and Group IV transition metals in mixed powder, TiB_2 powder-Ti metal, and solid-solid contact geometries. They heated their samples in vacuum for 1 and 3 hours at 100°C intervals between 900-1700°C. Their powders were -325 mesh mixed in proportions of 50-50 volume %. Metallographic and x-ray examination showed that the initial formation of a 1-2 μm product began after 3 hours heating at 900°C for the powdered samples and at 1000°C for the solid-solid contacts. In the mixed powders, this phase was reported as "rhombic"

TiB (FeB orthorhombic type), which increased with increasing time and temperature of reaction, and after 1 hour at 1400°C no more TiB₂ x-ray lines could be detected (the initial Ti content was in excess of that required for a stoichiometric product). The powder-metal contact reaction layer increased to about 20 μm at 1300°C, but microhardness results on the product layer were anomalously low: $\approx 1050 \text{ kg/mm}^2$ compared to $\approx 2700 \text{ kg/mm}^2$ reported for TiB.³³ After 1 hour at 1500°C, the microhardness of this layer increased to 1650-1780 kg/mm^2 , which was still uncharacteristically low for TiB. The possibility that this layer was Ti₂B or a solid solution of B in Ti was proposed; however, the previous section has shown that neither of these mechanisms is credible in the Ti-B system. Since no micrographs of this layer or starting material purity data were presented, it is difficult to assess whether poor metallographic preparation, contamination, or some other factor could have caused this result. The solid-solid contact reaction appeared to form a surface fusion zone at 1500°C after 1 hour with a microhardness of $\approx 1700 \text{ kg/mm}^2$. Pore formation was observed for this reaction geometry at 1300-1400°C and was attributed to differences in diffusivities of "various components" and to volatilization. The authors also claim this product was

not "rhombic" TiB. The possibility of eutectic liquid formation at 1500°C or higher was not mentioned by Strashinskaya and Stepanchuk.³² Comparing their comments with the eutectic temperature evidence presented by Rudy and St. Windisch²⁵ and Garfinkle and Davis²⁶ suggests contamination may have lowered the eutectic temperature from 1540°C to 1500°C. Examination of their micrographs for this reaction zone also suggest the possibility that their "pores" are pullout created during polishing. Since the two studies discussed above were the only ones found by this writer to deal with the Ti-TiB₂ reaction and their interpretations are based on insufficient or questionable results, this provides additional justification to examine this reaction in greater detail.

Investigations of direct Ti and B interaction show conflicting results, which may be related in part to kinetics. Epik³⁴ and Samsanov and Epik³⁵ reported the kinetics of forming TiB₂ from the elements is parabolic. They utilized a mixture of B₁₂C₃ and borax as a B source packed around solid Ti rods, heated this to 1100-1500°C under a dry hydrogen atmosphere for 1 - 8 hours, and measured the thickness of product layer formed on the rods and their weight gain. This layer was a single phase, TiB₂, which was well bonded due to "wedges" of boride

phase formed into the metal along grain boundaries. They also claimed there was no counter-diffusion of Ti through the boride because no porosity was seen at the Ti-TiB₂ interface. No mention was made of the greater molar volume of TiB₂ compared to Ti, which could expand into this porosity. Zhunkovskii and Samsonov³⁶ and Zhunkovskii³⁷ continued similar experiments, but heated their samples under vacuum ($\sim 10^{-3}$ mm Hg) and used amorphous B instead of a B₁₂C₃-borax mixture. They also found an equally adherent product layer, but during metallographic examination two distinct phases were seen while x-ray showed only the presence of TiB₂. They postulated that a fcc TiB formed at temperature, it reverted to TiB₂ and Ti upon cooling, and that residual Ti present influenced metallographic appearance. This proposal shows a misunderstanding of the phases in the Ti-B system. The discrepancy between metallographic and x-ray results suggests either inadequate x-ray sensitivity or poor metallographic preparation. The micrograph provided by Zhunkovskii³⁷ was not sufficiently clear to judge the latter possibility. These authors also reported that the kinetics of forming TiB₂ changes with temperature: diffusion controlled growth became the dominant mechanism at higher temperatures. Burykina and Evtoshok³⁸ studied the application of protective boride coatings on graphite crucibles to avoid car-

burization of molten metals. An intermediate step to produce $B_{12}C_3$ was followed by application of Ti. The subsequent boriding of the Ti produced both TiB and TiB_2 layers with a sharp boundary between them, as determined by microhardness measurements; with increasing time and temperature the TiB_2 layer increased at the expense of the TiB. This result is in contrast to that of Samsonov and Epik,³⁵ where only TiB_2 was reported. The part played by the $B_{12}C_3$ -borax mixture in favoring TiB_2 formation over TiB is not clear. However, the results of Burykina and Evtushok³⁸ suggest that when the elements are reacted, their relative diffusion rates through the TiB and TiB_2 layers influence the relative rates of boride formation. This is further supported by the work of Krzyminski,³⁹ who reacted metal-powder samples under conditions very similar to Samsonov and Zhunkovskii,³⁶ but got two definite boride layers. Even though the boride layers appear to form on the Ti, it is not clear whether B diffuses into the Ti, Ti diffuses through the boride layer to react at the surface, or both occur simultaneously.

The above experiments utilized a Ti specimen in a B matrix; several studies have also been conducted on B fibers in a Ti matrix. The primary aim of these investigations was to assess the degree of chemical interaction

between fibers and matrix: this interaction would reduce the suitability of these fibers for use as fiber reinforcement. Burykina et al.⁴⁰ used vapor phase decomposition to prepare B-coated W filaments which were then compacted with Ti powder. They found some W contamination of the B fibers by this method of preparation. Heating in vacuum at 900°C produced only a 1 μm reaction layer after 10 hours. At higher temperatures (1100°C) another ragged layer appeared near the Ti and a measured microhardness of 2700 kg/mm^2 suggested it was TiB. This layer remained thin but the rate of TiB₂ layer increase appeared to be controlled by the rate of interface reaction at 900°C, the rate of volume diffusion at 1000-1100°C, and influenced by interphase and grain boundary diffusion at higher temperatures. After 300 hours at 900°C, only TiB₂ was apparent. This change of mechanism with temperature is similar to that reported by Zhunkovskii and Samsonov³⁶ for Ti samples packed in B powder. In contrast to the above results, Staudhammer et al.⁴¹ obtained only TiB when they reacted B fibers with a Ti matrix. The main difference between their work and that of Burykina et al.⁴⁰ was that the latter had W contaminated fibers. These results suggest the Ti-B interaction is too great to allow use of B fiber reinforcement of Ti. However, Schmitz and

Metcalfe⁴² found that the alloy Ti 1310 (Ti - 13V - 10 Mo - 5 Zr - 2.5% Al) reacted with B fibers at $\approx 850^{\circ}\text{C}$ sufficiently to give a good bond during fabrication of fiber reinforced samples, but that negligible further reaction occurred during 10,000 hours use at 600°C . The studies of Ti-B interaction show conflicting results with TiB_2 , $\text{TiB}_2 + \text{TiB}$, and solely TiB, reported as product phases. This range of results is caused by differences of purity, temperature, and method of contact, which alter the relative diffusion rates of Ti and/or B through the product layer.

Investigations into the bonding mechanisms of the borides have been spurred by the influence of relative diffusion rates on chemical reactivity and a desire to understand their refractory properties. However, the degree to which the Ti-B and B-B bonds are metallic, covalent, or ionic has not yet been resolved. Samsonov and Latysheva⁴³ investigated the diffusion of B, C and N in transition metals and related this to bonding. They found the diffusion rate was inversely dependent on atomic radius, contrary to expectation, and suggested the amount of chemical interaction or degree of bonding was more important than size. They formulated this dependence as a relationship between activation energy and the parameter

$1/Nn$, where N is the principal quantum number and n the number of electrons in the incomplete d-shell of the transition metal. The activation energy decreased monotonically with increasing $1/Nn$, supporting their contention that diffusion was controlled by the availability of an unfilled d-shell to bond electrons from the non-metal. An activation energy for B diffusion in Ti of 9.15 ± 2.80 kcal/mole was reported; an error in calculating these results was subsequently corrected⁴⁴ to give a value of 11.2 kcal/mole. Silver and his coworkers^{45,46} used NMR to investigate bonding in the borides and from their results proposed that the metal atoms contributed electrons to the B. Tyan et al.⁴⁷ tested a theory of electron transfer from B to Ti in TiB_2 and TiB with low temperature specific heat measurements. Although the results for TiB_2 did not conflict with the theory, the TiB results were anomalously low. They suggested this was due to a strong Ti-B bond or to transfer of additional electrons from the B to the bonding part of the band structure. They could not choose between these alternatives from their data. Gillies and Lewis⁴⁸ measured strain of ball milled powders by x-ray line-broadening analysis and demonstrated that the bonding strength in hexagonal TiB_2 is almost isotropic. This feature is further supported by Philipp⁴⁹ who reacted TiB_2 in

a variety of acidic solutions and found it was difficult to selectively dissolve either Ti or B; he obtained both elemental species in solution in the stoichiometric ratio, suggesting none of the Ti-Ti, B-B, or Ti-B bonds are significantly stronger than the others. The possibility of a mixture of bond types in these borides could help explain their range of properties; different bond types become more predominant in different environments. For example, partial metallic bonding between Ti atoms contributes to conductivity in an electric field while ionic and covalent characteristics of the B-B and Ti-B bonds give these materials their brittle, incompressible nature under mechanical loading. Such conjecture requires additional experimental evidence to clearly establish the nature of this behavior in the titanium borides.

The studies of chemical interaction in the Ti-B system have led to a variety of results. Some of these differences may be attributed to misunderstandings about the possible phases in the system. Others may be artifacts due to contamination or poor metallography. The observance of TiB_2 , $TiB_2 + TiB$, or TiB product layers suggests relative diffusion rates of Ti and/or B through the borides affect the kinetics of these reactions. These reactions are also strongly influenced by temperature and degree of contact between reactants.

Quantitative Microscopy

The description of a powder compact structure and its evolution during a solid state chemical reaction is a complex geometric problem. Most powders are irregular in shape and size and when compacted their geometry becomes even more complex since elements of porosity are also present. For the system studied here, a qualitative geometric description includes the initial observance of Ti, TiB_2 , and porosity, and as the reaction proceeds, TiB also appears. Associated with each of these four phases are their volumes, the areas of contact between two identical or different phases or particles, the triple lines of contact between three phases, and the quadruple points where four phases meet. Appendix 2 shows the possible combinations of these features for a four-phase structure and also for the case where features common to one material are ignored. For example, there is no porosity-porosity interface in a powder compact; for this study when particles of the same phase were in contact, they were considered as one element of the structure. Thus, there are four types of volumes, six types of interfaces, four types of triple lines, and a single quadruple point for this case. As the reactants are consumed to form product, these geometric features may be created or destroyed, thus

changing the qualitative description of the microstructure with time. Such a description at any given time has been called a qualitative microstructural state.⁵⁰ The compact or its constituents may also be described qualitatively by terms such as "uniform," "dispersed," "segregated," "web-like," "coated," "filamentary," "globular," etc. The imprecision provided by such language is often sufficient for many purposes.

In some cases, however, more quantitative information is necessary, especially if a structure is examined as a function of reaction time or some other experimental variable. Quantitative information on phase volume can be obtained by quantitative x-ray or chemical analysis, while BET analysis gives information on surface area. Such methods do not provide insight into the influence of an arbitrary compact structure on the process being studied and may not always detect interior volume or area components. Usually additional qualitative examination, for example by optical or electron microscopy, is necessary to characterize the structure and to interpret changes occurring with time.

The principles of Quantitative Microscopy⁵¹ provide a quantitative description of topological and metric properties of an arbitrary piece-wise smooth and continuous geo-

metric structure. Topological properties measure the number and connectivity of elements of the structure. Metric properties include volume fraction, surface area, triple line length, and surface curvature, among others. The generality of this method is not restricted to simple shapes or structures and is admirably suited to describing complex powder compact microstructures.

To obtain information about a three dimensional structure, a number of representative two dimensional sections must be examined. Topological measurements at the present state of the art require sectioning serially through the sample structure and counting the number of elements of interest and also noting their appearance or disappearance. It can be shown⁵¹ that metric information is obtained by placing a grid of points on a series of random sections and making several simple counting measurements from this superposition. The results of this series are averaged to give structural information. Figure 4 shows a grid on a section of A particles in a B matrix. The volume fraction of the i^{th} phase, V_V^i , is directly proportional to the average number fraction of points falling within that phase, \bar{P}_P^i , or

$$V_V^i = \bar{P}_P^i \quad (1)$$

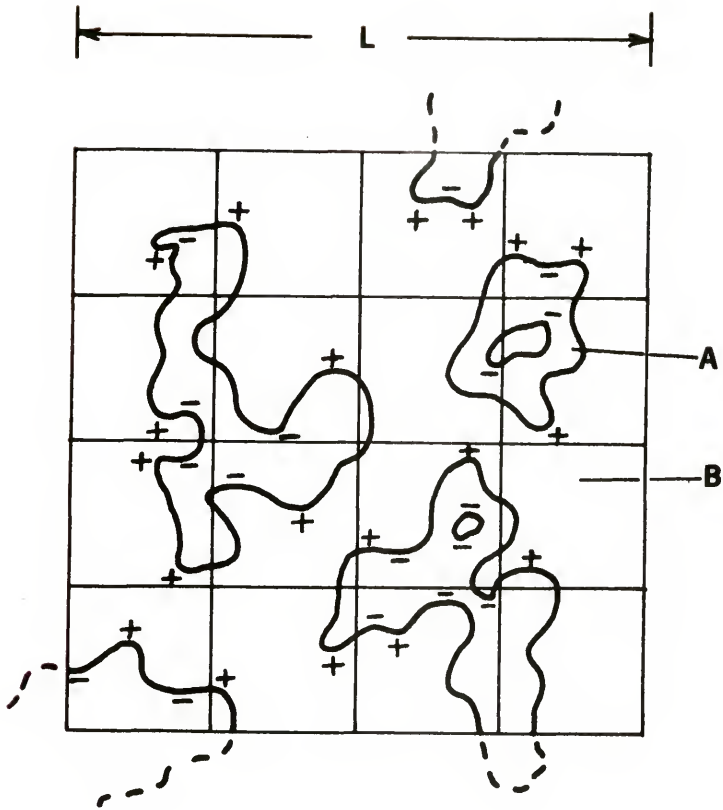


Figure 4. Grid of length L placed on a section showing particles of A in a matrix of B.

The surface area per volume, S_V^i , of the i^{th} phase is related to the number of times one of the grid lines intersects the phase boundary per total grid line length, \bar{P}_L^i , or

$$S_V^i = 2 \bar{P}_L^i \quad (2)$$

If the \bar{P}_L^i counts are restricted to the i - i or a particular i - j boundary, only the corresponding interface area is measured. Similarly, the three-dimensional triple line length per volume, L_V^{ijk} , can be related to the number of triple points per grid area \bar{P}_A^{ijk} :

$$L_V^{ijk} = 2 \bar{P}_A^{ijk} \quad (3)$$

The total curvature of a phase boundary, M_V^i , is defined as the integral over the surface of the local mean surface curvature, H .

$$M_V^i = \iint_S H ds = \iint_S \frac{1}{2} (\kappa_1 + \kappa_2) ds \quad (4)$$

where κ_1 and κ_2 are the principal normal curvatures at the surface element ds . This may be related to the number of tangents a sweeping grid line makes with the i^{th} phase boundary as seen in a two-dimensional section.

$$M_V^i = \pi \bar{T}_{\text{Anet}}^i \quad (5)$$

A tangent may be arbitrarily designated positive if the curvature vector (at the tangent point) points into the

phase (convex perimeter arc) and negative if it points out (concave perimeter arc). This is the scheme used in Figure 4. The difference between the number of positive and negative tangents per unit of swept area is the net tangent count, T_{Anet}^i . The tangent count can be applied to specific i-j boundaries if tangents to the edge formed between two or more partial surfaces (or corners as seen in a polished section) are also counted.⁵² Thus, the total curvature of specific interface or faceted areas may also be measured if the additional counts are made. Applying the above relations to Figure 4, for example, gives

$$V_V^A = 1 - V_V^B = 8/25 = 0.32$$

$$S_V^{AB} = 2(32)/10L = 6.4/L$$

$$M_V^A = -M_V^B = (\pi(19 - 17))/L^2 = 2\pi/L^2$$

$$L_V = 0$$

Thus, the metric parameters, V_V , S_V , L_V and M_V can be quantitatively determined for each phase of a complex microstructure through the simple counting measurements and application of Equations (1), (2), (3) and (5). Each parameter provides an independent item to characterize the structure. For example, two structures having the same V_V^i could have significantly different S_V^i and M_V^i val-

ues and would certainly have different microstructural geometries. The only restrictions on the generality of the above relations are that the sections must provide a suitably random sampling of available structural features and that a sufficient number of grid placements or fields of view must be measured to assure adequate statistics. Usually 25 - 100 placements are made, depending on the accuracy desired. Most isotropic microstructures are homogeneously uniform and locally random so a single section plane contains all the statistical metric information of the three dimensional compact. The accuracy of these determinations improves with increasing number of points in the grid, but must be compromised with the effort required to achieve this accuracy. This effort has been reduced by electronic means, as described in greater detail later.

Several additional Quantitative Microscopy parameters obtainable from the simple counting measurements have been developed. One of these is the mean intercept length, $\bar{\lambda}$, the average surface to surface distance in a structure. It is a measure of scale of the features examined and may be applied to grain size of a given phase or "phase size" of a multiphase material. It can be shown that

$$\bar{\lambda} = \frac{4V_V}{S_V} \quad (6)$$

Although $\bar{\lambda}$ has a definite geometric meaning, its physical interpretation is not as straightforward in arbitrary structures since it is not usually numerically equal to an average grain diameter or edge length, even for features of regular shape. Such diameters and lengths have little meaning when applied to a powder compact. Another parameter is the average mean surface curvature, \bar{H} , defined as

$$\bar{H} = \frac{\int \int H dS}{\int \int dS} = \frac{\int \int \frac{1}{2}(\kappa_1 + \kappa_2) dS}{\int \int dS} \quad (7)$$

where κ_1 and κ_2 are defined as before. It is thus the local mean curvature averaged over the surface. It is obtained from the counting measurements by the expression

$$\bar{H} = \frac{M_V}{S_V} \quad (8)$$

Although \bar{H} is an average and does not specify the distribution of curvature values, if a phase volume is changing due to a change in the energy of its surface, changes in \bar{H} will indicate an extension or contraction of this boundary and the magnitude of the net average driving force. The motion of interfaces is discussed further in the next section. Another parameter has been proposed by Dorfler:⁵³ the proximity parameter is defined as the fraction of a phase area interfaced with another phase, or

$$P_X = \frac{S_{ij}}{S_i} \quad (9)$$

This could be used to weight a known surface to that portion which was undergoing reaction, for example, the oxidation of one metal in a mixture of metal powders. The presence or absence of a particular proximity parameter may also indicate in what order phases have appeared or disappeared during a transformation.

Topological information requires serial sectioning of the microstructure; other information obtainable by Quantitative Microscopy, such as particle size distribution, requires measurements not made in this study.^{50,51} A discussion of these topics is beyond the scope of this report.

The principles of Quantitative Microscopy have been discovered and rediscovered by workers in many fields, including geology, metallurgy, biology and medicine.⁵⁴ In spite of their generality, they have not been applied to materials science problems to any great extent,⁵⁵ primarily because of the manual effort involved and the availability of presumably adequate alternatives, such as x-ray, density determinations, TGA, etc. However, some applications of Quantitative Microscopy have been reported. A few examples include studies of the kinetics of

transformations in metals,⁵⁶ sintering of metals⁵⁷ and ceramics,^{58,59} and the effect of microstructure on mechanical⁶⁰ and electrical properties.⁶¹ The advent of automated electronic equipment permits its use as a means of quality control of slag inclusions in steel.⁶² However, no previous attempt to follow the evolution of a solid state reaction in a powder compact by this means could be found by this writer.

Kinetic Models

One viewpoint of solid state kinetic studies is that only by studying the reaction between single crystal couples can any meaningful information be gained about the rates of reaction. This is done by measuring the change in the composition profile with time or the geometric extent of product and determining the direction and diffusion rate of various atomic species. This ideal is often difficult to achieve experimentally and is usually not representative of technological practice. Because of this, many reactions are studied between mixed and compacted powders.

Several models of solid state reactions in powders have been proposed; and these have been reviewed by Hulbert.⁶³ These models assume spherical particles of one

phase are completely coated by the other matrix phase. These models are formulated mathematically as

$$Kt = f(x) \quad (10)$$

where K is the reaction constant, t is time, and $f(x)$ is some function of the extent of reaction, x . In these cases, x is usually the volume fraction of spherical reactant phase transformed. Expressions for the various models are summarized in Table 1.

For diffusion controlled growth, Jander⁶⁴ proposed a spherical product shell whose thickness, y , increases at a parabolic rate, i.e.,

$$\frac{dy}{dt} = \frac{Dk}{y} \quad (11)$$

where D is the diffusion coefficient. Ginstling and Brounshtein⁶⁵ used the same geometry, Figure 5a, but modified the relationship to account for the decrease in interface area as the reaction proceeds. The model was further modified by Valensi⁶⁶ and (apparently independently) by Carter⁶⁷ to allow for any volume change that occurs during the transformation (Figure 5b). Thus, Z is the ratio of volume of product formed per unit volume of reactant consumed. Carter⁶⁸ later learned about the existence of the Ginstling-Brounshtein model and noted the difference between the Ginstling-Brounshtein and the Valensi-Carter models was small when $Z < 2$. Clark et al.⁶⁹

Table 1
Powder Compact Kinetic Models

Model	Equation
Jander	$K_J t = \frac{2 k D t}{r_0} = [1 - (1-x)^{1/3}]^2 \quad (12)$
Ginstling-Brounshtein	$K_{GB} t = \frac{2 k D t}{r_0} = 1 - \frac{2}{3}x - (1-x)^{2/3} \quad (13)$
Valensi-Carter	$K_{VC} t = \frac{2 k D t}{r_0} = \frac{Z - (Z-1)(1-x)^{2/3} - [1 + (Z-1)x]^{2/3}}{Z-1} \quad (14)$
Kroger-Ziegler	$K_{KZ} \ln t = \frac{2 k \ln t}{r_0} = [1 - (1-x)^{1/3}]^2 \quad (16)$
Hulbert <u>et al.</u>	$K_{VCH} \ln t = \frac{2 k \ln t}{r_0} = \frac{Z - (Z-1)(1-x)^{2/3} - [1 + (Z-1)x]^{2/3}}{Z-1} \quad (17)$
Zhuravlev <u>et al.</u>	$K_{ZLT} t = \frac{2 k D t}{r_0} = [(\frac{1}{1-x})^{1/3} - 1]^2 \quad (19)$

Table 1 - continued.

Model	Equation
Dunwald-Wagner	$K_{DW} t = \frac{\pi^2 D t}{r_0^2} = \ln \frac{6}{\pi^2 (1-x)} \quad (20)$
Nuclei Growth	$K_{NG} t^m = \ln \left(\frac{1}{1-x} \right) \quad (21)$
Phase Boundary	$K_{PB} t = \frac{k t}{r_0} = 1 - (1-x)^{1/3} \quad (23)$

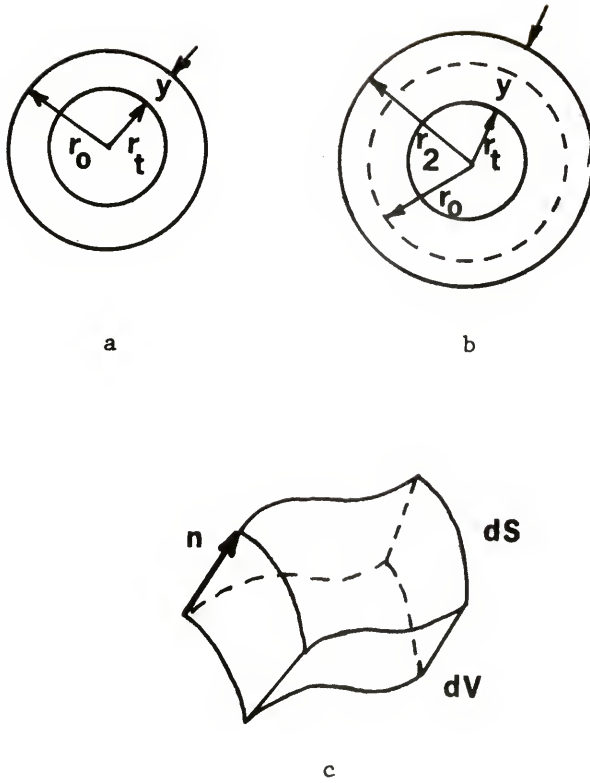


Figure 5. Model geometries: a) Jander and Ginstling-Brounshtein, b) Valensi-Carter, c) interface displacement of arbitrary surface element.

disagreed with Carter concerning $Z < 2$. They introduced the effect of thermal expansion into the Valensi-Carter model and noted that deviations from the true value of Z can have a significant influence on the accuracy of $f(x)$ and of K determined from it, especially in the early stages of reaction. The desirability of high temperature data to accurately determine Z was also mentioned by Hulbert.⁶³

Tammann⁷⁰ assumed the diffusion coefficient is not constant but varies inversely with time.

$$\frac{dy}{dt} = \frac{k}{yt} \quad (15)$$

This may occur due to changes in defect concentration or because the matrix is a decreasing source of reactant, for example. Kroger and Ziegler⁷¹ applied this to the Jander geometry [Equation (16)], while Hulbert et al.⁷² claimed the Tammann relation and Valensi-Carter geometry gave good results for the kinetics of forming some spinels.

Zhuravlev et al.⁷³ assumed the activity of the reacting phase depended on the fraction of unreacted material in developing their kinetic equation.

$$\frac{dy}{dt} = \frac{kD}{y}(1 - x) \quad (18)$$

This reduces the reaction rate with time. To introduce local concentration gradients, Serin and Ellickson⁷⁴

altered Dunwald and Wagner's⁷⁵ solution of Fick's second law for spheres to incorporate the extent of reaction parameter.

The above relations present geometric and diffusion coefficient modifications into shrinking spherical shell particle models for diffusion controlled reactions.

If one phase is partially miscible in another, reactions in powders may follow nucleation and growth models. Although the probability of a transformation initiating at nuclei in the interior of one phase is greater in a cast material, this phenomenon is possible in powder compacts. When several possible nucleation and growth rates and nuclei geometries (sphere, plates or rods) are considered, the equation in Table 1 provides a general expression;⁶³ where the parameter m may take on the values given in Table 2, and is a function of reaction mechanism, nucleation rate, and nuclei geometry. Table 2 shows that obtaining the value of m does not unequivocally establish the conditions and geometry of the reaction.

If the interface reaction controls the overall reaction rate, this rate is directly proportional to the available interface area

$$-\frac{dV}{dt} = k S(t) \quad (22)$$

For uniform size spheres, the relation in Table 1 holds.⁶³

Table 2
 Summary of m Values for Nucleation
 and Growth Models

	<u>Phase boundary controlled</u>	<u>Diffusion controlled</u>
Three dimensional growth (spheres)		
Constant nucleation rate	4	2.5
Zero nucleation rate (saturation of point sites)	3	1.5
Decreasing nucleation rate	3-4	1.5-2.5
Two dimensional growth (plates)		
Constant nucleation rate	3	2
Zero nucleation rate (saturation of point sites)	2	1
Decreasing nucleation rate	2-3	1-2
One dimensional growth (rods)		
Constant nucleation rate	2	1.5
Zero nucleation rate (saturation of point sites)	1	0.5
Decreasing nucleation rate	1-2	0.5-1.5

Several Quantitative Microscopy relationships have been developed that permit the average velocity of an interface (or the average growth rate of the phase it bounds) to be determined from the counting measurements. These are not restricted to a particular shape, but do require a continuously smooth (arbitrary) surface. If an element of this surface dS moves a distance n (Figure 5c) with velocity

$$v = \frac{dn}{dt} \quad (24)$$

the surface sweeps out a volume at the rate

$$\frac{dV}{dt} = \int_S v dS \quad (25)$$

It can be shown⁵⁰ the corresponding changes in area and total curvature are

$$\frac{dS}{dt} = 2 \int_S v H dS \quad (26)$$

$$\frac{dM}{dt} = \int_S v \kappa^* dS \quad (27)$$

where H is defined in Equation (4) and $\kappa^* = \kappa_1 \kappa_2$, the Gaussian curvature. If the velocity integral [Equation (25)] is normalized to the area of interest, an average velocity, \bar{v}_S may be defined that is obtainable from Quantitative Microscopy parameters.⁷⁶

$$\bar{v}_S = \frac{\int_S v dS}{\int_S dS} = \frac{1}{S} \frac{dV}{dt} = \frac{1}{S_V} \frac{dV_V}{dt} \quad (28)$$

Similarly, the other weighted velocities may be averaged to give

$$\bar{v}_H = \frac{\int \int v H dS}{\frac{S}{\int \int H dS}} = \frac{1}{2M} \frac{dS}{dt} = \frac{1}{2M_V} \frac{dS_V}{dt} \quad (29)$$

$$\bar{v}_K = \frac{\int \int v_k^* dS}{\frac{S}{\int \int k dS}} = \frac{1}{4(N-G)} \frac{dM}{dt} = \frac{1}{4(N_V-G_V)} \frac{dM_V}{dt} \quad (30)$$

where N and G are the topological parameters number and genus (connectivity) of the structure, $\int \int k dS$ is the Integral Curvature, and the unsubscripted symbols in the terms second from the right are for unit mass or moles. The parameters N and G , and hence \bar{v}_K , require serial sectioning to be determined.

If the weighted velocity expressions Equations (25) through (27) are normalized to the rate of volume change, two additional curvature averages may be defined. Also recall that

$$\bar{H} = \frac{\int \int H dS}{\frac{S}{\int \int dS}} = \frac{M}{S} - \frac{M_V}{S_V} \quad (7,8)$$

$$\bar{H}_G = \frac{\int \int v H dS}{\frac{S}{\int \int v dS}} = \frac{\frac{1}{2}(dS/dt)}{(dV/dt)} = \frac{1}{2} \frac{dS}{dV} = \frac{1}{2} \frac{dS_V}{dV_V} \quad (31)$$

$$\bar{K}_G = \frac{\int \int v_k dS}{\frac{S}{\int \int v dS}} = \frac{dM/dt}{dV/dt} = \frac{dM}{dV} = \frac{dM_V}{dV_V} \quad (32)$$

The average mean surface curvature, \bar{H} , has already been mentioned: \bar{H}_G is the growth rate average mean surface curvature; and \bar{K}_G is the growth rate average Gaussian curvature. The latter two parameters were first proposed by Cahn⁷⁷ and DeHoff,^{50,78} respectively. DeHoff notes these parameters "provide some insight into the distribution of interface velocities in the system, and, in particular, into any correlations that may exist between velocity and curvature."⁵⁰ If the interface velocity does not vary much with position, then from Equations (28) through (30), $\bar{v}_S = \bar{v}_H = \bar{v}_K = \bar{v}$, or from Equations (7) and (31), $\bar{H} \approx \bar{H}_G$. In this special case, Equations (28) and (30) also imply

$$N_V - G_V = \frac{S_V}{4\pi} \frac{dM_V}{dV_V} \quad (33)$$

or that some topological information may be obtained from metric quantities. If $\bar{H}_G < \bar{H}$ or $\bar{H}_G > \bar{H}$, it suggests that curvature decreases or increases interface motion, respectively.

Thus, metric measurements of V_V , S_V , and M_V provide potentially useful information about the kinetics of a reaction in terms of an interface velocity. Analogously with Equation (22), an average growth rate, $\bar{G}(t)$, may be

obtained.

$$\bar{v}_S = \frac{dV_V/dt}{S_V} = \bar{G}(t) \quad (34)$$

If $\bar{G}(t) = K$, the reaction is controlled by the boundary reaction; if $\bar{G}(t) = K/t$, a Tamman dependence is indicated; and if $\bar{G}(t) = K\sqrt{t}$, diffusion through the product layer limits the reaction rate. A comparison of weighted velocities or curvatures helps interpret these velocities. The lack of geometric restrictions suggests this velocity is a useful extension of kinetic models based on spheres. However, the range of velocities occurring during a reaction cannot be too great for the average to be representative of a particular mechanism.

The studies of phase relations in the Ti-B system²⁻²⁹ have shown an evolutionary understanding of these refractory materials. Some of the misunderstandings resulting from this work have contributed to misinterpretations of the chemical interactions occurring in the Ti-B system. The investigations of the Ti-TiB₂ interaction^{31,32} were inconclusive and provided little information about the rates or mechanisms involved. The related work on direct Ti-B reactions³⁴⁻⁴⁴ resulted in a range of boride products and suggested the kinetics of these reactions influenced what products were observed. Although

B-TiB₂-TiB-Ti layers were reported, only the advance of TiB₂ was measured. Why TiB was kinetically favored over the more stable TiB₂ during the reaction¹ between Ti and B₁₂C₃ has not been answered. This evidence of rapid degradation of a potentially useful refractory material also merits attention. The ability of Quantitative Microscopy to describe a complex powder microstructure suggests a means to examine this problem. Thus, the aim of this study is to investigate the kinetics and mechanisms involved in the reaction between Ti and TiB₂ in a mixed powder compact.

SECTION II EXPERIMENTAL PROCEDURE

Since a simple additive solid state reaction proceeds by transport of the reactant phases into contact with each other and their chemical combination to form a product phase, several alternative mechanisms were available to model the various stages of reaction studied here. These include:

- 1) Vapor transport, surface diffusion, or volume diffusion of the Ti with subsequent reaction.
- 2) A similar transport of B to the Ti.
- 3) Some combination of the above.
- 4) Diffusion of Ti or B through a TiB product layer at a parabolic or a Tammann rate.
- 5) Interface motion controlled by the rate of reaction at the boundary.
- 6) Reaction rate controlled by the rate of nucleation of TiB.
- 7) Reaction controlled by the decomposition of some intermediate metastable or impurity stabilized phase.

Several experiments were designed and run to demonstrate the validity of some mechanisms and exclude the others.

Sample Preparation

The starting powders were 99.7% purity Ti produced by grinding commercial metal (Atomergic Chemetals Corporation) under a neutral atmosphere and 99.8% purity TiB_2 (Ventron, Inc.) made by reducing the oxides of B and Ti with C. The particle size distribution of these powders obtained by sieving is shown in Figure 6. The data below 20 μm were obtained using sedimentation methods. The Ti particles were predominantly 20-50 μm with some particles as large as 120 μm and had a platelike morphology characteristic of grinding swarf (Figure 7). A negligible amount was smaller than 20 μm . The TiB_2 powder was primarily 20-30 μm with some finer material and some larger conglomerates 30-80 μm in size (Figure 8). Although large numbers of small particles ($\sim 1 \mu m$) were detected in the SEM and by Coulter Counter measurements, they constituted a very small fraction of the total on a mass or volume basis; attempts to obtain the complete size distribution using the Coulter Counter were unsuccessful due to particle settling problems. The TiB_2 particles were rough but fairly equiaxed. Metallographic examination showed very small amounts of another phase in the interstices of the conglomerated particles. Electron microprobe analysis of these regions suggested the presence of

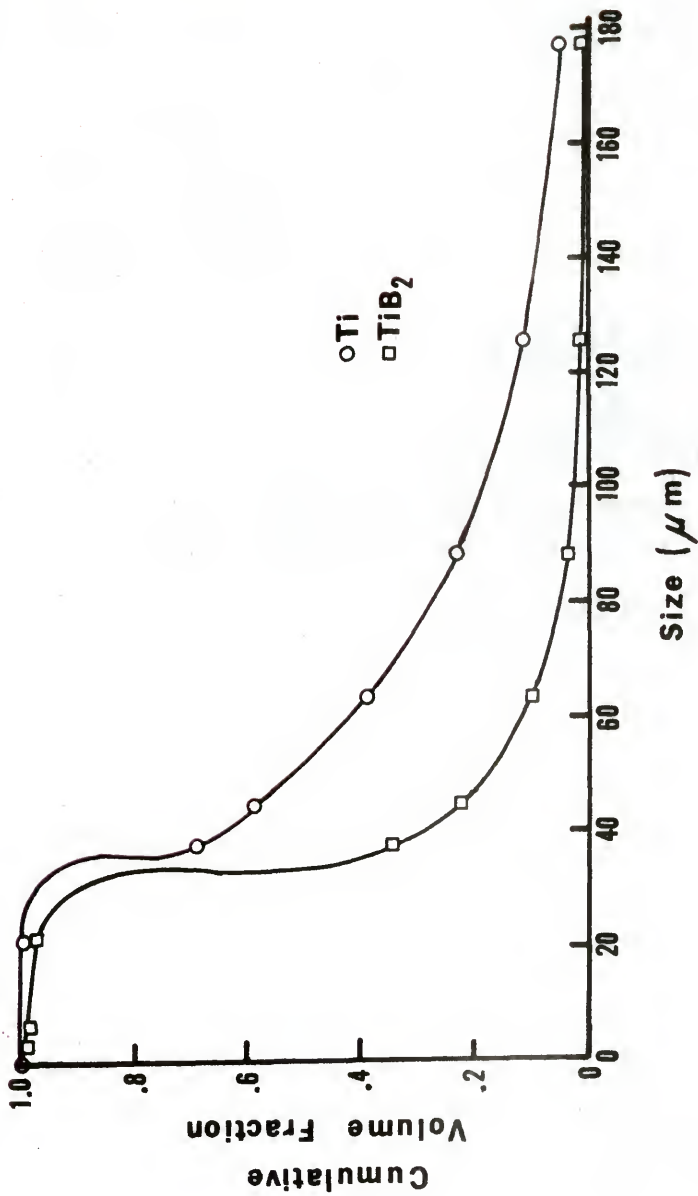


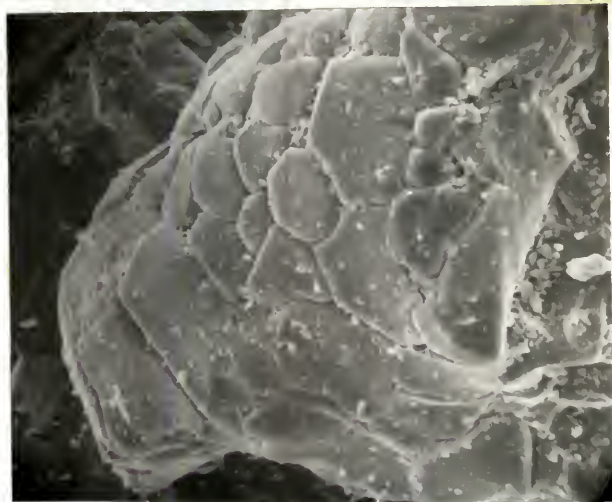
Figure 6. Particle size distribution of reactant powders.



Figure 7. Micrograph of Ti particles (470 X).



a



b

Figure 8. Micrographs of TiB_2 particles: a) many small particles present on larger ones (950 X), b) large particle conglomerate of several smaller particles (950 X).

TiC or Ti_3B_4 residue from the material preparation process. Surface area measurement of these powders by BET analysis gave $66.2 \text{ m}^2/\text{gm}$ for TiB_2 and $56.5 \text{ m}^2/\text{gm}$ for Ti.

These powders were mixed in equimolar amounts in a V-blender for 24 hours and then compacted in a uniaxial die at 3500 kg/cm^2 pressure. The resulting discs (approximately 6 mm in diameter and 2 mm thick, containing 2.5-3.0 gm of material) were placed in a tungsten element resistance furnace (Centorr Associates, Inc., Figure 9), which was evacuated and backfilled with high-purity gettered Ar three times. Minimal contact between sample and support was obtained by placing the discs on edge. A positive pressure of flowing Ar (approximately 860 mm Hg) was maintained during the heating and cooling cycles. The furnace temperature was increased at a rate of $100^\circ\text{C}/\text{min}$. until the desired temperature of 1100, 1200, 1300, 1400, or 1500°C was achieved. This temperature was maintained for 0, 5, 15, 30, 60, or 120 min. and then the sample was quenched at $400^\circ\text{C}/\text{min}$. by turning off the furnace. An additional sample was heated to 900°C for 180 min. to obtain a comparison with the results of Strashinskaya and Stepanchuk.³² To allow for the energy input to the sample during heat-up, reaction time was considered as holding time plus heating time above 1100°C . Temperatures were

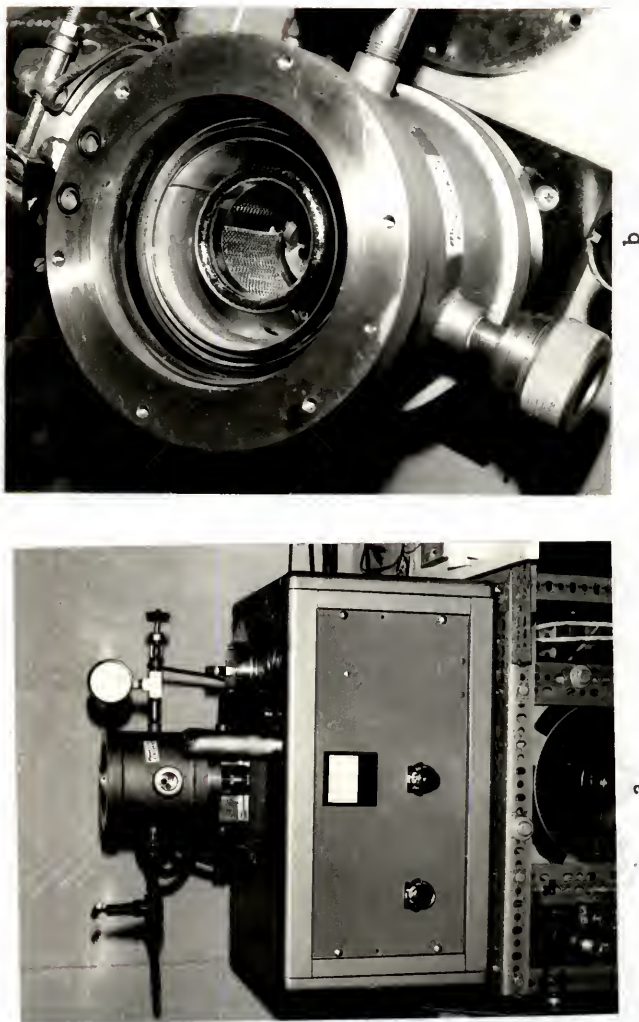


Figure 9. Centorr furnace: a) overall view, b) view showing concentric heat shields, heating element, and pressed disc mounted on edge.

measured using a W-5% Re - W-26% Re alloy thermocouple, positioned approximately 5 mm from the sample.

These sinter-reacted discs were broken into nuggets for metallographic preparation or pulverized to pass a 325 mesh screen for x-ray diffraction analysis. The nuggets were mounted in epoxy and the porosity filled by vacuum impregnation to improve their strength during polishing. These were polished using metal-bonded diamond discs (3M Company) and 0.3 μm alumina slurry on nylon cloths. The solid phases were decorated by electro-staining^{25,30} in 20 volume % NH_4OH electrolyte at 18 volts for 60-80 sec. (current density approximately 100 $\mu\text{amps}/\text{cm}^2$). The anode was a screw placed through the back of the mount and the apparatus is shown schematically in Figure 10. Under an optical microscope, the Ti appeared blue-purple, the TiB was tan, and the TiB_2 was white or light tan. The epoxy-porosity remained gray (Table 3). Unreacted pressed discs were also mounted, polished and stained to gain metallographic information about the initial compact.

Quantitative Microscopy Measurements

Quantitative Microscopy measurements were made using a combination of manual and electronic counts on an Imanco

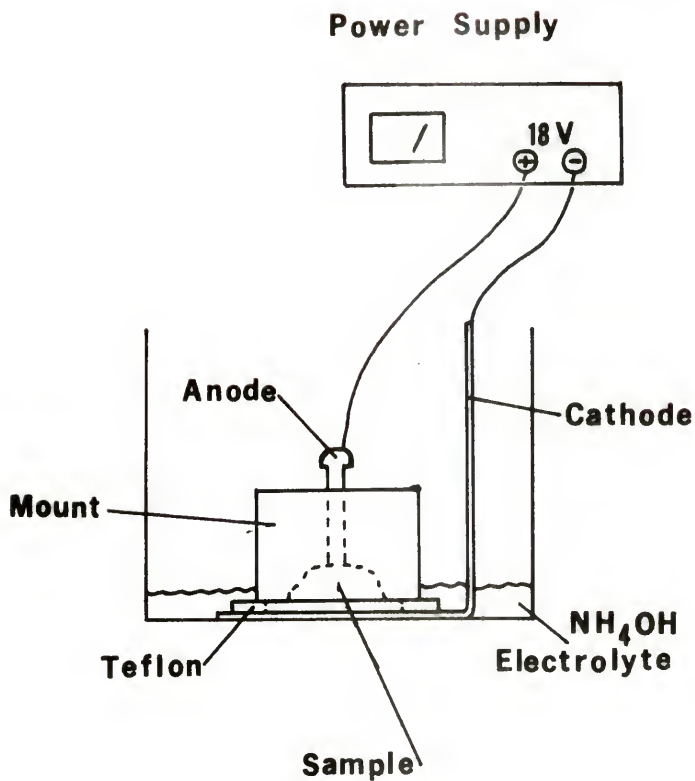


Figure 10. Schematic of electrostaining apparatus.

Table 3
Results of Electro staining

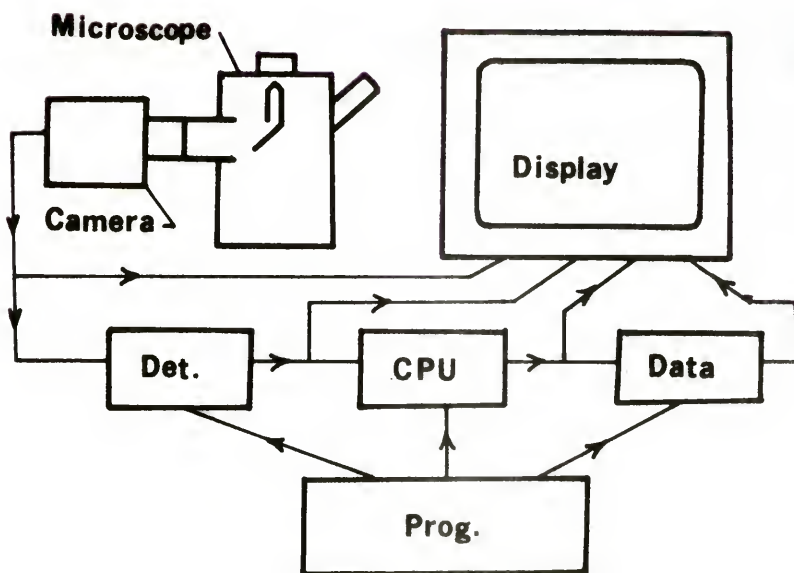
<u>Phase</u>	<u>Symbol</u>	<u>Color</u>	<u>Gray-shade</u>
Ti	α	blue-purple	gray
TiB ₂	β	white	white
TiB	γ	tan	light gray
porosity	δ	gray	dark gray

Quantimet 720 image analyzing computer. A block diagram of this instrument is shown in Figure 11. The optical image of a metallographic microscope is scanned using a vidicon tube and the image displayed as a series of picture points of varying intensity on a television screen. The gray-shade intensities of this representation depend on the contrast between various phases of the optical image. The number of picture points of a given intensity (or voltage pulse) may be detected and separated by setting suitable threshold windows electronically. Reference to Figure 12 shows a gray (G) and a white (W) particle in a black (B) matrix. If the phase boundaries were sharp and the vidicon tube provided an ideal signal, threshold settings at A and B could unambiguously separate these phases. All picture points with intensity below A would be detected as black, all points with intensity greater than B would be white phase, and the rest would be detected as gray phase.

Actual vidicon capabilities are not ideal and a transition range of intensity across a boundary is obtained in practice. For phases separated by a single threshold, the best agreement between displayed and detected image is usually achieved by setting the threshold midway in the intensity range. For phases separated by



a



b

Figure 11. The Quantimet 720 Image Analyzing Computer:
 a) view of instrument, b) block diagram of its
 operation.

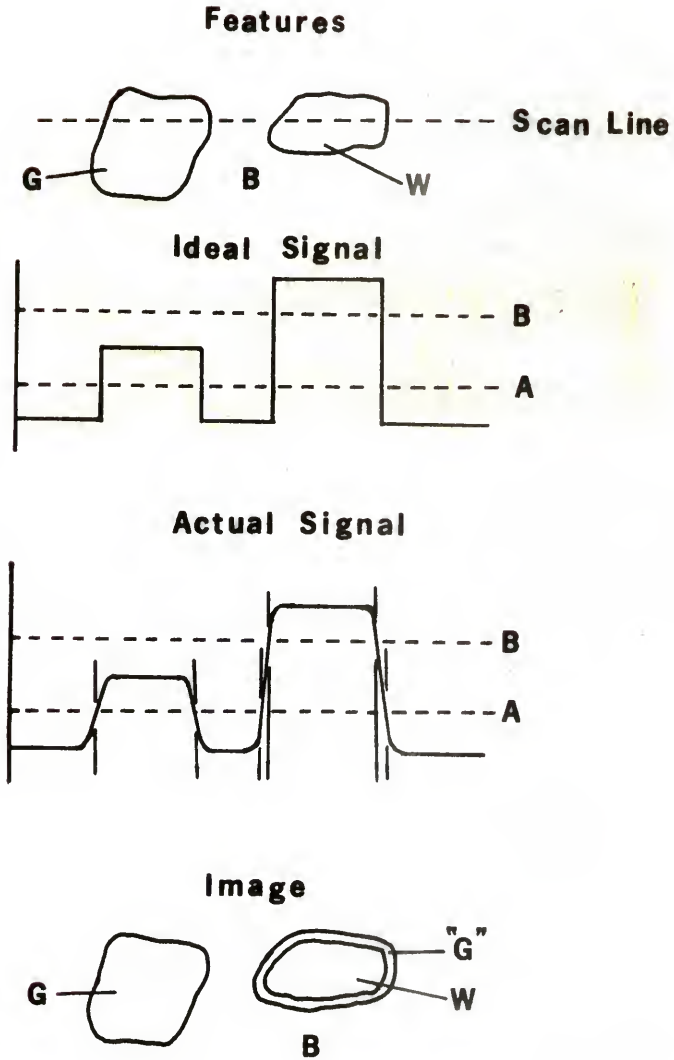


Figure 12. Effect of nonideal signal on detected image.

two or more thresholds, as at the black-white boundary, however, a web or halo of gray phase ("G") is detected around the white phase since some picture point intensities fall within the A-B threshold window. This is an artifact produced by the instrument; although methods exist to deal with this problem, the required accessories were not available for this study and an alternative was found. The "sizer" feature of the Quantimet subtracts a band of selected picture point width from one side of a detected particle or region (shown in black on Figure 13). Since most of the "G" halo was less than 10 picture points wide, setting the sizer to subtract a 10 picture point wide band from the edge of the detected gray phase removed most of the artifact. That portion of the true gray phase (G) also removed was then estimated manually and added to the reduced picture point count; allowance was also made for the small portion of "G" that was not subtracted by the sizer. Another problem is uneven illumination that may cause distortion, as shown in Figure 14. This was minimized by using only a small central portion of the available image for analysis. The Quantimet has three independent threshold settings and can thus separate four phases. The resulting colors and gray shades are summarized in Table 3. Figure 15 shows a view observed

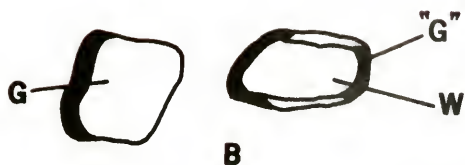


Figure 13. Effect of sizer on detected image.

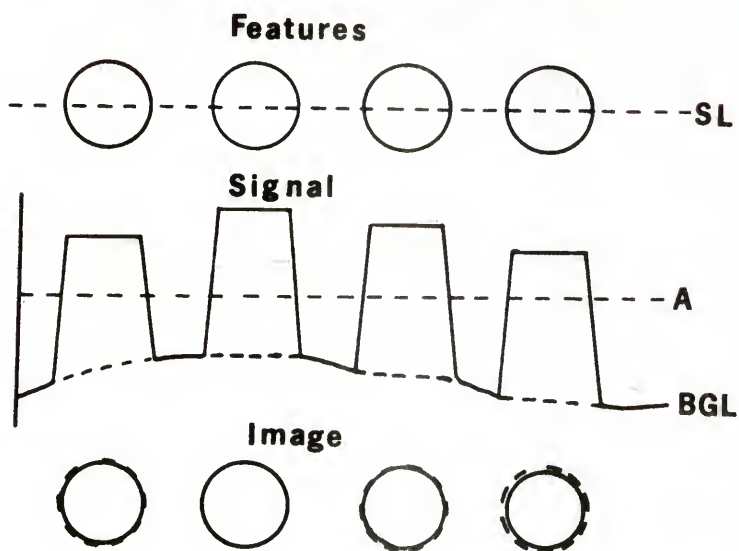


Figure 14. Effect of nonuniform background level on detected image.

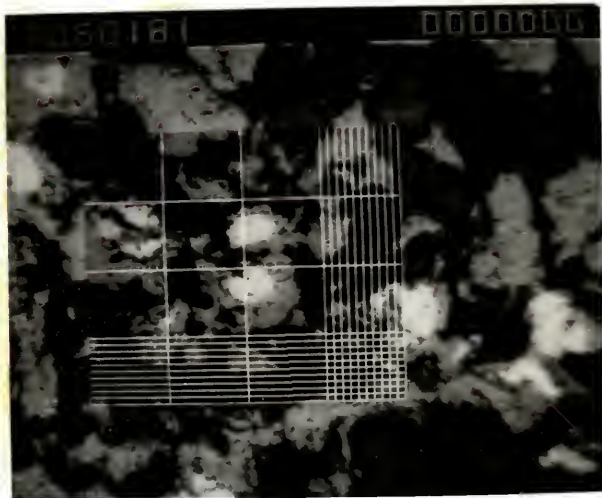


Figure 15. Image of microscope view displayed on Quantimet screen; grid indicates portion of available area analyzed for each grid placement.

by the instrument and the grid delineating the analyzed area. The sequence of black, gray, and white phases detected from it and the "G" halo may also be seen in Figure 16.

The image analyzing computer calculates the equivalent of the various Quantitative Microscopy counting measurements by considering each picture point as a point in a grid. For this study, a grid size of 400 x 400 points (or a total of 160,000) was selected. The actual size of this area (corresponding to L in Figure 4) was measured by a stage micrometer to be 200 μm x 200 μm or $4 \times 10^{-4} \text{ cm}^2$. The number of points detected for a phase, Q_V^i , divided by the total number of grid points provides a point count reading, P_P^i . The computer logic detects a change from one threshold range to another at a boundary and counts the number of points, Q_S^i , on the boundary between either increasing or decreasing intensity regions, i.e., on only one side of a particle or phase region. If the length of grid "line" is known, this gives a modified intercept count, P_L^i . Since the point density in the grid is so high, an approximation to the area fraction and phase perimeter, respectively, may be observed on the display. A one line memory permits counting the number of convex and concave tangent points per unit



Figure 16. Images detected by Quantimet: a) black phase, b) gray phase (note halo around white phase), c) white phase.

area for each phase, T_A^{i+} or T_A^{i-} , by "remembering if the point is the first or last one of that phase from a previous scan. This feature detects tangents on only one side of the phase but if enough counts are obtained, the statistics remain satisfactory. Fifty placements of the grid were made to obtain a distribution of values. These were averaged and the 95% confidence interval and coefficient of variation calculated (Appendix 3). Using these averages, the actual grid size (200 μm), and the Quantimet restrictions, the expressions for V_V , S_V , and M_V were modified as follows:

$$V_V^i = \bar{Q}_V^i / 160,000 \text{ cm}^3 / \text{cm}^3 \quad (35)$$

$$S_V^i = (0.50) \bar{Q}_S^i \text{ cm}^2 / \text{cm}^3 \quad (36)$$

$$M_V^i = 15,708 \bar{Q}_{Tnet}^i \text{ cm} / \text{cm}^3 \quad (37)$$

where \bar{Q}_V^i , \bar{Q}_S^i , and \bar{Q}_{Tnet}^i ($= \frac{\bar{Q}_{T+}^i - \bar{Q}_{T-}^i}{2}$) are the averaged instrument counts in the area, intercept, and tangent count modes, respectively. These parameters were determined for each of the four phases. Manual estimates of \bar{Q}_V^i , \bar{Q}_S^i , and \bar{Q}_T^i were made for TiB in the early stages of the reaction when it was present in small amounts. The contrast between the gray epoxy and the blue-purple Ti was not always great enough to give an unambiguous determination of Ti,

so manual estimates were also made of Q_S^i and Q_T^i for this phase. Although individual interface areas can be determined from P_L counts on particular combinations of boundaries, i.e., Ti-TiB₂ interface, the Quantimet could only determine a Q_S^i count for the complete boundary of a phase. Therefore, Q_S^i counts for the (Ti + TiB) and (TiB + TiB₂) phases combined were also measured to make solution of the following set of equations for six specific interface areas possible.

$$\begin{aligned}
 S_V^\alpha &= S_V^{\alpha\beta} + S_V^{\alpha\gamma} + S_V^{\alpha\delta} \\
 S_V^\beta &= S_V^{\alpha\beta} + S_V^{\beta\gamma} + S_V^{\beta\delta} \\
 S_V^\gamma &= S_V^{\alpha\gamma} + S_V^{\beta\gamma} + S_V^{\gamma\delta} \\
 S_V^\delta &= S_V^{\alpha\delta} + S_V^{\beta\delta} + S_V^{\gamma\delta} \\
 S_V^{\alpha+\gamma} &= S_V^{\alpha\beta} + S_V^{\alpha\delta} + S_V^{\beta\gamma} + S_V^{\gamma\delta} \\
 S_V^{\beta+\gamma} &= S_V^{\alpha\beta} + S_V^{\alpha\gamma} + S_V^{\beta\delta} + S_V^{\gamma\delta}
 \end{aligned}
 \tag{38}$$

The symbols α , β , γ , and δ are for the Ti, TiB₂, TiB, and porosity phases, respectively. Quantitative Microscopy measurements were also made on the mounted and polished starting material. The results of the above series of measurements were used to compute $\bar{\lambda}^i$, \bar{H}^i , the proximity parameter, P_x , selected velocity and curvature averages,

and the solutions for the different models presented above (Table 1). Data reduction was accomplished using several APL computer programs (Appendix 4).

Typical operation during sample measurements required that a field of view be selected and the focus and threshold adjusted. An independent measure of the variability of each of these steps was found by sixteen trials on the unstained starting material (this was essentially a two "phase" sample of solid and porosity). First, the instrument variability was determined by counting Q_V , Q_S , and Q_T sixteen times on a single field of view with the focus and threshold constant. Next, measurements were made with the focus readjusted after each reading and the threshold held constant. Finally, the focus adjustment remained undisturbed for a series of readings where the threshold was reset each time. Moore⁷⁹ has discussed many of the aspects affecting the accuracy of Quantitative Microscopy measurements.

Transport Experiments

Several additional experiments to determine the transport species and mechanism were performed. These are shown schematically in Figure 17. To determine if vapor transport is responsible for material movement, pressed powder discs of Ti and TiB_2 were placed in a Mo

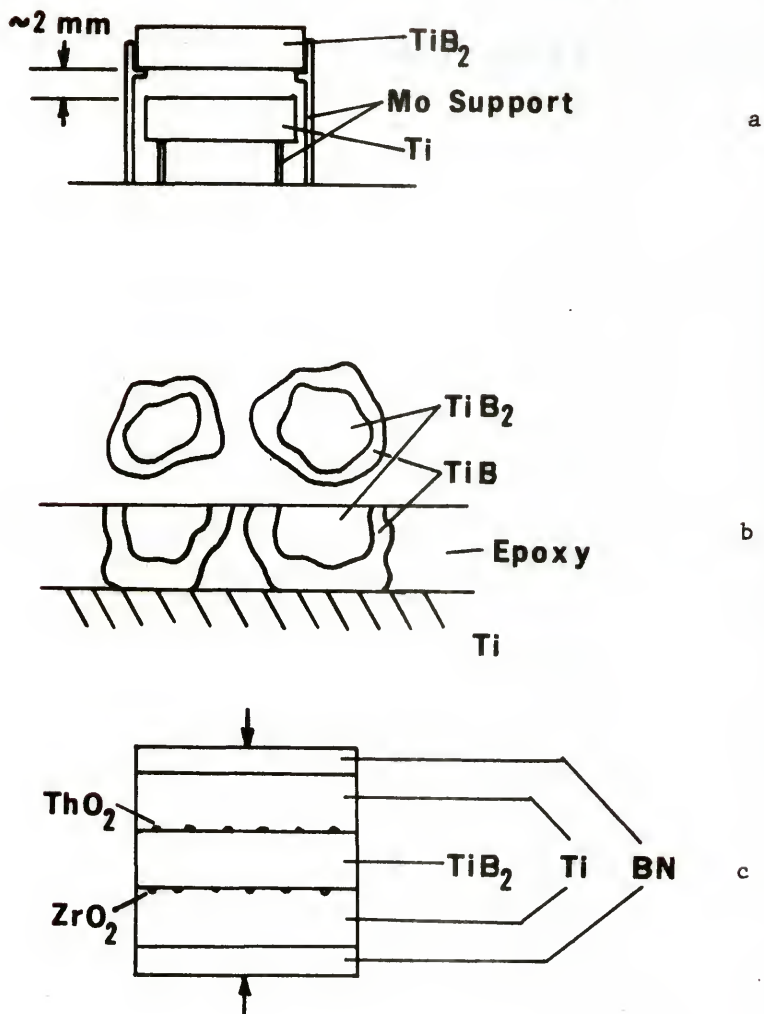


Figure 17. Schematic of transport experiments: a) vapor transport, b) surface or volume diffusion, c) diffusion couple.

cylinder, separated by approximately 2 mm. Weight and dimensional measurements were made on each disc before and after heating at 1500°C for 2 hours, the maximum time and temperature of this study. Since the Ar gas flow was from below, this would aid any transport that occurred from the lower disc; configurations with either Ti or TiB₂ as the lower disc were used. Significant weight changes would indicate operation of vapor transport from one or both of the starting materials.

A comparison of surface diffusion to volume diffusion for material transport was obtained by placing grains of TiB₂ 60 - 70 μm in size on polished solid Ti discs (obtained by hot pressing powder) and Ti grains on TiB₂, and heating to 1500°C for 2 hours. These samples were then polished to remove part of the grains. If surface diffusion was significantly faster than volume diffusion, a TiB reaction layer on the grains would be revealed by electrostaining as a ring with unreacted material in the center, as depicted in Figure 17b. If surface diffusion was not significant, then the reaction interface would move up through the grain more uniformly by volume diffusion and no product ring would be observed - a relatively sharp change from reactant to product would be seen polishing through the grains.

To learn which species was diffusing, a Ti-TiB₂ diffusion couple was prepared (Figure 17c). This provided a geometry with minimal porosity and so was a case where either volume diffusion or grain boundary diffusion might predominate. Solid discs of Ti and TiB₂ were obtained by hot pressing pressed powder discs. These were polished to 0.3 μm with Al₂O₃ slurry. A TiB₂ disc was sandwiched between two Ti discs to provide two different interfaces and two types of markers were used. One was ThO₂ powder of approximately 2 - 4 μm size, obtained by ultrasonically dispersing the powder in ethanol, allowing it to settle for 2 hours, and removing the liquid near the surface. This was placed on one of the Ti surfaces and allowed to evaporate. A similar area dispersion on a glass slide is shown in Figure 18. The other marker was ZrO₂ fibers (Union Carbide Corporation), approximately 10 μm in diameter. This sandwich was heated to 1300°C for 3 hours in a vacuum hot press; a light pressure was maintained on the sample through the heating cycle to insure good contact between the discs. The result was mounted and polished perpendicular to the two interfaces to observe the location of the reaction layer and the markers.

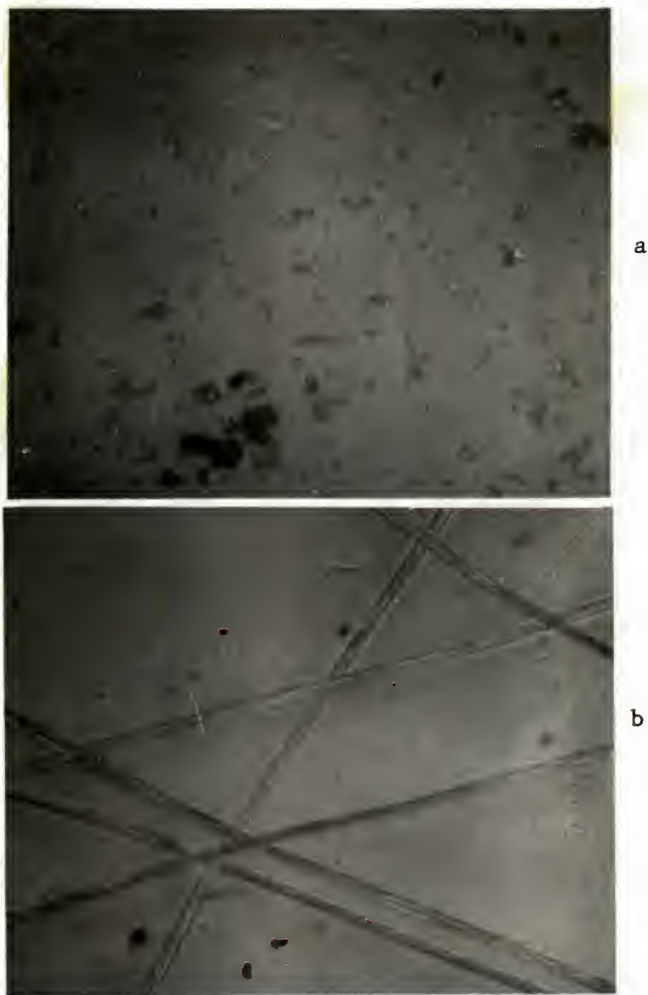


Figure 18. Diffusion couple markers dispersed on glass slides: a) ThO₂ powder (440 X), b) ZrO₂ fibers (220 X).

Quantitative X-Ray Analysis

To confirm the results of Quantitative Microscopy, a quantitative x-ray analysis of the sinter reacted material was made using the internal standard method.⁸⁰

A Philips Electronics instrument with a vertical goniometer was used. Goniometer speed was $1/2^\circ$ 2 θ /min. An automatic theta compensating divergence slit provided a constant irradiated sample volume. The $1/2^\circ$ receiving slit and graphite crystal monochromator focussed the diffracted beam into a Norelco Scintillation detector. The output pulses were sorted by a pulse height analyzer to reduce background counts. This signal was recorded on a strip chart recorder (chart speed 1 in./min.) and the peak integrated intensity measured using a scaler-timer counting over the duration of a peak. Excitation voltage of 45 kv and filament current of 20 ma. were used on the copper target x-ray tube.

To reduce the effects of particle orientation, the sample holder was rotated at 20 rpm. The phenolic holder, Al support, and cable drive are shown in Figure 19. The disc-shaped sample volume is approximately 1 mm deep and 18 mm in diameter. The irradiated area is rectangular, 12 mm x 15 mm, centered within the disc.

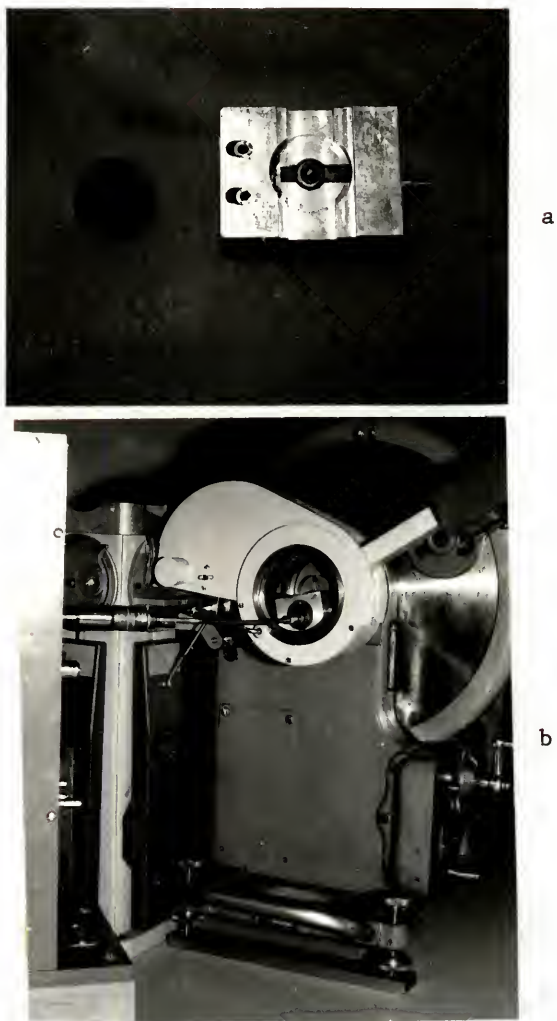


Figure 19. X-ray equipment: a) phenolic sample holder and Al support, b) cable drive and goniometer (protective cover not shown).

The sample loading technique consisted of placing the loose powder on the disc, pressing it with the flat of a glass slide, and scraping the excess off with the edge of the slide. An earlier attempt to load samples using the McCreery technique⁸¹ to improve sample packing was made (on a non-rotating sample holder), but the small improvement obtained for these powders did not justify the extra effort and the rotating holder was retained.

The sinter-reacted samples were pulverized in a mortar and pestle until they could pass a 325 mesh sieve. The ductile Ti in the early stage reaction material would not all pass the screen and so was re-added after sieving the rest. The mass of these samples was in the range of 0.5 - 1.5 gm. The internal standard material chosen was NaCl as it has strong, sharp peaks that do not significantly overlap those of the other materials and can be ground easily to -325 mesh. Ten weight % of -325 mesh NaCl was mixed with each sample. The calibration standards were made by mixing reactant and product powders containing 10 weight % NaCl in the appropriate amounts to give nominal volume fractions of 0, 10, 25, 50, 70, 90, and 100% TiB. The reactant powder was obtained by mixing equimolar amounts of -325 mesh Ti and TiB₂ powders with -325 mesh NaCl. Since commercial TiB was not available,

it was made by reacting several pressed pellets of mixed Ti and TiB_2 at $1500^\circ C$ for 2 hours. These conditions were chosen to avoid the formation of eutectic liquid and because longer times did not provide a greater yield of TiB . The product mixture for standards was made by pulverizing this to pass 325 mesh and mixing it with $NaCl$. The mass of the standards was 0.5 - 2.5 gms. and was high enough to ensure accurate weights.

Prior to analyzing the samples, the experimental deviation of several factors was determined. Machine error was determined by making 10 separate measurements of the major peak for pure TiB_2 and $NaCl$ samples with and without sample rotation and/or goniometer motion. Next, the deviation due to particle orientation and sample loading technique was determined from 10 measurements of each material. Samples were removed and remounted after each run. The deviation of a single peak indicated the packing error and the deviation of the ratio between two peaks of the same material indicated the influence of particle orientation. The variability due to mixing was found from 10 runs on mixtures of Ti and TiB_2 and of TiB and $NaCl$. This effect was determined from the deviation in peak intensity ratios of the two mixed materials. Calculation of the average, 95% confidence interval (using

Student's *t* correction), and coefficient of variation were made for each of the above (Appendix 3).

An internal standard calibration curve was obtained from 10 runs on each standard. A background count was measured for 100 sec. at $2\theta = 50.8^\circ$ ($d = 1.7959 \text{ \AA}$). The integrated intensity of the Ti ($d = 2.244 \text{ \AA}$), TiB_2 ($d = 2.033 \text{ \AA}$), NaCl ($d = 2.821 \text{ \AA}$), and TiB ($d = 2.140$ and 2.161 \AA) peaks was measured from the difference of the scaler-timer count and background. The angular range of 2θ used was $45 - 30^\circ$. The two TiB peaks were combined into one measurement to increase the TiB count and avoid errors due to peak overlap. The ratios of metal and boride to NaCl were averaged and plotted as a function of known volume fraction. Alexander and Klug⁸⁰ have shown this calibration curve should be linear.

A similar technique was used for analyzing the reacted samples (1100 - 1400°C) except that only four runs were made on each. The volume fraction for each sample constituent was found from the calibration curve. The extent of reaction parameter, x , and various model functions, $f(x)$ (Table 1), were computed.

SECTION III RESULTS AND DISCUSSION

The results of the above experiments are presented and related to the several alternative mechanisms presented earlier.

Metallographic Examination

A qualitative examination of the series of metallographic samples for each temperature shows the quantities of Ti and TiB_2 decreasing and TiB increasing with time. The porosity also increases and, at higher temperatures and longer times, is estimated to be about 50%. Some pullout due to polishing is observed, especially at the shorter times or lower temperatures, where less sinter bonding occurs. Edge rounding of the TiB and TiB_2 and relief polishing of the epoxy is also seen, as would be expected from samples of this particle size and range of hardness. In some cases, the boundary between the borides could also be detected due to differential relief during polishing. During the grinding stage with 15 μm metal-bonded diamond discs, the brittle TiB_2 often fractured and left many small pits on the surface. These were usually removed by the polishing step, but those that re-

mained often became sites of pitting corrosion during the electrostaining; a compromise between allowing sufficient staining time to achieve adequate color contrast and yet avoiding excessive corrosion of Ti or TiB_2 at longer times was required for some specimens. The deterioration of the decorated colors with time, especially for Ti, occasionally required that samples be repolished and restained for examination in the Quantimet.

The TiB product first appeared at the contact regions between Ti and TiB_2 and began growing into the TiB_2 . As the reaction proceeded, the TiB began extending to the sides of this region and coating the TiB_2 particles. It took approximately 60, 30, and 15 min. to coat the larger particles at 1100, 1200, and 1300°C, respectively, while at 1400 and 1500°C, most particles had a TiB product layer surrounding a TiB_2 kernel after only 5 - 8 min. Many smaller grains were fully converted to TiB by the time coating of the larger particles was complete. After 2 hours at 1500°C, almost all of the TiB_2 was consumed, although some of the larger particles had a central core of unreacted material and uncoated portions of some TiB_2 particles could still be seen. In contrast to the results of Strashinskaya and Stepanchuk,³² no contact reaction zones were seen in the sample heated to 900°C for 180 min.

This may be due to the smaller particle size or lesser purity of their samples. Some completely uncoated particles were found by electron microprobe examination to be reacted, suggesting these grains had become electrically insulated from the rest during vacuum impregnation and hence did not stain. Figure 20a - 20e shows a representative sequence of micrographs for this reaction, while Figure 20f illustrates this last point.

The Ti phase evolution shows these large platelike particles decreasing in both length and breadth but maintaining a non-equiaxed aspect until the reaction is near completion. At this stage, the particles are usually observed bonded to the TiB network with large voids surrounding them; these are presumably the regions formerly filled with larger Ti grains (center of Figure 20e). In some well-reacted specimens, a few Ti particles much larger than the rest are seen (Figure 21). During the course of the reaction, the Ti particle boundaries seen in section become rounded and smooth at local roughness while the boride boundaries remain ragged.

Figure 22 is an SEM micrograph of a polished and stained sample. The particle rounding, epoxy relief, and corrosion pits are readily visible in this view. Figure 23 shows fracture surfaces of the unreacted starting mate-



a

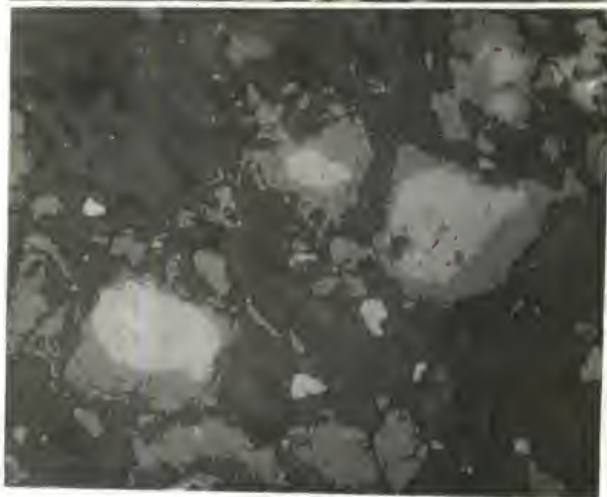


b

Figure 20. Sequence of reaction: a) starting material, b) initial contact reaction (both 440 X).



c



d

Figure 20. Sequence of reaction: c) reaction continues, d) TiB_2 particles coated (both 440 X).

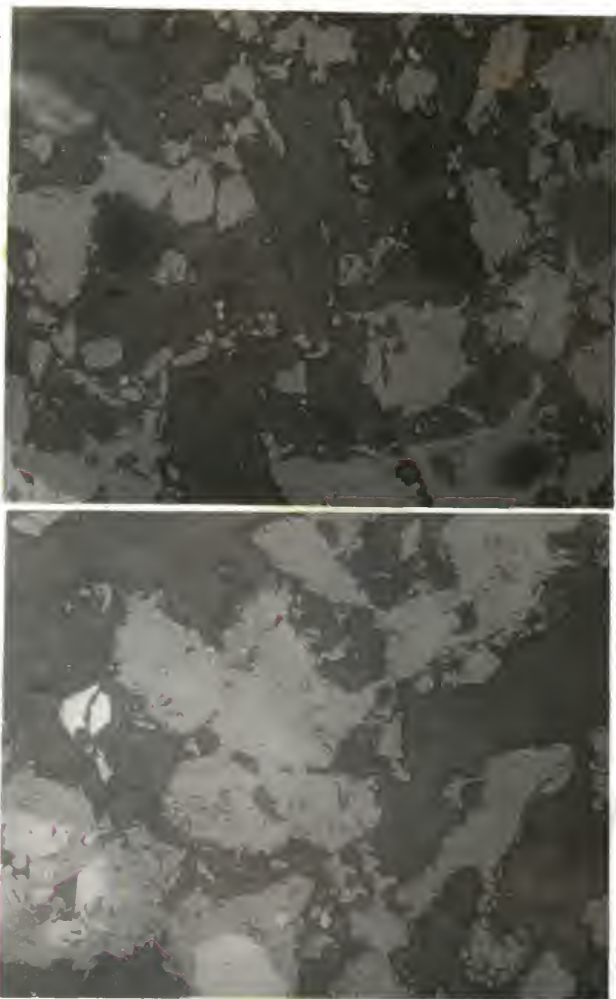


Figure 20. Sequence of reaction: e) near completion, f) unreacted TiB_2 (both 440 X).



Figure 21. Large Ti grain and surrounding porosity (110 X).

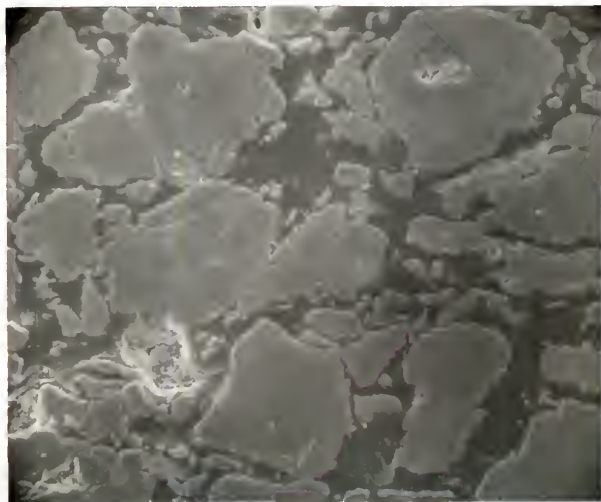


Figure 22. Polished and electrostained surface (540 X).



a



b

Figure 23. Micrographs of fracture surfaces: a) initial sample (570 X), b) sample reacted at 1300°C/17 min. (1950 X).



Figure 23. Micrographs of fracture surfaces: c) sample reacted at 1500°C/124 min. (1030 X).

rial, a 1300°C/17 min. sample, and a 1500°C/124 min. sample. The initial pointed contacts and openness of the structure may be seen. This open structure is retained and expanded with the development of projecting and apparently overlapping needles of TiB.

Transport Experiment Results

The metallographic examination suggested that Ti is the major diffusing species since TiB is seen to cover the TiB₂ and not the Ti. That the reaction proceeds from a contact region also supports volume or surface diffusion mechanisms - no initial uniform coating of Ti or TiB on TiB₂ was seen, as would be expected for vapor transport. Vapor transport of Ti or B is not a significant mechanism in this reaction, even though the Ti vapor pressure at these temperatures is fairly high ($\sim 10^{-4}$ min. Hg).⁸² This is confirmed by the separated discs experiment (Figure 17a); the weight change of either disc was less than 0.5%. In addition, the Mo support inadvertently touched the Ti disc and after heating was found with a gold coloration near the region of contact. Auger analysis of this surface showed the presence of O, N, Mo, Mg, C, and Ti, providing more evidence for surface diffusion of Ti. It has been reported that TiB₂ vaporizes congruently⁸³ with a

vapor pressure of $<10^{-6}$ mm Hg at 2200°C , so little vaporization from this refractory material would be expected at the temperatures utilized here.⁸⁴

Confirmation that surface diffusion is the major mechanism of Ti transport is provided by the experiment in which TiB_2 grains were placed on Ti. Figure 24 shows the product ring microstructure expected (Figure 17b) if surface diffusion is significantly faster than volume diffusion. This view also demonstrates the fracture holes characteristic of grinding TiB_2 - additional polishing to remove them was not attempted for fear of polishing through the grains.

Initial observation of the shrinking TiB_2 phase suggested Ti was diffusing through the product layer. However, it was subsequently recognized that even though Ti was coating the TiB_2 by surface diffusion, product formation could either occur by reaction of Ti with TiB_2 at the TiB-TiB_2 interface or by diffusion of B through TiB to react with Ti at the particle surface; both mechanisms might also operate simultaneously. The diffusion couple results demonstrate that both Ti and B diffuse, but Ti diffuses at a faster rate. Figure 25 shows the two couples with ThO_2 and ZrO_2 markers. The reaction layer is $\approx 25 - 30 \mu\text{m}$ thick. The markers are at the Ti-TiB



Figure 24. Result for surface diffusion transport experiment (440 X).

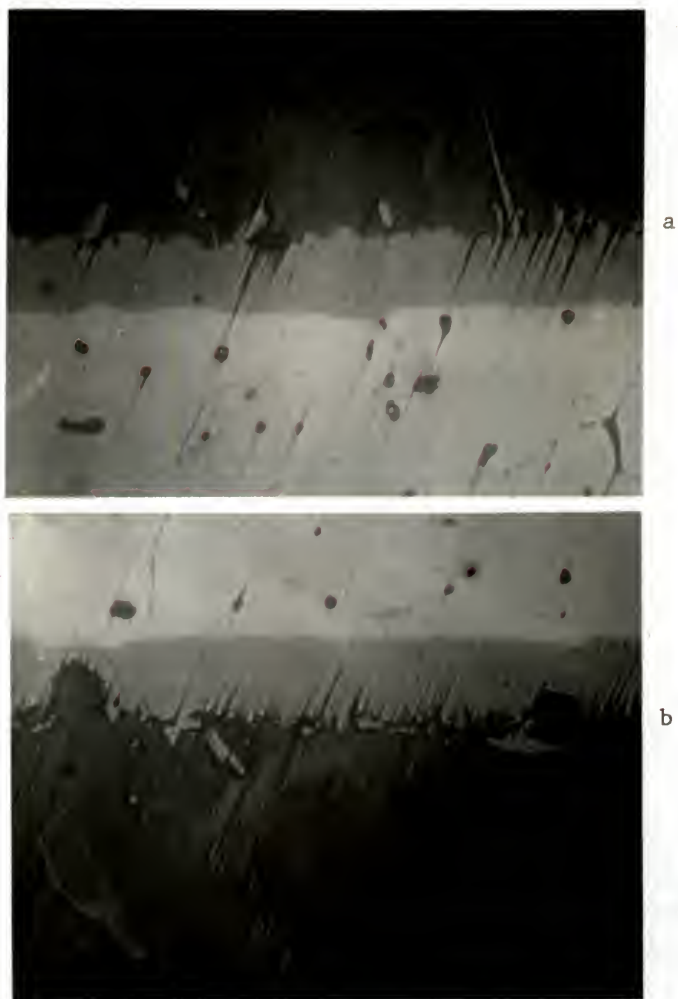


Figure 25. Diffusion couple interfaces: a) ThO_2 markers (440 X), b) ZrO_2 markers (440 X).

interface, demonstrating that Ti diffused into the TiB_2 and TiB. This result contradicts the contention of several previous investigators^{31,32} that B is the major diffusing species. However, they did not use markers and none of the visible observations made here conflicts with their micrographs or the descriptions of their couples. Several needles of TiB projecting into the Ti may be seen, as well as particles of TiB present in the Ti with no visible connection to the TiB layer. These correspond to the wedges or teeth of boride phase that have been reported by earlier researchers. They provide evidence of counter diffusion of B, which precipitated from solid solution during cooling. The distance of these precipitates from the TiB layer ($\approx 10 - 40 \mu m$) suggested diffusion occurred along grain boundaries. However, etching in a very dilute solution of HF and H_2O_2 showed these particles are located at grain boundaries and within grains. The TiB grain structure was revealed as moderately columnar with many grains extending completely across the product layer.

Hot pressing the TiB_2 at $1900^\circ C$ for 3 hours gave about 85% dense material. To achieve greater densities, higher temperatures ($\approx 2300^\circ C$) and/or much higher pressures ($\approx 20,000$ atmospheres) are required.⁸⁵⁻⁸⁷ The porosity is

visible in the TiB_2 but not in the TiB layer, indicating it was absorbed during the transformation by expansion of the TiB. Comparison of the TiB wedges visible on the diffusion couples and the overlapped TiB needles in Figure 23 show a similar morphology. An excess of Ti appears necessary to form these needles: Decker and Kasper¹⁹ used an excess of Ti in producing their TiB single crystal needles for x-ray crystal structure analysis.

The results of metallographic analysis and the transport experiments show the reaction initiates at the contact points between Ti and TiB_2 particles and subsequent reaction proceeds rapidly due to surface diffusion of Ti over the TiB. The Ti then reacts to form TiB and continues to react with TiB_2 by diffusing through the TiB reaction layer.

Quantitative Microscopy Results

The Quantitative Microscopy results follow qualitative observations. The Ti and TiB_2 volume fractions, surface area per volume, and total curvature per volume all decrease as the reaction proceeds; the TiB parameters all increase initially with a slight decrease in surface area later. The porosity generally increases or holds steady with time. These results were accelerated with increasing

temperature. They are tabulated in Appendix 5 and shown graphically in the figures indicated below. Where shown, the error bars designate the 95% confidence interval. Data for 1100°C samples were not collected because of excessive pullout during polishing.

The volume fraction data (Figures 26 through 29) for the solid phases fit the trends well except for the 1200°C/31 min. reactant point; although this point may reflect a real plateau in the volume-time relation, there is no corresponding plateau in TiB. Since $\sum V_V^i = 1$, an equal but opposite shift in porosity fraction gave the results as drawn. These results also show that at 1400 and 1500°C, the reaction goes almost to completion very quickly but then advances very little. At these temperatures, the value of V_V^{Ti} is very small; during its determination many fields of view gave $Q_V^{Ti} = 0$. Since the molar volume of Ti is 2/3 that of TiB₂, the observed values for Ti are too low. The metallographic examination for these times and temperatures suggests that most of the Ti is isolated in a few large grains. Thus, the sample is not representative of the true volume fraction of Ti since it is no longer as homogeneous or uniform as before. A random sectioning plane could easily miss this portion of the Ti volume fraction, and many more fields of view

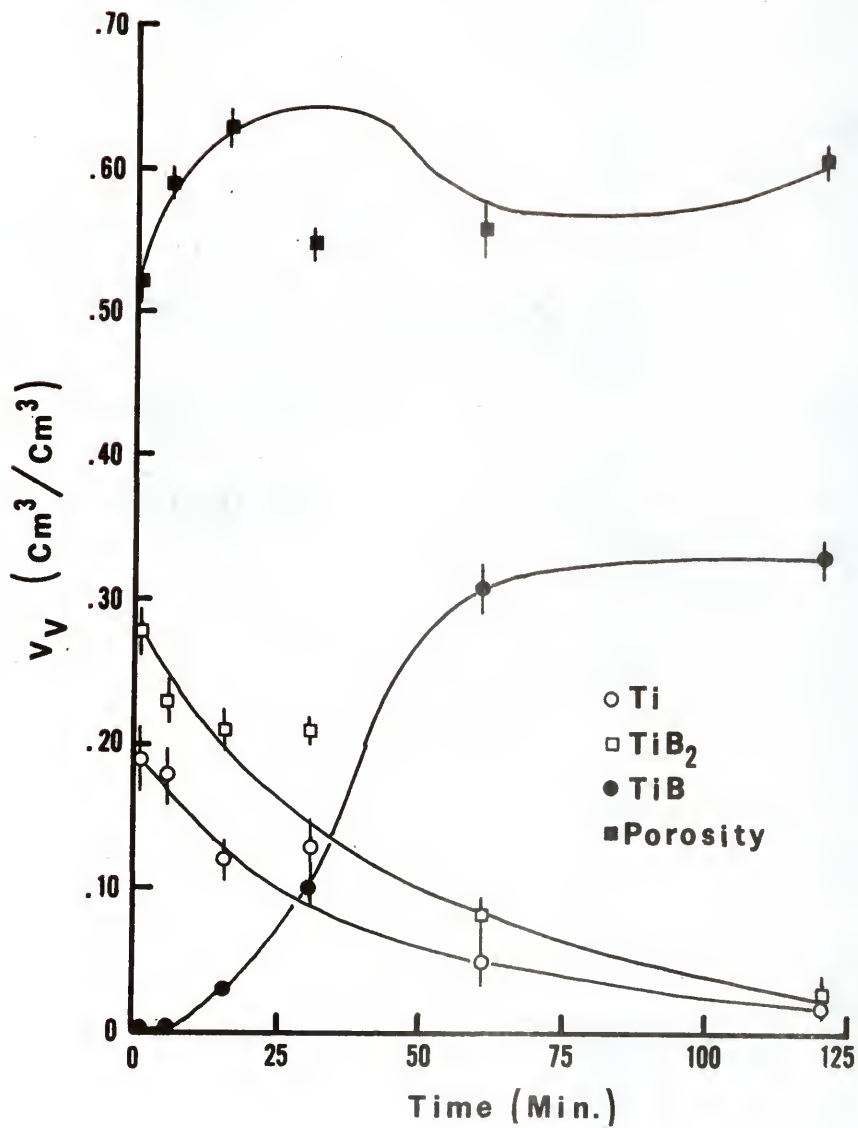


Figure 26. Quantitative Microscopy volume fraction results for 1200°C .

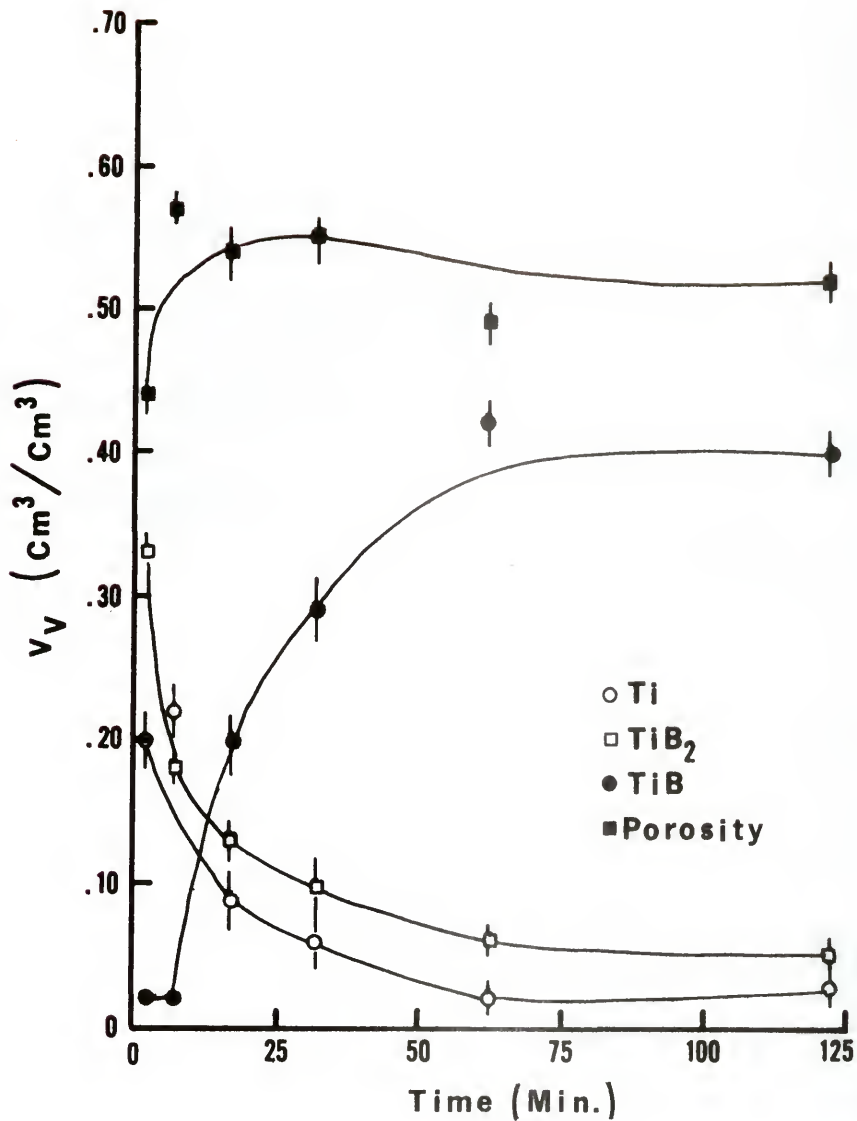


Figure 27. Quantitative Microscopy volume fraction results for 1300°C .

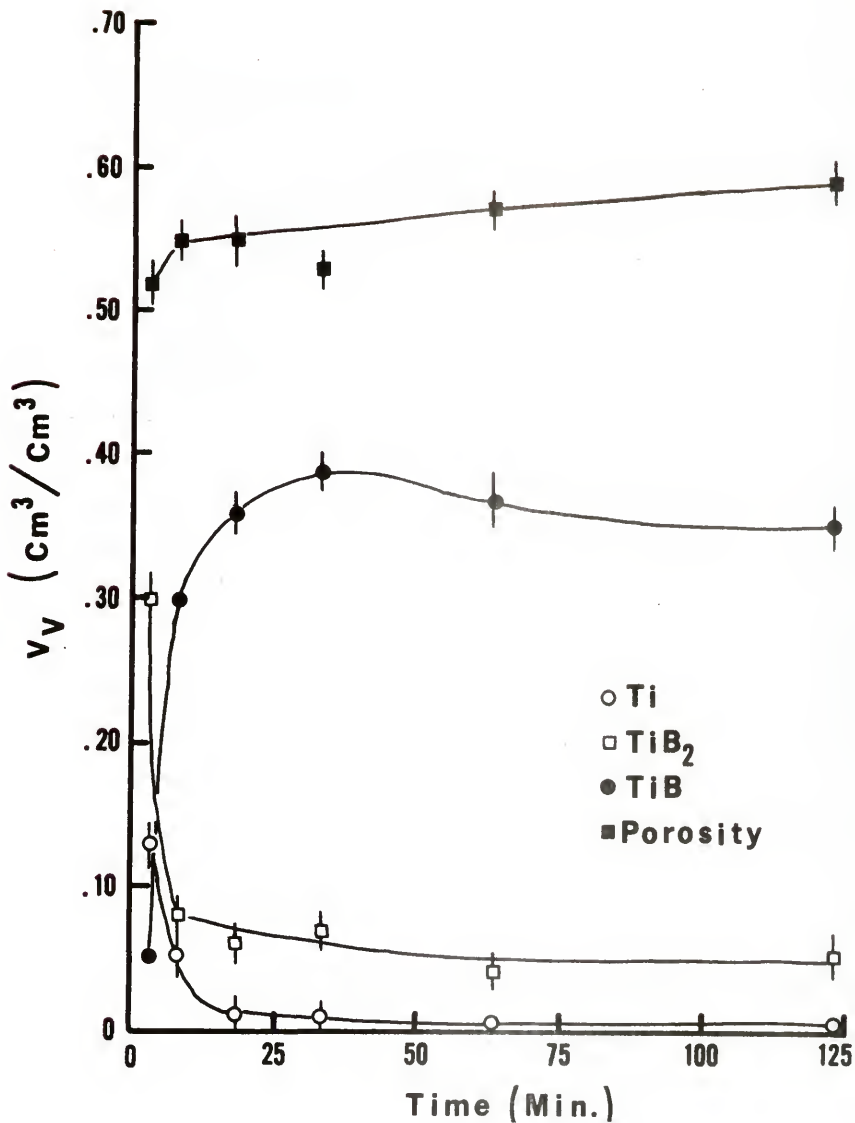


Figure 28. Quantitative Microscopy volume fraction results for 1400°C .

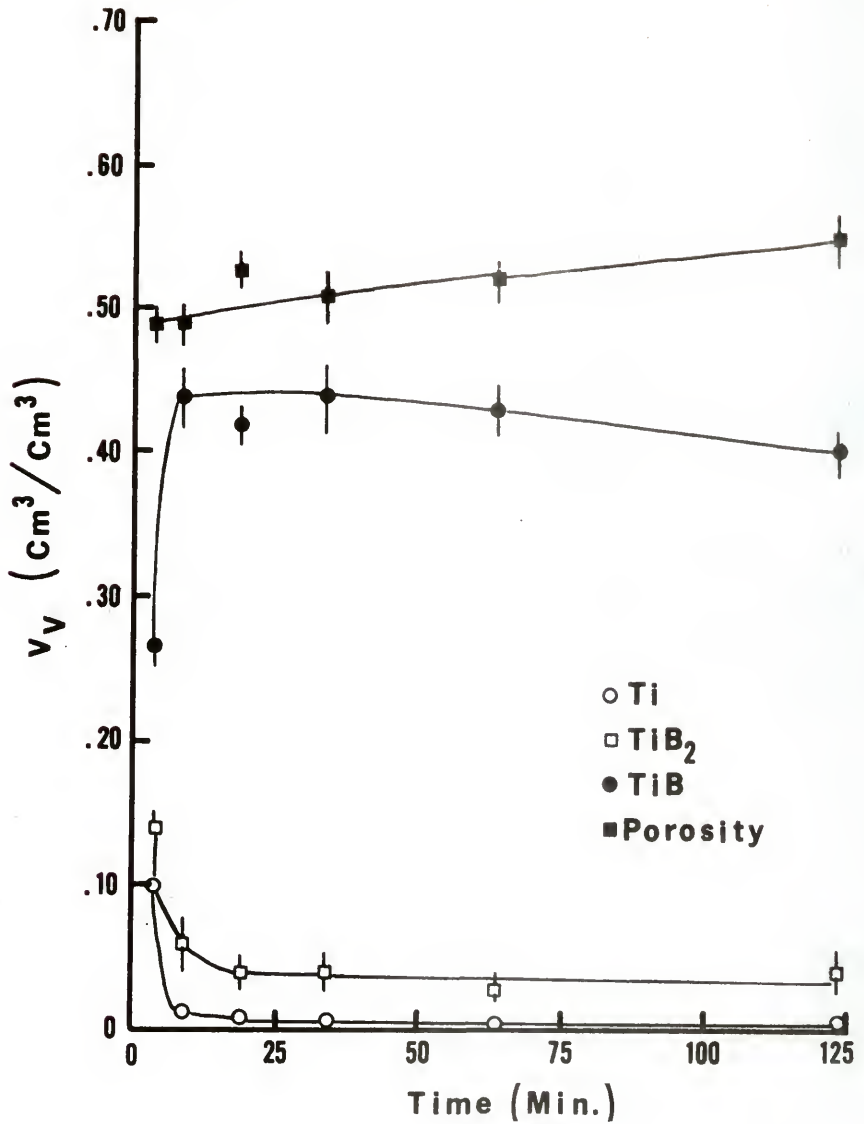


Figure 29. Quantitative Microscopy volume fraction results for 1500°C .

and/or polish planes would have to be examined to reflect the true volume of Ti in the samples.

The measurements for volume fraction porosity were in the range 45 - 60%; these were considered high although in qualitative agreement with the observed microstructure. To check these results, the porosity of the remaining unmounted samples was measured by an independent immersion method (using wax impregnation). These results are tabulated in Appendix 6; a graphical comparison of the porosity measured by both techniques is given in Figures 30 and 31. The immersion method shows a porosity range of 30 - 45%, which is much closer to the expected result. The slight porosity increase for initial times may be due to the use of several smaller nuggets for their measurement rather than one or two larger ones. The discrepancy in values between the two methods can be explained in the early stages of the reaction by pullout and in all stages by rounding of grains during polishing. This causes the solid volume "seen" by the Quantimet to be smaller than it really is, and the porosity to be correspondingly larger. This difference amounts to 10 or 15%, equivalent to approximately 16,000 - 24,000 picture points. If a representative value of $\bar{Q}_S = 2,500$ counts is taken for the solid-porosity interface, this number of points may be

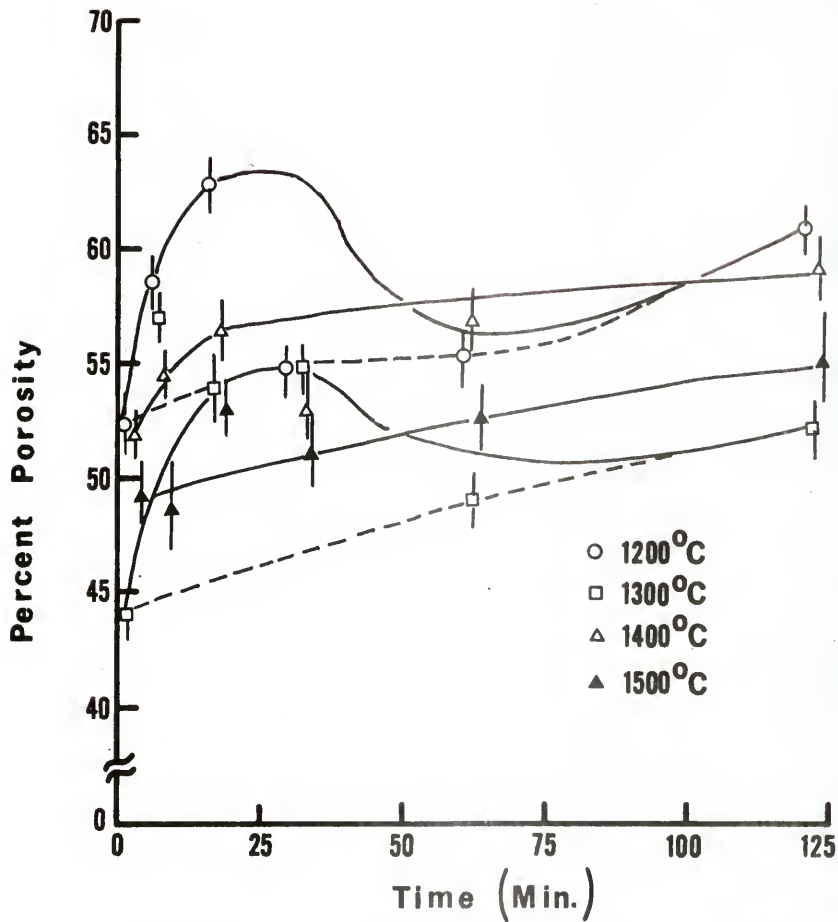


Figure 30. Porosity determined by Quantitative Microscopy.

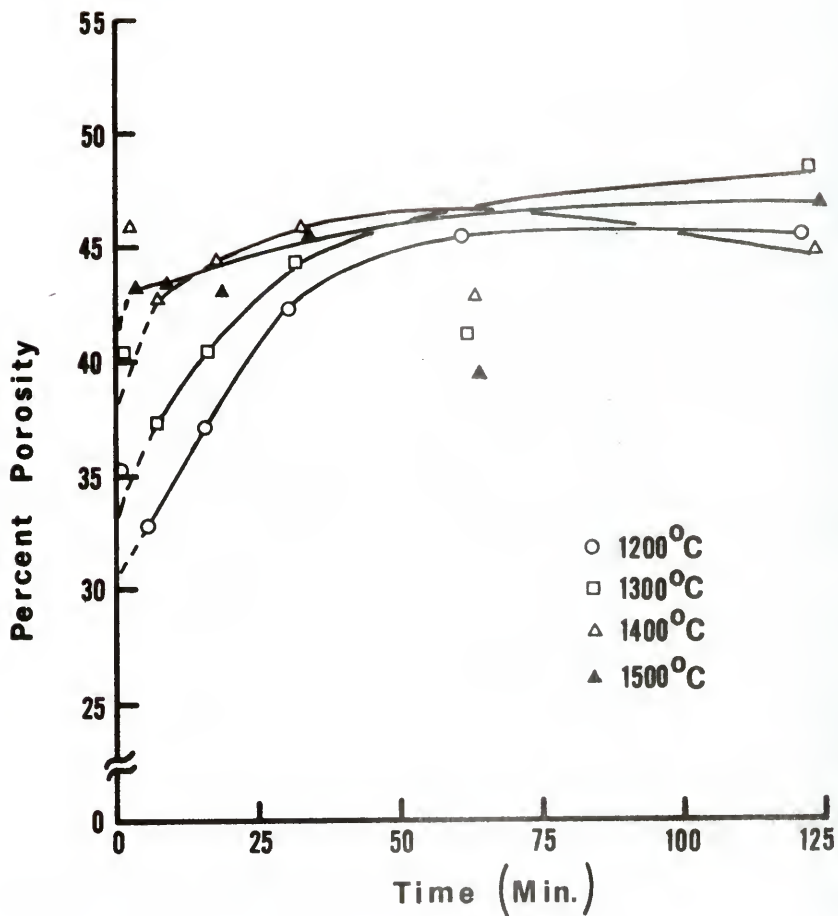


Figure 31. Porosity determined by immersion displacement.

doubled to account for both sides of a phase. Since each picture point is a $1/2 \mu\text{m}$ square, doubling or quadrupling this value is equivalent to a $1 - 2 \mu\text{m}$ band around the solid phase. Rounding by this amount is possible and would explain most of the point count difference. This would increase at later stages where the \bar{Q}_S count is closer to 3,000. The remaining point count deficit would be due to pullout; data in Figure 30 reflect the greater influence of pullout at lower temperatures since greater porosity is seen, contrary to expectation. This porosity discrepancy was not attributed to instrumental errors because the sum of individual volume fractions is equal to unity within 0.5% for almost every case, as shown by tabulations of Point Count Errors in Appendix 5. To determine if this discrepancy altered the relative amounts of solid phases measured, the mole fractions of each solid phase were calculated (Appendix 5) and plotted (Figures 32 - 35). The results show the reactants to have been measured in equimolar amounts for 1200 and 1300°C; the influence of large isolated Ti particles cited above distort these results for 1400 and 1500°C. Thus, it was felt the rounding affected the solid phases in approximately the same proportions and confidence in their relative amounts was retained.

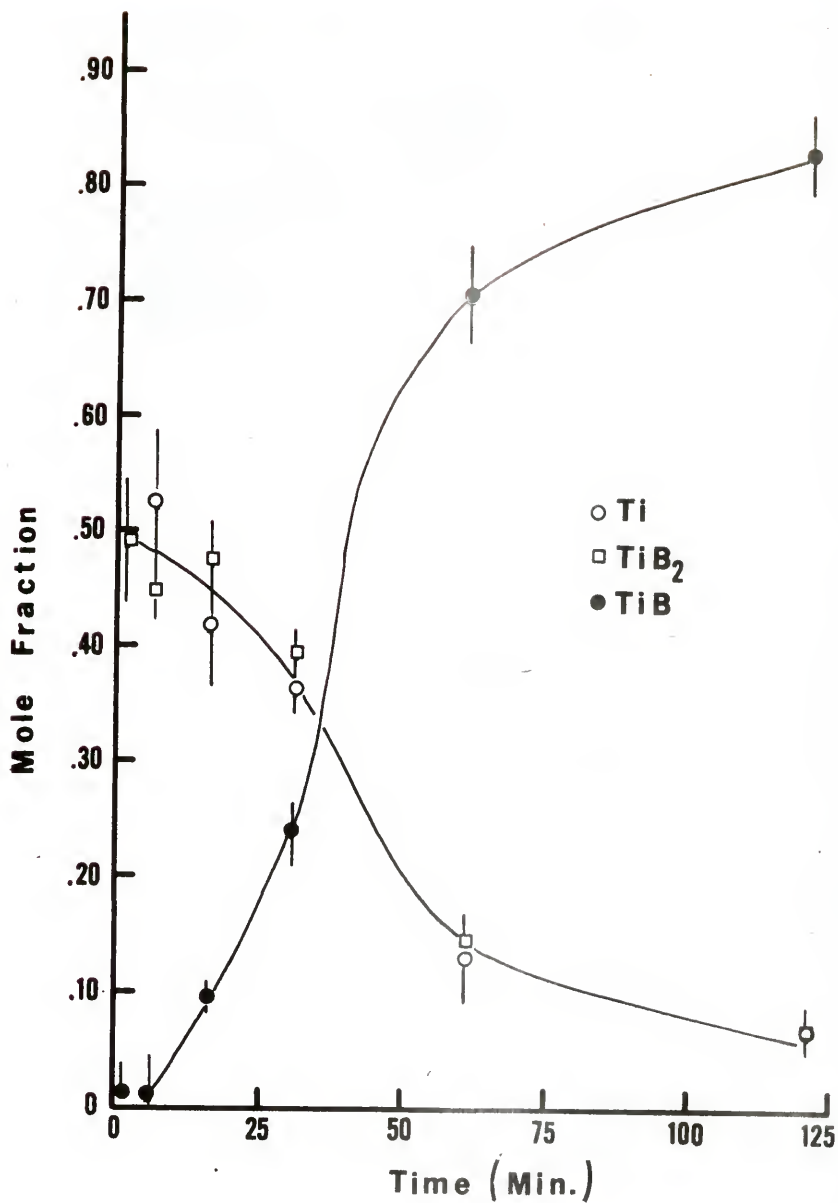


Figure 32. Quantitative Microscopy mole fraction results for 1200°C.

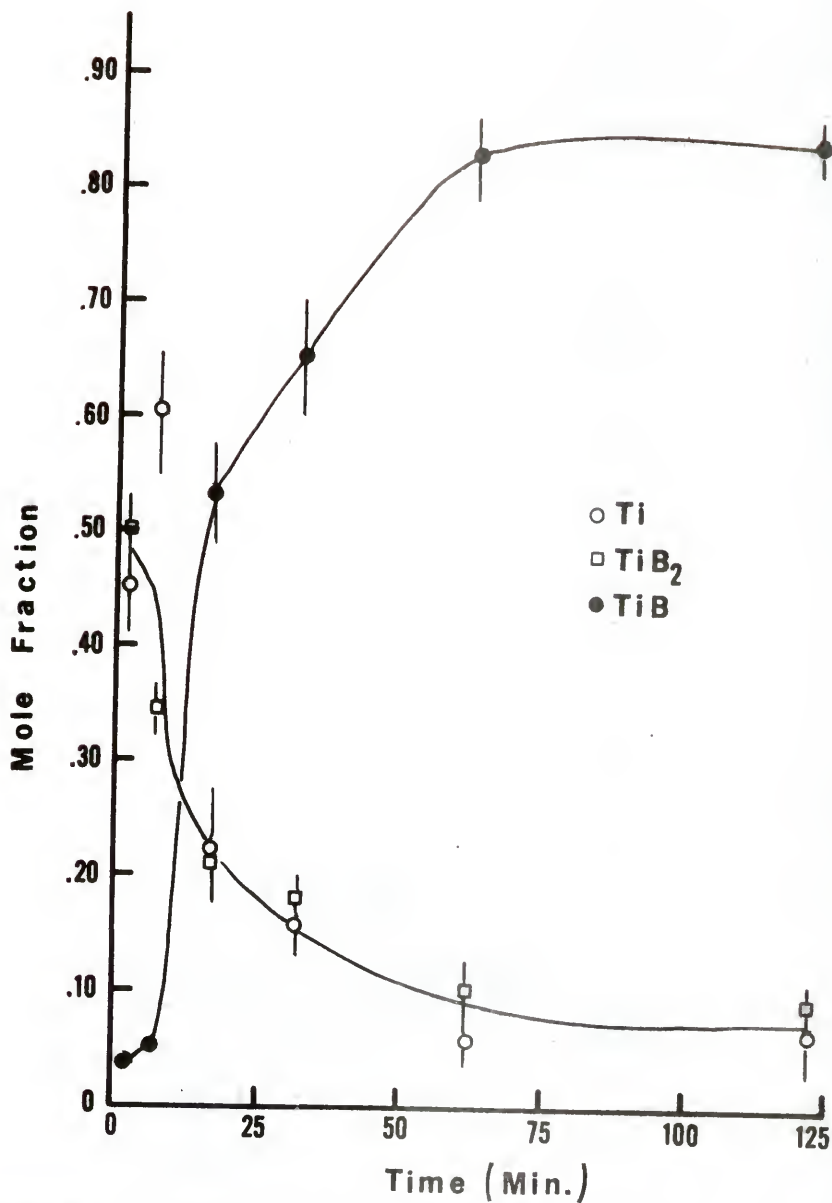


Figure 33. Quantitative Microscopy mole fraction results for 1300°C.

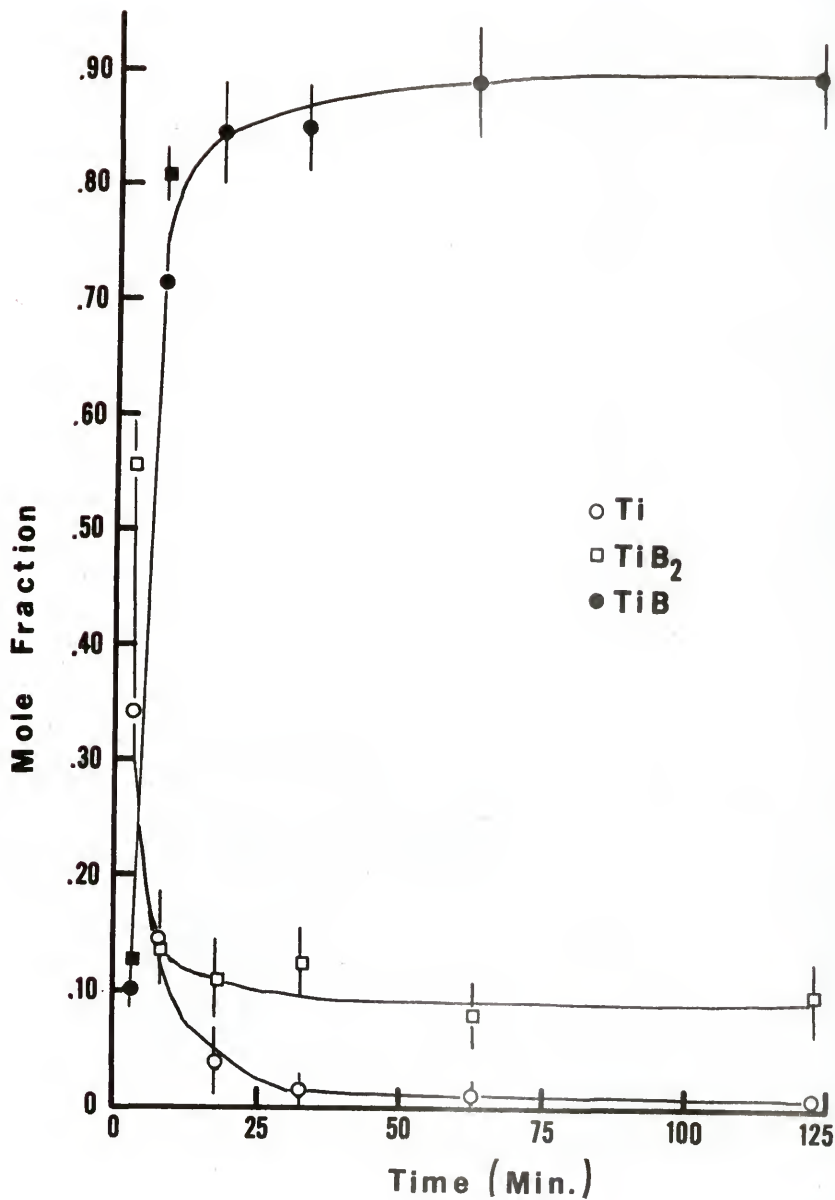


Figure 34. Quantitative Microscopy mole fraction results for 1400°C.

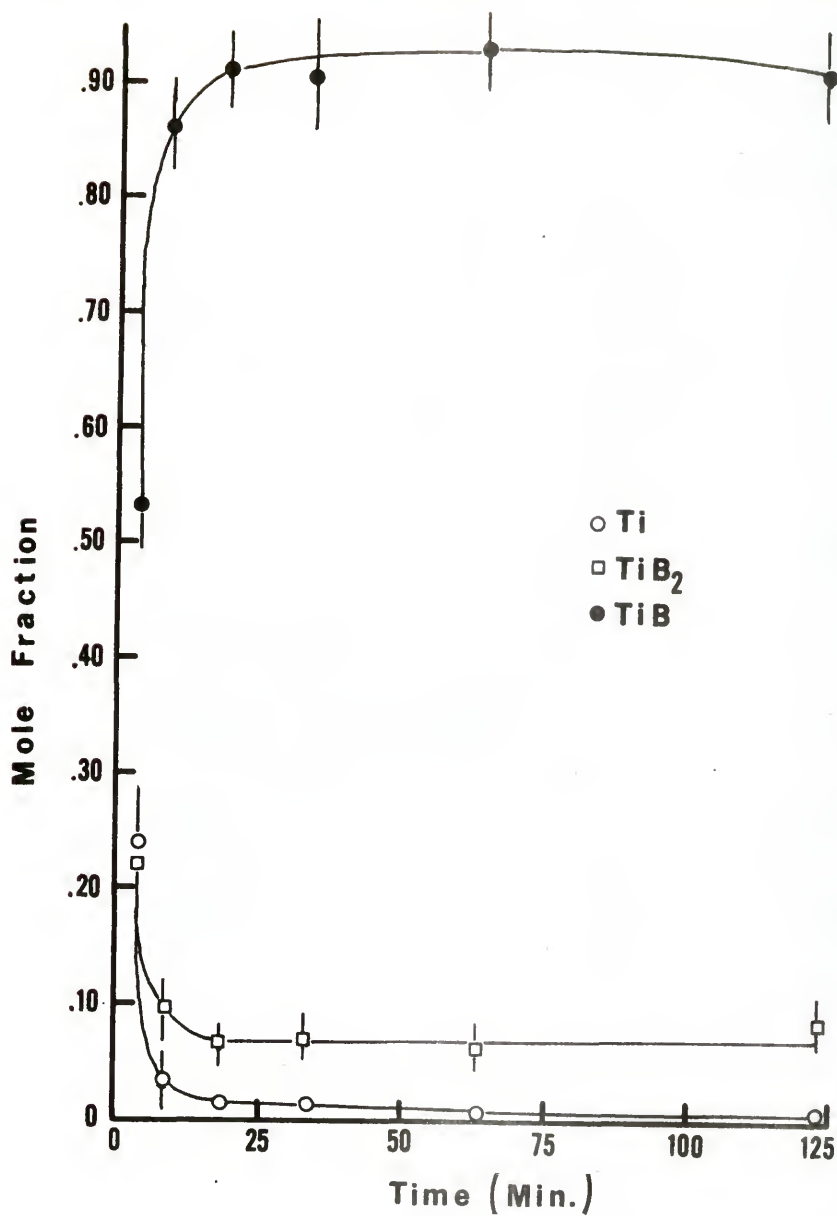


Figure 35. Quantitative Microscopy mole fraction results for 1500°C.

Figure 31 also shows a pronounced increase in porosity with time and temperature. This increase was observed independently on the six pressed samples used to make TiB for x-ray standards. The mass and external dimensions of these discs were measured before and after heating. These data, presented in Table 4, show the consistency of the disc pressing step and a definite increase in porosity from 31 to 42%. The slight difference from the immersion method is due to the greater proportion of surface pore volume to total pore volume in the small nuggets used for displacement measurements compared to the larger pressed discs.

In seeking an explanation for this porosity increase, it may be noted that two moles of TiB form for each mole of TiB_2 consumed and cause a boride volume increase of 67%. If this expansion does not totally replace the volume of Ti consumed, the powder compact will expand unless greater densification due to sintering occurs. The influence of sintering TiB or TiB_2 on the density of the powder compact was determined by weighing and measuring the volume of pressed discs of these powders before and after heating to 1500°C for 2 hrs.; densification of less than 1% was realized. It may be recalled⁸⁵⁻⁸⁷ that higher temperatures and pressures than used here are required for

Table 4
Data for TiB Standard Material

Sample Number	1	2	3	4	5	6
<u>Before Heating</u>						
mass gms	2.7125	2.5825	2.6793	2.9870	2.7245	2.8120
diameter cm	1.768	1.768	1.768	1.768	1.768	1.768
height cm	.356	.338	.351	.391	.358	.368
nugget volume cm ³	.873	.829	.860	.960	.879	.904
solid volume cm ³	.603	.574	.595	.664	.605	.625
porosity %	30.94	30.78	30.79	30.86	30.12	30.87
<u>After Heating</u>						
mass gms	2.7006	2.5723	2.6680	2.9743	2.7146	2.7990
diameter cm	1.859	1.859	1.859	1.859	1.854	1.862
height cm	.379	.358	.371	.417	.381	.391
nugget volume cm ³	1.028	.972	1.007	1.131	1.029	1.065
solid volume cm ³	.592	.564	.585	.652	.595	.614
porosity %	42.38	41.98	41.89	42.33	42.14	42.37
mass loss %	.439	.395	.422	.425	.363	.462
porosity change	11.44	11.20	11.10	11.47	12.02	11.50

Samples are equimolar Ti and TiB₂ powders mixed and pressed into discs. Heating conditions: 1500°C for 2 hrs. Porosity change is final porosity percentage minus initial porosity percentage.

significant densification of TiB_2 . Thus, the 10 - 15% porosity increase that occurs during this reaction is due primarily to the volume increase upon transformation of TiB_2 to TiB .

The surface area per volume determinations are in agreement with the volume fraction results, as shown in Figures 36 through 39. The S_V^{Ti} and $S_V^{TiB_2}$ decrease as their volume decreases, while the rapid increase in S_V^{TiB} reflects the formation of interior TiB - TiB_2 interface and exterior TiB -porosity interface. This value subsequently decreases as TiB_2 volume is removed and approaches the total solid-porosity area. The decrease in total solid-porosity area at higher temperatures mirrors the increase in porosity discussed above. Those points where $S_V^{TiB} > S_V^{porosity}$ are due to different Q_S counts on opposite sides of the solid phases of the microstructure. This $S_V^{porosity}$ ($\sim 1200 \text{ cm}^2/\text{cm}^3$) corresponds to $\sim 5 \times 10^{-2} \text{ m}^2/\text{gm}$, which is much lower than the BET values given earlier (56 - 66 m^2/gm) for the starting powders. This difference can be attributed to the limits of optical resolution of the microscope, the larger number of small TiB_2 particles, and the crevices of the deformed Ti powder swarf.

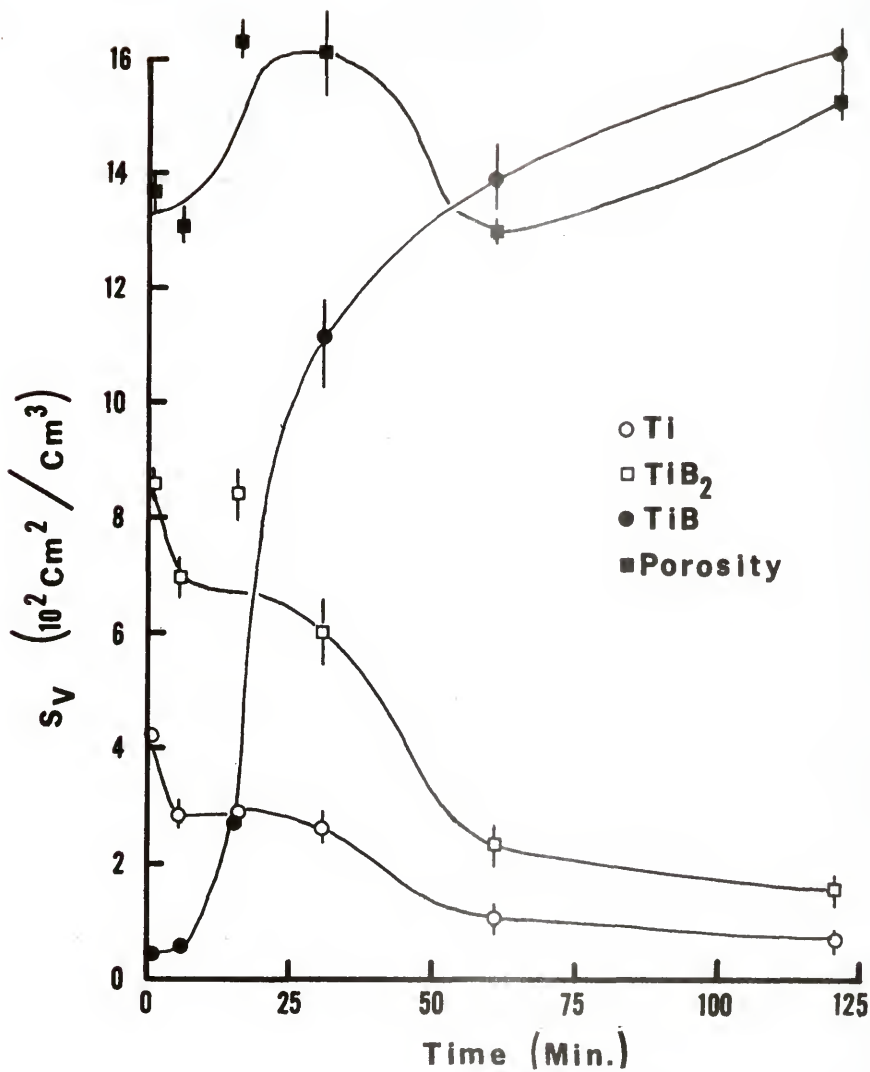


Figure 36. Quantitative Microscopy surface area per volume for 1200°C .

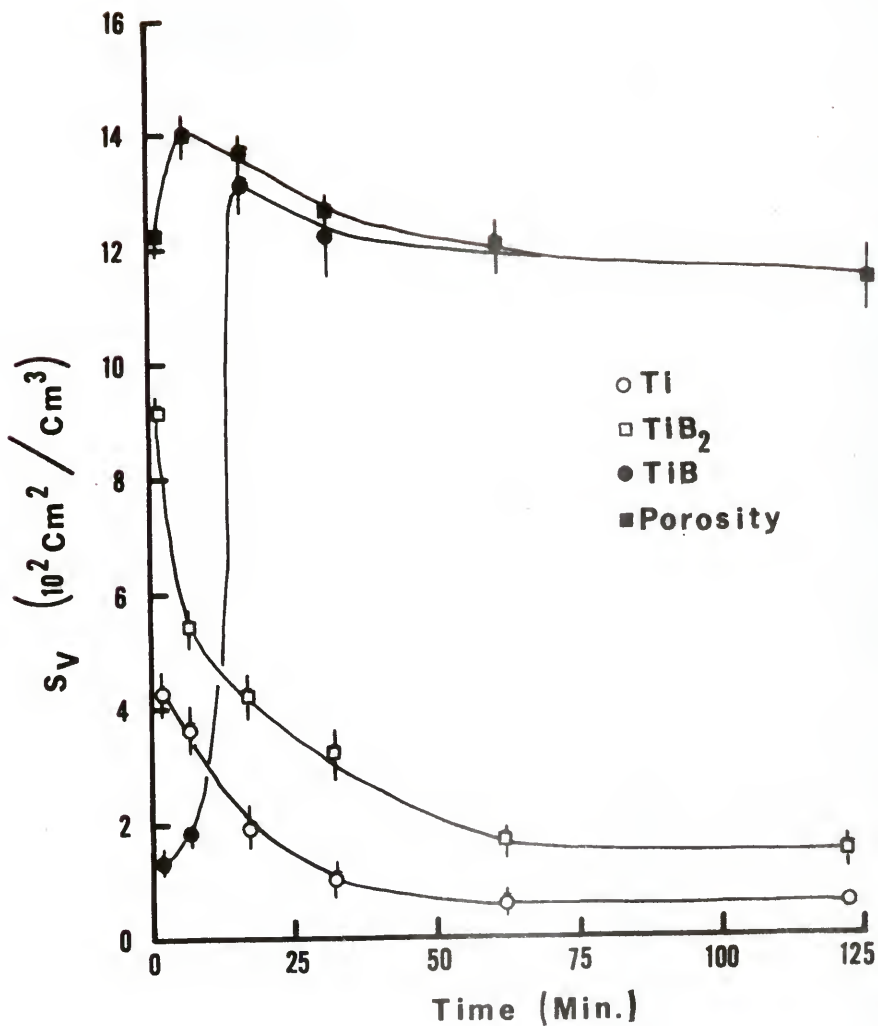


Figure 37. Quantitative Microscopy surface area per volume for 1300°C .

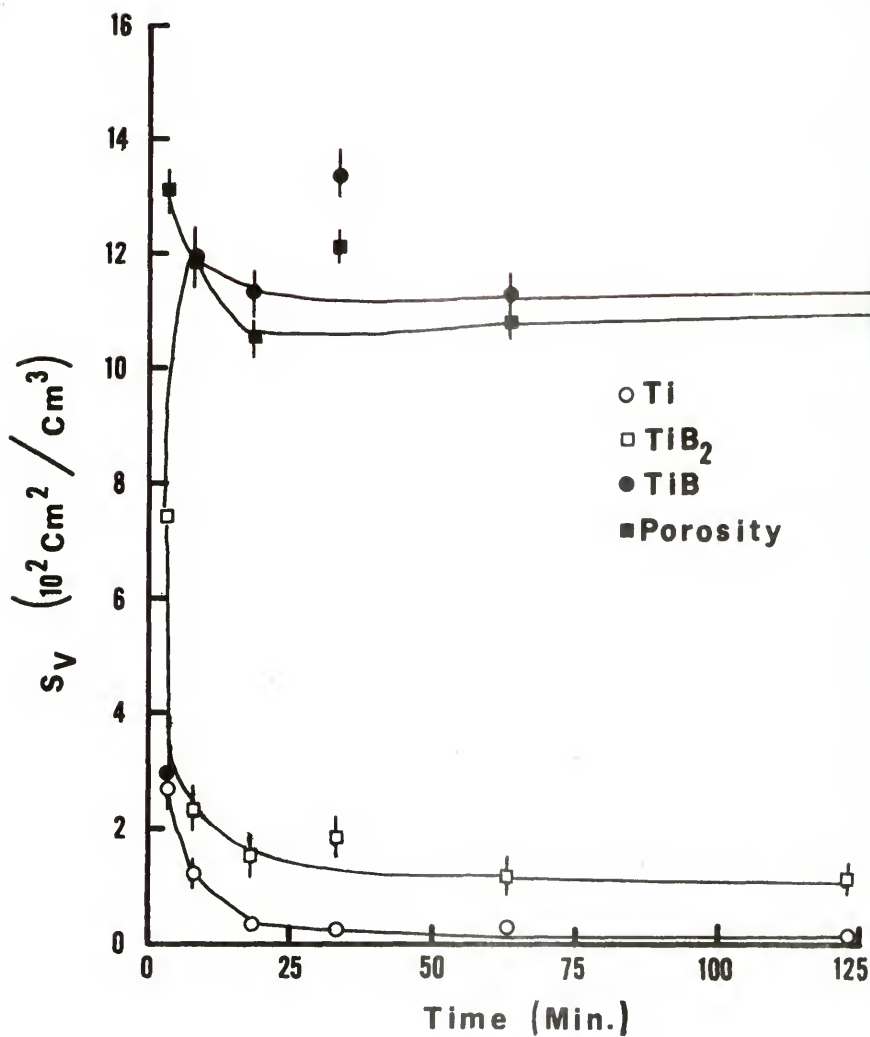


Figure 38. Quantitative Microscopy surface area per volume for 1400°C .

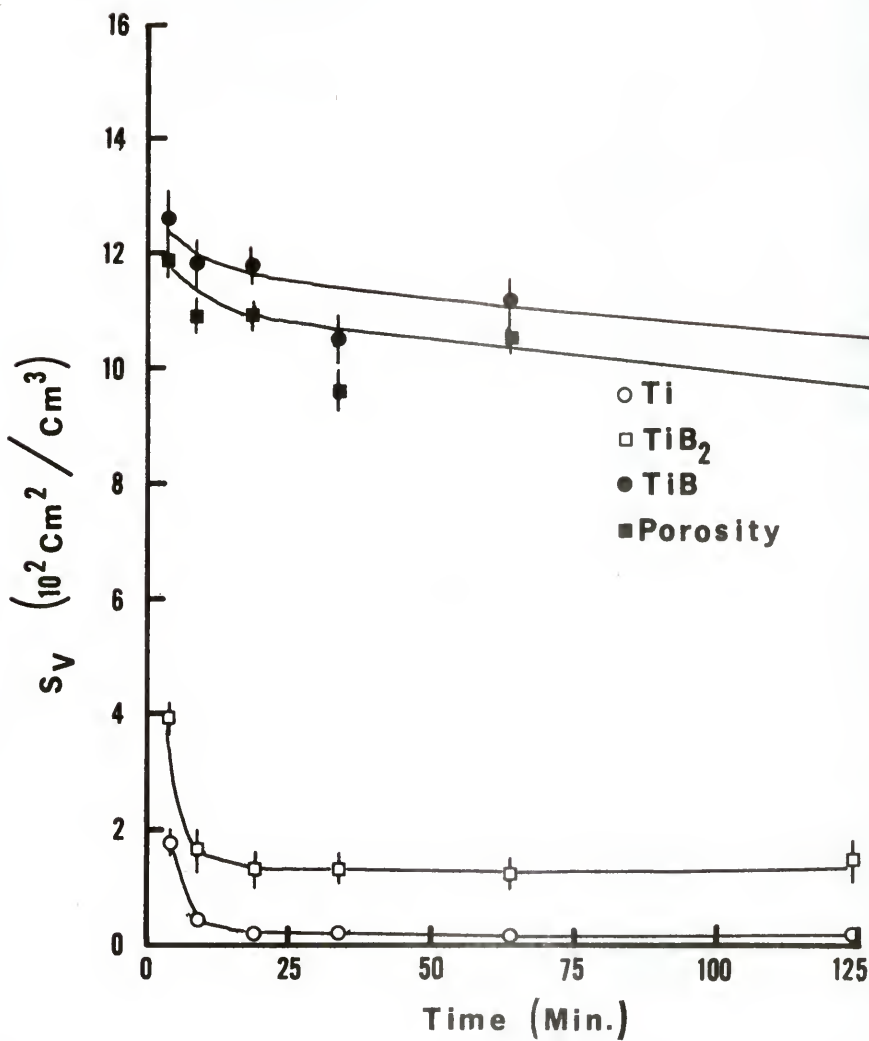


Figure 39. Quantitative Microscopy surface area per volume for 1500°C.

The specific interface areas between phases calculated from the S_V^i data are also given in Appendix 5 and Figures 40 through 43. Except for the Ti-TiB₂ interface, all results follow the pattern expected from the previous qualitative and quantitative information. The Ti-TiB₂ contacts are small initially and are expected to quickly go to zero as TiB forms between them. The calculated results for this couple show negative values, which have no physical meaning. This results because of errors in Q_S^i due to the halo thickness and different Q_S^i values measured on opposite sides of the same phase. Also, the \bar{Q}_S^i values are averages of the distribution in Q_S^i values obtained from the fifty grid placements. When these are combined in Equation (38), the statistical variation increases and negative numbers may result. However, the trend with increasing time and temperature is towards zero; except for early 1200°C data, the zero line falls within the 95% confidence intervals. The Ti-TiB area remains small in all cases, indicating the small initial Ti contacts in the compact do not change much during the reaction. The TiB-TiB₂ values follow the increased coating of TiB₂ by TiB and the later shrinkage of TiB₂, approaching $S_V^{TiB_2}$ as coating is almost complete. The specific solid-porosity values all approach the corre-

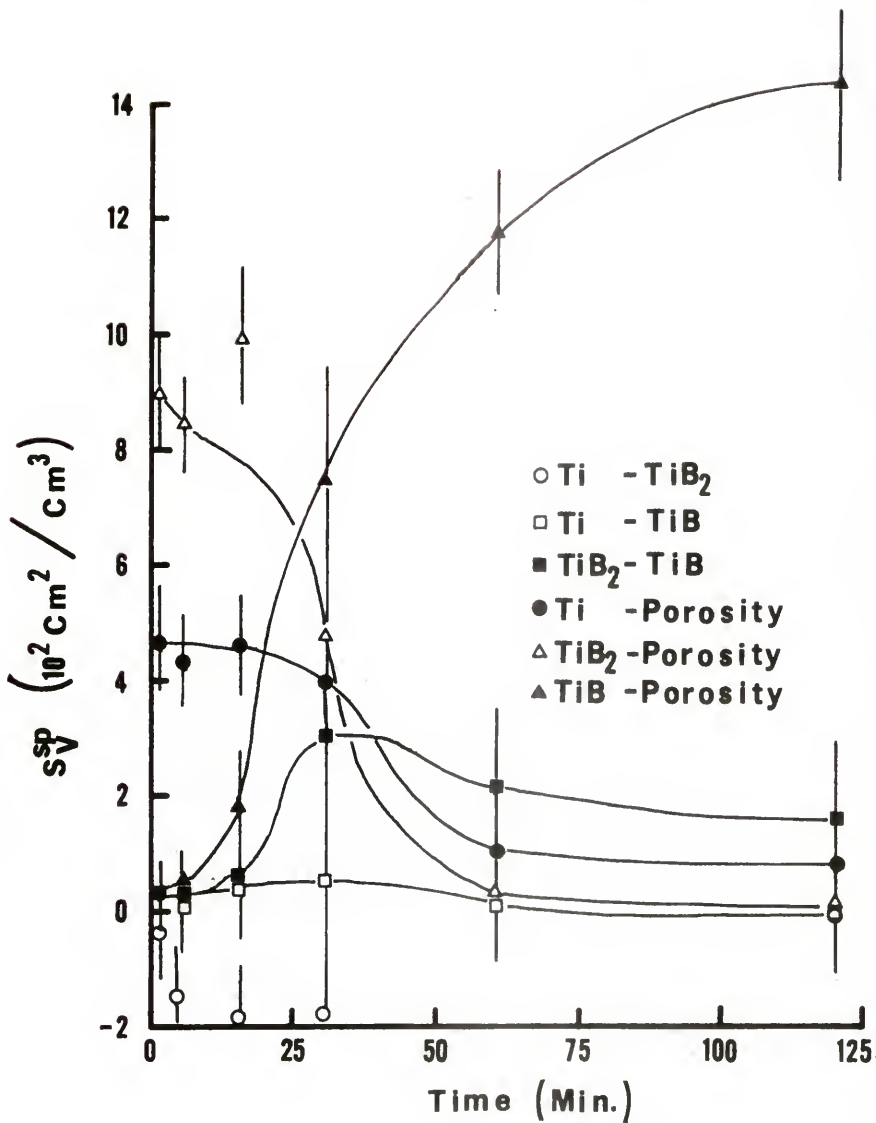


Figure 40. Quantitative Microscopy specific interface area for 1200°C .

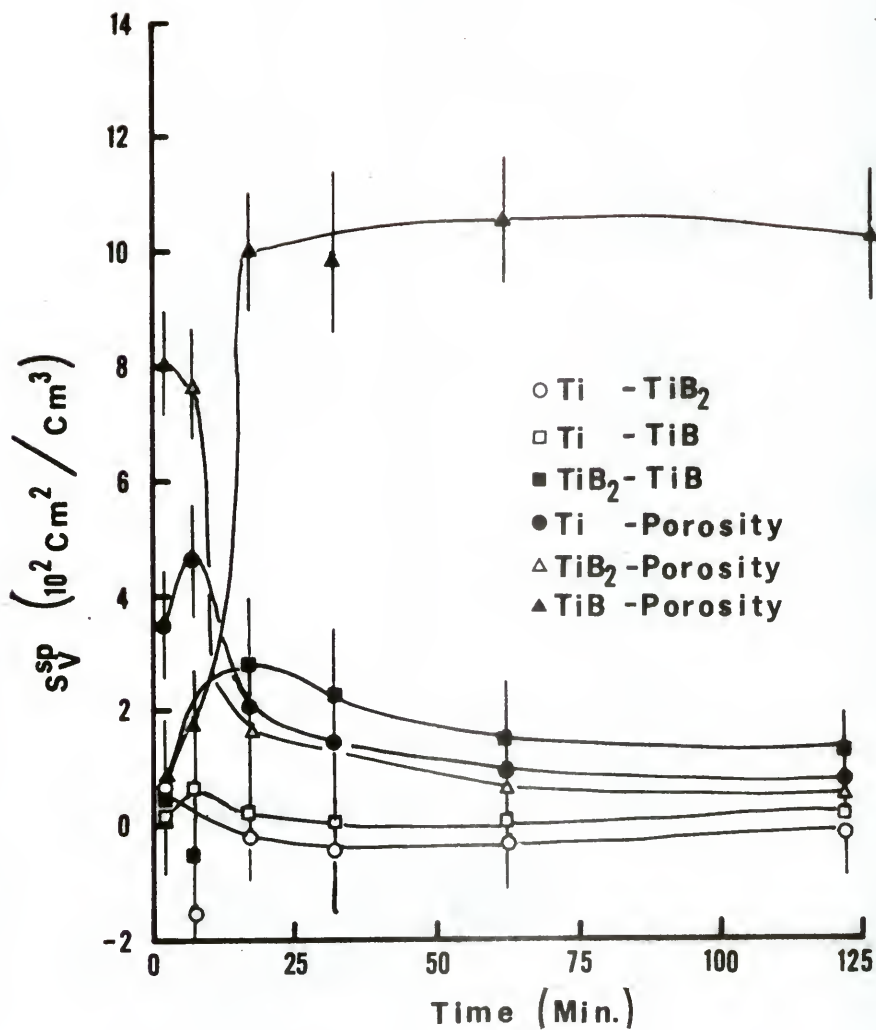


Figure 41. Quantitative Microscopy specific interface area for 1300°C .

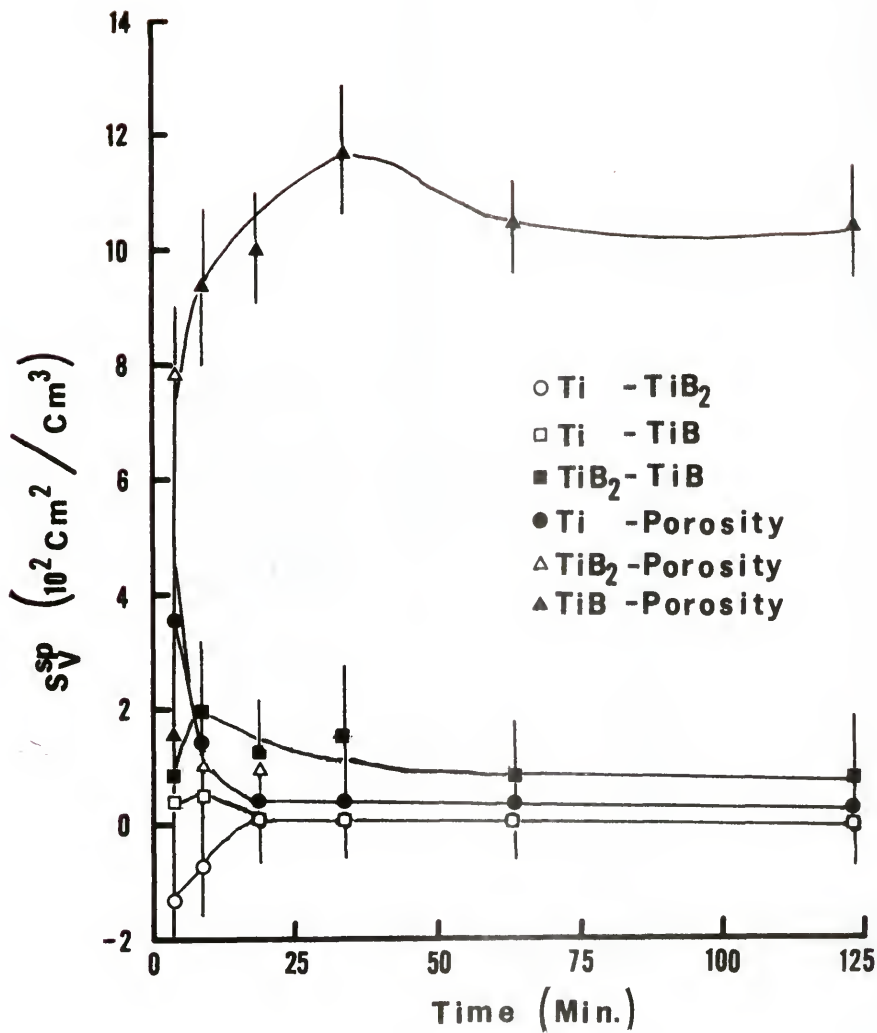


Figure 42. Quantitative Microscopy specific interface area for 1400°C.

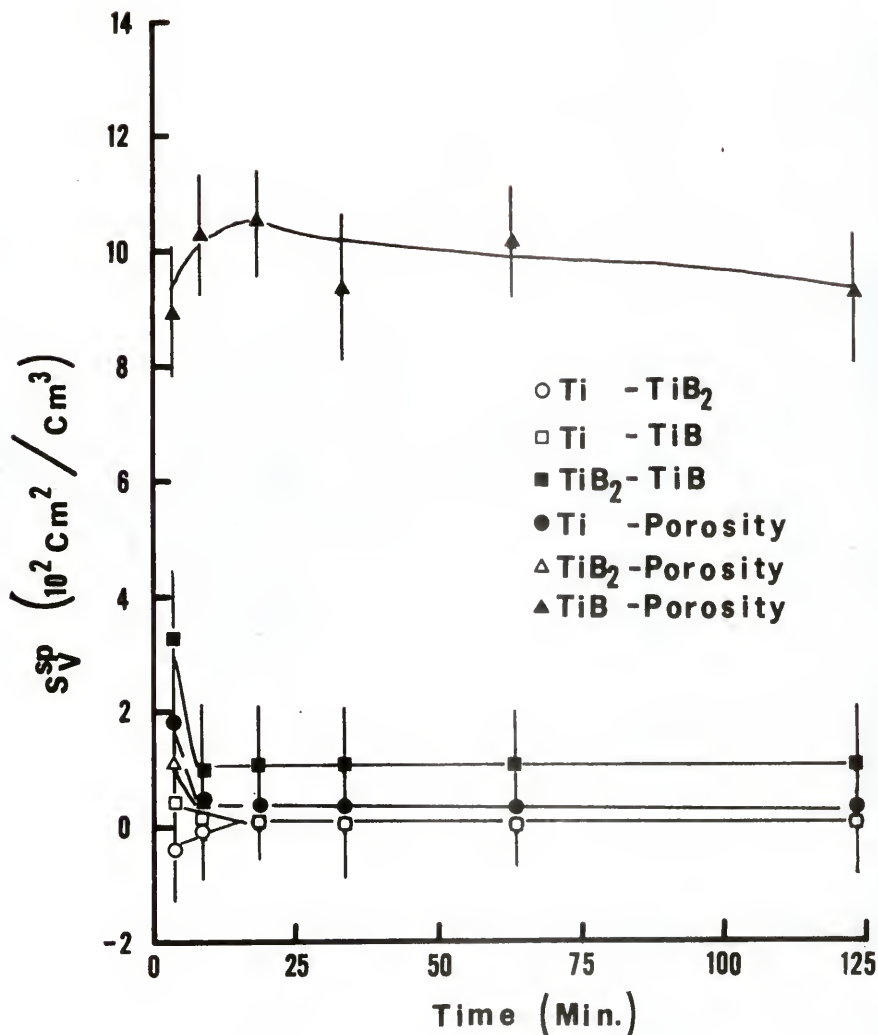


Figure 43. Quantitative Microscopy specific interface area for 1500°C .

sponding solid phase area. The proximity parameter shows some of these data in a combined form (Figure 44). The proximity results give the average degree of TiB_2 particle coating by TiB. The metallographic examination showed complete coating of some particles after 30 and 15 min. for 1200 and 1300°C specimens, respectively, while Figure 52 shows longer times required for significant coverage. This may result from examination of a two dimensional section through only partially coated three dimensional particles, similar to that of Figure 17b. The range of TiB_2 particle size may also give a distribution of coating percentages that shifts the average to later times. The 1400 and 1500°C data show nearly complete coating very early.

The total curvature results (Figures 45 through 48) are less reliable due to limits of optical resolution and particle rounding during polishing. In addition, the picture point resolution could be no better than 0.5 μm and the Quantimet detection system tends to remove the raggedness of boundaries because of non-ideal signal characteristics (Figure 12). This was less of a problem for Ti since the Q_T^{Ti} were determined by manual inspection of the image and for TiB_2 in the later stages because the TiB-TiB₂ boundary tended to become smooth. The poor con-

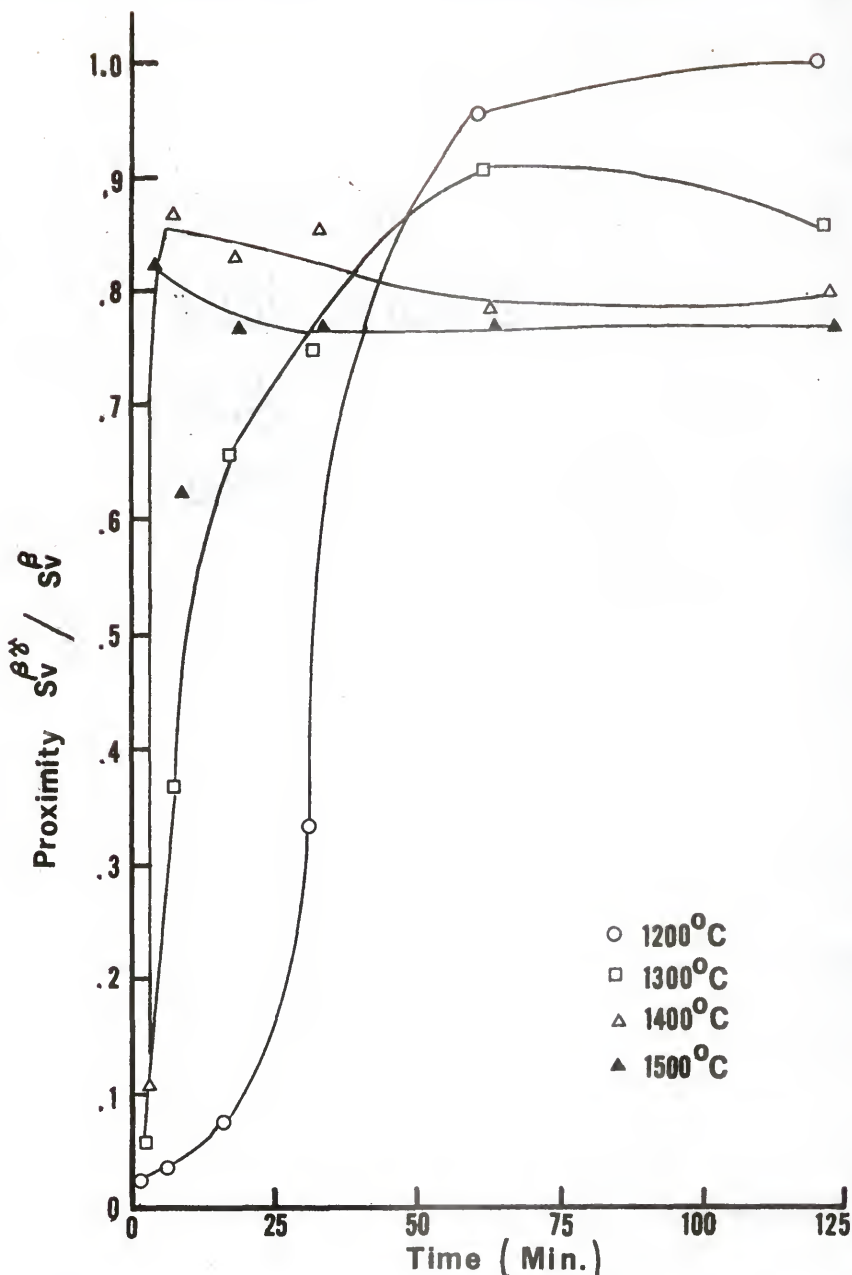


Figure 44. The proximity parameter $\frac{\beta_{Sv}^{\beta}}{\beta_{Sv}}$.

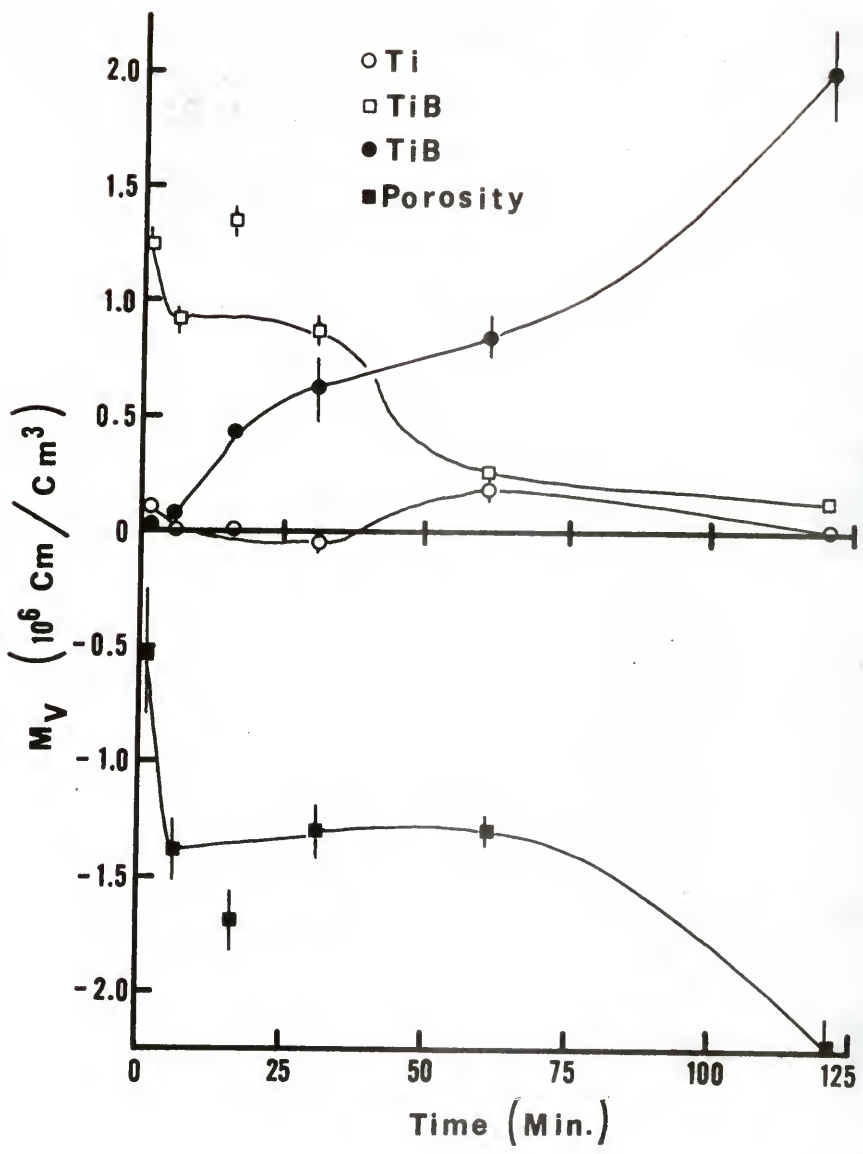


Figure 45. Quantitative Microscopy total curvature results for 1200°C.

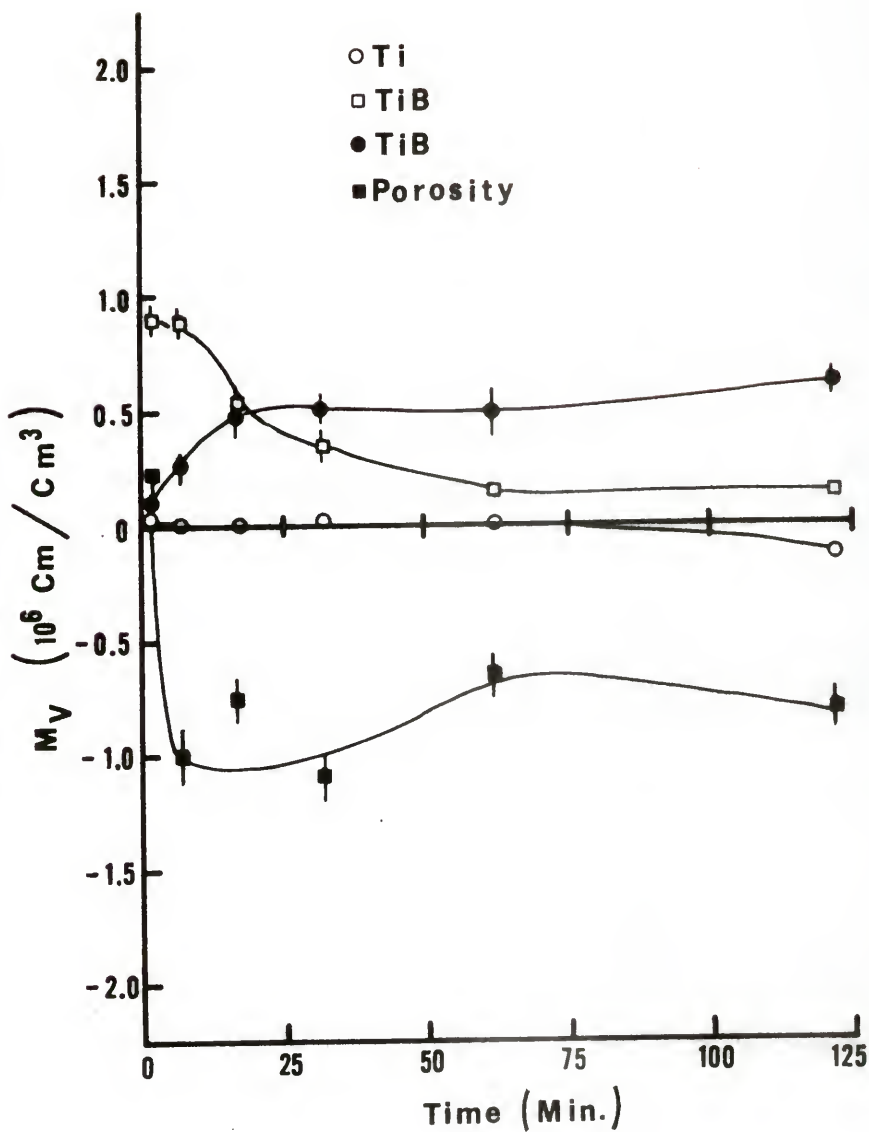


Figure 46. Quantitative Microscopy total curvature results for 1300°C.

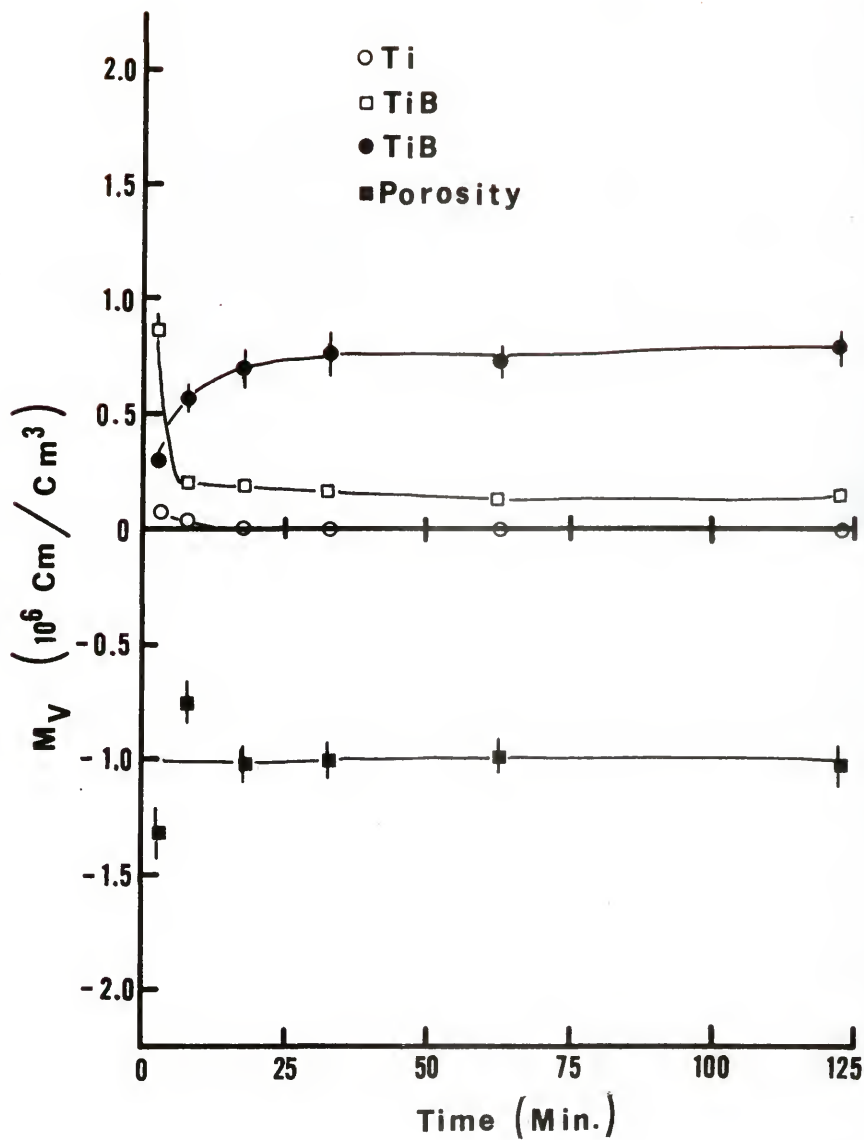


Figure 47. Quantitative Microscopy total curvature results for 1400°C.

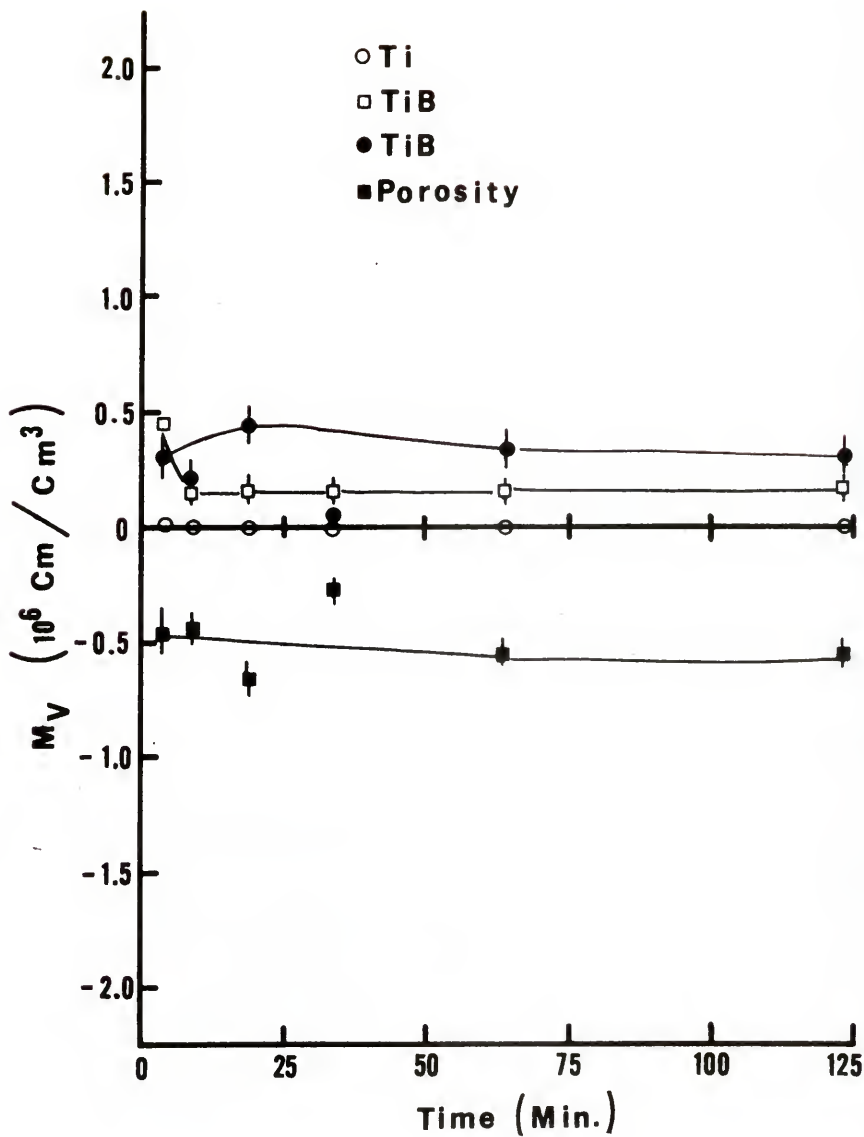


Figure 48. Quantitative Microscopy total curvature results for 1500°C.

trast between epoxy and stained Ti also made some detected boundaries fuzzy, which caused the Q_T^{porosity} counts to be high, especially during the early stages of reaction.

However, the observed trends are fairly consistent. The Q_{T+}^{Ti} and Q_{T-}^{Ti} values decreased but remained approximately equal to each other so $M_V^{\text{Ti}} \approx 0$ for all times. The originally rough TiB_2 boundary became smooth and decreased in area as the reaction proceeded so $M_V^{\text{TiB}_2}$ decreased. Since the TiB_2 -porosity boundary was replaced by TiB -porosity, the M_V^{TiB} increased toward the initial $M_V^{\text{TiB}_2}$ value. And, although the initial M_V^{porosity} values are questionable, they tend to become equal and opposite to those of TiB at later times. The scale of roughness and needle dimensions shown in previous SEM micrographs (Figure 23) suggest the magnitudes of M_V^{porosity} values presented do not reflect the true curvature of the solid surfaces during the later stages. This resolution limitation is less serious for the TiB-TiB_2 boundary.

The above data are combined in the $\bar{\lambda}$ and \bar{H} parameters. The porosity increase discussed above should also be reflected in the $\bar{\lambda}$ values for porosity as a general scale factor. Figures 49 through 52 show only a modest change at 1200 and 1300°C while the increase in 1400 and 1500°C data is more definite. The $\bar{\lambda}$ values for TiB follow

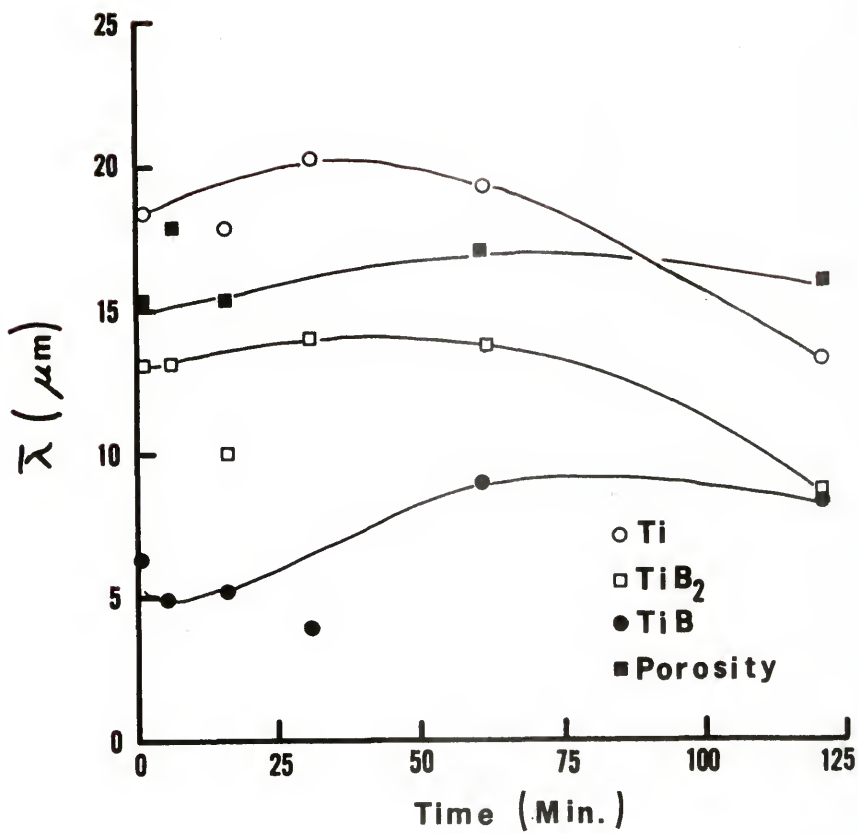


Figure 49. The $\bar{\lambda}$ parameters for 1200°C .

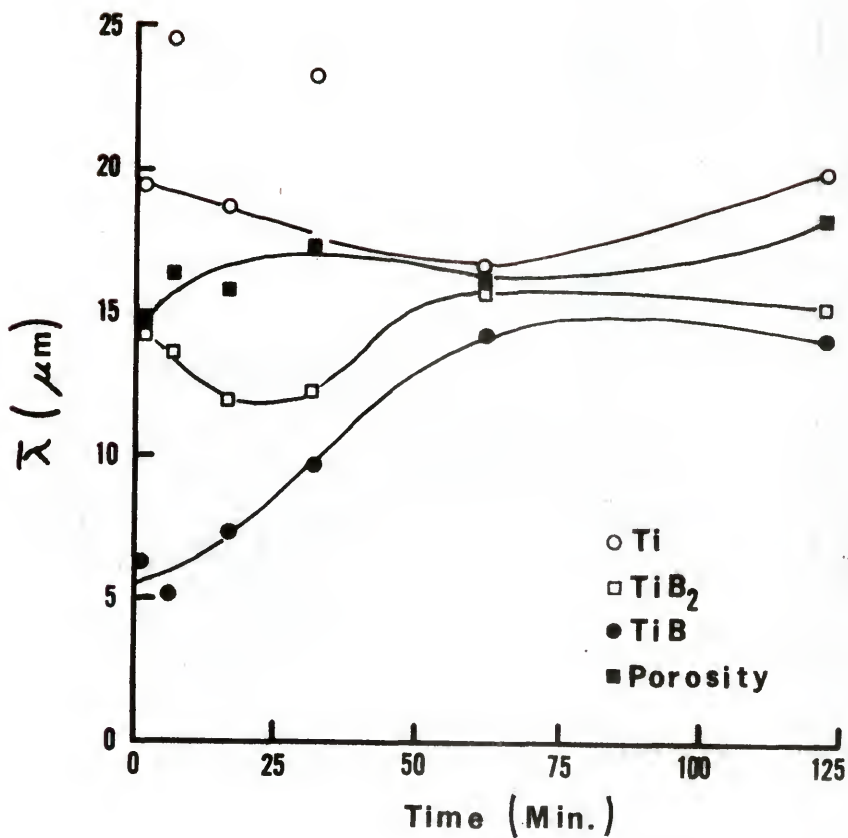


Figure 50. The $\bar{\lambda}$ parameters for 1300°C.

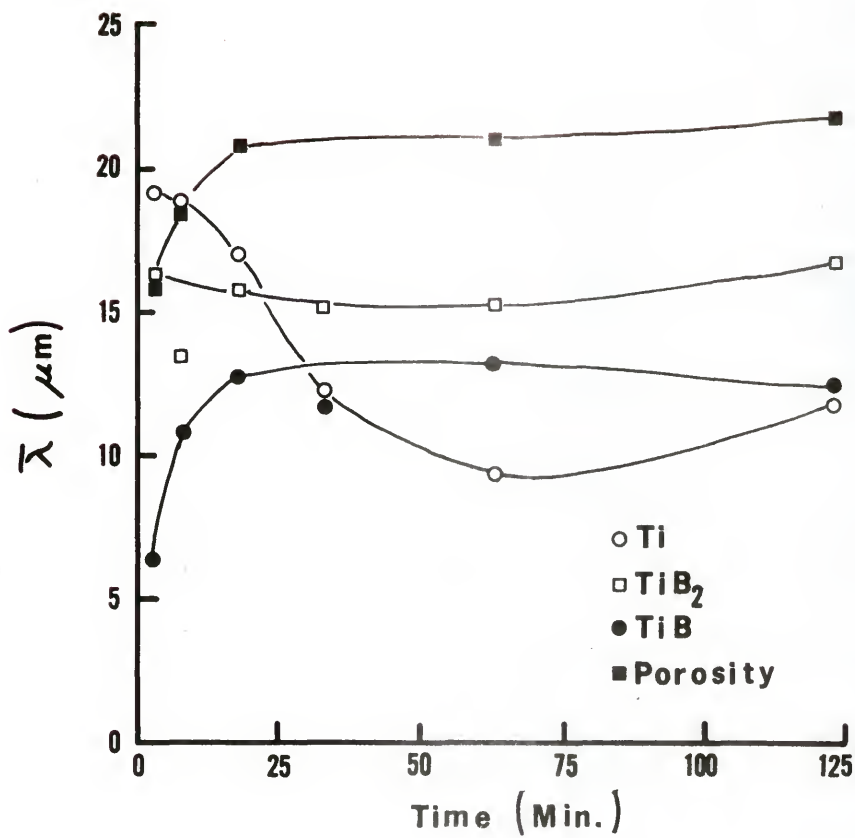


Figure 51. The $\bar{\lambda}$ parameters for 1400°C.

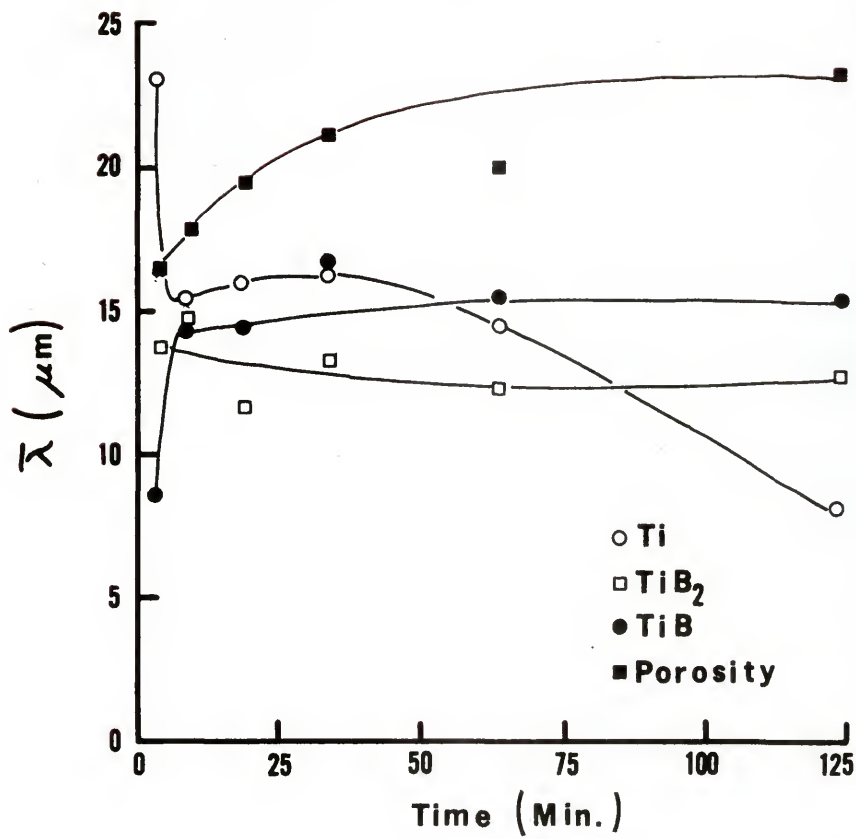


Figure 52. The $\bar{\lambda}$ parameters for 1500°C.

the increase in TiB volume, but the magnitude of 10 - 15 μm is approximately half that expected if this parameter measured a particle diameter. Part of this difference is due to the distribution of particle size and to the TiB_2 core which divides the larger particles. The average distance between TiB surfaces then approaches the distance between exterior and interior surfaces rather than the distance across the complete particle. It is also the nature of $\bar{\lambda}$ to underestimate a "diameter;" for example, the $\bar{\lambda}$ for monosized spheres is 2/3 of their diameter. The results for Ti and TiB_2 show a little more scatter. The general trend is for $\bar{\lambda}^{\text{Ti}}$ and $\bar{\lambda}^{\text{TiB}_2}$ to decrease, especially in the early stages when smaller particles are consumed and removed from the population. At later stages, the remaining large particles experience surface rounding and slower rates of volume transformation, causing the $\bar{\lambda}$ values to increase slightly. The $\bar{\lambda}$ parameter is a more sensitive indicator of changes in scale when there is a significant change in the surface to volume ratio of the phase; this occurs when the elongated Ti grains shrink and the TiB forms a spherical shell.

The \bar{H} values (Figures 53 through 56) follow the trends expected for the ratios of M_V and S_V . The Ti grains initially become less rough but retain their elon-

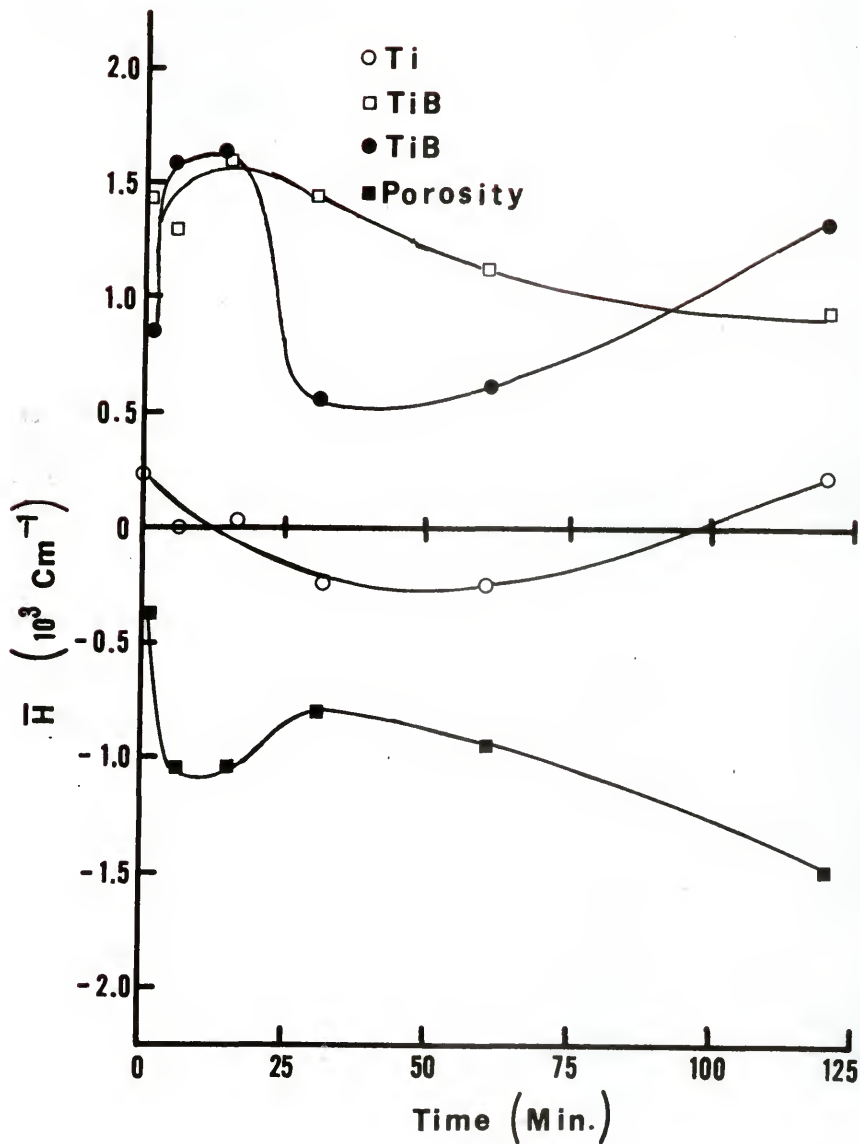


Figure 53. The \bar{H} parameters for 1200°C .

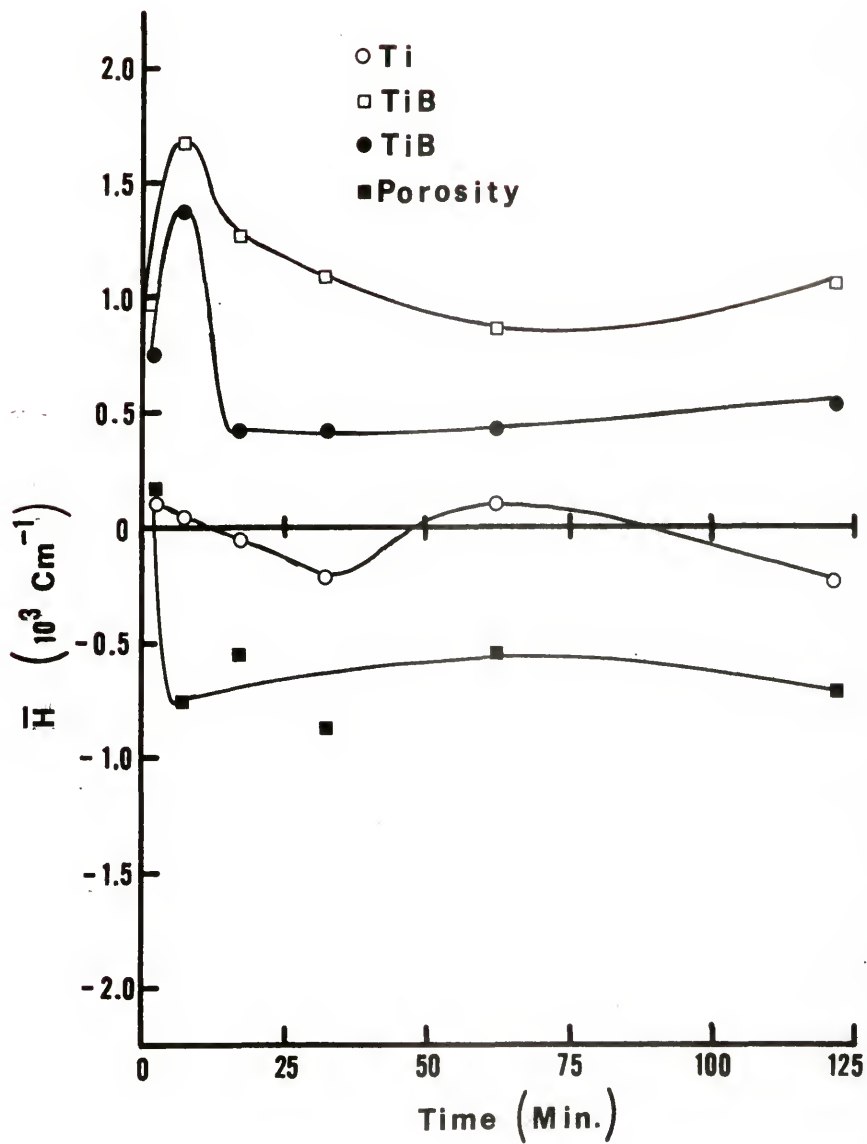


Figure 54. The \bar{H} parameters for 1300°C.

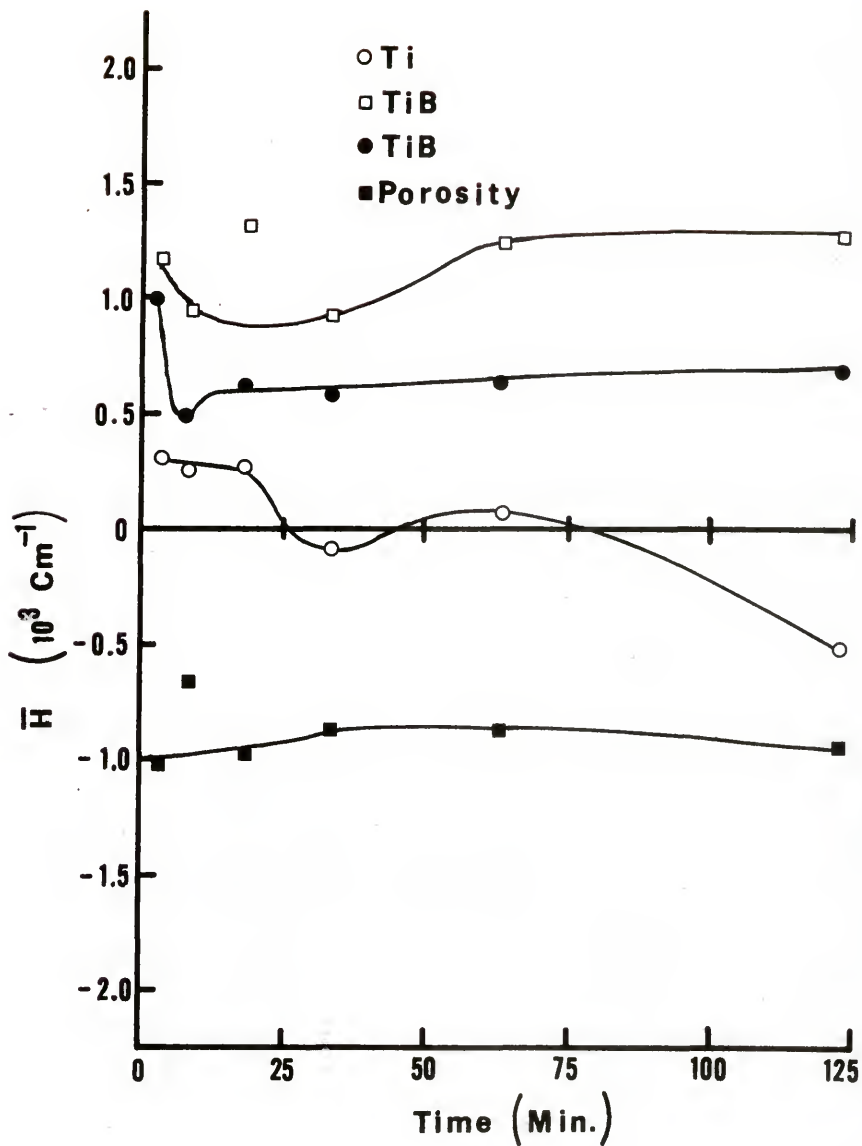


Figure 55. The \bar{H} parameters for 1400°C.

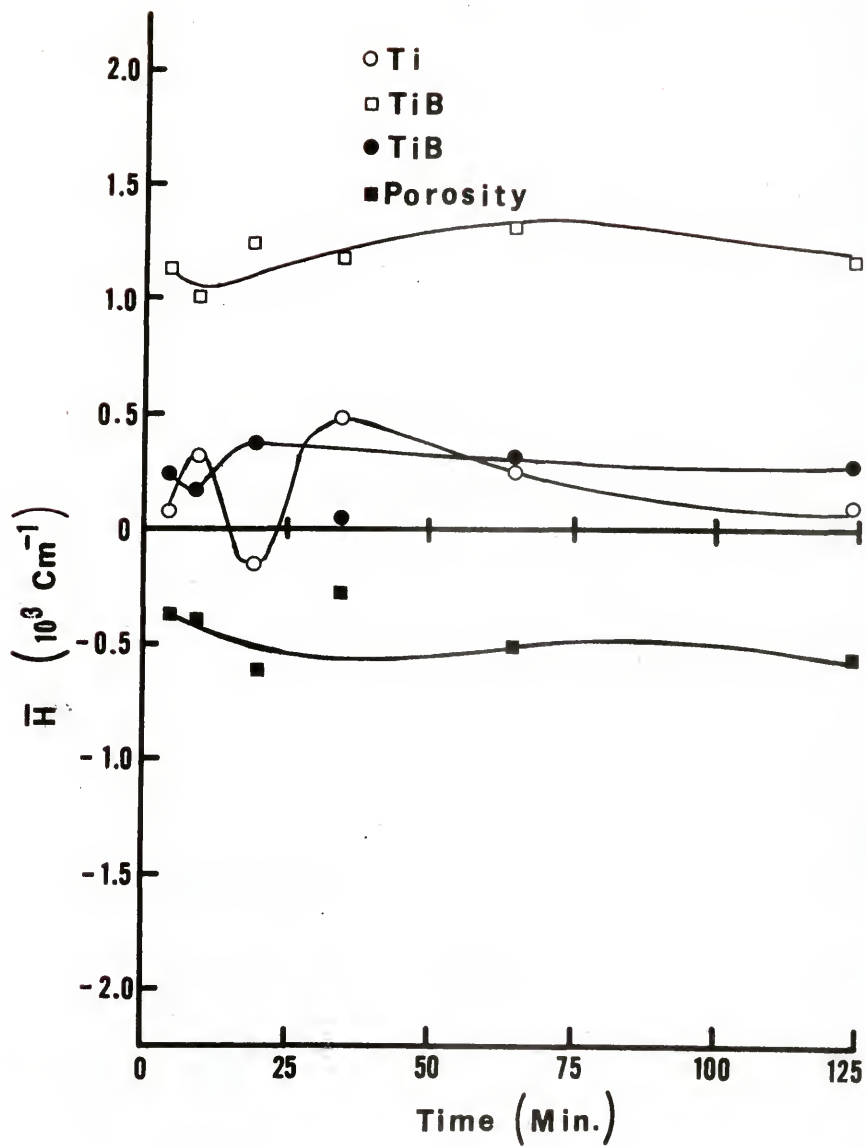


Figure 56. The \bar{H} parameters for 1500°C .

gated shape so the surface area decrease is more gradual (Figures 30 and 31). Thus, the decrease in M_V^{Ti} causes \bar{H}^{Ti} to decrease. Later, the grains shrink in length and their surface to volume ratio also decreases: with decreasing S_V^{Ti} , the \bar{H}^{Ti} parameter increases slightly. These changes in \bar{H}^{Ti} and metallographic examination suggest the decrease in surface energy driving the surface rounding only operates over a 1 - 5 μm distance. Whether the source for Ti diffusion is the surface and/or the interior of the Ti particles can not be answered from these data. Since the transformation to form TiB occurs at the TiB_2 grains, no experiments to determine this source were attempted. However, the reaction sequence micrographs (Figure 20b and c) show some holes in the particle interior; it is not clear if these are really pores developed due to Ti diffusion from the interior or deep concave surface depressions sectioned by the polishing plane. The changes in \bar{H}^{TiB_2} reflect the initial decrease in $S_V^{\text{TiB}_2}$ as smaller TiB_2 particles are consumed and the later decrease in $M_V^{\text{TiB}_2}$ as coating by TiB smooths the TiB_2 surface. Finally, the \bar{H}^{TiB_2} approaches a steady value after complete coating of most of the TiB_2 particles. Observations of initial TiB-TiB₂ interface show it is relatively smooth when created (within the resolution of the optical microscope). An \bar{H}

determination restricted to this interface would be a more useful measure of the influence of surface curvature on this reaction. This requires a determination of M_V for this partial surface but measurements could not be made with the Quantimet on this restricted feature. In the later stages of reaction, the TiB_2 area is approximately equal to the specific $TiB-TiB_2$ interface: in this case, \bar{H}^{TiB_2} does not change much as the coated TiB_2 particles are consumed. Thus, the curvature of this interface does not appear to influence the reaction rate appreciably. The \bar{H}^{TiB} results appear similar to those for TiB_2 . The initial reaction zones on large particles and the smaller particles of consumed TiB_2 have a rough surface but small area so \bar{H}^{TiB} exhibits a sharp initial increase. The continued rapid formation of smooth interior and rough exterior TiB surface causes \bar{H}^{TiB} to then decrease sharply. The subsequent increase for the $1200^\circ C$ data reflects the corresponding increase in M_V^{TiB} for $1200^\circ C$: since higher temperature data do not show this increase, it is attributed to pullout increasing this Q_T^{TiB} count (see Figure 30). The magnitude of \bar{H}^{TiB} is not truly representative of the TiB surface because of the overlapped needle morphology discussed above (Figure 23). The \bar{H} porosity remains fairly constant as the proportion between area and

roughness of this surface is not significantly changed by the consumption of Ti particles.

The results of Quantitative Microscopy measurements on the initial compact are presented in Table 5. However, due to pullout during polishing, these values are not considered reliable. The variability in operating technique of the Quantimet is shown in Table 6. These results indicate the deviation is only a fraction of a percent, except for the Q_T counts, where the smaller sample size (total number of counts) influences the statistical calculations. Examination of the tabulations in Appendix 5 shows the confidence intervals to be fairly constant, while the coefficient of variability increases as the mean value decreases, as expected. The percent error in point count indicates how closely $\Sigma V_V^i = 1$. The difference between V_V^{porosity} and $(1 - \Sigma V_V^{\text{solid}})$ was divided by 160,000 and by each V_V count. The results indicate this difference is about 0.1% for the total counts and usually less than 1% for the individual phases, except where they were present in very small amounts (early stage TiB and later stage Ti and TiB_2). Two other characteristics also influenced overall accuracy. The higher porosity values caused the errors in solid phases to be a greater fraction than would have been the case for more accurate porosity measure-

Table 5
Quantitative Microscopy Data for Starting Material Compact

Volume Fraction	Area per volume	Total Curvature
VVA	SVA 356.0 cm ⁻¹	MVA 37037 cm ⁻²
±	± 30.9 cm ⁻¹	± 25240 cm ⁻²
VVB	SVB 814.8 cm ⁻¹	MVB 1,229,620 cm ⁻²
±	± 42.6 cm ⁻¹	± 69820 cm ⁻²
VVD	SVD 1313 cm ⁻¹	MVD -134530 cm ⁻²
±	± 29.7 cm ⁻¹	± 223360 cm ⁻²
V CV A	S CV A .0433 cm ⁻¹	M CV A .3404 cm ⁻²
V CV B	S CV B .0261 cm ⁻¹	M CV B .0284 cm ⁻²
V CV D	S CV D .0133 cm ⁻¹	M CV D -.0830 cm ⁻²

Specific Interface Area

SV AB	-71.12 cm ⁻¹
SV AD	427.13 cm ⁻¹
SV BD	885.99 cm ⁻¹

Table 6

Variability in Quantimet Operating Technique

Machine variability: constant focus and threshold adjustment					
$\bar{Q}_V^i =$	72959	$\bar{Q}_S^i =$	1676.8	$\bar{Q}_{Tnet}^i =$	19.5
\pm	83.6	\pm	1.5050	\pm	0.8266
CV =	0.00057	CV =	0.00042	CV =	0.02145
Focus adjustment: constant threshold setting					
$\bar{Q}_V^i =$	80837	$\bar{Q}_S^i =$	1630.8	$\bar{Q}_{Tnet}^i =$	28.81
\pm	377.6	\pm	13.046	\pm	2.532
CV =	0.00234	CV =	0.00400	CV =	0.0439
Threshold adjustment: focus unchanged					
$\bar{Q}_V^i =$	81213	$\bar{Q}_S^i =$	1610.6	$\bar{Q}_{Tnet}^i =$	29.06
\pm	376.4	\pm	9.460	\pm	2.432
CV =	0.00232	CV =	0.00294	CV =	0.0418

Notes:

Results are averages of 16 runs. Sample was starting material compact, unstained. A single field of view was examined.

ments. Under ideal conditions, the Quantimet can distinguish 25 - 30 gray shade levels, but the gray of the epoxy, as the "blackest" phase, reduced this available contrast range; this decreased the ability to accurately detect separate phases, especially between Ti and porosity.

The trends of the Quantitative Microscopy data for V_V^i , S_V^i , and M_V^i are in agreement with qualitative observations. These data are combined to obtain specific interface, $\bar{\lambda}^i$, and \bar{H}^i information, which also behave as expected. However, the magnitudes of S_V^{TiB} , M_V^{TiB} , and \bar{H}^{TiB} for the exterior portion of the TiB surface do not properly represent the overlapped needle structure seen in Figure 23 because of resolution limits. The instrumental errors are <0.5% and the variability from the 50 grid placements is usually 1 - 2%. The 10 - 15% discrepancy in $V_V^{porosity}$ is attributed to difficulties of metallographic preparation. In addition, the 10 - 15% increase in porosity demonstrated by the immersion displacement data is almost totally from the volume increase of TiB_2 particles upon transformation to TiB.

Quantitative X-Ray Results

The results of x-ray error determinations are shown in Table 7. Rotating the sample significantly reduced the variability compared to the non-rotating case. The machine error (run on a single sample) was about 0.5%, while the particle orientation, sample packing, and mixing errors (with samples remounted after each run) were 1 - 3, 1 - 4, and 1 - 2%, respectively. The higher values are due to the variability in the second TiB_2 peak ($d = 2.62 \text{ \AA}$). Overall, the errors are closer to 1 or 2%.

The strip chart results for several 1200°C samples are shown qualitatively in Figure 57. The NaCl peaks remain constant while the TiB_2 and Ti peaks decrease and the TiB peaks increase. Selected x-ray data (of lines within the 2θ range $30 - 48^\circ$) for the compounds in the Ti-B system are given in Appendix 7. Figure 57 and Appendix 7 show that selection of peaks for measurement required some compromise between peak intensity and peak separation. To avoid overlap problems, the two TiB peaks ($d = 2.140 \text{ \AA}$ and $d = 2.161 \text{ \AA}$) were combined - this also increased the TiB intensity. The second and third most intense Ti and TiB peaks ($d = 2.557 \text{ \AA}$, 2.543 \AA and $d = 2.342 \text{ \AA}$, 2.346 \AA) overlapped too much to be used. This required measurements on the most intense and broad Ti peak ($d = 2.244 \text{ \AA}$), although

Table 7
X-ray Error Determinations

<u>Error</u>	<u>Sample</u>	<u>Peaks Measured</u>	<u>Condition</u>	<u>CVf</u>
Machine errors	TiB2	I	NG, NR	.002
			NG, R	.004
Particle Orientation ^b	NaCl	I	G, NR	.010
			G, R	.006
			G, NR	.004
			G, R	.003
	TiB2	I/II	G, NR	.066
			G, R	.030
	NaCl	I/II	G, NR	.015
			G, R	.012
Sample Packing ^b	Ti	I/II	G, R	.012
	TiB	I/II	G, R	.010
	TiB2	I	G, NR	.036
		II	G, NR	.063
		I	G, R	.021
		II	G, R	.039
		I	G, NR	.014
		II	G, NR	.010
		I	G, R	.013
		II	G, R	.008
		I	G, R	.008
		II	G, R	.016
	I	G, R	.012	
	II	G, R	.009	

Table 7 - continued.

Error	Sample ^c	Peaks Measured ^d	Condition ^e	Cv ^f
Mixing ^b	TiB ₂ +NaCl	(I+II)TiB/I ₁ NaCl	G, R	.015
	TiB ₂ +Ti	ITiB ₂ /ITi	G, R	.011

^aTen runs on a single mounted sample.

^bTen samples remounted between runs.

^c-325 mesh powders.

^dpeak d spacings:

TiB ₂	I: d = 2.033 Å	II: d = 2.62 Å
NaCl	I: d = 2.821 Å	II: d = 1.994 Å
Ti	I: d = 2.244 Å	II: d = 2.342 Å
TiB	I: d = 2.140 Å	II: d = 2.161 Å

^eNG = no goniometer motion.

G = goniometer moving at 1/2°/min.

NR = no sample rotation.

R = sample rotating at 20 rpm.

^fSee Appendix 3.

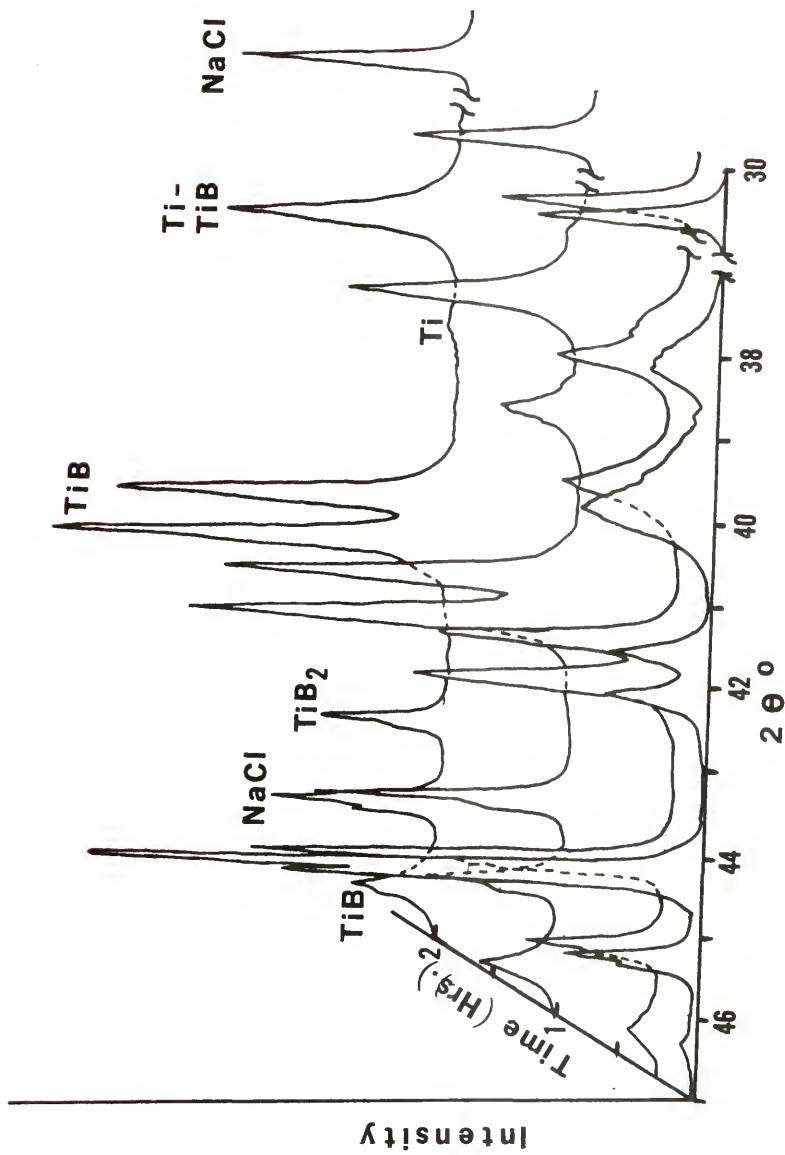


Figure 57. Qualitative x-ray strip chart patterns.

it also overlapped the neighboring Ti-TiB peak to some extent. This overlap problem was compounded by a peak shift with time, which is discussed more fully later. The TiB_2 peaks are very intense and sufficiently separated to cause no problem. The pattern for NaCl is suitably intense and separated to be used as an internal standard in spite of the number of close and overlapping peaks of the Ti-B system (Appendix 7). The proximity of many peaks in this system helps explain the difficulties early researchers had interpreting their x-ray data.

The data for x-ray standards and samples are given in Appendix 8. The standard calibration curves (Figure 58) are approximately linear, as expected.⁸⁰ The reaction to form TiB material for standards did not go to completion in a reasonable length of time and residual amounts of Ti and TiB_2 contaminated the nominal volume fraction quantities. Attempts to remove this residue by dissolving in several different acids produced distorted x-ray patterns and were abandoned. Utilizing the method of additions⁸⁸ (inset, Figure 58), the residual amounts were determined to be 4 volume % Ti and 6 volume % TiB_2 (10% total). The nominal volume fractions were corrected by these amounts to give the calibration curves in Figure 58. The slight positive and negative deviations for TiB and TiB_2 , re-

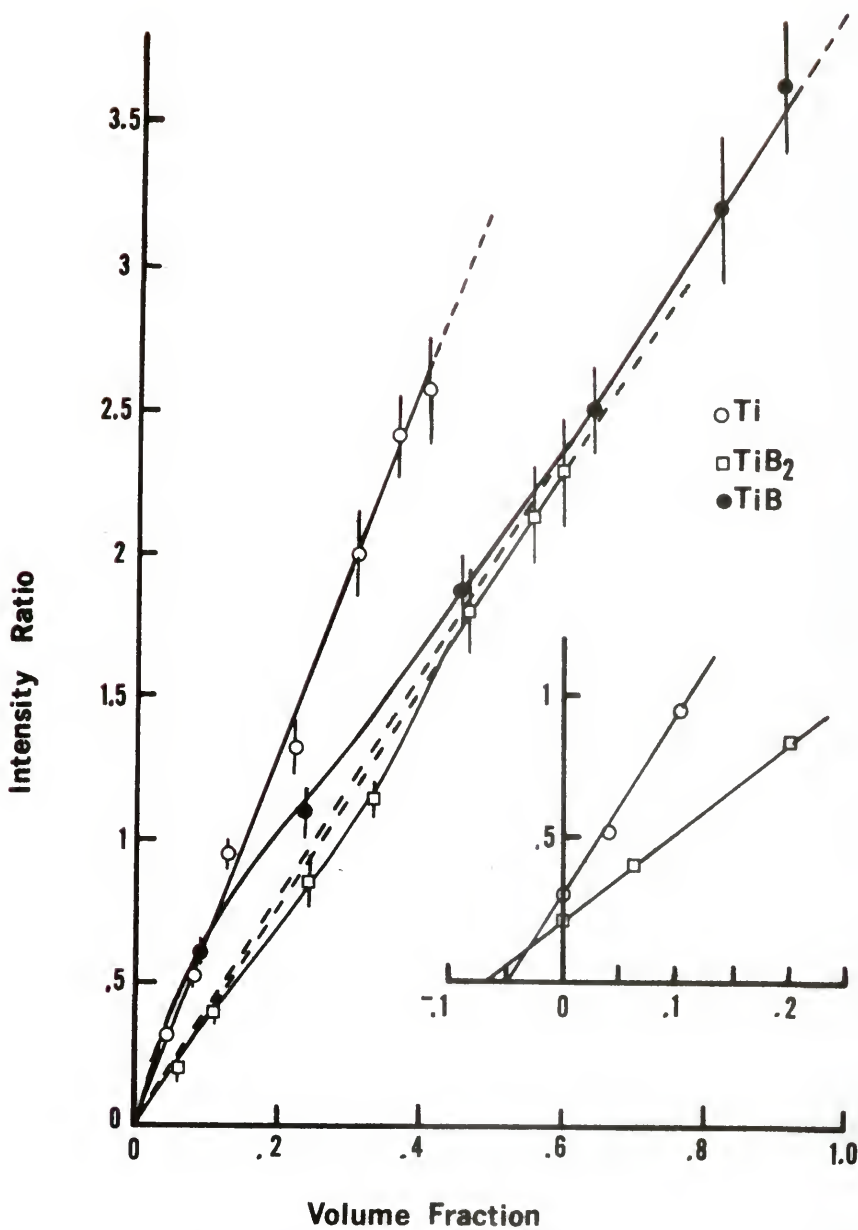


Figure 58. Internal standard calibration curves.

spectively, reflect the finer particle size of the pulverized TiB, which would pack between the harder and less compressible TiB₂ and hence appear in the exposed surface layer in greater proportion than its actual volume. This is supported by the more gritty feel of the standards and samples with high reactant volume fractions.

The sample count data (Appendix 8) were used in conjunction with Figure 58 to obtain the volume fractions for each phase, shown in Figures 59 through 62 (solid lines). The resultant trends are similar to the Quantitative Microscopy results and are accelerated with increasing temperature. However, the initial Ti volume fractions are lower than expected (~40%) and the TiB₂ fractions are higher than they should be (~60%). The total of these volume fractions is ~110 - 130%. There are several differences between samples and standards that may account for this. These include the presence of

- 1) sieved and unsieved Ti;
- 2) pulverized and unpulverized material;
- 3) total mass differences;
- 4) coated and uncoated TiB₂; and
- 5) reacted and unreacted Ti and an associated peak shift.

Each of these factors is discussed below.

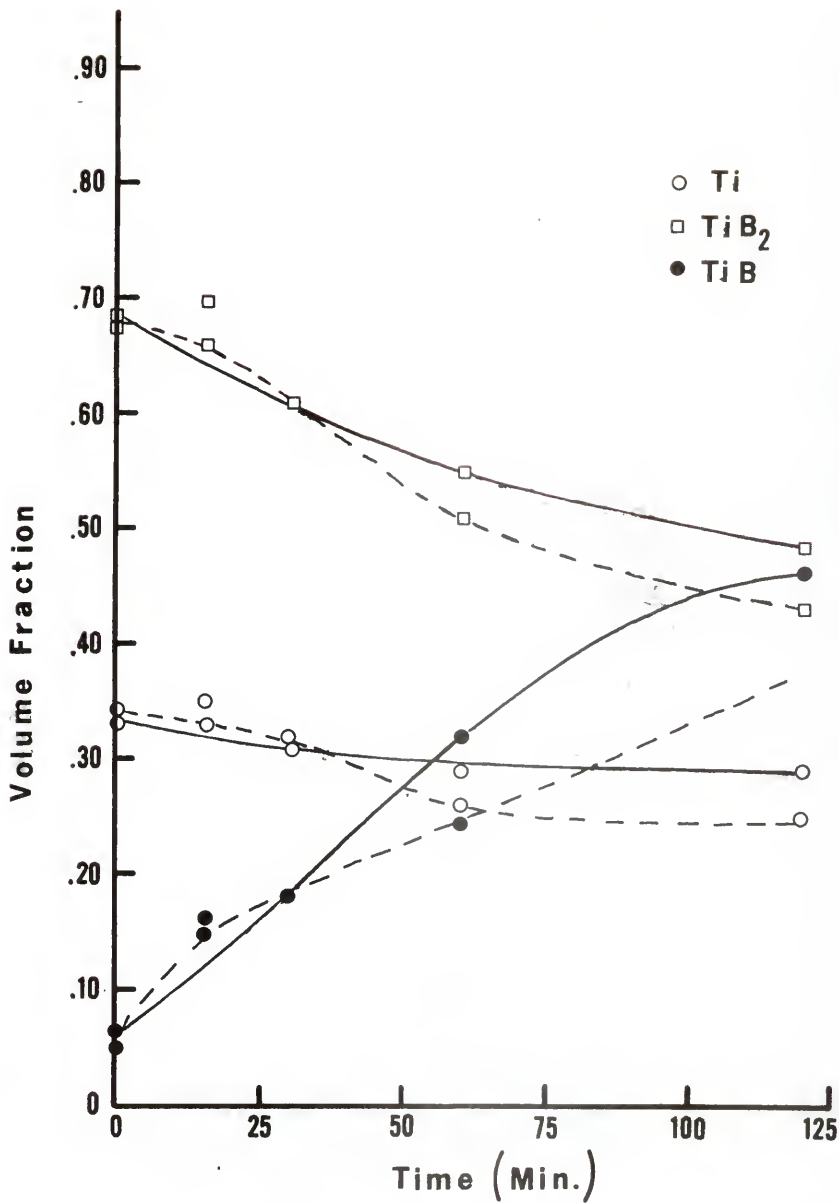


Figure 59. Quantitative x-ray volume fraction results for 1100°C (solid line: internal standard method; dashed line: direct comparison method).

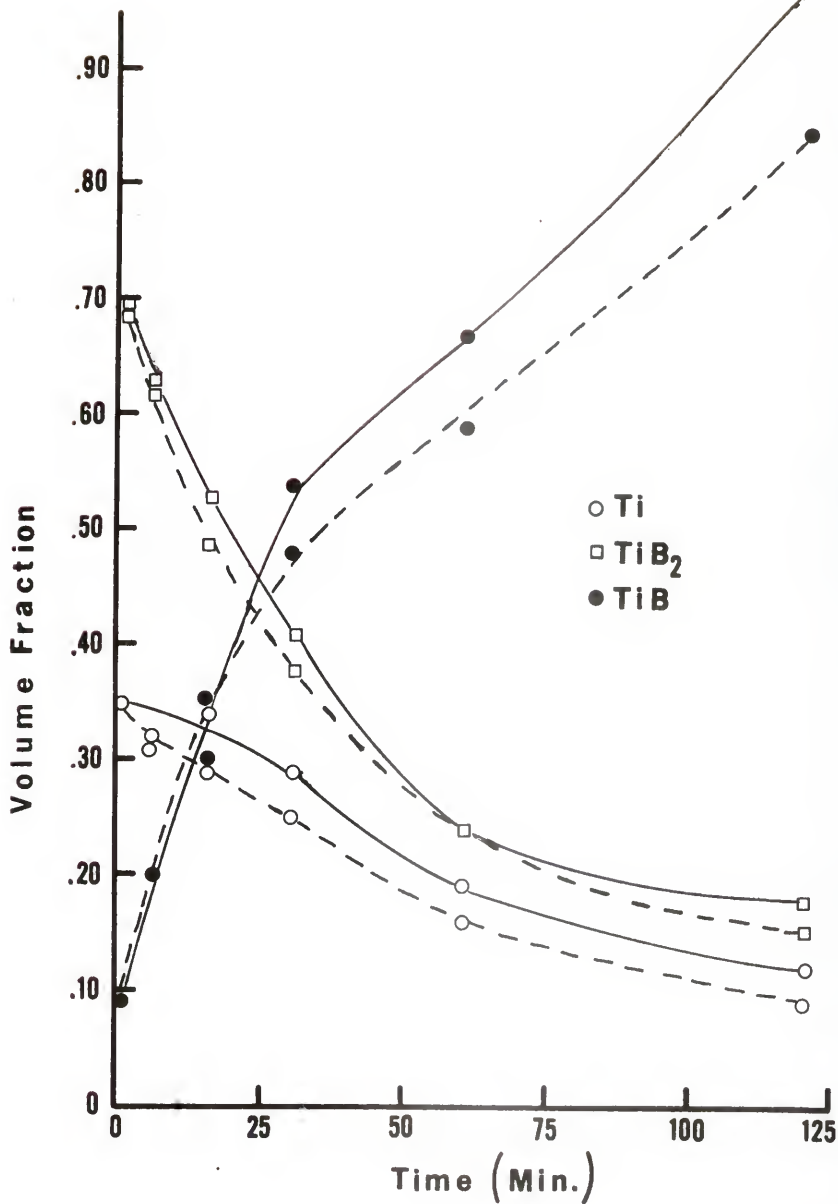


Figure 60. Quantitative x-ray volume fraction results for 1200°C (solid line: internal standard method; dashed line: direct comparison method).

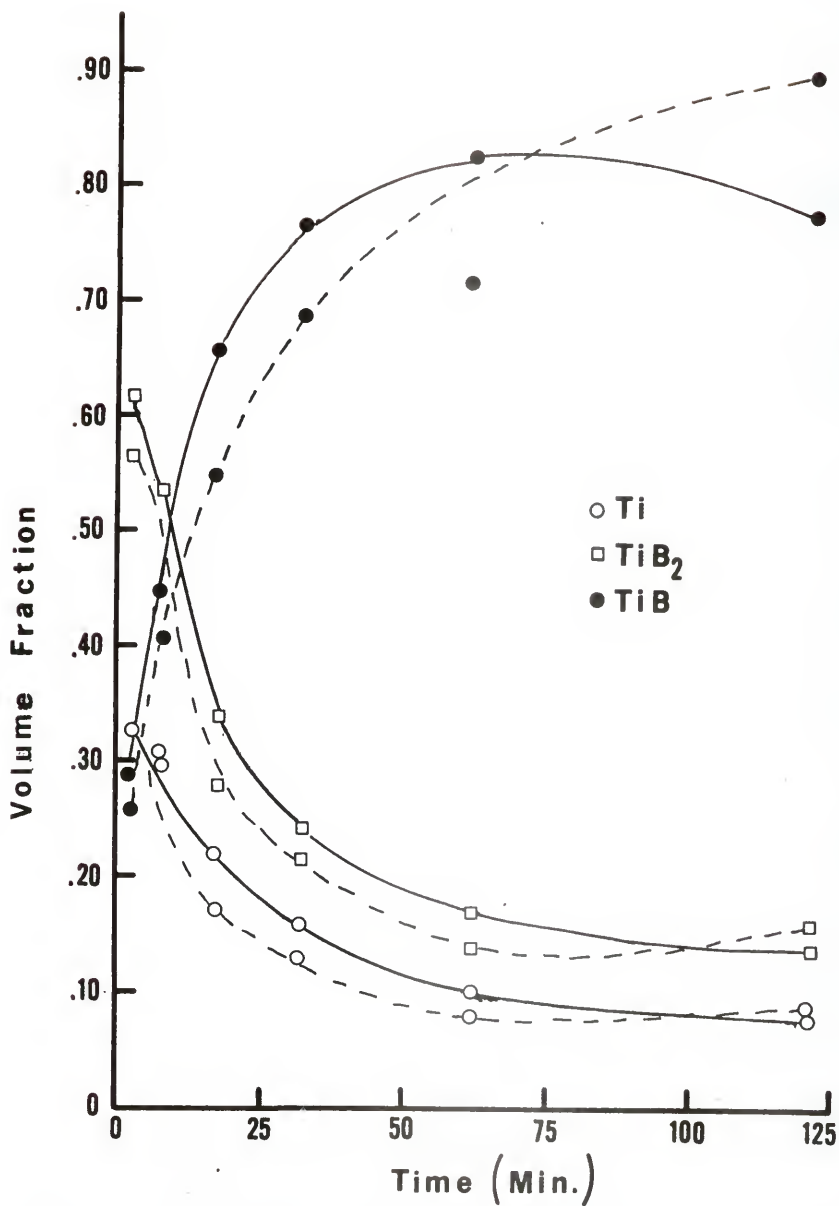


Figure 61. Quantitative x-ray volume fraction results for 1300°C (solid line: internal standard method; dashed line: direct comparison method).

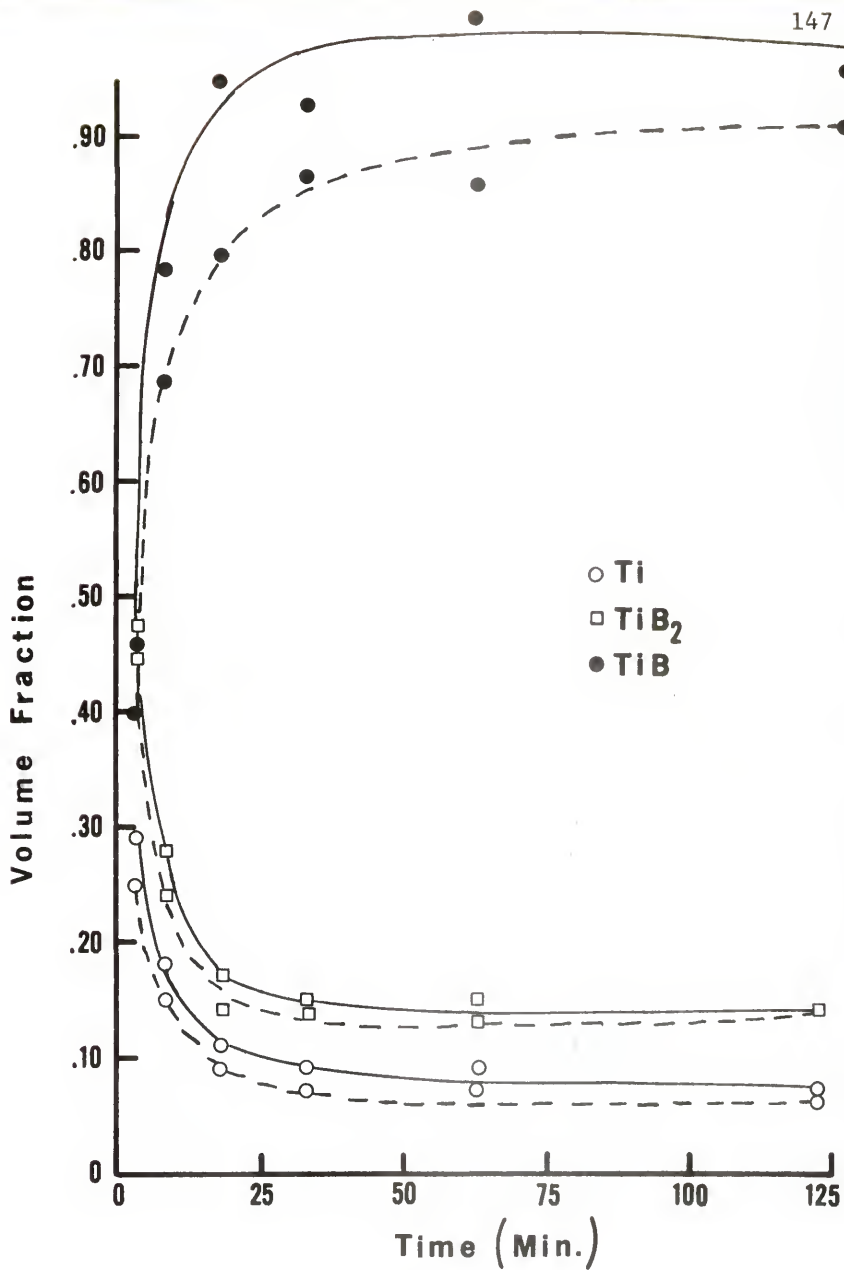


Figure 62. Quantitative x-ray volume fraction results for 1400°C (solid line: internal standard method; dashed line: direct comparison method).

1) The ductile Ti grains in the samples that did not pass the 325 mesh sieve were re-added to the already sieved material while -325 mesh Ti powder was used in mixing the standards. Thus, the larger Ti particles from the samples would be under-exposed on the surface layer in comparison to the Ti powder used in the standards. This explains the greater than 60 volume % TiB_2 measured for the samples initially, since it would increase relative to the Ti deficit.

2) A similar effect is caused by pulverizing the sample, where the harder boride phases become embedded in the ductile Ti and/or form an adherent coating of fine particles (Figure 63), which decreases Ti intensity.

3) The smaller available sample mass required less NaCl to make 10 weight %, increasing the possible error in weighing this small amount of material ($\approx 0.05 - 0.10$ gm). To check the possibility of variation in NaCl content, the volume fractions were re-determined using the direct comparison method.^{80,89} Calibration curves of intensity vs. known volume fraction (Figure 64) were generated from the integrated intensity counts of the standards. A few points were off this calibration curve because of a small change in the x-ray tube filament current (20 to 21 ma.) that occurred during the internal standards determinations

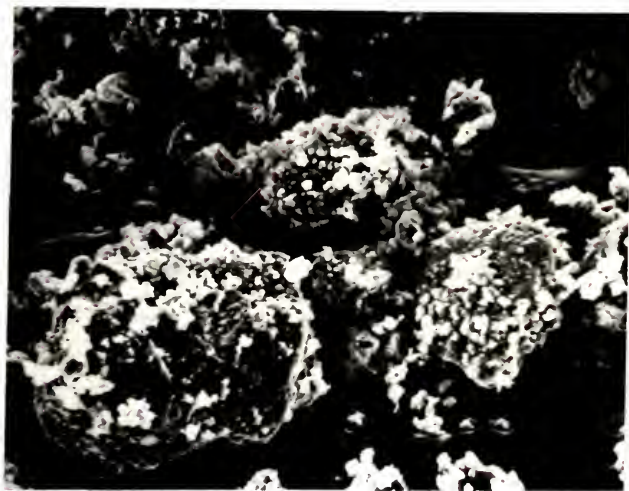


Figure 63. Pulverized x-ray sample heated to 1300°C for 16 min. (905 X).

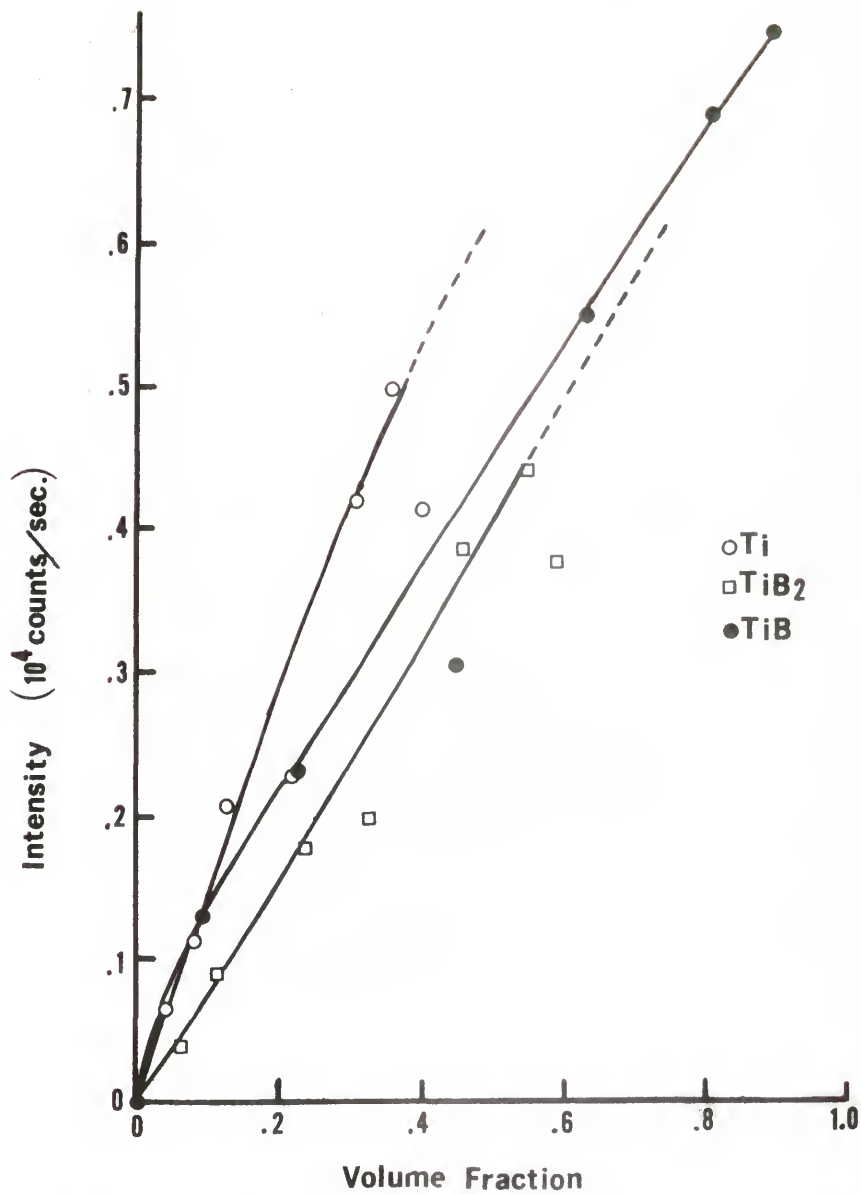


Figure 64. Direct comparison calibration curves.

and prior to running the samples. This does not affect the internal standard measurements; and the trends in Figure 64 for direct comparison are clear. Comparing these results with the sample data counts provided another measure of volume fraction (independent of NaCl amount) shown as dashed lines in Figures 59 through 62. This method is less reliable because of variation in the mass of material put into the sample holder, but is an adequate check on the other technique. The results are similar to those of the internal standard technique and the total volume fractions are lower (105 - 115%). The differences between the two methods are greatest in the later stages of the reaction, with the TiB curve showing the most deviation. This suggests two other factors concerning TiB that may influence differences between standards and samples.

4) The standards were made from mixed, separate powder phases, while in the samples, the TiB and TiB₂ phases were present in the same particles. During pulverizing, the TiB could "flake off" but still leave a coating that would diminish TiB₂ intensity and hence distort the boride volume determinations. Calculation of the mass absorption coefficients and the penetration depth (Table 8) show some absorption effects could occur. How-

Table 8

X-ray Absorption for TiB and TiB₂Calculate mass absorption coefficients: ⁸⁹

$$(\mu/\rho)_{Ti} = 204 \text{ cm}^2/\text{gm} \text{ and } (\mu/\rho)_B = 3 \text{ cm}^2/\text{gm} \text{ for Cu K}\alpha \text{ radiation.}$$

$$\text{TiB: } (\mu/\rho)_{TiB} = \left[\frac{47.9}{58.72} \times 204 \right] + \left[\frac{10.82}{58.72} \times 3 \right] = 166.4 + .6 = 167 \frac{\text{cm}^2}{\text{gm}}$$

$$\text{TiB}_2: (\mu/\rho)_{TiB_2} = \left[\frac{47.9}{69.54} \times 204 \right] + \left[\frac{21.6}{69.54} \times 3 \right] = 140.5 + 1.0 = 141.5 \frac{\text{cm}^2}{\text{gm}}$$

Calculate penetration depth: ⁸⁹

$$h = \frac{\ln(1/(1 - G_x)) \sin \theta}{2(\mu/\rho)_{TiB} \rho_{TiB}}$$

where:

h = penetration depth

 θ = angle for line of interest G_x = fraction of incident radiation absorbedFor $\theta = 21^\circ$, $G_x = 0.99$, and $\rho_{TiB} = 4.56 \text{ gm/cm}^3$

$$h = \frac{(4.605)(.358)}{(9.12)(167)} = 10.8 \text{ } \mu\text{m}$$

ever, the coating before grinding is only approximately 10 μm , so if it flakes off, an even thinner layer should remain. Further, metallographic examination of a pulverized sample showed most fractures to be across the particles and not just flaking, so each boride (TiB and TiB₂) should have been exposed equally to the x-ray beam.

5) Another possibility is peak overlap between Ti ($d = 2.244 \text{ \AA}$) and TiB ($d = 2.346 \text{ \AA}$) combined with an observed shift in Ti peak with reaction time. This effect is shown schematically in Figure 65. The standards made with unreacted Ti showed the Ti peak in its normal position, while for the samples, the Ti peak shifted toward its neighboring Ti-TiB peak ($d = 2.342 \text{ \AA}$ and 2.346 \AA , respectively). Thus, the number of Ti counts made for the sample would be lower than the corresponding number obtained from the standard and the volume fraction of Ti in the sample would be underestimated.

From the above discussion, Ti is the phase with the least reliable volume measurement. Since the parameter of interest is the extent of reaction, x , or relative amounts of the borides, this error is not serious if the borides are measured in the proper proportions. The shift in the Ti peak (Figure 65) measured relative to the

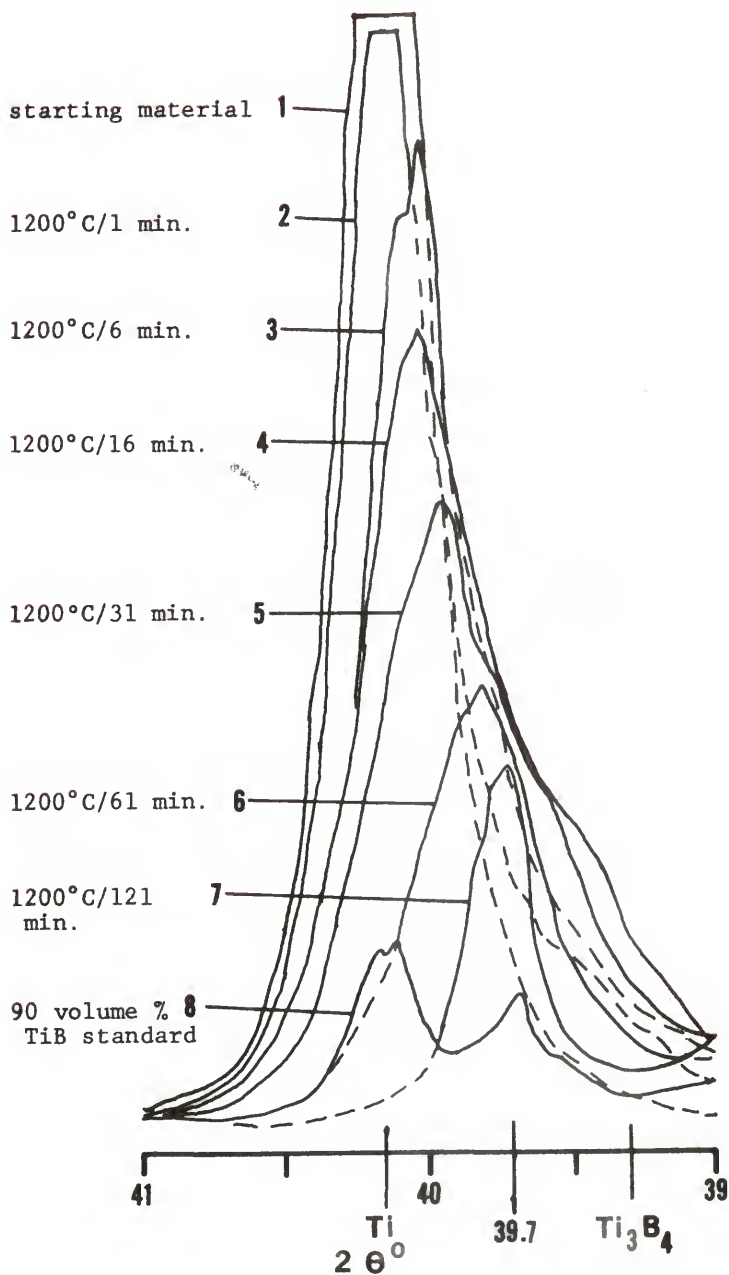


Figure 65. Peak shift for Ti (011) line.

neighboring TiB peaks (2.140 \AA and 2.161 \AA) is seen to occur gradually as the reaction proceeds. This shift is not an experimental artifact because the results for the 90 volume % standard (curve 8, Figure 65) show peaks from both residual Ti in the TiB and 4 volume % unreacted Ti added to make the standard. This curve indicates a definite separation of $\approx 0.45^\circ 2\theta$. This shift could be due to formation of Ti_3B_4 or to solid solution of B or some contaminant. The final peak location is not shifted sufficiently to support the conclusion that Ti_3B_4 has formed, although development of the shoulder on curves 4 and 5 (Figure 65) suggests it. Examination of alternative major Ti_3B_4 peaks ($d = 2.533 \text{ \AA}$ or 2.117 \AA) is not possible due to overlap with Ti and TiB peaks. Clark⁹⁰ has shown the influence of O and N on the Ti lattice constants: there is negligible change in a_0 and an increase in c_0 . The peak measured here is for the (011) plane; the corresponding shifts in d spacing for it and for c_0 are given in Table 9, assuming that a_0 remains constant. These results suggest that whatever O or N contamination is present is already in the starting material since the initial c_0 of 4.6923 \AA corresponds to ≈ 0.4 weight % of these elements in Ti.⁹⁰ No report of a change in Ti c_0 with known B content could be found⁹¹ to check the possibility of B

Table 9
Ti Peak Shift Data

Sample	$2\theta^\circ$	$d_{011}\text{\AA}^a$	c_{O}^b	curve ^c number	Comments ^c
starting material	40.15	2.2440	4.6923	1	
1200°C/1 min.	40.15	2.2440	4.6923	2	broadened
1200°C/6 min.	40.07	2.2483	4.7320	3	
1200°C/16 min.	40.05	2.2494	4.7423	4	shoulder forms
1200°C/31 min.	39.95	2.2548	4.7936	5	
1200°C/61 min.	39.82	2.2618	4.8619	6	shoulder disappears
1200°C/121 min.	39.70	2.2684	4.9285	7	

^aUsed Cu K α radiation

^bCalculated from ⁸⁹

$$\frac{1}{d^2} = \left(\frac{4}{3}\right)\frac{1}{a^2} + \frac{1}{c^2}$$

^cRefer to Figure 65

causing this shift in d spacing from 4.6923 to 4.9285 Å. The measuring conditions used here are not accurate enough to specify the exact amount or cause of this shift, but Figure 65 shows it does occur.

The x-ray results show a more gradual change in volume fractions than the Quantitative Microscopy data. The Ti results are anomalously low and several reasons for this have been discussed. The internal standard curves are almost linear, as expected.

SECTION IV MODEL ANALYSES

Several models were considered as possible explanations for the results obtained from Quantitative Microscopy and quantitative x-ray measurements in an attempt to determine the kinetic mechanisms for the formation of TiB in a powder compact. These models may be distinguished principally by the rate controlling processes upon which they are predicated. These controlling mechanisms are the rate of nucleation and growth, phase boundary or interaction, and diffusion. Diffusion controlled models may be divided into those which assume a constant diffusion coefficient (Jander,⁶⁴ Ginstling-Brounshtein,⁶⁵ Valensi-⁶⁶ Carter⁶⁷, and Dunwald-Wagner⁷⁵) and those where the diffusion coefficient changes with time (Zhuravlev et al.,⁷³ Kroger-Kieglner,⁷¹ and Hulbert et al.⁷²), usually at an inverse rate.⁷⁰

Except for the interface displacement models, discussed below, all the models assume that a matrix phase completely coats and reacts with spherical particles of the other reactant to form a spherical shell of product (Figure 5). As the reaction proceeds, this shell thickens to consume the spherical reactant. The extent of reaction

parameter, x , is defined as the fraction of original spherical volume consumed to form a product shell. This geometry is an ideal case that is seldom exactly met in practice unless a special effort to obtain spheres is made.⁶⁷ However, the spherical models have proven useful.⁶³ In particular, the microstructure observed during the later stages of TiB formation approximates the geometric assumptions of the spherical models fairly closely so application of the models in this later stage of reaction may be valid.

The utility of the interface displacement relations [Equations (28), (29), and (30)] is the ability to determine the average interface velocity for arbitrary (smooth) shapes and relate this velocity to the average curvature of the reacting surface: the spherical approximation is relaxed and a physically more realistic geometry may be treated. If the average interface velocity is determined to have a constant, inverse, or square root time dependence, the result supports interpreting the reaction mechanism as phase boundary, Tammann, or diffusion controlled, respectively. If one of these time dependences is not found, this suggests the models are inapplicable due to variation of interfacial velocities with location in the microstructure. However, a nonconstant interface

velocity is evidence that the rate controlling mechanism is not interface reaction.

The influence of particle size distribution on powder compact reaction kinetics has been treated in several models,⁹²⁻⁹⁵ but these still assume the particles are spherical and require detailed size distribution information. Though the computations required are very complex, a model proposed by Sasaki⁹³ was examined, since the particle size variation observed for TiB_2 could influence the rate of TiB formation. This treatment generalizes the Valensi-Carter model by the use of a particle size distribution with diameters increasing in geometric series:

$$r_n = a^{n-1} r_0 \quad (39)$$

where r_0 and r_n are the initial and final radii of the series and a is the ratio of the mean radii of adjacent size groups. The value $a = 1.2$ was used by Sasaki and also in this study. As the reaction proceeds, larger and larger spheres are completely reacted, and the extent of reaction, x , for these groups is one. If the i^{th} group is the next larger size not completely reacted, then the x_i to x_n decrease for the i^{th} to the n^{th} size groups. The overall reacted fraction for the distribution of spheres is

$$x = \sum_1^{i-1} m_n + \sum_i^n m_n x_n \quad (40)$$

where m_n is the fraction of total material in each group before reaction. Substituting the particle size distribution into the Valensi-Carter model for the incompletely reacted spheres gives

$$\sum_i^n I(x_i) = \sum_i^n \frac{Z - (1+(Z-1)x_i)^{2/3} - (Z-1)(1-x_i)^{2/3}}{(Z-1)} = \frac{2K_{VCS} t}{r_o^2} \sum_i^n \frac{1}{a^{2(n-1)}} = 2 K_{VCS} t \sum_i^n \frac{1}{r_n^2} \quad (41)$$

and for the reacted spheres gives

$$I(x_{\max}) = \frac{Z - Z^{2/3}}{(Z-1)} \quad (42)$$

The $I(x_{\max})$ is a constant independent of time and so provides no information about the reaction constant K_{VCS} .

If each $I(x_i)$ can be determined, then K_{VCS} can be determined and the Sasaki⁹³ model evaluated. However, it is difficult to obtain each x_i from the overall x measured experimentally. To solve for the reaction constant of this series, Sasaki proposed a graphical solution utilizing a standard model curve that incorporates an experimentally measured particle size distribution. The TiB_2 particle size distribution in Figure 6 was used for this study. A plot of the Valensi-⁶⁶Carter⁶⁷ model [Equa-

tion (14)] is shown in Figure 66. An arbitrarily selected x_i value establishes $I(x_i)$ and from this, a series of $I(x_{i+1})$ through $I(x_n)$ values are obtained by

$$I(x_{i+j}) = \frac{I(x_{i+j}-1)}{a^2} \quad (43)$$

The corresponding values of x_{i+j} are also determined. From this the sums $\Sigma I(x_i)$, Σx_i , and $\Sigma \frac{1}{r_i^2}$ can be calculated. Equations (40) and (41) permit the construction of a standard model curve of K_{VCS}^t vs. overall extent of reaction x (Figure 67). Three values of x_i ($x_i = 1.00$, 0.98 and 0.957) were arbitrarily selected and used to construct Figure 67; the details of the calculation are given in Appendix 9.

The extent of reaction for this study is measured as $\frac{V_V^{TiB}}{(V_V^{TiB} + V_V^{TiB_2})}$. Figures 68 and 69 show this parameter determined from the Quantitative Microscopy and quantitative x-ray analyses, respectively. Figure 68 shows a sigmoid behavior with an induction period, a rapid increase of the reaction, and an approach to a final value. The results in Figure 69 show a more gradual increase without any induction period. These curves increase smoothly and are accelerated with increasing temperature. The differences between these two sets of curves are due to the pullout and rounding during

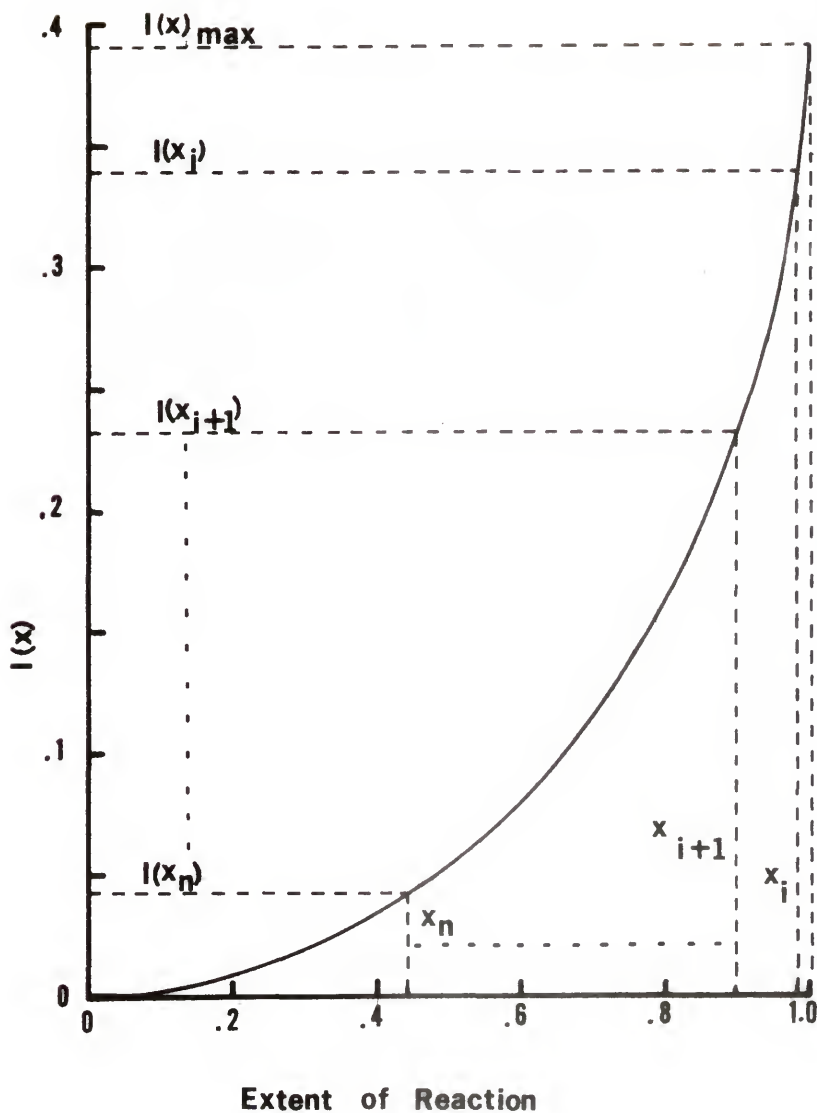


Figure 66. Valensi-Carter model as a function of extent of reaction.

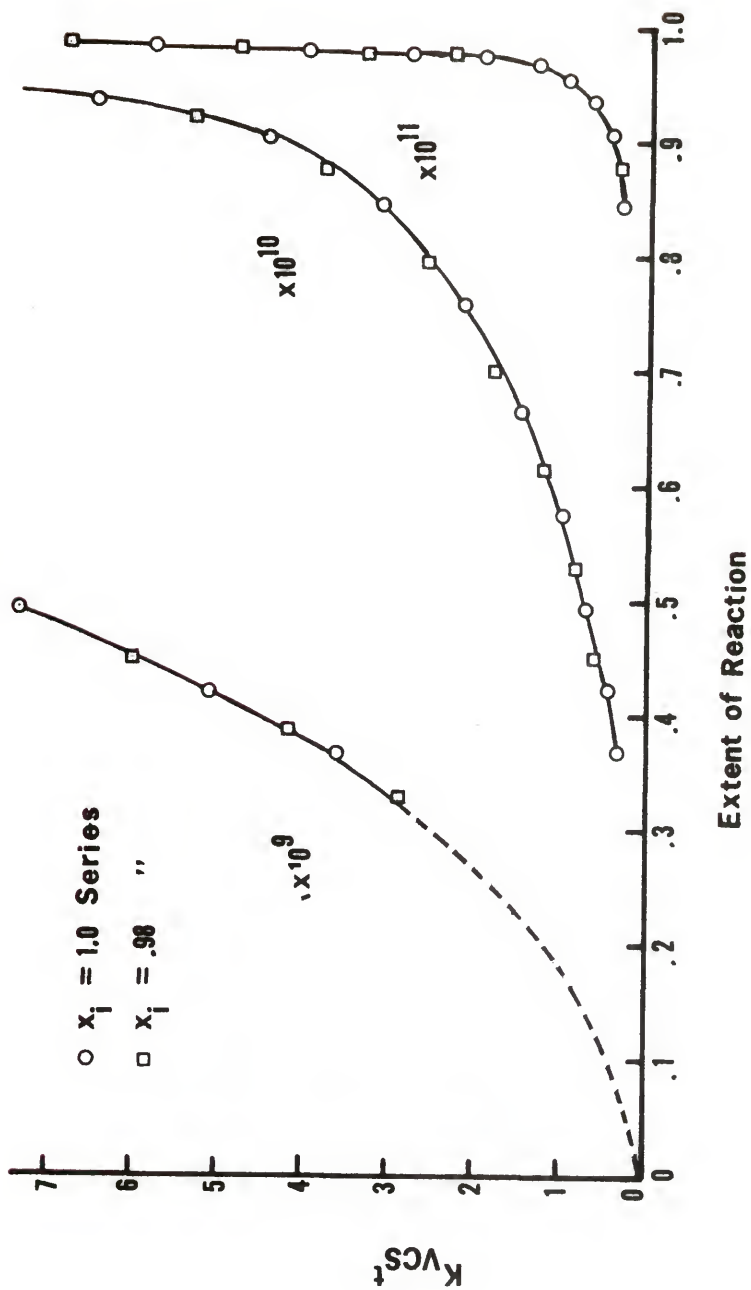


Figure 67. Standard curve for Sasaki model. The $x_i = 0.957$ series is not shown for clarity.

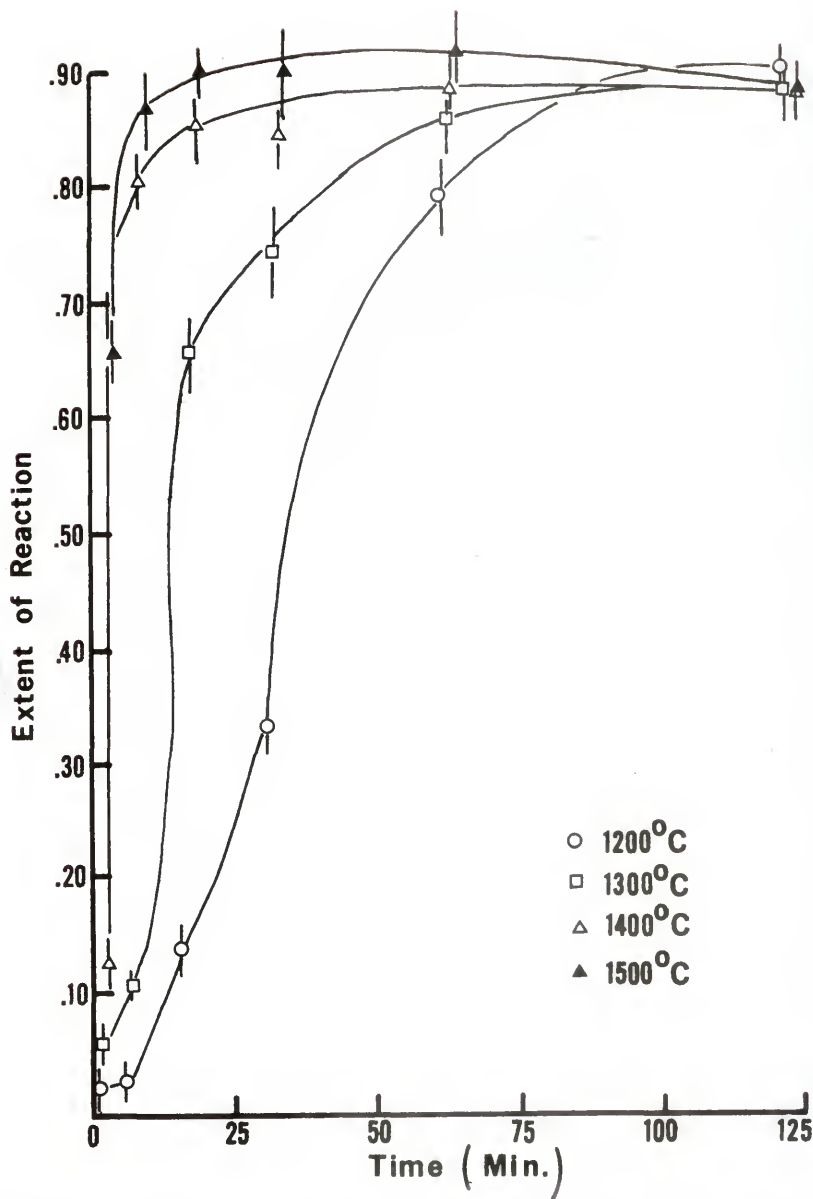


Figure 68. Extent of reaction for Quantitative Microscopy data.

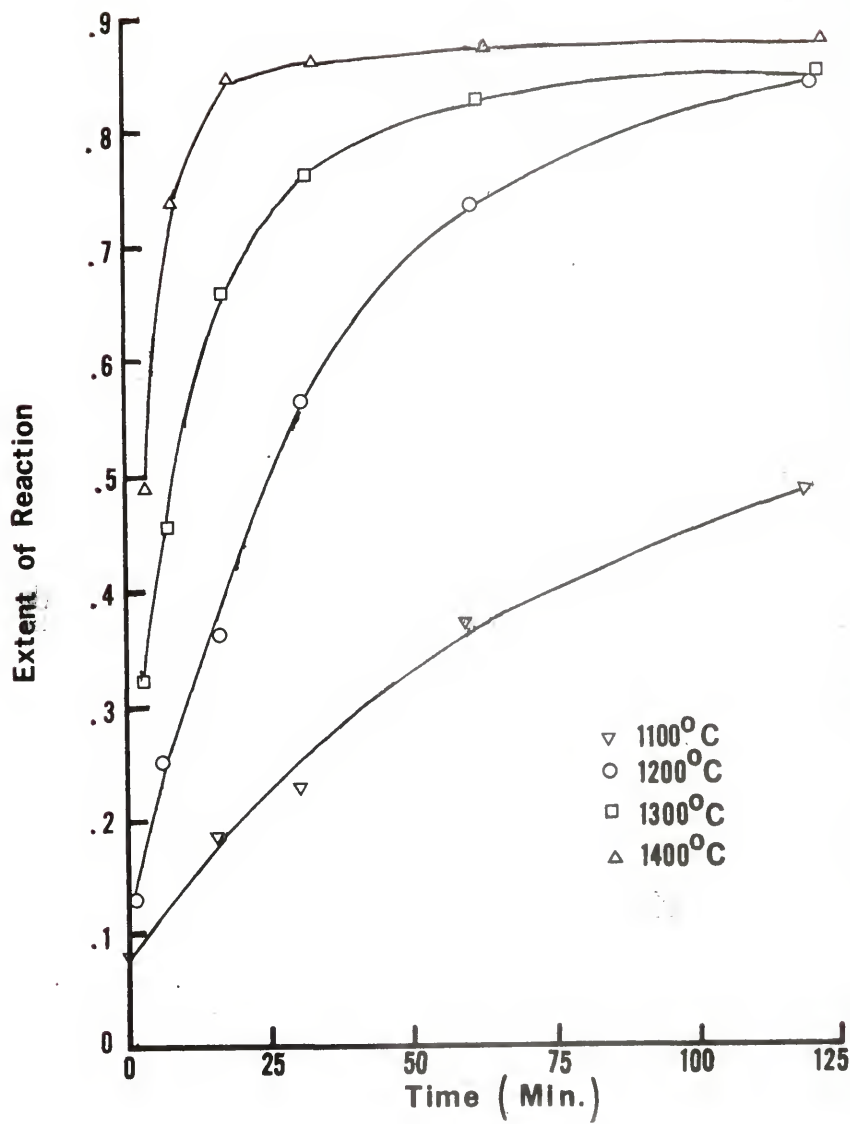


Figure 69. Extent of reaction for quantitative x-ray data.

polishing for Quantitative Microscopy and the distortions in Ti volume fractions measured by quantitative x-ray analysis. The calculated model results (Appendices 10 and 11) obtained by substituting experimentally determined values of x in the model expressions of Table 1 also reflect these differences. Plots of these results are discussed below; a straight line indicates agreement with the model and supports interpretation of reaction data in terms of the applicable mechanism modeled.

The model results using Quantitative Microscopy data are shown in Figures 70 through 79. The data for 1400 and 1500°C are too near completion of the reaction to be useful since the model results cluster near the final values. The 1300°C data give straight or nearly straight line segments for all the models. This may be attributed to the range of x covered by these data, i.e., $x = .66$ to $x = .87$. Assuming the spherical shell geometry of these models (Figure 5) and the initial volume equal to unity, the initial radius is .62 and the corresponding radii of the unreacted core at $x = .66$ and $x = .87$ are $r = .433$ and $r = .314$, respectively. The volume change is 21% of the initial value while the radius change is 19%. Thus, over this range of reaction, the volume change is almost directly proportional to the change in radius and basically

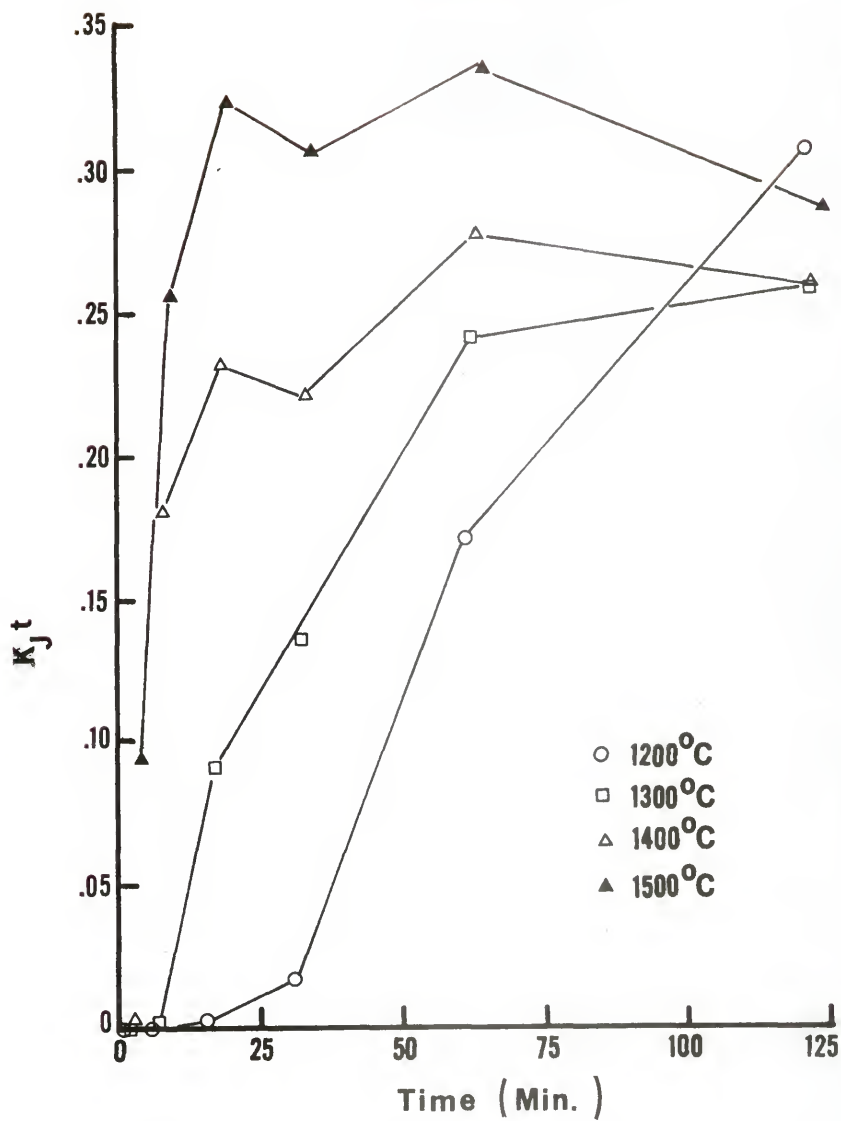


Figure 70. Jander model results for Quantitative Microscopy data.

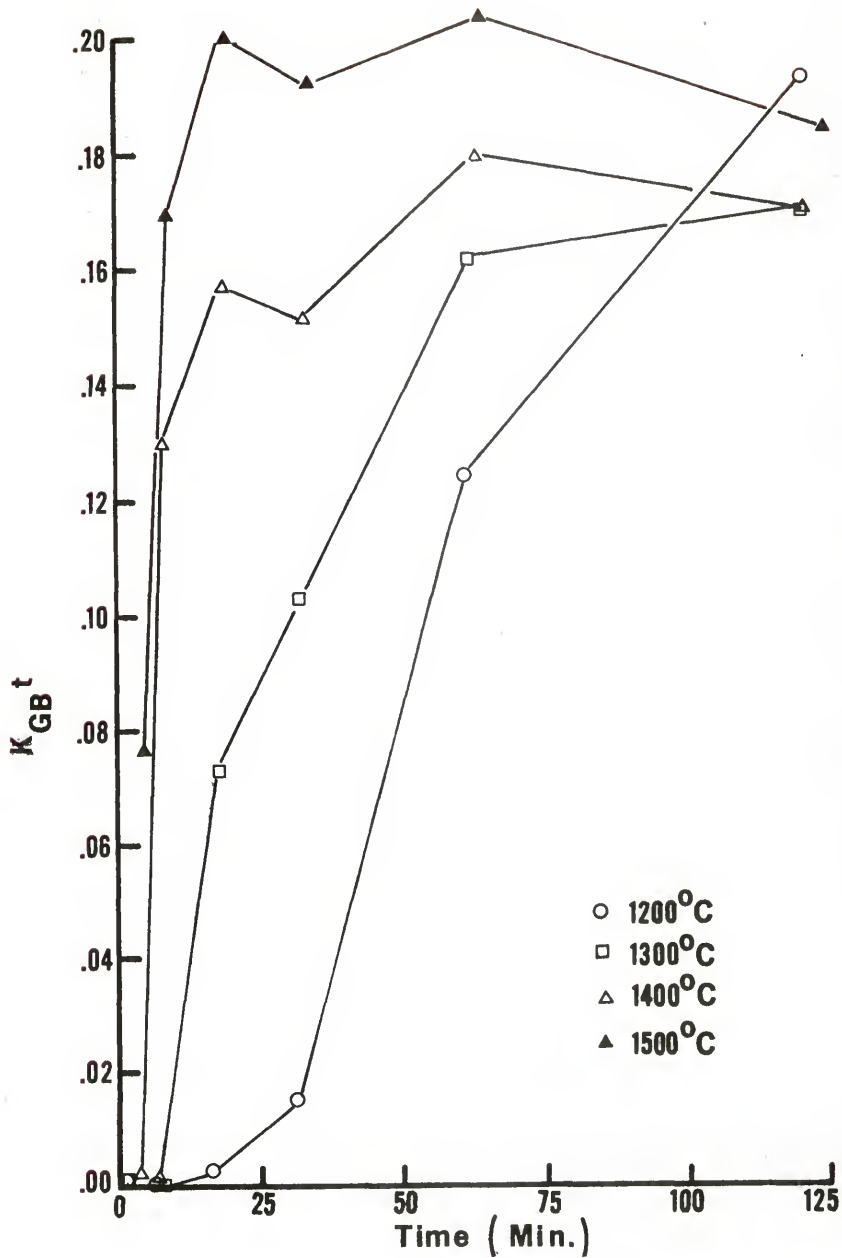


Figure 71. Ginstling-Bronshtein model results for Quantitative Microscopy data

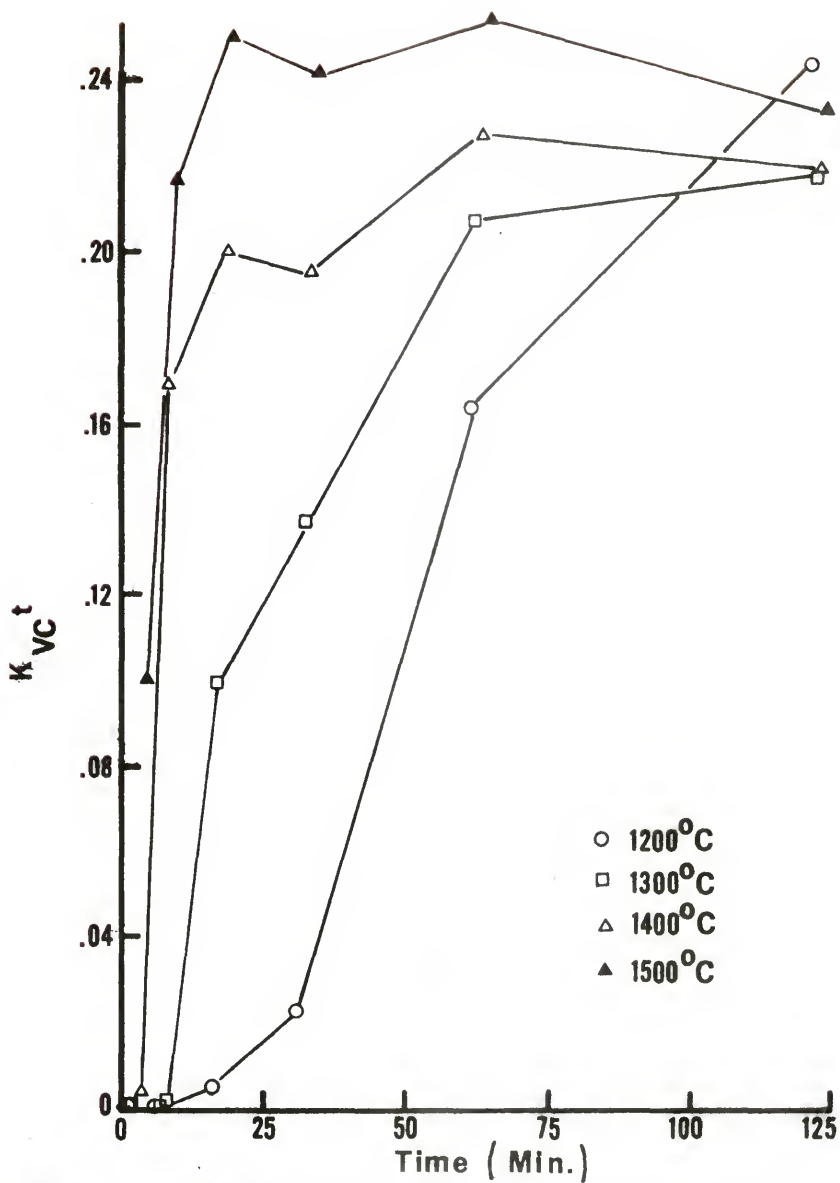


Figure 72. Valensi-Carter model results for Quantitative Microscopy data.

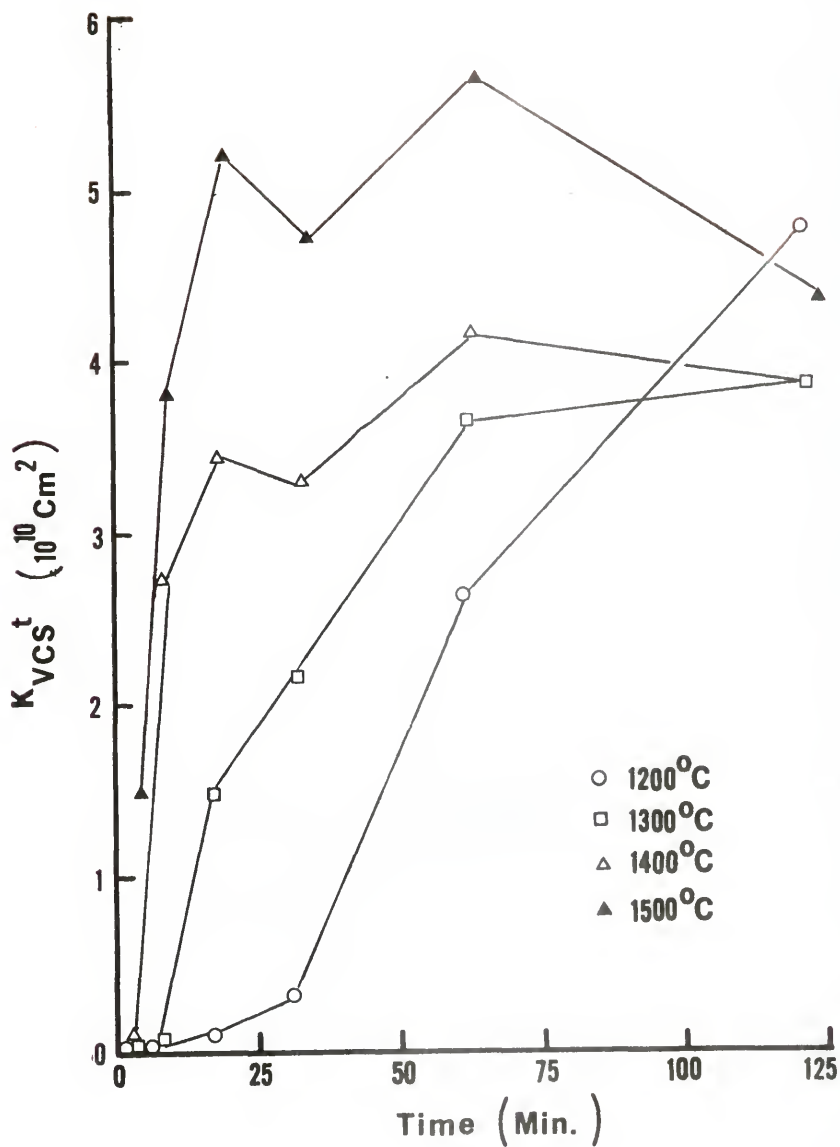


Figure 73. Sasaki model results for Quantitative Microscopy data.

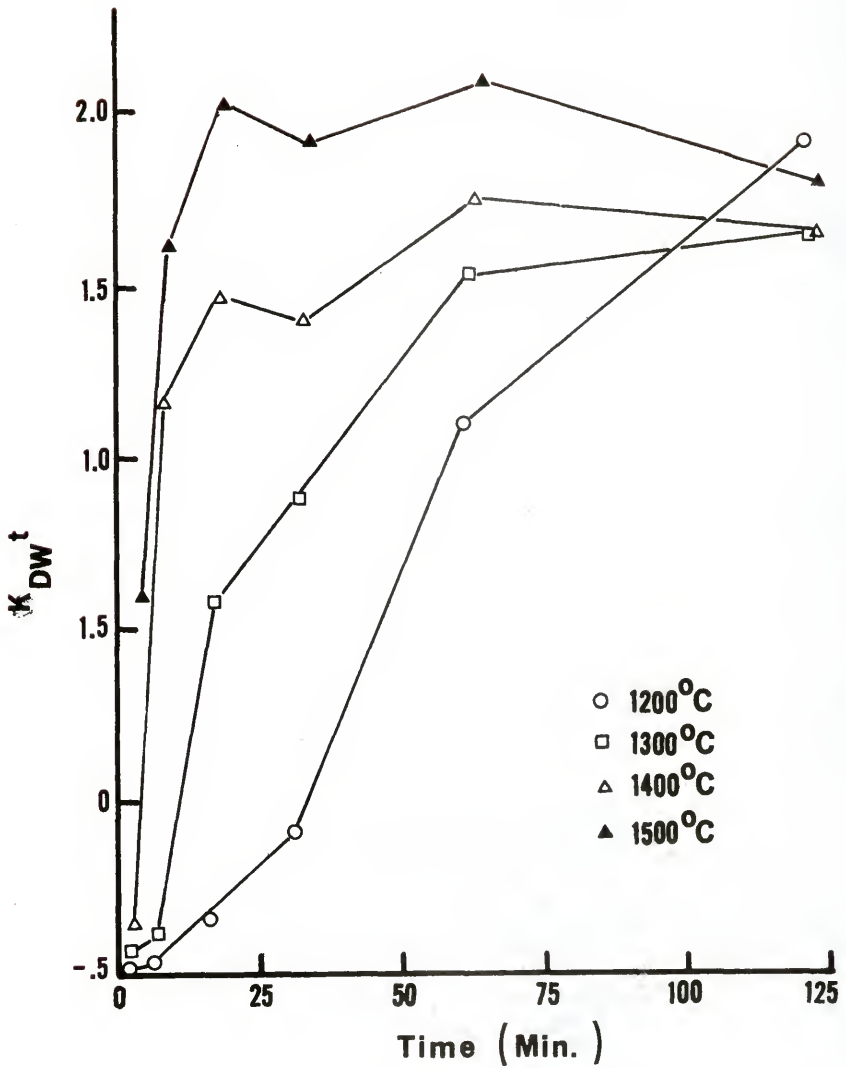


Figure 74. Dunwald-Wagner model results for Quantitative Microscopy data.

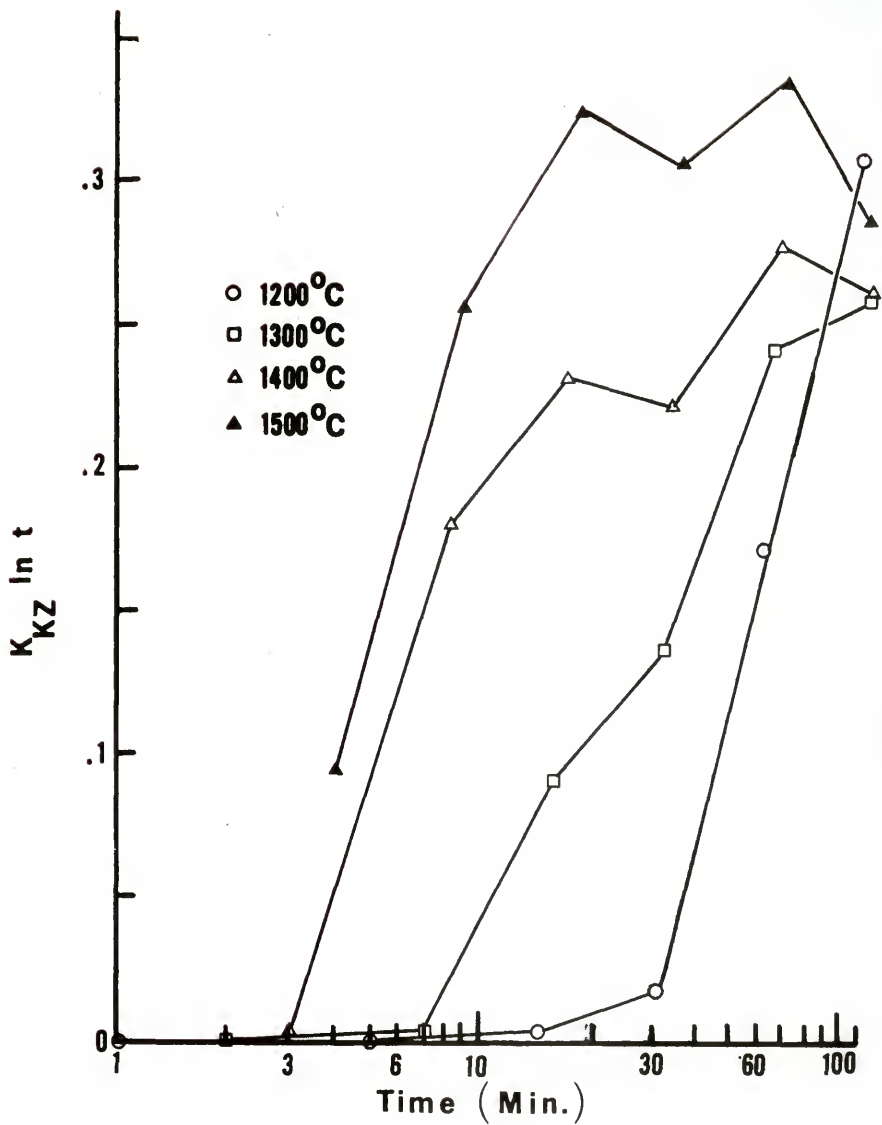


Figure 75. Kroger-Ziegler model results for Quantitative Microscopy data.

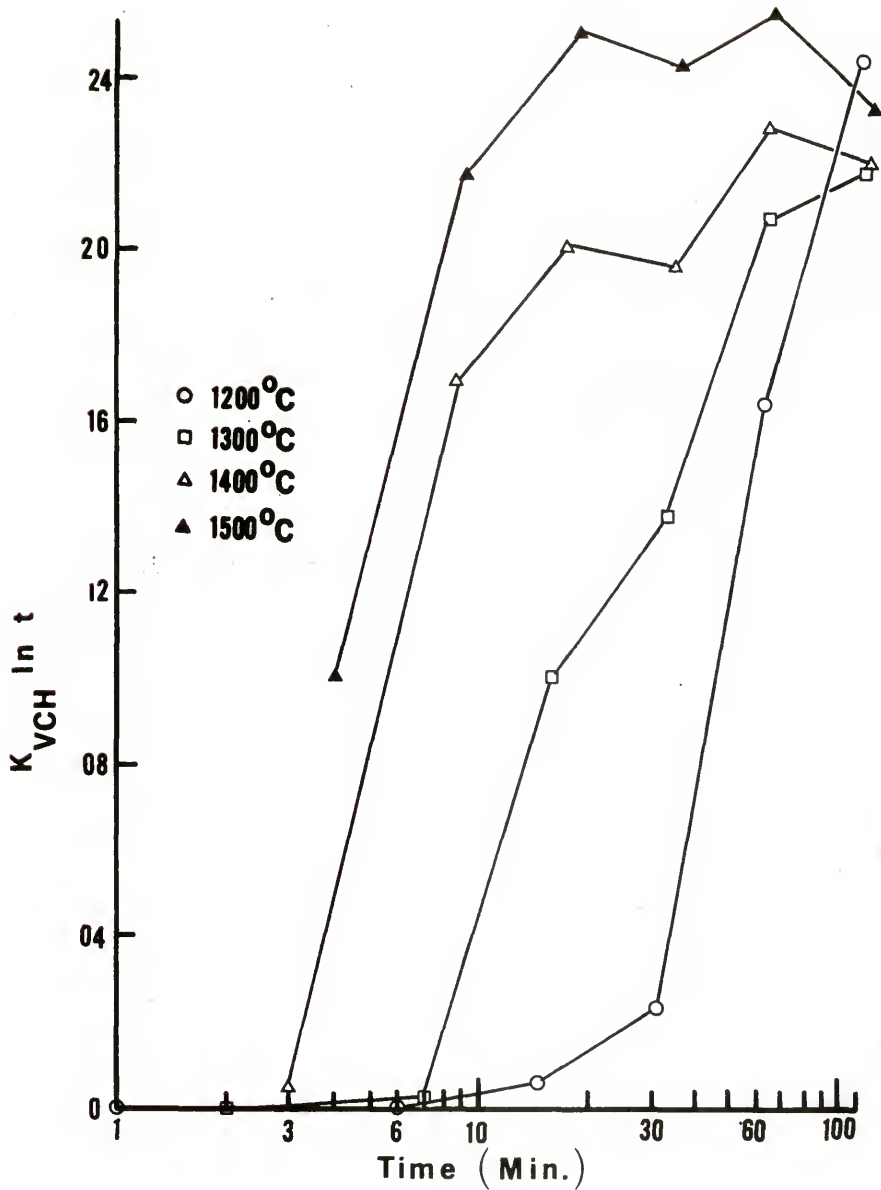


Figure 76. Hulbert *et al.* model results for Quantitative Microscopy data.

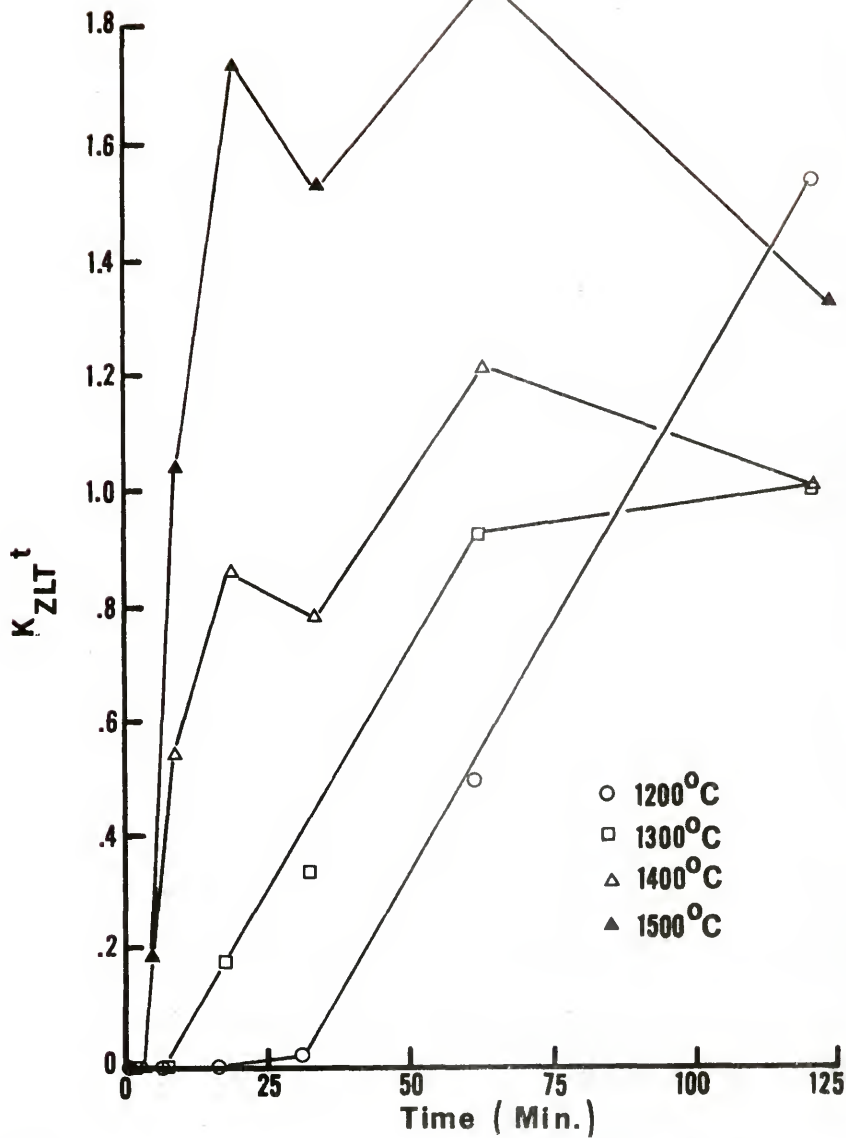


Figure 77. Zhuravlev *et al.* model results for Quantitative Microscopy data.

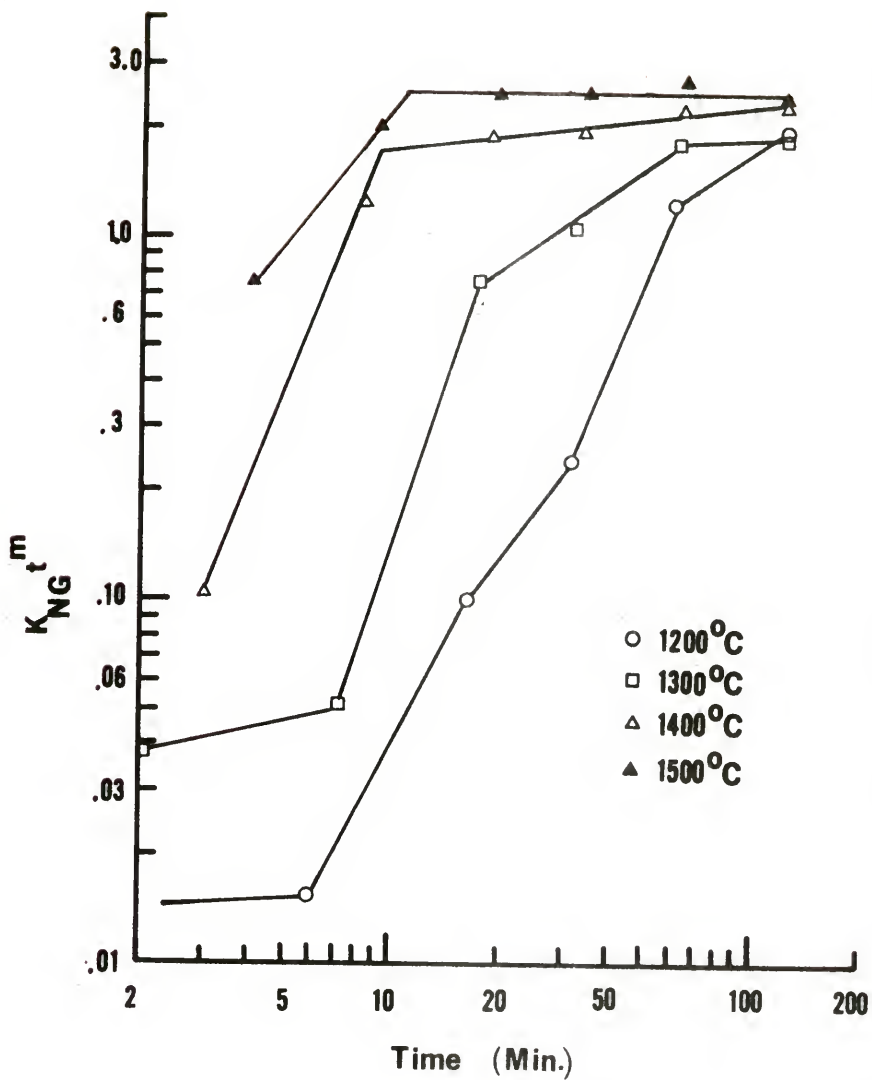


Figure 78. Nucleation and growth model results for Quantitative Microscopy data.

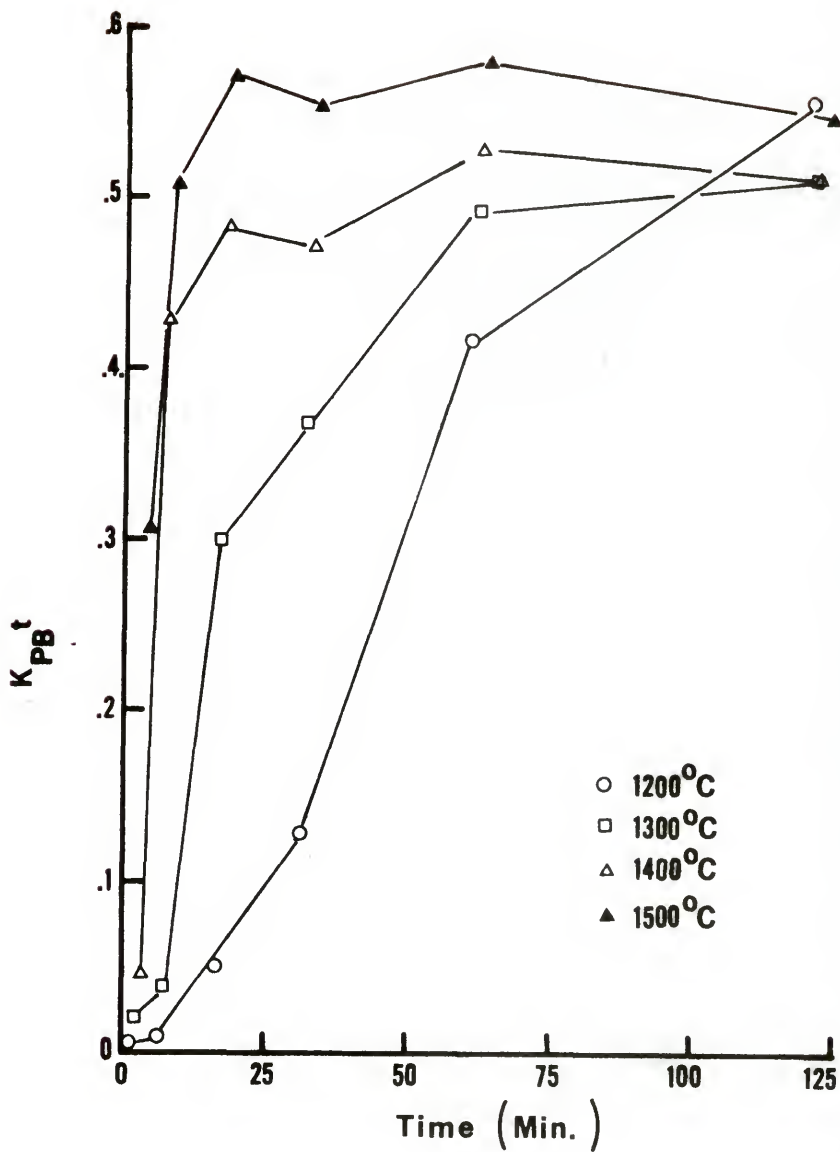


Figure 79. Phase boundary model results for Quantitative Microscopy data.

independent of the rate (or mechanism) of this radius decrease. This leaves only the 1200°C Quantitative Microscopy data to distinguish among alternative mechanisms.

The model results from x-ray data (Figure 80 through 87) are most useful since straight lines are seen over a wider temperature range. The data fit the model at progressively earlier times with increasing temperature. That the data give straight lines at earlier times for some models and at later times for others suggests the rate controlling mechanism changes during the reaction.

The x-ray data provide the best evidence for a diffusion controlled growth mechanism for this reaction. When the early stage data are fit to the Valensi-⁶⁶ Carter,⁶⁷ Sasaki,⁹³ and Dunwald-Wagner⁷⁵ models (Figures 80 through 82), straight line segments are obtained, while during later stages, the data fit the models of Kroger-Ziegler,⁷¹ Hulbert et al.,⁷² and Zhuravlev et al.⁷³ better (Figures 83 through 85). The Quantitative Microscopy data also fit the Zhuravlev et al.⁷³ model (Figure 77). These results suggest the reaction rate is diffusion controlled with an initially constant diffusion coefficient which later decreases inversely with time.

The model of Zhuravlev et al.⁷³ assumes the decrease in spherical reactant controls the rate of the reaction,

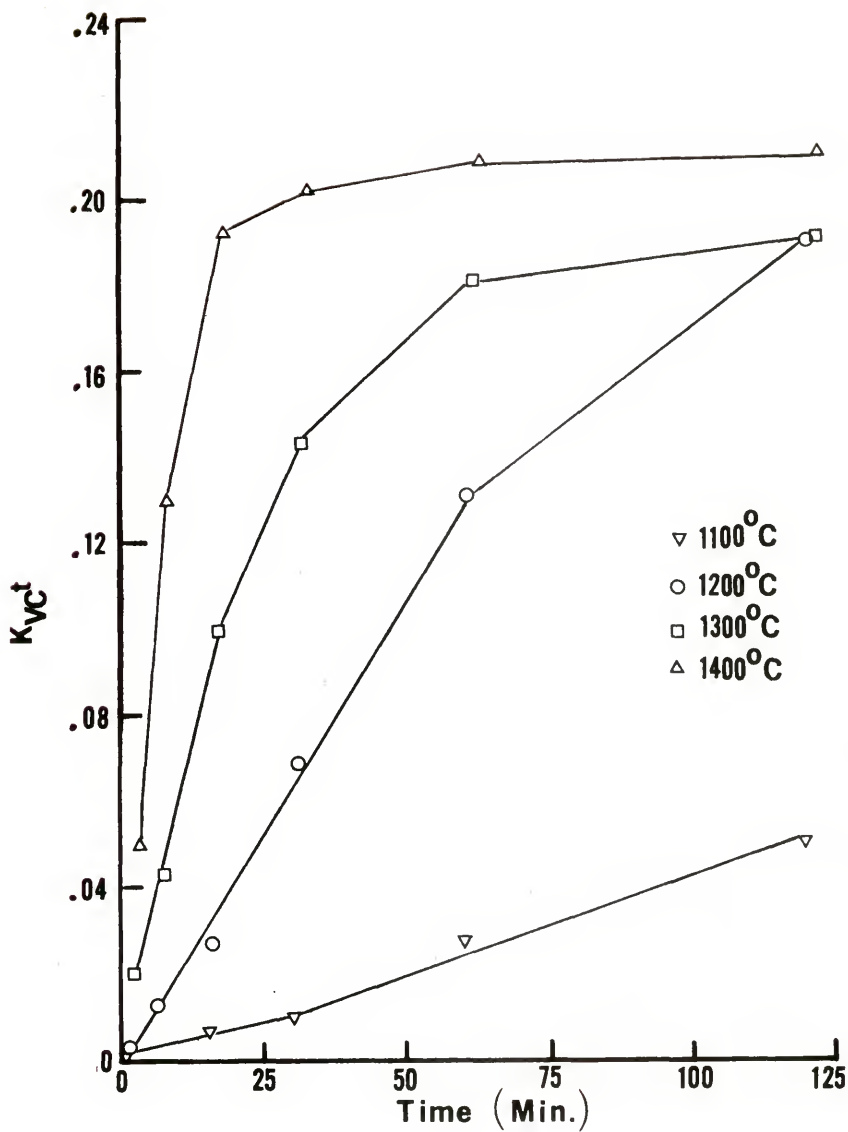


Figure 80. Valensi-Carter model results for quantitative x-ray data.

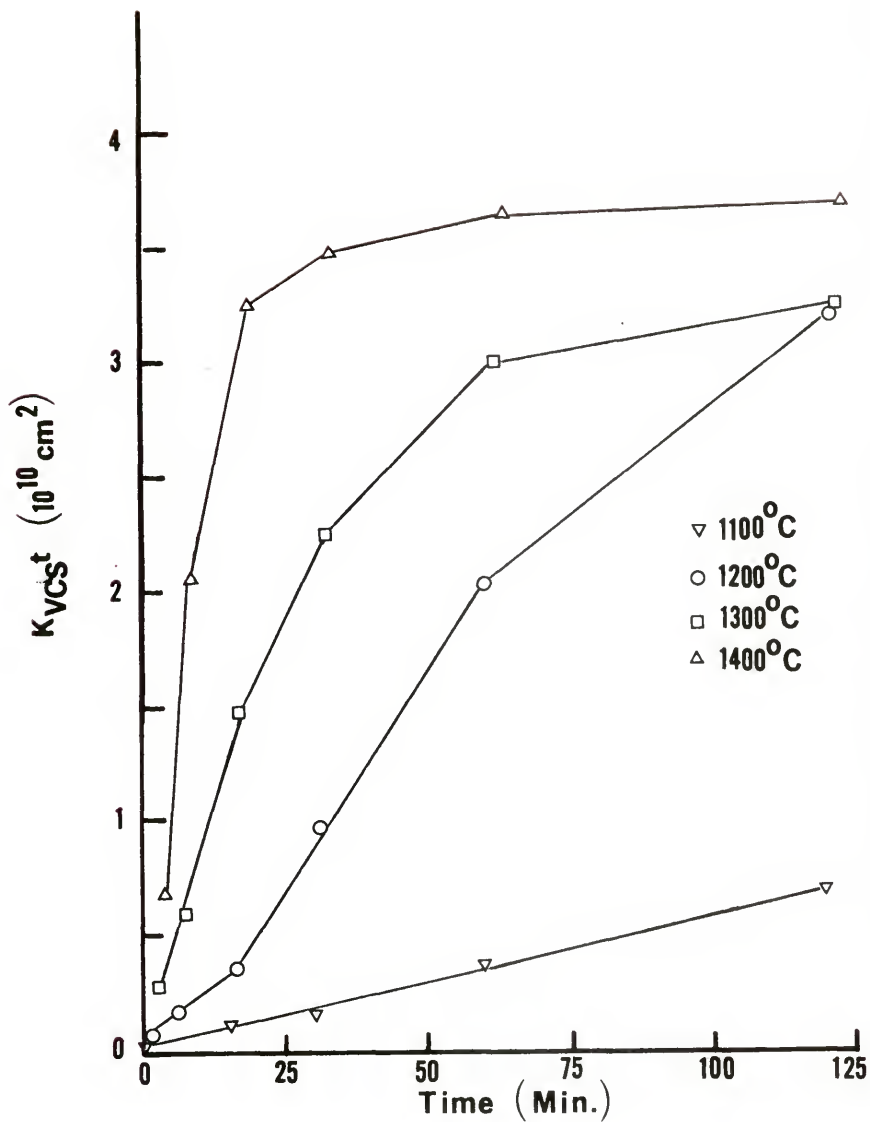


Figure 81. Sasaki model results for quantitative x-ray data.

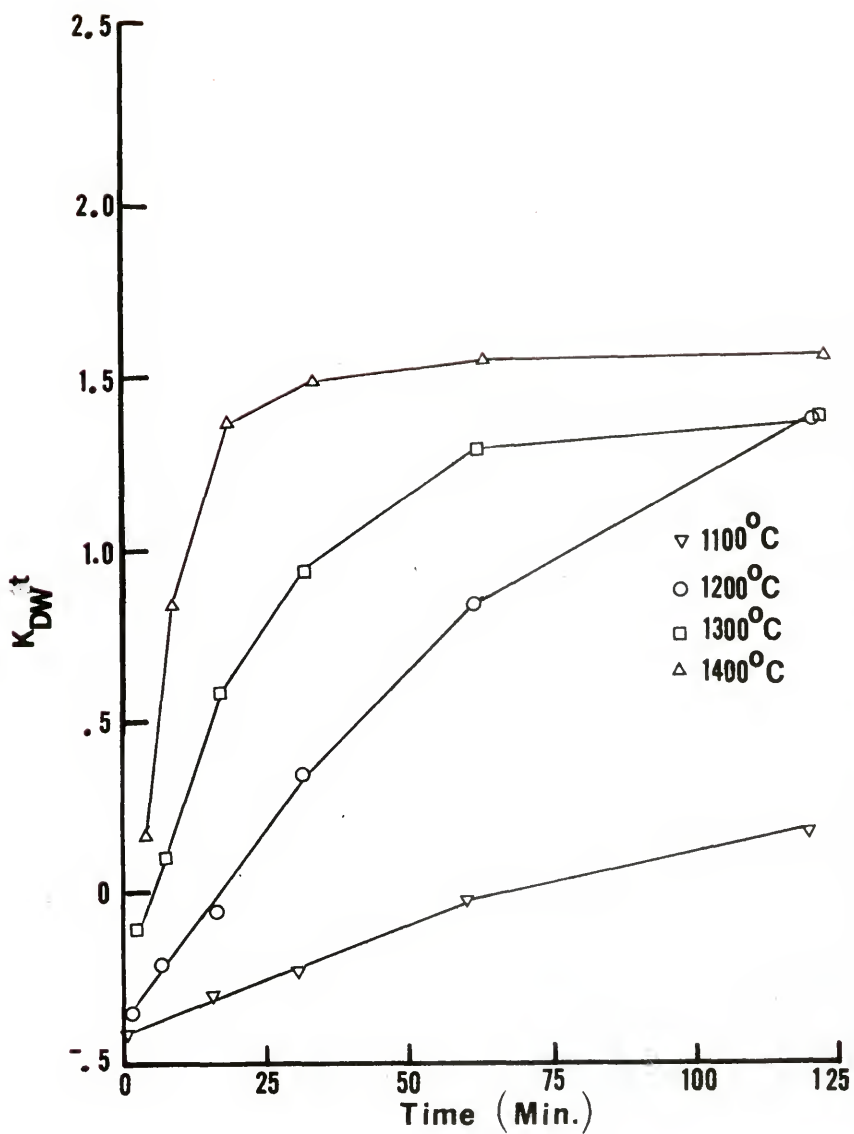


Figure 82. Dunwald-Wagner model results for quantitative x-ray data.

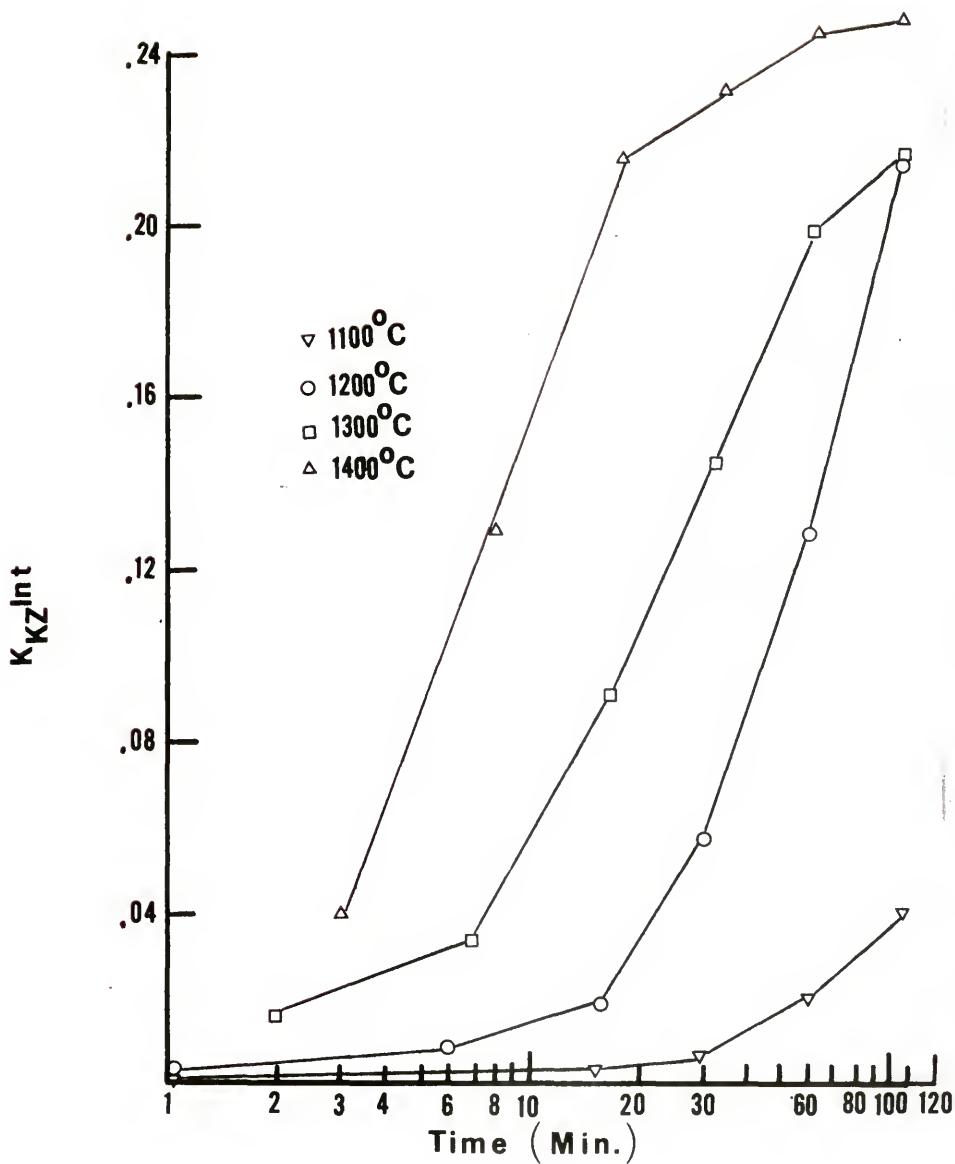


Figure 83. Kroger-Ziegler model results for quantitative x-ray data.

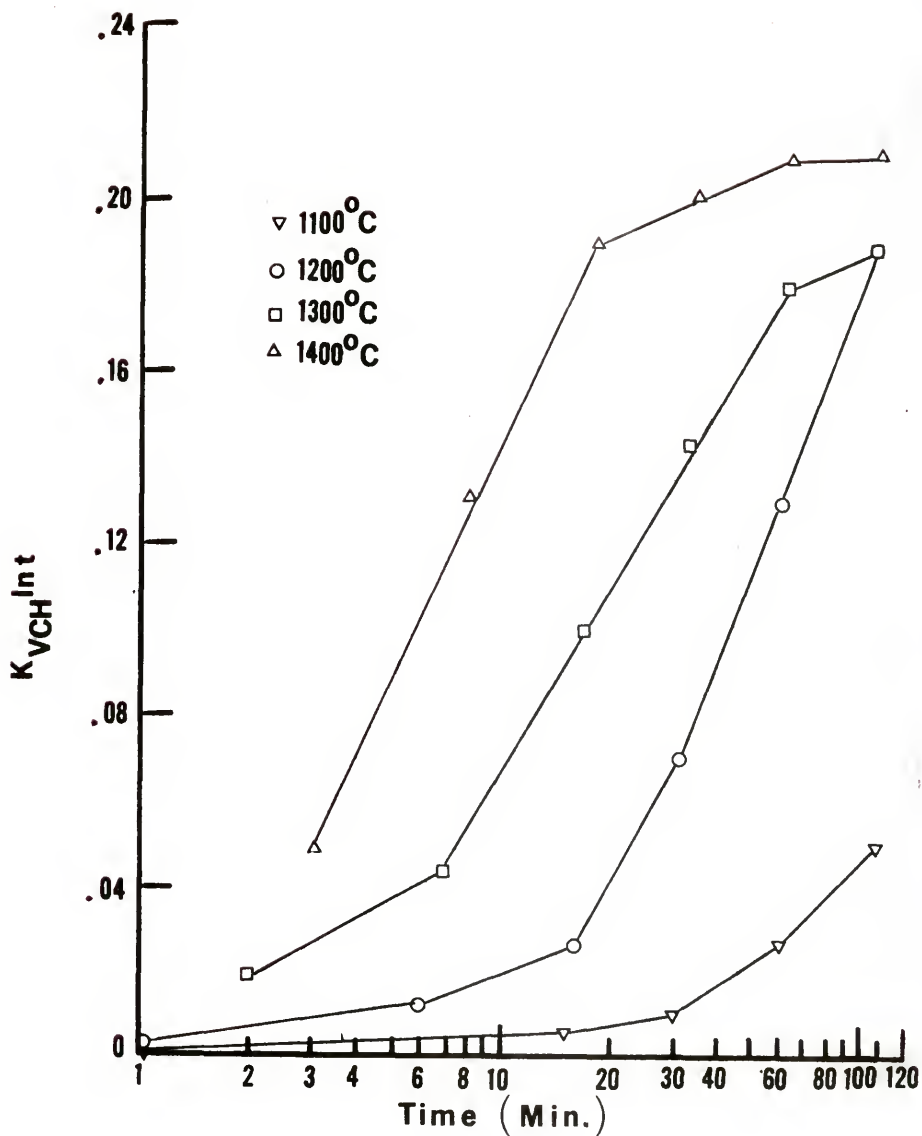


Figure 84. Hulbert *et al.* model results for quantitative x-ray data.

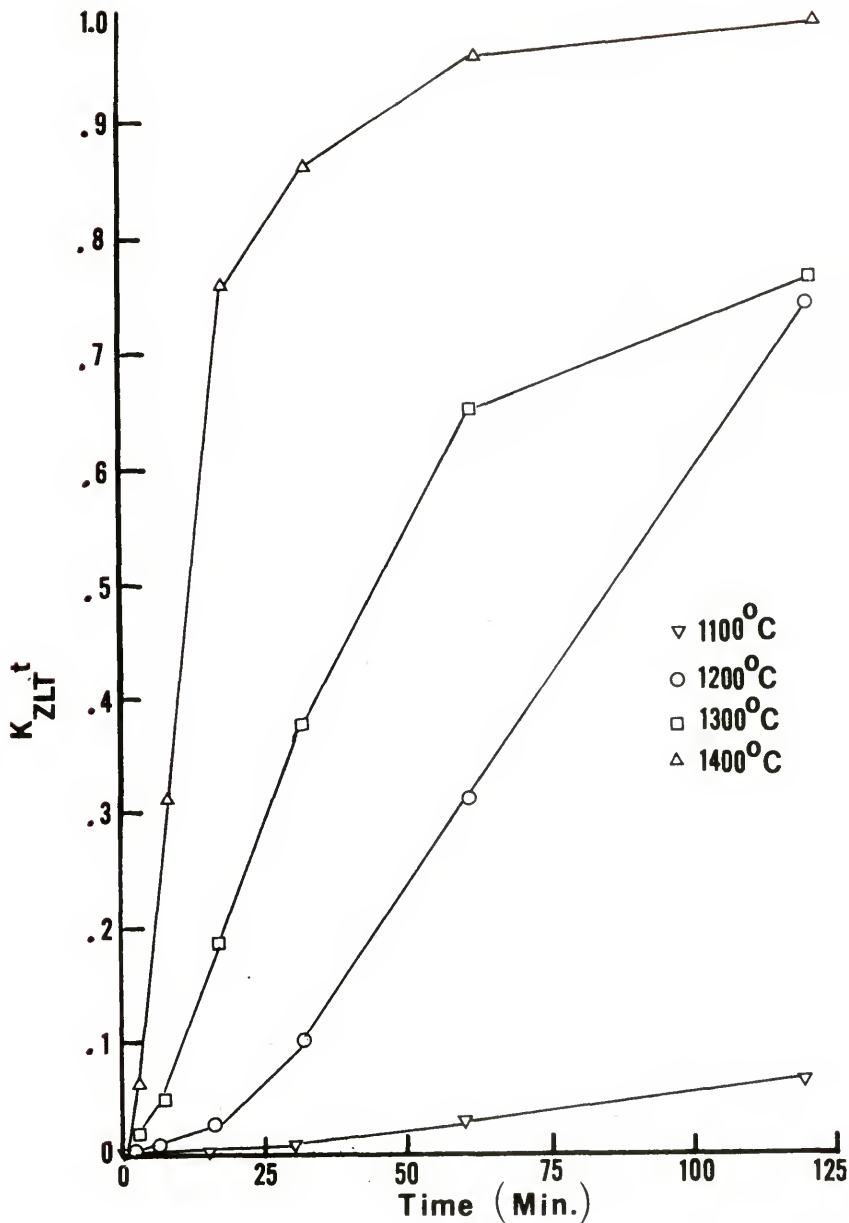


Figure 85. Zhuravlev et al. model results for quantitative x-ray data.

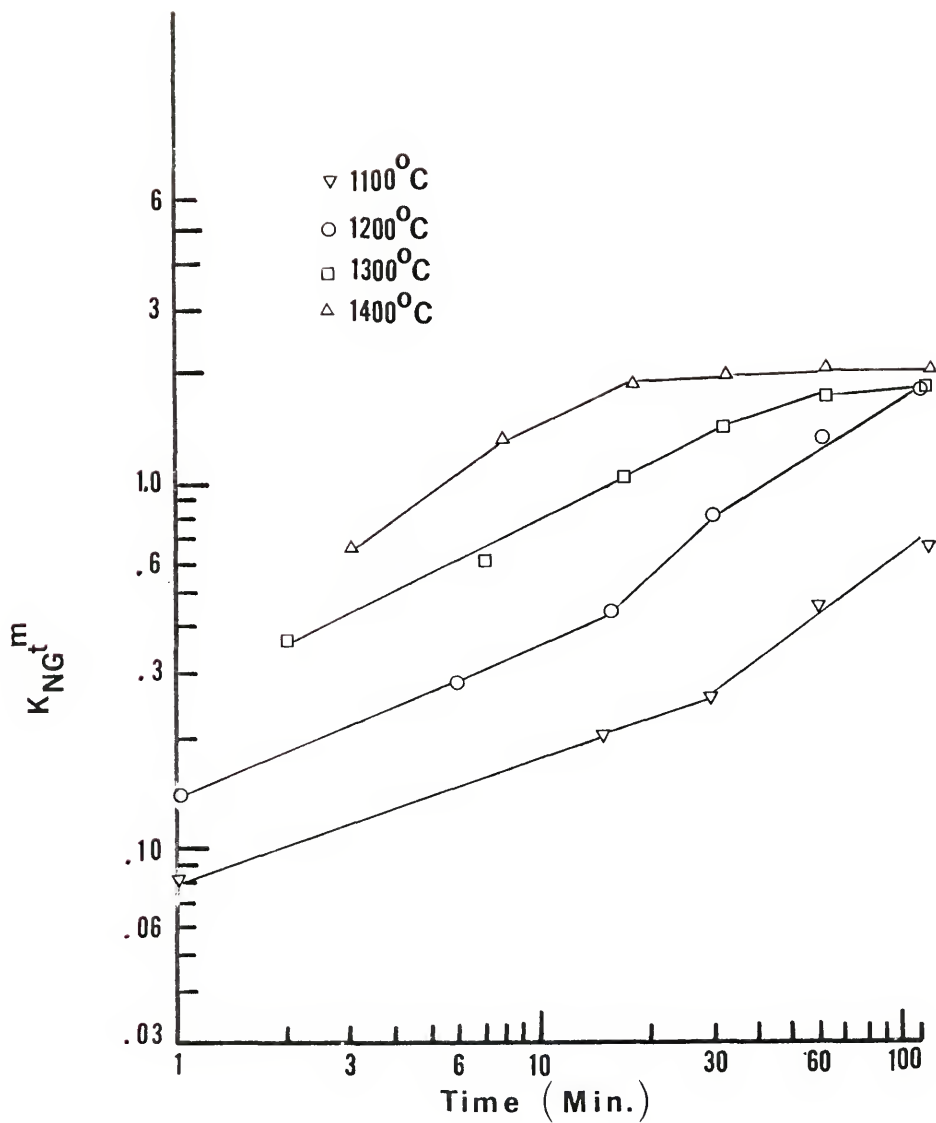


Figure 86. Nucleation and growth model results for quantitative x-ray data.

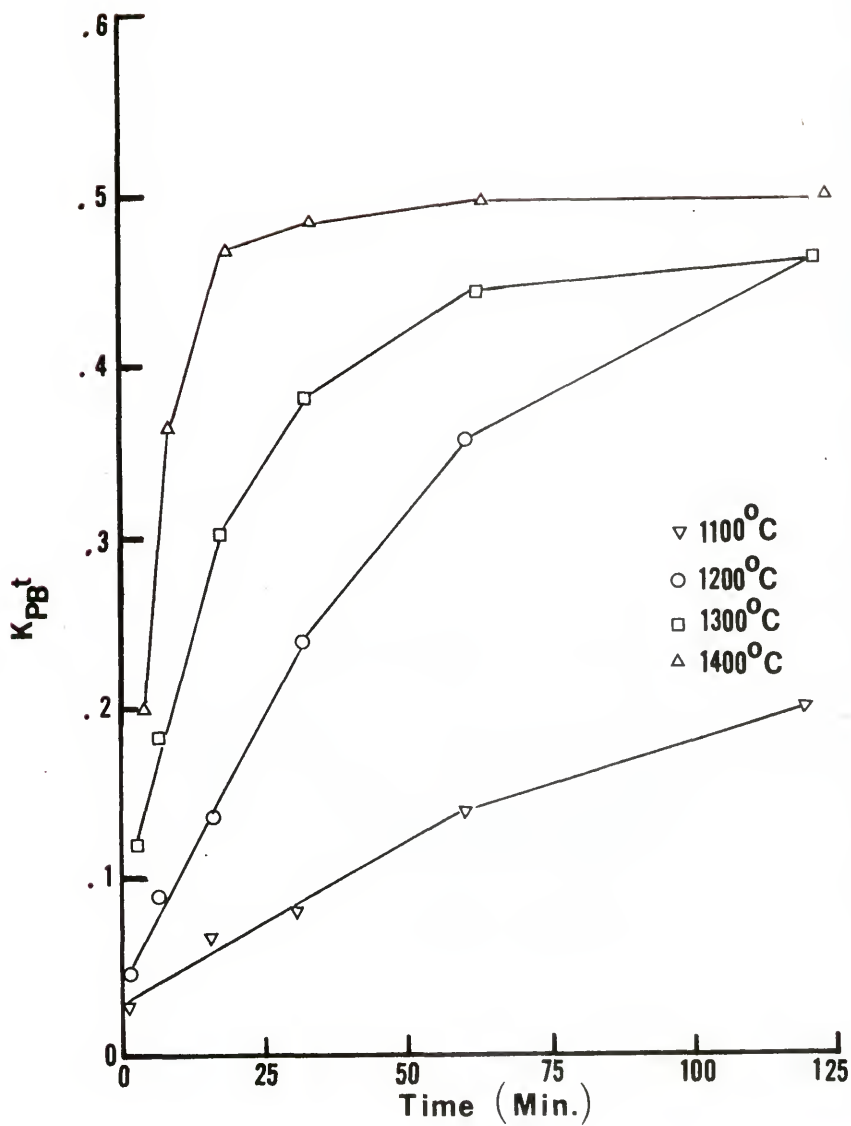


Figure 87. Phase boundary model results for quantitative x-ray data.

while the models based on the Tammann⁷⁰ expression assume the diffusion coefficient changes inversely with time, for example with the removal of lattice defects in excess of an equilibrium number. Since $(1-x)$ decreases with time, it may have an inverse dependence in some cases $[(1-x) \propto \frac{1}{t}]$, giving the same behavior for these models. The above models assume an infinite supply of matrix material, but an inverse time dependence of the Ti available for reaction would also give $[(1-x) \propto \frac{1}{t}]$. This is possible since the Ti volume is decreasing and the distance Ti must diffuse over the TiB surface and through the TiB product layer is increasing. This explains the good fit between later stage data and the models of Kroger-Ziegler,⁷¹ Hulbert et al.,⁷² and Zhuravlev et al.⁷³

It is surprising that the early stage x-ray data show straight line fits to the models since the assumed spherical shell geometry is not seen metallographically until later in the reaction. However, Figure 66 shows the Valensi-⁶⁶Carter⁶⁷ model is not very sensitive to changes in x at low x values. This suggests that thicker TiB product zones covering only part of the TiB_2 particles provided extent of reaction data which is equivalent to thinner product layers that completely coat the particles. Also, the small particles of TiB_2 present with larger ones

(Figure 8a) would convert to TiB rapidly and provide a volume of product equivalent to a shell; this volume is preferentially detected by x-ray measurements because of the sample packing and nearly ignored by the Quantimet because of optical resolution and nonideal signal limitations. The results for the Sasaki⁹³ particle size modification are similar to the Valensi-⁶⁶Carter⁶⁷ model for both Quantitative Microscopy and x-ray data (Figures 73 and 81), indicating the particle size distribution measured by sieve analysis is fairly narrow and does not significantly alter the model results.

The nucleation and growth models assume the reaction rate is limited by the number of product nuclei that form and grow. This may apply in this study to the formation of product at the contact points between Ti and TiB₂. However, the rapid surface diffusion and reaction of Ti to form product growing to the sides of the initial contact regions is evidence this mechanism does not operate for this reaction. The TiB appears to form as rapidly as Ti advances over its surface and is not limited by formation of TiB nuclei; the TiB layer grows by motion of the previous TiB-TiB₂ interface and does not initiate at random sites on the TiB₂ particles. The nucleation and growth model plots obtained from the Quantitative Micro-

scopy and x-ray data (Figures 78 and 87) do show straight line segments supporting agreement between the data and the model. However, the Quantitative Microscopy results are straight during later stages when the model is not expected to be valid; and the slopes of the x-ray results during early stages are too low to be valid in terms of the m values listed in Table 2.

The interface or phase boundary controlled reaction mechanism assumes the rate of reactant combination at the interface to form a product limits the reaction. Therefore, the rate of volume consumed is directly proportional to the available reacting interface area. The phase boundary model results obtained from the x-ray data (Figure 87) provide evidence that this mechanism operates during the early stages of this reaction. However, these results are contradicted by Quantitative Microscopy and electron microprobe evidence. The small homogeneity ranges of TiB and TiB₂ (Figure 2) suggest that if an interface reaction is rate controlling, then Ti would accumulate and precipitate at the TiB-TiB₂ interface. However, an electron microprobe scan of this interface shows a smooth decrease of Ti concentration from the TiB to the TiB₂ over a 2 μm distance and no increase in Ti counts was observed in this region. The Quantitative

Microscopy phase boundary model (Figure 79) does not show the same straight line behavior. Also, the determination of interface velocities from Quantitative Microscopy data do not show a direct proportion between volume change and area available for reaction; this is not restricted to the spherical geometry of the phase boundary model.

The average interface velocities and curvature, \bar{v}_S , \bar{v}_H , and \bar{H}_G , for TiB_2 and TiB-TiB_2 surfaces were obtained from the slopes of Figures 26 through 41 and Equations (28), (29), and (31). These slope data are presented in Appendix 12. The average interface velocity was calculated only for the TiB-TiB_2 interface, since specific interface area information was available.

$$\bar{v}_S = \frac{d V_V^{\text{TiB}_2}/dt}{S_V^{\text{TiB-TiB}_2}} \quad (40)$$

The results are given in Appendix 13 and Figure 88. Because of the $t^{5/2}$ and $t^{1/2}$ dependence in early and later stages, respectively, these results were initially interpreted as supporting a mechanism of rapid surface diffusion of Ti followed by the rate controlling volume diffusion of Ti through the TiB product layer. However, when the velocity data were converted to a mass basis (Appendix 13) to correct for the change in porosity with time, this

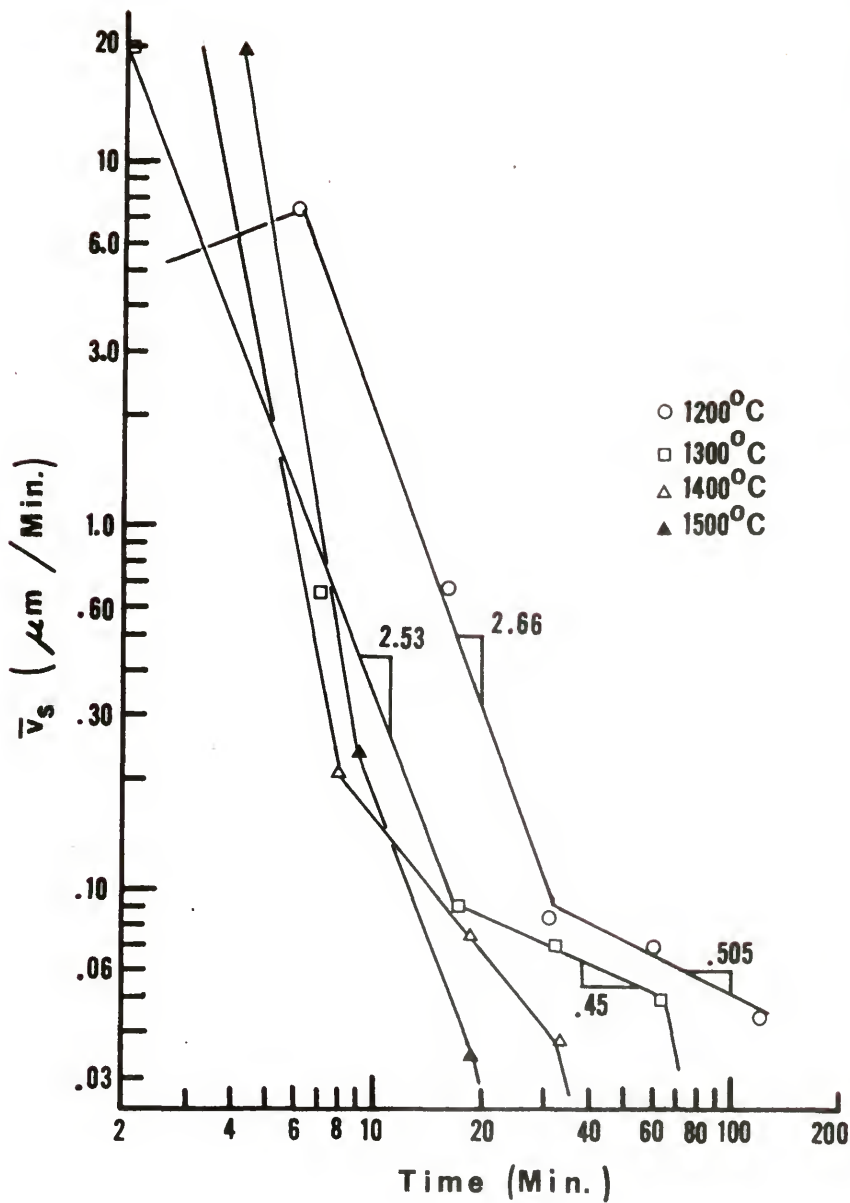


Figure 88. Average interface velocity results.

two stage behavior was no longer apparent (Figure 89);

$$\bar{v}_S^* = \frac{d(v_V^{\text{TiB}_2}/(1 - v_V^{\text{porosity}^*}))/dt}{S_V^{\text{TiB-TiB}_2}/(1 - v_V^{\text{porosity}^*})} \quad (41)$$

where $v_V^{\text{porosity}^*}$ is the volume fraction porosity obtained from the immersion displacement measurements (Figure 43). Since \bar{v}_S^* does not fit the conditions for interface reaction, diffusion, or Tammann controlling mechanisms, these results suggest there was a distribution of interface velocities. The growth of TiB to the sides of the initial Ti-TiB₂ contact region is faster than the advance of the initial TiB-TiB₂ interface into the TiB₂ particle, giving a variation of product thickness on each particle and thus a range of diffusion distances.

Since M_V data for the TiB-TiB₂ interface were not available, a direct comparison of \bar{v}_S and \bar{v}_H is not possible except in the later stages where the specific and total interfaces are approximately equal. These results (Appendix 12) show \bar{v}_H to be approximately equal to \bar{v}_S so in this later stage the interface curvature has little influence on the interface velocity, in agreement with the observations on \bar{H}^{TiB_2} discussed above. Comparing \bar{H}^{TiB_2} and $\bar{H}_G^{\text{TiB}_2}$ gives the same information as comparing \bar{v}_S and \bar{v}_H . These curvatures are also of comparable magnitude,

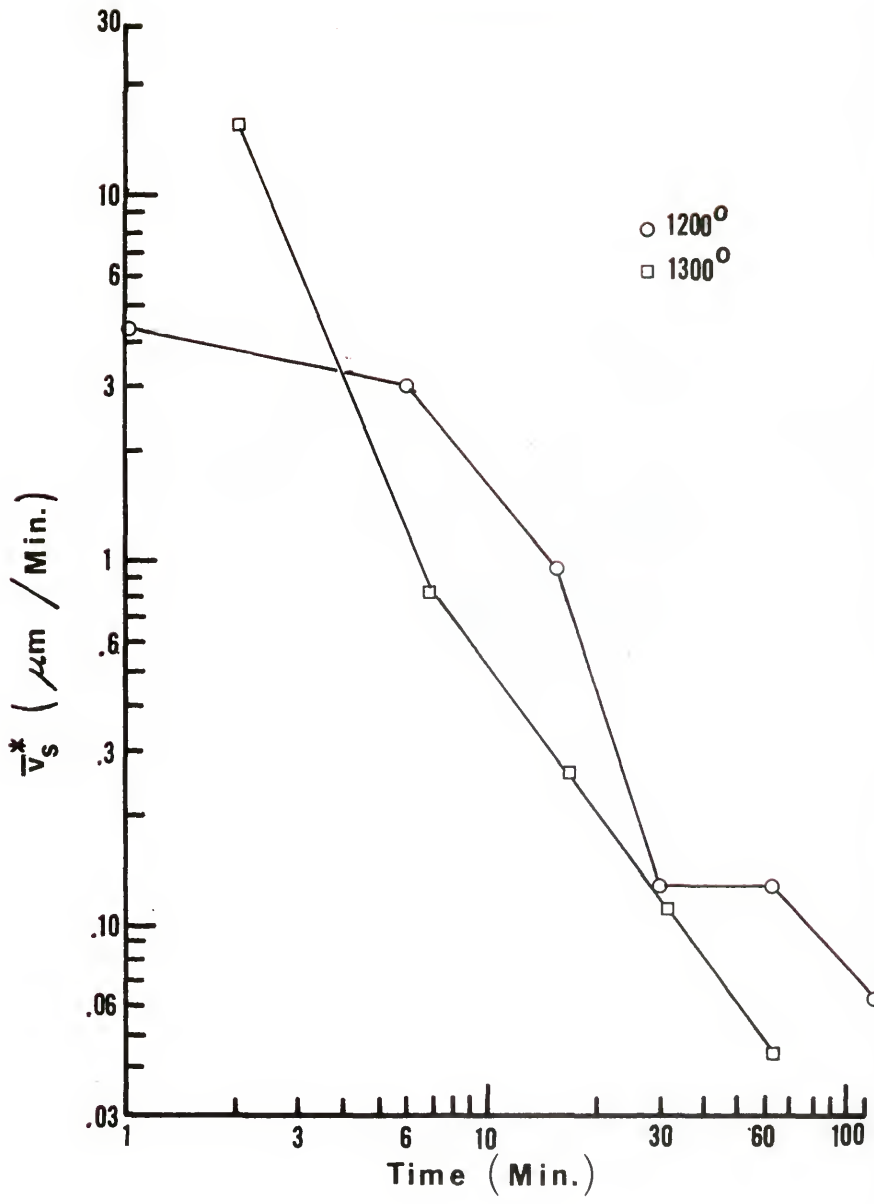


Figure 89. Modified average interface velocity results.

again demonstrating that the scale of curvature detected optically does not significantly influence this reaction.

The model results do not conclusively distinguish among alternative kinetic mechanisms. This is attributed to the deviations of the actual microstructure from the spherical geometry assumed in the models. Some TiB_2 particle size distribution is observed and these particles are not exactly spherical, even when they are completely coated by TiB. The point contacts between Ti and TiB_2 do not provide a complete matrix coating until the later stages of reaction and the Ti surface diffusion appears to occur primarily over TiB rather than TiB_2 , or where the reaction has already started. The interface velocity results suggest there is a distribution of interface velocities rather than a single value. Thus, the structure of the powder compact is seen to strongly influence the reaction rate and mechanism determinations.

However, there is some evidence to exclude the nucleation and growth and phase boundary models. Therefore, the available data best support an interpretation that this reaction is initially controlled by diffusion of Ti through the TiB product and later follows an inverse time dependence (Tammann rate) as the amount of Ti available for reaction is reduced. This reduction occurs because of the decreasing Ti volume and the increasing distance the Ti must diffuse to react with TiB_2 .

SECTION V CONCLUSIONS

From the results of metallographic examination, transport experiments, and model analyses, the following may be concluded about the reaction of Ti and TiB_2 to form TiB in a powder compact:

1) The reaction initiates at the contacts between Ti and TiB_2 particles. No initially uniform coating of TiB or Ti is observed on the TiB_2 particles.

2) The reaction proceeds rapidly due to surface diffusion of Ti over the TiB_2 particles. Vapor transport of Ti or B is excluded as a transport medium. This also explains the rapid formation of TiB seen in the reaction between Ti and $B_{12}C_3$.¹ The overlapped needle structure of Figure 23 is seen where a local excess of Ti occurs.

3) The initial reaction is controlled by the rate of Ti diffusion through the TiB product layer as evidenced by observation of the markers at the Ti-TiB interface of the diffusion couple. Some counter diffusion of B also occurs, shown by the side plates, needles, and precipitates of TiB present in Ti. That Ti is the major diffusing species for this reaction is contrary to the contentions of Antony and Cummings³¹ and Strashinskaya and

Stepanchuk;³² however, their viewpoint is not supported by any marker evidence.

4) The later stage of reaction is limited to a Tammann⁷⁰ rate by the availability of Ti, which decreases in volume and is further limited by increases in the diffusion distance that Ti must traverse to react with TiB_2 . The metallographic observations and interface velocity measurements show that nucleation and growth and phase boundary reaction rates are not rate controlling for this reaction.

5) The powder compact expands 10 - 15% due to the volume increase in the transformation of TiB_2 to TiB. Competing densification from sintering of TiB or TiB_2 is negligible. The porosity increase resulting from this reaction suggests any articles of TiB made by a sinter-reaction process would have little strength.

6) The curvature of the TiB- TiB_2 interface detected within the resolution of the optical microscope does not significantly influence the reaction.

Recommendations on Use of Quantitative Microscopy

The primary aim of this study was to examine the kinetics of TiB formation. However, as a result of this work, several recommendations concerning the use of

Quantitative Microscopy to study powder compact reaction kinetics may be made.

1) Good metallographic preparation is important. If a difficult material is to be polished, care and additional effort are necessary to achieve reliable Quantitative Microscopy results. Use of a Quantimet or other electronic image analyzing instrument also requires good optical contrast and efforts should be made to maximize the range of gray shades, for example, by impregnating with a "black" epoxy or using filters. The instrument errors were seen to be much smaller than the sample preparation errors or the variability between fields of view.

2) If a halo problem exists for a multiphase analysis, the sizer technique used for this study may be satisfactory, but the required corrections are very time consuming. This effort may justify ignoring measurements on the phase causing the halo or else using the appropriate accessories to remove this error.

3) Selecting the appropriate magnification is a compromise between the resolution required for accuracy and the effort required to examine a representative number of fields of view. If an electronic instrument can be used and curvature information is desired, it is recom-

mended that higher magnification be used and more fields of view examined since the electronics reduce the counting effort. To examine the curvature of the TiB needle surfaces seen in this study would have required using the SEM, assuming an undistorted section could be obtained. Since few results have been reported using this level of magnification to obtain curvature information, the effort required to examine this scale of microstructure is probably justified.

4) The utility of Quantitative Microscopy is its ability to abstract simple feature averages from the complex arbitrary microstructural geometry. It must be remembered that the parameters obtained are averages and not invariant throughout this structure. If the information desired required weighting some feature of the structure, such as particle size distributions or area and curvature measurements of a specific i-j interface, the experiments should be carefully thought out to minimize wasted time.

General Recommendations for Future Work

This study has shown several questions remain unanswered and further investigation is recommended.

1) The nature and stability of Ti_3B_4 should be examined to resolve the conflicts between the results of Rudy and St. Windisch²⁵ and the results of Walther and Whitney¹ and Fenish.²⁹

2) The peak shift observed for the major (011) Ti peak as the reaction increases remains to be explained. The influence of B solid solution in Ti on the Ti lattice parameters may be responsible for this result, but has yet to be determined.

3) The TiB needle morphology shown in Figure 23 appears to form at a surface with an excess of Ti. How these needles are formed and the influence of the overlapped needle structure on surface diffusion of Ti is unknown.

APPENDIX 1 - continued.

Orthorhombic TiB Decker and Kasper		Hexagonal Ti ₂ B Palty et al.		α Ti + Ti Superlattice ^a Ehrlich	
hk1	dÅ	hk1	dÅ	hk1	dÅ
403	1.079	440	1.078		1.084
421	1.051				
512	1.017	600	1.015		1.019
214	1.008				<u>1.000</u>
031	.994				
131	.981				
230	.966				
323	.953				.954
611	.945				
521	.934				.932
132	.920	541	.924		<u>.916</u>
024	.914				
423	.881				
414	.876	105	.875		
115	.866				<u>.845</u>
332	.847				
133	.839				
305	.833				<u>.830</u>
711	.827	641	.826		
702	.816				

^a Superlattice lines are underlined; ^b Observed intensity;

^c Estimated intensity; ^d Considerable line broadening;

^e Doublet

APPENDIX 2

List of Qualitative Microstructural Features for a Four Phase System

For a system of four phases, α , β , γ , δ , there are
4 volumes seen as areas in a two dimensional section

α β γ δ

10 interfaces seen as lines in a two dimensional section

$\alpha\alpha$	$\beta\beta$	$\gamma\gamma$	$\delta\delta$
$\alpha\beta$	$\beta\gamma$	$\gamma\delta$	
$\alpha\gamma$	$\beta\delta$		
$\alpha\delta$			

20 triple lines seen as points in a
two dimensional section

$\alpha\alpha\alpha$	$\beta\beta\beta$	$\gamma\gamma\gamma$	$\delta\delta\delta$
$\alpha\alpha\beta$	$\beta\beta\gamma$	$\frac{\gamma\gamma\delta}{\gamma\delta\delta}$	
$\alpha\alpha\gamma$	$\frac{\beta\beta\gamma}{\beta\gamma\delta}$	$\gamma\delta\delta$	
$\frac{\alpha\alpha\delta}{\alpha\beta\beta}$	$\frac{\beta\gamma\delta}{\beta\delta\delta}$		
$\alpha\beta\gamma$	$\beta\delta\delta$		
$\frac{\alpha\beta\delta}{\alpha\gamma\gamma}$			
$\frac{\alpha\gamma\delta}{\alpha\delta\delta}$			

APPENDIX 2 - continued.

36 quadruple points not visible in a
two dimensional section

$\alpha\alpha\alpha\alpha$	$\alpha\beta\beta\beta$	$\beta\gamma\gamma\gamma$	$\delta\delta\delta\delta$
$\alpha\alpha\alpha\beta$	$\beta\beta\beta\beta$	$\gamma\gamma\gamma\gamma$	
$\alpha\alpha\alpha\gamma$	$\beta\beta\beta\gamma$	$\gamma\gamma\gamma\delta$	
$\alpha\alpha\alpha\delta$	$\beta\beta\beta\delta$	$\gamma\gamma\delta\delta$	
$\alpha\alpha\beta\beta$	$\beta\beta\gamma\gamma$		
$\alpha\alpha\beta\gamma$	$\beta\beta\gamma\delta$	$\gamma\delta\delta\delta$	
$\alpha\alpha\beta\delta$	$\beta\beta\delta\delta$		
$\alpha\alpha\gamma\gamma$			
$\alpha\alpha\gamma\delta$	$\beta\gamma\gamma\gamma$		
$\alpha\alpha\delta\delta$	$\beta\gamma\gamma\delta$		
	$\beta\gamma\delta\delta$		
$\alpha\beta\beta\gamma$			
$\alpha\beta\beta\delta$	$\beta\delta\delta\delta$		
$\alpha\beta\gamma\gamma$			
$\alpha\beta\gamma\delta$			
$\alpha\beta\delta\delta$			
$\alpha\gamma\gamma\gamma$			
$\alpha\gamma\gamma\delta$			
$\alpha\gamma\delta\delta$			
$\alpha\delta\delta\delta$			

For the case where features common to the
same phase are ignored there are

4 volumes

α β γ δ

6 interfaces

$\alpha\beta$ $\beta\gamma$ $\gamma\delta$
 $\alpha\gamma$ $\beta\delta$
 $\alpha\delta$

4 triple lines

$\alpha\beta\gamma$ $\alpha\beta\delta$ $\alpha\gamma\delta$ $\beta\gamma\delta$

1 quadruple point

$\alpha\beta\gamma\delta$

APPENDIX 3

Calculation of Statistical Parameters for a Random Sample of Size n

Sample average -

unbiased estimate of sample mean

$$\bar{Q}^i = \frac{\sum_{m=1}^n Q_m^i}{n}$$

Confidence interval -

sample variance

$$S^2 = \frac{\sum_{m=1}^n (\bar{Q}^i - Q_m^i)^2}{n}$$

since S^2 is a biased estimate of the population
variance σ^2 , apply Bessel's correction

$$\sigma^2 = \left(\frac{n}{n-1}\right) S^2 = \frac{\sum_{m=1}^n (\bar{Q}^i - Q_m^i)^2}{n-1}$$

apply the Central Limit theorem to obtain

standard error of the mean $\sigma_{\bar{Q}^i}$

$$\sigma_{\bar{x}} = \frac{\sigma}{\sqrt{n}}$$

the 95% confidence interval is $\pm 2 \sigma_{\bar{Q}^i}$ so

Appendix 3 - continued.

$$CI = 2\sigma_{\bar{Q}^i}$$

Coefficient variation -

ratio between standard error of the mean
and the average: a measure of variability

$$CV = \frac{\sigma_{\bar{Q}^i}}{\bar{Q}^i}$$

APPENDIX 4
Computer Programs

```

▽ DATAIN
[1]  J+1
[2]  TEMP+100*10+15
[3]  TIME+ 0 5 15 30 60 120
[4]  PARAM+ 18 7 ρ'PPA      PPB      PPG      PPD      NLA      NLB
      NLG      NLD      NLAG      NLBG      TAAPOS      TAANEG      TABPOS
      TABNEG      TAGPOS      TAGNEG      TADPOS      TADNEG '
[5]  FLNAMES+ 5 8 ρ'DATA1100DATA1200DATA1300DATA1400DATA1
      500'
[6]  'THIS PROGRAM BUILDS A 3D DATA MATRIX AND'
[7]  'PUTS IT IN A FILE THAT MUST ALREADY BE CREATED OR T
      IED'
[8]  TPLOOP:'FOR WHAT TEMP IS THIS DATA?'
[9]  DEGC+□
[10] I+TEMP\DEGC
[11] TMLOOP:RNTM+TIME[J]
[12] RAWQV+ 18 50 ρ0
[13] 'ENTER DATA FOR TIME = ';RNTM
[14] K+1
[15] QVLOOP:'ENTER THE FIRST 25 DATA FOR ',PARAM[K;]
[16] START:CTS1+□
[17] →((ρCTS1)=25)/CONT1
[18] 'YOU GOOFED REENTER DATA FOR ',PARAM[K;]
[19] →START
[20] CONT1:'ENTER SECOND HALF OF DATA FOR ',PARAM[K;]
[21] CTS2+□
[22] →((ρCTS2)=25)/CONT2
[23] 'ERROR IN ENTERING LAST DATA SET'
[24] →CONT1
[25] CONT2:CTS+CTS1,CTS2
[26] RAWQV[K;]+CTS
[27] 'THAT IS THE END OF DATA FOR ',PARAM[K;]
[28] K+K+1
[29] →(K>18)/TMCONT
[30] →QVLOOP
[31] TMCONT:'THAT IS THE END OF DATA FOR TIME = ';RNTM
[32] 'THIS DATA WILL BE ADDED TO THE FILE ',FLNAMES[I;]
[33] 'AS COMPONENT ';J
[34] RAWQV FAPPEND DEGC
[35] 'FILE SIZE IS NOW'
[36] FSIZE DEGC
[37] →(J=6)/MAT
[38] 'DO YOU WANT TO CONTINUE ADDING DATA? YES OR NO'
[39] →(['='NO']/MAT
[40] J+J+1
[41] →TMLOOP
[42] MAT:'THAT IS THE LAST DATA FOR TEMP = ';DEGC
[43] 'DATAIN MUST BE CALLED AGAIN FOR ANOTHER TEMP'
[44] ' '
[45] 'END OF PROGRAM'

```

▽

Appendix 4 - continued.

▽ QMCALC

```

[1]  'THIS PROGRAM CONVERTS RAW QM DATA TO QM PARAMETERS'
[2]  TEMP+100*10+15
[3]  TIME← 0 5 15 30 60 120
[4]  'FOR WHAT TEMP IS DATA BEING USED?'
[5]  DEGC←[
[6]  'FOR WHICH TIME SHOULD CALC START?'
[7]  RNTM←[
[8]  I←TEMP\DEGC
[9]  QV← 14 6 ρ0
[10] QVCI← 14 6 ρ0
[11] TAN← 12 6 ρ0
[12] LCLERROR←6ρ0
[13] TMLOOP:J←TIME\RNTM
[14] CALCLOOP:RAWQV←FREAD DEGC,J
[15] →TANET×1(J<(6-I))
[16] TAGCORRECTION:RAWQV[16;]+RAWQV[16;]+RAWQV[13;]
[17] TAN[1 2 3 4 5 6 7 8 ;J]←+/RAWQV[11 13 15 17
    12 14 16 18 ;]÷50
[18] TAN[9 10 11 12 ;J]←+/(RAWQV[11 13 15 17 ;]+RAWQV[
    12 14 16 18 ;])÷50
[19] TANET:RAWQV[11 13 15 17 ;]+RAWQV[11 13 15 17 ;]-RAWQV
    [12 14 16 18 ;]
[20] QV[;J]←(+/RAWQV[1 2 3 4 5 6 7 8 9 10 11 13
    15 17 ;])÷50
[21] QVCI[;J]←((((((+/RAWQV[1 2 3 4 5 6 7 8 9 10
    11 13 15 17 ;]*2))-((+/RAWQV[1 2 3 4 5 6 7
    8 9 10 11 13 15 17 ;])*2)÷50))÷49)*
    0.5)÷(50*0.5))×2
[22] J←J+1
[23] →CALCLOOP×1(J≤6)
[24] 'TO AVOID A FULL WS, ERASE RAWQV AND THEN CALL PROG
    QMCALCCONT'
[25] 'END OF QMCALC'

```

▽

Appendix 4 - continued.

```

V QMCALCCONT
[1] 'THIS PROG MUST BE CALLED AFTER QMCALC'
[2] QV[1 2 3 4 ;]+QV[1 2 3 4 ;]÷160000
[3] QV[5 6 7 8 9 10 ;]+QV[5 6 7 8 9 10 ;]*
0.5
[4] QV[11 12 13 14 ;]+QV[11 12 13 14 ;]*15708
[5] QVCI[1 2 3 4 ;]+QVCI[1 2 3 4 ;]÷160000
[6] QVCI[5 6 7 8 9 10 ;]+QVCI[5 6 7 8 9 10 ;]*
0.5
[7] QVCI[11 12 13 14 ;]+QVCI[11 12 13 14 ;]*15708
[8] QVCV+(QVCI÷2):QV
[9] SVMAT+ 6 6 ρ 1 1 1 0 0 0 1 0 0 1 1 0 0 1 0 1 0 0
1 0 1 1 1 0 1 1 0 1 1 0 0 1 1
[10] SVEA+ 12 6 ρ0
[11] SVEA[1 3 5 7 9 11 ;]+QV[5 6 7 8 9 10 ;]FSVMAT
[12] SVEA[2;]+(3÷2)×(QVCI[5;]+QVCI[6;])
[13] SVEA[4;]+÷QVCI[5 7 9 ;]
[14] SVEA[6;]+÷QVCI[5 8 10 ;]
[15] SVEA[8;]+÷QVCI[6 7 10 ;]
[16] SVEA[10;]+÷QVCI[6 8 9 ;]
[17] SVEA[12;]+(3÷2)×(QVCI[7;]+QVCI[8;])
[18] VV+ 14 6 ρ0
[19] VV[1 3 5 7 ;]+QV[1 2 3 4 ;]
[20] VV[2 4 6 8 ;]+QVCI[1 2 3 4 ;]
[21] VV[9;]+1-(÷QV[1 2 3 ;])
[22] VV[10;]+(÷(QVCI[1 2 3 ;]*2)) +
0.5
[23] VV[11 12 13 14 ;]+QVCV[1 2 3 4 ;]
[24] ERR+ 5 6 ρ0
[25] ERR[1;]+|(1-(÷QV[1 2 3 4 ;]))×100
[26] ERR[2 3 4 5 ;]+(4 6 ρERR[1;])÷QV[1 2 3 4 ;]
[27] MOLES+ 6 6 ρ0
[28] MOLVOL+ 6 3 ρ 10.644 15.453 12.877
[29] TOTMOLES+(÷QV[1 2 3 ;]÷MOLVOL)
[30] MOLES[1 3 5 ;]+(QV[1 2 3 ;]÷MOLVOL)÷(3 6 ρTOTMOLES)
[31] MOLES[2 4 6 ;]+(QVCI[1 2 3 ;]÷MOLVOL)÷(3 6 ρ
TOTMOLES)
[32] EX+ 3 6 ρ0
[33] EX[1;]+QV[3;]+(÷QV[2 3 ;])
[34] EX[2;]+((QVCI[3;]*2)+(QVCI[2;][QVCI[3;])*2)*
0.5
[35] EX[3;]+1-EX[1;]
[36] SV+ 18 6 ρ0
[37] SV[1 3 5 7 9 11 ;]+QV[5 6 7 8 9 10 ;]
[38] SV[2 4 6 8 10 12 ;]+QVCI[5 6 7 8 9 10 ;]
[39] SV[13 14 15 16 17 18 ;]+QVCV[5 6 7 8 9 10 ;]
[40] SM+ 12 6 ρ0
[41] SM[1 3 5 7 9 11 ;]+QV[5 6 7 8 9 10 ;]÷(6 6 ρTOTMOLES
)
[42] SM[2 4 6 8 10 12 ;]+QVCI[5 6 7 8 9 10 ;]÷(6
6 ρTOTMOLES)
[43] SMFA+SVEA÷(12 6 ρTOTMOLES)

```

Appendix 4 - continued.

```

[44] MV← 12 6 ρ0
[45] MV[1 3 5 7 ;]+QV[11 12 13 14 ;]
[46] MV[2 4 6 8 ;]+QVCI[11 12 13 14 ;]
[47] MV[9 10 11 12 ;]+QVCV[11 12 13 14 ;]
[48] MM←MV[1 2 3 4 5 6 7 8 ;]+(8 6 ρTOTMOLES)
[49] MM←MM÷1000
[50] MV[1 2 3 4 5 6 7 8 ;]+MV[1 2 3 4 5 6 7 8 ;]÷
1000000
[51] LAM← 16 6 ρ0
[52] LAM[1 2 3 4 ;]+((QV[1 2 3 4 ;]×4)+QV[5 6 7
8 ;])×10000
[53] LAM[5 6 7 8 ;]+QV[11 12 13 14 ;]+QV[5 6 7 8 ;]
[54] LAM[9 10 11 12 ;]+LAM[1 2 3 4 ;]×LAM[5 6 7
8 ;]÷10000
[55] LAM[13 14 15 16 ;]+LAM[1 2 3 4 ;]÷(4 6 ρTOTMOLES)
[56] QMP←VV,[1] ERR,[1] MOLES,[1] EX,[1] SV,[1] SVEA,[1]
SM,[1] SMEA,[1] MV,[1] MM,[1] LAM
[57] 'THE CALC OF QM PARAMETERS IS COMPLETE FOR TEMP = ';
DEGC
[58] QMP FAPPEND 17
[59] 'THIS DATA IS NOW ADDED TO THE FILE RESULTS AND FILE
SIZE IS NOW:'
[60] FSIZE 17
[61] 'END OF PROG QMCALCCONT'

```

Appendix 4 - continued.

```

▽ WAX
[1] VN+MWAX-MSUS
[2] VS+MDRY÷4.5
[3] POR+(VN-VS)÷VN
[4] PAUSE+□
[5] WAXPRNT
▽

▽ WAXPRNT
[1] '          TABLE          '
[2] '          RESULTS OF ARCHIMEDEAN POROSITY'
[3] '          '
[4] TIME+ 0 5 15 30 60 120
[5] '[ TIME = [ ,6I8' [FMT(1 6 0TIME)
[6] '          '
[7] LAB+ 4 8 0' 1200      1300      1400      1500 '
[8] 'TEMP °C          PERCENT POROSITY'
[9] '8A1,X3,6F8.4' [FMT(LAB;POR)
[10] '          '
[11] '          NUGGET VOLUME CM3'
[12] '8A1,X3,6F8.4' [FMT(LAB;VN)
[13] '          '
[14] '          SOLID POWDER VOLUME CM3'
[15] '8A1,X3,6F8.4' [FMT(LAB;VS)
[16] '          '
[17] '          DRY MASS GRAMS'
[18] '8A1,X3,6F8.4' [FMT(LAB;MDRY)
[19] '          '
[20] '          SUSPENDED MASS GRAMS'
[21] '8A1,X3,6F8.4' [FMT(LAB;MSUS)
[22] '          '
[23] '          WAX IMPREGNATED NUGGET MASS GRAMS'
[24] '8A1,X3,6F8.4' [FMT(LAB;MWAX)
[25] PAUSE+□
[26] 'END OF PRINTOUT  END OF PROGRAM'
▽

```

Appendix 4 - continued.

```

▽ SASAKI
[1]  Z←1.6666666666666667
[2]  R← 3.2 3.8 4.6 5.5 6.6 7.9 9.5
      11.4 13.7 16.4 19.6 23.6 28.3
      33.9 40.7 48.9 58.7 70.4 84.4
      101.3 121.6 145.8 175
[3]  VVCS← 0.1 0.1 0.2 0.2 0.2 0.3
      0.3 0.3 0.3 0.5 0.5 3 6 52 12
      7.5 5.5 3.5 2.5 1.5 1 0.6 0.3
[4]  'WHAT ARE THE ARBITRARY XI VALUES?'
[5]  XIARB←□
[6]  NETKT←NETR←NETIX←NETX←10
[7]  J←1
[8]  RRECIP←(÷((R×10000)*2))
[9]  CALCLOOP:XI←(¯23+(22+J)†((×122),XIARB))
[10] X←(-J)†XI
[11] X3←((-X)+1)*(2÷3)
[12] KTVCS←((-1+(¯1+Z)×X)*0.6666666666666666)+(-
      ¯1+Z)×X3)+Z)÷(¯1+Z)
[13] TOTX←+/(VVCS×XI)
[14] IXSUM←+/KTVCS
[15] RSUM←+/((-J)†RRECIP)
[16] KT←IXSUM+RSUM
[17] NETX←NETX,TOTX
[18] NETR←NETR,RSUM
[19] NETKT←NETKT,KT
[20] NETIX←NETIX,IXSUM
[21] J←J+1
[22] →CALCLOOP×1(J<32)
[23] 'THE NET X VALUES ARE:'
[24] NETX
[25] 'THE NET IX VALUES ARE:'
[26] NETIX
[27] 'THE NET R VALUES ARE:'
[28] NETR
[29] 'THE NET KT VALUES ARE:'
[30] NETKT
[31] 'END OF PROGRAM'

```

▽

APPENDIX 5

Glossary of Computer Variables

Since the computer symbols do not allow superscripts, subscripts, or lower case letters, the following correspondence between computer and text notation was used. Not every symbol is listed because the scheme used is apparent from the examples given below.

<u>Table</u>	<u>Symbol</u>	<u>Meaning</u>
A1-A4	A, B, G, D	Ti, TiB ₂ , TiB, and porosity, respectively
	V	volume
	S	area
	M	total curvature
	VVA, etc.	V_V^{Ti} , etc.
	SVA, etc.	S_V^{Ti} , etc.
	MVA, etc.	M_V^{Ti} , etc.
	CV	coefficient of variation
	+ OR -	±, 95% confidence interval
	MOLFR A, etc.	mole fraction of Ti, etc.
	MACH ERR	machine error
	X	extent of reaction, x
	LAM A, etc.	$\bar{\lambda}^{Ti}$, etc.
	HBAR A, etc.	\bar{H}^{Ti} , etc.
A6	CPS	counts per second
	I	intensity
A7	DC	direct comparison
	I/I TI	intensity of Ti ÷ intensity of NaCl

Appendix 5 - continued.

<u>Table</u>	<u>Symbol</u>	<u>Meaning</u>
A7	IS	internal standard
A8	XIARB	arbitrary x_i
	SUMXI	$\sum_i^n x_i$
	SUMIX	$\sum_i^n I(x_i)$
	SUMR	$\sum_i^n \frac{1}{r_i^2}$
	KT	Kt
A9-A10	KT PB - KT NG	see Table 1
	KT VCS	Sasaki model
A11	D VVB/DT	$\frac{dV_V^{TiB2}}{dt}$
A12	VBARS	\bar{v}_S
	VBARS*	\bar{v}_S^*
	VBARH	\bar{v}_H
	HBARG	\bar{H}_G

Appendix 5 - continued.

TABLE A1
 QUANTITATIVE MICROSCOPY RESULTS FOR $T = 1200 \text{ }^\circ\text{C}$

TIME =	1	6	16	31	61	121
VOLUME FRACTION						
VVA	0.1928	0.1816	0.1271	0.1343	0.0501	0.0224
+OR-	0.0207	0.0188	0.0134	0.0177	0.0175	0.0074
VVB	0.2793	0.2277	0.2091	0.2123	0.0793	0.0326
+OR-	0.0168	0.0163	0.0165	0.0115	0.0164	0.0081
VVG	0.0068	0.0065	0.0358	0.1079	0.3144	0.3353
+OR-	0.0022	0.0022	0.0045	0.0130	0.0174	0.0138
VVD	0.5233	0.5857	0.6281	0.5458	0.5552	0.6111
+OR-	0.0159	0.0134	0.0133	0.0127	0.0202	0.0139
V CV A	0.0536	0.0518	0.0528	0.0659	0.1746	0.1665
V CV B	0.0300	0.0358	0.0395	0.0270	0.1032	0.1242
V CV G	0.1598	0.1692	0.0627	0.0601	0.0277	0.0205
V CV D	0.0152	0.0115	0.0106	0.0116	0.0182	0.0114
AREA PER VOLUME CM^{-1}						
SVA	419.26	278.50	284.90	262.90	103.60	67.50
+OR-	30.40	24.96	22.98	32.99	28.02	19.05
SVB	862.23	694.13	839.27	602.65	231.99	149.35
+OR-	28.58	36.34	50.87	62.65	37.60	30.22
SVG	42.40	52.20	272.70	1113.15	1394.19	1607.50
+OR-	12.64	15.86	34.78	94.67	48.74	56.31
SVD	1364.40	1310.95	1637.92	1613.26	1296.71	1524.08
+OR-	36.04	29.10	31.55	35.47	26.59	36.64
SVA+G	449.70	322.10	491.90	1264.50	1491.93	1672.46
+OR-	34.46	27.81	36.35	89.52	42.49	49.31
SVB+G	864.46	731.47	997.72	1093.28	1194.32	1435.50
+OR-	28.24	35.72	43.43	50.90	33.72	68.25
S CV A	0.0363	0.0448	0.0403	0.0627	0.1352	0.1411
S CV B	0.0166	0.0262	0.0303	0.0520	0.0810	0.1012
S CV G	0.1491	0.1519	0.0638	0.0425	0.0175	0.0175
S CV D	0.0132	0.0111	0.0096	0.0110	0.0103	0.0120
S CV A+G	0.0383	0.0432	0.0369	0.0354	0.0142	0.0147
S CV B+G	0.0163	0.0244	0.0218	0.0233	0.0141	0.0238
TOTAL CURVATURE PER VOLUME ($\times 10^{-6}$) CM^{-2}						
MVA	0.0892	0.0025	0.0057	-0.0672	-0.0232	0.0141
+OR-	0.0420	0.0264	0.0288	0.0312	0.0195	0.0093
MYB	1.2340	0.9101	1.3449	0.8655	0.2589	0.1335
+OR-	0.0666	0.0743	0.0955	0.0799	0.0477	0.0294
MVG	0.0368	0.0826	0.4357	0.6220	0.8489	2.0571
+OR-	0.0181	0.0256	0.0564	0.1551	0.0982	0.1961
MYD	-0.5306	-1.3719	-1.6974	-1.2997	-1.2290	-2.2899
+OR-	0.2649	0.1289	0.1312	0.1271	0.0831	0.1739
M CV A	0.2353	5.2530	2.5443	-0.2318	0.1746	0.3303
M CV B	0.0270	0.0408	0.0355	0.0462	0.0921	0.1102
M CV G	0.2456	0.1550	0.0648	0.1246	0.0578	0.0477
M CV D	-0.2496	-0.0470	-0.0387	-0.0489	-0.0338	-0.0380

Appendix 5 - continued.

TABLE A1 CONTINUED

TIME =	1	6	16	31	61	121
<i>MOLE FRACTION</i>						
MOLFR A	0.4934	0.5283	0.4227	0.3632	0.1374	0.0695
+OR-	0.0529	0.0547	0.0446	0.0478	0.0480	0.0231
MOLFR B	0.4923	0.4562	0.4788	0.3956	0.1498	0.0697
+OR-	0.0295	0.0327	0.0378	0.0214	0.0309	0.0173
MOLFR G	0.0144	0.0155	0.0985	0.2412	0.7128	0.8608
+OR-	0.0046	0.0053	0.0124	0.0290	0.0396	0.0353
<i>PERCENT ERROR IN POINT COUNT</i>						
VVD NET	0.5211	0.5842	0.6279	0.5456	0.5563	0.6098
+OR-	0.0267	0.0250	0.0218	0.0248	0.0296	0.0176
MACH ERR	0.2275	0.1487	0.0162	0.0200	0.1125	0.1309
VV ERR A	1.1798	0.8189	0.1278	0.1490	2.2466	5.8520
VV ERR B	0.8145	0.6532	0.0777	0.0942	1.4193	4.0215
VV ERR G	33.4559	23.0174	0.4534	0.1854	0.3579	0.3905
VV ERR D	0.4347	0.2540	0.0259	0.0366	0.2026	0.2143
<i>EXTENT OF REACTION</i>						
X	0.0238	0.0276	0.1463	0.3369	0.7986	0.9115
+OR-	0.0169	0.0164	0.0171	0.0183	0.0247	0.0195
(1-X)	0.9762	0.9724	0.9537	0.6631	0.2014	0.0885
<i>SPECIFIC INTERFACE AREA PER VOLUME CM⁻¹</i>						
SVAB	46.32	154.79	210.50	184.31	2.32	11.81
+OR-	88.47	91.95	110.78	143.45	98.42	73.90
SVAG	5.98	4.30	32.85	55.78	2.93	1.27
+OR-	77.50	68.63	94.11	217.18	119.25	124.66
SVAD	459.60	428.99	462.55	391.44	103.00	78.04
+OR-	94.68	89.79	97.96	119.35	88.33	123.94
SVBG	20.08	7.43	57.12	311.26	215.93	160.67
+OR-	69.46	87.91	129.07	208.21	120.05	154.77
SVBD	888.46	841.49	992.64	475.70	18.39	0.49
+OR-	99.08	93.25	118.77	187.64	106.68	116.17
SVGD	16.34	40.47	182.73	746.11	1175.33	1445.55
+OR-	73.02	67.44	99.48	195.20	113.00	139.43
<i>LAMBDA BAR MICRONS</i>						
LAM A	18.397	26.088	17.850	20.428	19.334	13.259
LAM B	12.958	13.122	9.966	14.092	13.667	8.720
LAM G	6.415	4.952	5.257	3.876	9.019	8.343
LAM D	15.343	17.870	15.339	13.532	17.126	16.038
<i>HBAR CM⁻¹</i>						
HBAR A	212.8	9.0	19.8	255.7	224.4	209.4
HBAR B	1431.2	1311.2	1602.5	1436.2	1115.9	894.0
HBAR G	866.9	1582.8	1597.9	558.8	608.9	1279.7
HBAR D	388.9	1046.5	1036.3	805.6	947.8	1502.5

Appendix 5 - continued.

TABLE A2
 QUANTITATIVE MICROSCOPY RESULTS FOR $T = 1300 \text{ } ^\circ\text{C}$

TIME =	2	7	17	32	62	122
VOLUME FRACTION						
VVA	0.2046	0.2235	0.0909	0.0583	0.0237	0.0258
+OR-	0.0186	0.0196	0.0227	0.0224	0.0102	0.0151
VVB	0.3318	0.1838	0.1255	0.0983	0.0641	0.0534
+OR-	0.0143	0.0119	0.0155	0.0191	0.0118	0.0136
VVG	0.0211	0.0228	0.2436	0.2938	0.4232	0.3985
+OR-	0.0050	0.0037	0.0203	0.0250	0.0174	0.0175
VVD	0.4418	0.5699	0.5406	0.5481	0.4896	0.5209
+OR-	0.0124	0.0140	0.0222	0.0177	0.0140	0.0157
V CV A	0.0454	0.0440	0.1247	0.1923	0.2155	0.2922
V CV B	0.0215	0.0323	0.0618	0.0973	0.0918	0.1276
V CV G	0.1178	0.0816	0.0417	0.0426	0.0205	0.0220
V CV D	0.0140	0.0123	0.0205	0.0161	0.0143	0.0150
AREA PER VOLUME CM^{-1}						
SVA	423.80	364.76	194.80	100.00	57.80	51.87
+OR-	35.41	33.96	29.40	28.00	19.07	17.92
SVB	918.80	540.16	421.16	322.16	163.09	140.64
+OR-	26.78	30.05	45.15	46.09	26.93	28.78
SVG	134.30	182.49	1311.90	1219.87	1196.44	1139.30
+OR-	25.94	23.44	42.49	66.05	47.56	52.71
SVD	1223.09	1401.60	1371.47	1264.22	1208.77	1130.71
+OR-	36.43	39.59	32.11	31.93	25.61	32.49
SVA+G	537.00	414.92	1470.80	1306.77	1245.33	1186.52
+OR-	36.16	31.38	43.51	53.62	39.81	42.62
SVB+G	955.47	841.23	1160.17	1076.64	1084.62	1048.59
+OR-	27.05	35.10	33.68	53.40	41.21	39.27
S CV A	0.0418	0.0466	0.0755	0.1400	0.1650	0.1727
S CV B	0.0146	0.0278	0.0536	0.0715	0.0825	0.1023
S CV G	0.0966	0.0642	0.0162	0.0271	0.0199	0.0231
S CV D	0.0149	0.0141	0.0117	0.0126	0.0106	0.0144
S CV A+G	0.0337	0.0378	0.0148	0.0205	0.0160	0.0180
S CV B+G	0.0142	0.0209	0.0145	0.0248	0.0190	0.0187
TOTAL CURVATURE PER VOLUME ($\times 10^{-6}$) CM^{-2}						
MVA	0.0380	0.0162	-0.0085	-0.0220	0.0063	-0.0113
+OR-	0.0284	0.0267	0.0245	0.0191	0.0108	0.0091
MVB	0.9079	0.9029	0.5366	0.3531	0.1436	0.1499
+OR-	0.0789	0.0676	0.0946	0.0630	0.0339	0.0376
MVG	0.0986	0.2504	0.5526	0.5234	0.5030	0.6205
+OR-	0.0234	0.0512	-0.1068	0.0951	0.0968	-0.0687
MVD	0.2271	-1.0784	-0.7502	-1.1080	-0.6613	-0.8096
+OR-	0.1627	0.1272	-0.1075	0.1150	0.1109	0.0886
M CV A	0.3739	0.8263	-1.4434	-0.4348	0.8571	-0.4009
M CV B	0.0434	0.0374	0.0881	0.0891	0.1180	0.1255
M CV G	0.1187	0.1022	0.0966	0.0908	0.0963	0.0554
M CV D	0.3582	-0.0590	-0.0717	-0.0519	-0.0838	-0.0547

Appendix 5 - continued.

TABLE A2 CONTINUED

TIME =	2	7	17	32	62	122
<i>MOLE FRACTION</i>						
MOLFR A	0.4541	0.6059	0.2400	0.1580	0.0567	0.0658
+OR-	0.0413	0.0533	0.0599	0.0607	0.0244	0.0384
MOLFR B	0.5072	0.3431	0.2283	0.1836	0.1057	0.0938
+OR-	0.0218	0.0222	0.0282	0.0357	0.0194	0.0239
MOLFR G	0.0387	0.0510	0.5317	0.6584	0.8376	0.8404
+OR-	0.0091	0.0083	0.0443	0.0561	0.0343	0.0370
<i>PERCENT ERROR IN POINT COUNT</i>						
VVD NET	0.4424	0.5700	0.5400	0.5496	0.4890	0.5224
+OR-	0.0240	0.0232	0.0342	0.0387	0.0233	0.0268
MACH ERR	0.0611	0.0063	0.0565	0.1475	0.0586	0.1506
VV ERR A	0.2987	0.0280	0.6215	2.5316	2.4749	5.8424
VV ERR B	0.1842	0.0340	0.4502	1.5000	0.9133	2.8220
VV ERR G	2.8935	0.2747	0.2319	0.5020	0.1384	0.3780
VV ERR D	0.1383	0.0110	0.1045	0.2691	0.1196	0.2892
<i>EXTENT OF REACTION</i>						
X	0.0599	0.1102	0.6600	0.7492	0.8684	0.8819
+OR-	0.0151	0.0124	0.0287	0.0354	0.0245	0.0248
(1-X)	0.9401	0.8898	0.3400	0.2508	0.1316	0.1181
<i>SPECIFIC INTERFACE AREA PER VOLUME CM⁻¹</i>						
SVAB	67.54	163.97	26.20	50.34	37.63	17.45
+OR-	93.28	96.01	111.83	111.14	69.00	70.05
SVAG	10.55	66.16	17.95	6.55	4.46	2.33
+OR-	97.51	88.78	115.40	147.68	106.45	113.25
SVAD	345.71	462.56	203.05	143.79	90.97	66.99
+OR-	98.88	108.66	95.19	113.33	85.89	89.67
SVBG	48.81	59.29	286.44	232.69	137.45	115.67
+OR-	79.78	88.59	121.32	165.53	115.70	120.77
SVBD	802.44	763.42	160.92	139.81	63.27	42.42
+OR-	99.37	101.02	120.77	131.64	92.35	103.89
SVGD	74.94	175.62	1007.50	980.62	1054.53	1021.30
+OR-	93.55	94.55	111.89	146.96	109.76	127.81
<i>LAMBDA BAR MICRONS</i>						
LAM A	19.313	24.511	18.667	23.305	16.375	19.881
LAM B	14.446	13.609	11.920	12.209	15.726	15.181
LAM G	6.292	4.987	7.427	9.634	14.150	13.989
LAM D	14.449	16.264	15.766	17.343	16.200	18.427
<i>HBAR CM⁻¹</i>						
HBAR A	89.7	44.3	43.5	219.9	108.7	218.0
HBAR B	988.2	1671.5	1274.1	1096.1	880.3	1065.5
HBAR G	734.5	1372.2	421.2	429.1	420.4	544.6
HBAR D	185.7	769.4	547.0	876.5	547.1	716.0

Appendix 5 - continued.

TABLE A3
 QUANTITATIVE MICROSCOPY RESULTS FOR $T = 1400 \text{ } ^\circ\text{C}$

TIME =	3	8	18	33	63	123
VOLUME FRACTION						
VVA	0.1288	0.0543	0.0127	0.0080	0.0058	0.0033
+OR-	0.0176	0.0149	0.0113	0.0038	0.0052	0.0026
VVB	0.3026	0.0757	0.0587	0.0687	0.0444	0.0472
+OR-	0.0212	0.0143	0.0177	0.0166	0.0146	0.0162
VVG	0.0461	0.3240	0.3634	0.3905	0.3741	0.3548
+OR-	0.0063	0.0164	0.0169	0.0169	0.0206	0.0170
VVD	0.5176	0.5494	0.5498	0.5306	0.5675	0.5901
+OR-	0.0172	0.0174	0.0199	0.0157	0.0170	0.0152
V CV A	0.0682	0.1377	0.4434	0.2416	0.4467	0.3978
V CV B	0.0350	0.0946	0.1503	0.1209	0.1647	0.1713
V CV G	0.0687	0.0254	0.0233	0.0216	0.0275	0.0240
V CV D	0.0167	0.0159	0.0181	0.0148	0.0149	0.0128
AREA PER VOLUME CM^{-1}						
SVA	268.70	115.10	29.80	25.90	24.70	11.25
+OR-	38.00	27.83	16.86	11.59	16.62	8.10
SVB	737.00	224.50	148.20	181.20	116.35	112.44
+OR-	53.00	32.12	34.57	39.20	32.12	28.44
SVG	289.00	1193.00	1130.40	1336.60	1131.00	1139.70
+OR-	34.93	56.46	39.73	42.69	36.82	38.37
SVD	1313.60	1178.90	1051.30	1214.00	1080.20	1083.00
+OR-	39.04	32.15	27.52	32.28	24.66	32.13
SVA+G	475.70	1207.20	1158.20	1355.00	1154.50	1149.50
+OR-	42.95	83.92	37.83	40.20	30.78	36.09
SVB+G	855.90	1014.10	1041.40	1211.60	1067.50	1073.60
+OR-	58.58	42.08	27.15	36.33	30.33	31.85
S CV A	0.0707	0.1209	0.2828	0.2237	0.3365	0.3601
S CV B	0.0360	0.0715	0.1166	0.1082	0.1380	0.1265
S CV G	0.0604	0.0237	0.0176	0.0160	0.0163	0.0168
S CV D	0.0149	0.0136	0.0131	0.0133	0.0114	0.0148
S CV A+G	0.0451	0.0348	0.0163	0.0148	0.0133	0.0157
S CV B+G	0.0342	0.0207	0.0130	0.0150	0.0142	0.0148
TOTAL CURVATURE PER VOLUME ($\times 10^{-6}$) CM^{-2}						
MVA	0.0804	0.0289	0.0079	0.0019	0.0016	0.0060
+OR-	0.0405	0.0165	0.0157	0.0067	0.0092	0.0065
MVB	0.8724	0.2152	0.1976	0.1693	0.1464	0.1445
+OR-	0.0774	0.0376	0.0416	0.0396	0.0364	0.0262
MVG	0.2915	0.5850	0.7050	0.7750	0.7254	0.7951
+OR-	0.0345	0.0939	0.1015	0.1146	0.0840	0.1117
MVD	-1.3415	-0.7512	-1.0364	-1.0678	-0.9472	-1.0279
+OR-	0.1433	0.1091	0.0977	0.1108	0.0812	0.1020
M CV A	0.2515	0.2861	1.0016	-1.7760	2.9172	-0.5416
M CV B	0.0444	0.0874	0.1054	0.1169	0.1244	0.0908
M CV G	0.0591	0.0803	0.0720	0.0739	0.0579	0.0702
M CV D	-0.0534	-0.0726	-0.0471	-0.0519	-0.0429	-0.0496

Appendix 5 - continued.

TABLE A3 CONTINUED

TIME =	3	8	18	33	63	123
<i>MOLE FRACTION</i>						
MOLFR A	0.3431	0.1451	0.0360	0.0211	0.0167	0.0101
+OR-	0.0468	0.0399	0.0319	0.0102	0.0149	0.0080
MOLFR B	0.5553	0.1393	0.1144	0.1251	0.0885	0.0987
+OR-	0.0389	0.0264	0.0344	0.0302	0.0291	0.0338
MOLFR G	0.1015	0.7156	0.8496	0.8538	0.8948	0.8912
+OR-	0.0139	0.0363	0.0396	0.0369	0.0493	0.0427
<i>PERCENT ERROR IN POINT COUNT</i>						
VVD NET	0.5225	0.5460	0.5652	0.5329	0.5757	0.5948
+OR-	0.0282	0.0264	0.0269	0.0240	0.0258	0.0236
MACH ERR	0.4913	0.3350	1.5388	0.2238	0.8263	0.4650
VV ERR A	3.8141	6.1708	120.8047	28.1005	143.0736	139.8496
VV ERR B	1.6233	4.4261	26.2026	3.2587	18.6145	9.8621
VV ERR G	10.6533	1.0339	4.2345	0.5730	2.2085	1.3107
VV ERR D	0.9492	0.6098	2.7989	0.4217	1.4561	0.7880
<i>EXTENT OF REACTION</i>						
X	0.1322	0.8106	0.8609	0.8505	0.8939	0.8827
+OR-	0.0221	0.0233	0.0245	0.0239	0.0291	0.0241
(1-X)	0.8678	0.1894	0.1391	0.1495	0.1061	0.1173
<i>SPECIFIC INTERFACE AREA PER VOLUME CM⁻¹</i>						
SVAB	135.50	75.30	8.95	8.00	5.40	0.20
+OR-	136.50	89.93	77.14	76.18	73.11	54.81
SVAG	41.00	50.45	1.00	3.75	0.60	0.73
+OR-	115.88	168.21	94.42	94.48	84.23	82.56
SVAD	363.20	139.95	19.85	14.15	18.70	10.32
+OR-	135.61	102.05	71.52	80.19	71.61	72.08
SVBG	85.05	201.70	118.60	153.10	89.92	89.27
+OR-	146.50	130.65	101.46	118.22	99.27	98.66
SVBD	787.45	98.10	20.65	20.10	21.03	22.97
+OR-	134.99	148.19	99.92	111.68	87.55	96.66
SVGD	162.95	940.85	1010.80	1179.75	1040.47	1049.70
+OR-	110.94	132.91	100.87	112.45	92.22	105.75
<i>LAMBDA BAR MICRONS</i>						
LAM A	19.174	18.866	17.097	12.297	9.352	11.822
LAM B	16.425	13.486	15.850	15.157	15.260	16.773
LAM G	6.382	10.864	12.859	11.687	13.232	12.452
LAM D	15.760	18.640	20.917	17.484	21.013	21.795
<i>HBAR CM⁻¹</i>						
HBAR A	299.3	251.1	263.6	72.8	63.6	530.6
HBAR B	1183.7	958.6	1333.4	934.5	1258.3	1285.3
HBAR G	1008.8	490.3	623.7	579.9	641.4	697.7
HBAR D	1021.2	637.2	985.8	879.6	876.9	949.2

Appendix 5 - continued.

TABLE A4
 QUANTITATIVE MICROSCOPY RESULTS FOR $T = 1500 \text{ }^{\circ}\text{C}$

TIME	4	9	19	34	64	124
VOLUME FRACTION						
VVA	0.1014	0.0143	0.0058	0.0056	0.0023	0.0014
+OR-	0.0215	0.0087	0.0039	0.0036	0.0021	0.0018
VVB	0.1355	0.0598	0.0367	0.0429	0.0350	0.0448
+OR-	0.0121	0.0190	0.0106	0.0127	0.0116	0.0139
VVG	0.2723	0.4363	0.4234	0.4378	0.4341	0.4031
+OR-	0.0158	0.0204	0.0161	0.0239	0.0188	0.0181
VVD	0.4917	0.4864	0.5314	0.5097	0.5246	0.5501
+OR-	0.0163	0.0193	0.0142	0.0216	0.0166	0.0199
V CV A	0.1058	0.3066	0.3389	0.3213	0.4559	0.6413
V CV B	0.0446	0.1585	0.1451	0.1479	0.1667	0.1547
V CV G	0.0290	0.0234	0.0191	0.0273	0.0217	0.0224
V CV D	0.0165	0.0199	0.0134	0.0212	0.0158	0.0180
AREA PER VOLUME CM^{-1}						
SVA	174.50	36.70	14.50	13.70	6.40	6.80
+OR-	27.57	14.28	8.94	7.40	5.03	7.06
SVB	394.30	163.30	125.30	128.55	113.30	141.50
+OR-	25.42	42.76	33.76	31.32	33.50	40.20
SVG	1260.90	1183.90	1178.00	1049.00	1121.60	1047.90
+OR-	53.65	44.30	37.88	46.17	39.64	45.57
SVD	1192.90	1088.80	1092.80	960.50	1051.40	945.50
+OR-	30.72	29.83	25.15	32.21	28.01	34.01
SVA+G	1351.20	1199.10	1185.60	1054.70	1126.70	1052.10
+OR-	45.58	42.70	36.57	46.47	39.28	44.82
SVB+G	1008.80	1059.20	1071.40	955.90	1031.40	941.80
+OR-	45.07	26.63	26.68	33.20	29.13	33.66
S CV A	0.0790	0.1946	0.3081	0.2701	0.3930	0.5192
S CV B	0.0322	0.1309	0.1347	0.1218	0.1478	0.1420
S CV G	0.0213	0.0187	0.0161	0.0220	0.0177	0.0217
S CV D	0.0129	0.0137	0.0115	0.0168	0.0133	0.0180
S CV A+G	0.0169	0.0178	0.0154	0.0220	0.0174	0.0213
S CV B+G	0.0223	0.0126	0.0124	0.0174	0.0141	0.0179
TOTAL CURVATURE PER VOLUME ($\times 10^{-6}$) CM^{-2}						
MVA	0.0132	0.0116	0.0022	0.0066	0.0016	0.0006
+OR-	0.0194	0.0146	0.0044	0.0066	0.0035	0.0028
MVB	0.4505	0.1674	0.1568	0.1517	0.1517	0.1652
+OR-	0.0396	0.0421	0.0475	0.0305	0.0406	0.0452
MVG	0.3135	0.1979	0.4379	0.0644	0.3377	0.3038
+OR-	0.0980	0.0988	0.0863	0.1027	0.0834	0.0829
MVD	-0.4499	-0.4386	-0.6732	-0.2721	-0.5400	-0.5397
+OR-	0.1018	0.0759	0.0898	0.1144	0.0730	0.0614
M CV A	0.7353	0.6259	-1.0000	0.5003	1.1157	2.2542
M CV B	0.0439	0.1258	0.1515	0.1005	0.1339	0.1367
M CV G	0.1563	0.2496	0.0985	0.7973	0.1235	0.1365
M CV D	-0.1131	-0.0866	-0.0667	-0.2102	-0.0676	-0.0569

Appendix 5 - continued.

TABLE A4 CONTINUED

TIME =	4	9	19	34	64	124
<i>MOLE FRACTION</i>						
MOLFR A	0.2416	0.0342	0.0152	0.0141	0.0061	0.0038
+OR-	0.0511	0.0210	0.0103	0.0091	0.0055	0.0049
MOLFR B	0.2222	0.0990	0.0663	0.0744	0.0625	0.0844
+OR-	0.0198	0.0314	0.0192	0.0220	0.0208	0.0261
MOLFR G	0.5362	0.8667	0.9185	0.9115	0.9314	0.9118
+OR-	0.0311	0.0406	0.0350	0.0497	0.0403	0.0409
<i>PERCENT ERROR IN POINT COUNT</i>						
VVD NET	0.4908	0.4896	0.5342	0.5137	0.5287	0.5507
+OR-	0.0293	0.0292	0.0197	0.0273	0.0222	0.0229
MACH ERR	0.0887	0.3213	0.2763	0.3988	0.4050	0.0638
VV ERR A	0.8751	22.5439	47.7322	71.0468	173.2620	45.9459
VV ERR B	0.6552	5.3698	7.5375	9.3003	11.5880	1.4230
VV ERR G	0.3259	0.7362	0.6525	0.9107	0.9330	0.1582
VV ERR D	0.1805	0.6605	0.5198	0.7823	0.7720	0.1159
<i>EXTENT OF REACTION</i>						
X	0.6678	0.8794	0.9203	0.9108	0.9255	0.9000
+OR-	0.0224	0.0289	0.0228	0.0338	0.0266	0.0256
(1-X)	0.3322	0.1206	0.0797	0.0892	0.0745	0.1000
<i>SPECIFIC INTERFACE AREA PER VOLUME CM⁻¹</i>						
SVAB	46.90	7.70	6.90	0.55	7.45	0.25
+OR-	79.48	85.56	64.04	58.08	57.79	70.89
SVAG	42.10	11.25	3.45	4.00	0.65	1.30
+OR-	126.80	101.28	83.38	100.05	83.95	97.45
SVAD	179.30	33.15	17.95	9.15	13.20	5.25
+OR-	103.36	70.74	60.76	72.81	62.17	74.73
SVBG	323.20	144.00	115.95	110.83	101.75	123.80
+OR-	124.14	113.68	98.31	110.69	102.27	119.43
SVBD	118.00	27.00	16.25	17.18	19.00	17.45
+OR-	101.72	115.29	95.47	110.01	100.79	119.03
SVGD	895.60	1028.65	1058.60	934.17	1019.20	922.80
+OR-	126.56	111.19	94.54	117.58	101.48	119.36
<i>LAMBDA BAR MICRONS</i>						
LAM A	23.246	15.531	15.966	16.387	14.609	8.162
LAM B	13.741	14.654	11.700	13.341	12.339	12.664
LAM G	8.639	14.742	14.376	16.695	15.480	15.386
LAM D	16.488	17.868	19.452	21.226	19.958	23.272
<i>HBAR CM⁻¹</i>						
HBAR A	75.6	316.7	151.7	481.6	245.4	92.4
HBAR B	1142.5	1025.4	1251.1	1180.4	1339.3	1167.8
HBAR G	248.7	167.2	371.8	61.4	301.1	289.9
HBAR D	377.1	402.8	616.1	283.3	513.6	570.8

APPENDIX 6

TABLE A5
RESULTS OF ARCHIMEDEAN POROSITY

TEMP °C	0	5	15	30	60	120
	<i>PERCENT POROSITY</i>					
1200	0.3551	0.3295	0.3722	0.4239	0.4555	0.4576
1300	0.4070	0.3741	0.4053	0.4439	0.4123	0.4854
1400	0.4616	0.4311	0.4462	0.4608	0.4307	0.4487
1500	0.4305	0.4354	0.4327	0.4573	0.3970	0.4701
	<i>NUGGET VOLUME CM3</i>					
1200	0.1288	0.3362	0.2938	0.1048	0.2677	0.1676
1300	0.1450	0.3105	0.1571	0.2290	0.5858	0.0748
1400	0.0608	0.2755	0.3472	0.3493	0.4976	0.3860
1500	0.1766	0.2220	0.3640	0.2690	0.3420	0.2414
	<i>SOLID POWDER VOLUME CM3</i>					
1200	0.0831	0.2254	0.1844	0.0604	0.1458	0.0909
1300	0.0860	0.1943	0.0934	0.1274	0.3443	0.0385
1400	0.0327	0.1567	0.1923	0.1884	0.2833	0.2128
1500	0.1006	0.1253	0.2065	0.1460	0.2062	0.1279
	<i>DRY MASS GRAMS</i>					
1200	0.3738	1.0144	0.8300	0.2717	0.6559	0.4091
1300	0.3869	0.8745	0.4204	0.5731	1.5492	0.1732
1400	0.1473	0.7053	0.8652	0.8476	1.2748	0.9576
1500	0.4526	0.5640	0.9293	0.6569	0.9280	0.5756
	<i>SUSPENDED MASS GRAMS</i>					
1200	0.2743	0.7421	0.5963	0.1864	0.4574	0.2810
1300	0.2805	0.6182	0.3120	0.4024	1.1108	0.1198
1400	0.1000	0.4900	0.6048	0.5807	0.8911	0.6647
1500	0.3161	0.3956	0.6614	0.4553	0.5727	0.3993
	<i>WAX IMPREGNATED NUGGET MASS GRAMS</i>					
1200	0.4031	1.0783	0.8901	0.2912	0.7251	0.4486
1300	0.4255	0.9287	0.4691	0.6314	1.6966	0.1946
1400	0.1608	0.7655	0.9520	0.9300	1.3887	1.0507
1500	0.4927	0.6176	1.0254	0.7243	0.9147	0.6407

APPENDIX 7

Selected X-Ray Data

<u>2θ</u>	<u>d$\overset{\circ}{\text{A}}$</u>	<u>hkl</u>	<u>I/I_o</u>	<u>Material</u>
46.38	1.956	211	40	TiB
45.45	1.994	220	55	NaCl
44.53	2.033	101	100	TiB ₂
42.99	2.102	150		Ti ₃ B ₄
42.67	2.117	121	75	Ti ₃ B ₄
42.19	2.140	102	100	TiB
41.76	2.161	210	64	TiB
40.55	2.223	101		Ti ₃ B ₄
40.15	2.244	011	100	Ti
39.31	2.29	060	75	Ti ₃ B ₄
38.40	2.342	002	26	Ti
38.33	2.346	111	80	TiB
35.41	2.533	031	100	Ti ₃ B ₄
35.26	2.543	201,011	80	TiB
35.06	2.557	010	30	Ti
34.19	2.62	100	60	TiB ₂
33.66	2.66	130		Ti ₃ B ₄
31.69	2.821	100	100	NaCl
29.26	3.05	200	32	TiB

APPENDIX 8

TABLE A6
X-RAY STANDARDS DATA

	TI DATA						
PERCENT	41	36	31	22	13	8	4
CPS	41748	49727	42360	22757	20859	11301	6413
+OR-	1274	537	510	502	270	252	107
CV	0.0137	0.0048	0.0054	0.0099	0.0060	0.0100	0.0130

I RATIO	2.5727	2.4113	1.9817	1.3210	0.9524	0.5241	0.3133
+OR-	0.2208	0.1259	0.1528	0.1047	0.0617	0.0385	0.0157
CV	0.0193	0.0234	0.0173	0.0181	0.0146	0.0165	0.0150

	TIB2 DATA						
PERCENT	60	55	46	33	24	11	6
CPS	37584	44151	38295	19754	17709	8738	3966
+OR-	1450	573	125	625	1036	236	156
CV	0.0173	0.0058	0.0073	0.0148	0.0258	0.0122	0.0290

I RATIO	2.2815	2.1393	1.7922	1.1453	0.8400	0.4061	0.1939
+OR-	0.1965	0.1771	0.1613	0.0683	0.0772	0.0484	0.0289
CV	0.0193	0.0162	0.0202	0.0133	0.0206	0.0267	0.0441

	TIB DATA						
PERCENT	0	9	23	45	63	81	90
CPS	0	13017	23327	30577	54734	69281	74536
+OR-	0	390	271	646	499	693	1143
CV	0.0000	0.0135	0.0052	0.0095	0.0042	0.0045	0.0086

I RATIO	0.0000	0.6307	1.0911	1.7747	2.4950	3.2161	3.6427
+OR-	0.0000	0.0281	0.0789	0.1354	0.1584	0.2785	0.2756
CV	0.0000	0.0200	0.0162	0.0172	0.0143	0.0194	0.0175

	NACL DATA--10 WT PERCENT						
CPS	16501	20672	21423	17264	21377	21614	20478
+OR-	633	958	711	630	860	945	579
CV	0.0172	0.0208	0.0149	0.0164	0.0180	0.0196	0.0145

Appendix 8 - continued.

TABLE A7
X-RAY SAMPLE DATA

TIME =	0	5	15	30	60	120
DATA FOR T = 1100 °C						
TI CPS	45491	0	44501	43261	36836	35431
TIB2 CPS	55564	0	52986	49793	41340	34457
TIB CPS	9253	0	17902	20242	27618	35773
DC VOL A	34	0	33	32	26	25
DC VOL B	68	0	66	61	51	43
DC VOL G	5	0	15	18	24	38
TOTAL	107	0	114	111	101	106
I/I TI	2.17	0.00	2.26	2.05	1.90	1.88
I/I TIB2	2.65	0.00	2.69	2.35	2.13	1.83
I/I TIB	0.44	0.00	0.91	0.96	1.42	1.90
IS VOL A	33	0	35	31	29	29
IS VOL B	69	0	70	61	55	48
IS VOL G	6	0	16	18	32	46
TOTAL	108	0	121	110	116	123
DATA FOR T = 1200 °C						
TI CPS	46542	42248	40300	34822	22963	13057
TIB2 CPS	55929	50890	39476	30206	18548	11547
TIB CPS	12896	21529	33431	43245	51352	70730
DC VOL A	35	31	29	25	16	9
DC VOL B	69	62	49	38	24	15
DC VOL G	9	20	35	48	59	85
TOTAL	113	113	113	111	99	109
I/I TI	2.24	1.99	2.10	1.76	1.19	0.73
I/I TIB2	2.69	2.40	2.05	1.53	0.96	0.62
I/I TIB	0.62	1.01	1.75	2.18	2.66	3.90
IS VOL A	35	32	32	27	19	12
IS VOL B	70	63	54	41	24	18
IS VOL G	9	20	42	54	67	92
TOTAL	114	115	128	124	110	128

Appendix 8 - continued.

TABLE A7 CONTINUED

TIME =	0	5	15	30	60	120
DATA FOR T = 1300 °C						
TI CPS	40815	40598	25409	19395	11369	12283
TIB2 CPS	45767	43738	21830	16579	11106	12222
TIB CPS	26027	37702	48411	59357	61441	74367
DC VOL A	30	30	17	13	8	9
DC VOL B	57	54	28	22	14	16
DC VOL G	26	41	55	69	72	90
TOTAL	113	125	100	104	94	115
I/I TI	2.08	1.95	1.38	0.99	0.61	0.51
I/I TIB2	2.33	2.08	1.19	0.84	0.59	0.51
I/I TIB	1.32	1.79	2.61	3.02	3.29	3.10
IS VOL A	33	31	22	16	10	8
IS VOL B	62	54	34	24	17	14
IS VOL G	29	45	66	77	83	78
TOTAL	124	130	122	117	110	100
DATA FOR T = 1400 °C						
TI CPS	36080	21675	12641	10858	9695	8986
TIB2 CPS	35739	17855	10577	10447	9731	10251
TIB CPS	37218	59448	67716	72458	71548	74923
DC VOL A	25	15	9	7	7	6
DC VOL B	45	24	14	14	13	14
DC VOL G	40	69	80	87	86	91
TOTAL	110	108	103	108	106	111
I/I TI	1.84	1.15	0.70	0.55	0.54	0.46
I/I TIB2	1.83	0.95	0.60	0.54	0.54	0.51
I/I TIB	1.90	3.14	3.76	3.69	4.01	3.78
IS VOL A	29	18	11	9	9	7
IS VOL B	48	28	17	15	15	14
IS VOL G	46	79	95	93	101	96
TOTAL	123	125	123	117	125	117

APPENDIX 9

TABLE A8
RESULTS OF SASAKI MODEL
XI = 0.957 SERIES

XIARB	SUMXI	SUMIX	SUMR	KT
0.957	98.387	0.29293	3.2653E ⁻¹³	8.9709E11
0.865	98.334	0.49779	7.9695E ⁻¹³	6.2462E11
0.76	98.204	0.64022	1.4732E ⁻¹²	4.3457E11
0.662	97.955	0.74103	2.4477E ⁻¹²	3.0274E11
0.565	97.517	0.81064	3.8516E ⁻¹²	2.1047E11
0.475	96.795	0.85791	5.8693E ⁻¹²	1.4617E11
0.41	95.657	0.89227	8.7714E ⁻¹²	1.0172E11
0.335	93.919	0.91464	1.2953E ⁻¹¹	7.0610E10
0.285	91.29	0.93061	1.8990E ⁻¹¹	4.9004E10
0.235	85.841	0.94132	2.7692E ⁻¹¹	3.3992E10
0.185	77.586	0.94788	4.0178E ⁻¹¹	2.3592E10
0.16	68.469	0.95276	5.8133E ⁻¹¹	1.6389E10
0.12	59.71	0.95548	8.4163E ⁻¹¹	1.1353E10
0.09	51.282	0.957	1.2134E ⁻¹⁰	7.8867E9
0.065	43.594	0.95779	1.7462E ⁻¹⁰	5.4849E9
0.05	37.344	0.95826	2.5157E ⁻¹⁰	3.8091E9
0.02	31.089	0.95833	3.6237E ⁻¹⁰	2.6446E9

RESULTS OF SASAKI MODEL
XI = 0.98 SERIES

XIARB	SUMXI	SUMIX	SUMR	KT
0.98	98.394	0.329	3.2653E ⁻¹³	1.0076E12
0.886	98.354	0.54991	7.9695E ⁻¹³	6.9001E11
0.782	98.246	0.70354	1.4732E ⁻¹²	4.7755E11
0.68	98.029	0.81112	2.4477E ⁻¹²	3.3138E11
0.583	97.644	0.88591	3.8516E ⁻¹²	2.3001E11
0.493	96.996	0.93721	5.8693E ⁻¹²	1.5968E11
0.425	95.972	0.97432	8.7714E ⁻¹²	1.1108E11
0.355	94.389	0.99961	1.2953E ⁻¹¹	7.7170E10
0.29	92.008	1.0162	1.8990E ⁻¹¹	5.3509E10
0.24	87.708	1.0273	2.7692E ⁻¹¹	3.7099E10
0.212	79.461	1.036	4.0178E ⁻¹¹	2.5786E10
0.17	70.392	1.0415	5.8133E ⁻¹¹	1.7917E10
0.14	61.415	1.0453	8.4163E ⁻¹¹	1.2419E10
0.1	52.948	1.0471	1.2134E ⁻¹⁰	8.6295E9
0.07	45.206	1.0481	1.7462E ⁻¹⁰	6.0018E9
0.06	38.79	1.0487	2.5157E ⁻¹⁰	4.1687E9
0.025	32.669	1.0488	3.6237E ⁻¹⁰	2.8944E9

Appendix 9 - continued.

TABLE A8 CONTINUED
 RESULTS OF SASAKI MODEL
 XI = 1.00 SERIES

<i>XIARB</i>	<i>SUMXI</i>	<i>SUMIX</i>	<i>SUMR</i>	<i>KT</i>
1	98.4	0.39142	3.2653E ⁻¹³	1.1987E12
0.943	98.383	0.6669	7.9695E ⁻¹³	8.3682E11
0.843	98.319	0.85652	1.4732E ⁻¹²	5.8139E11
0.735	98.169	0.98714	2.4477E ⁻¹²	4.0329E11
0.635	97.889	1.0784	3.8516E ⁻¹²	2.7999E11
0.54	97.4	1.1412	5.8693E ⁻¹²	1.9444E11
0.46	96.607	1.1853	8.7714E ⁻¹²	1.3513E11
0.412	95.367	1.22	1.2953E ⁻¹¹	9.4186E10
0.32	93.482	1.2404	1.8990E ⁻¹¹	6.5315E10
0.275	90.63	1.2552	2.7692E ⁻¹¹	4.5326E10
0.23	84.369	1.2654	4.0178E ⁻¹¹	3.1495E10
0.19	75.636	1.2723	5.8133E ⁻¹¹	2.1887E10
0.155	66.352	1.2769	8.4163E ⁻¹¹	1.5172E10
0.125	57.6	1.2799	1.2134E ⁻¹⁰	1.0548E10
0.085	49.436	1.2812	1.7462E ⁻¹⁰	7.3371E9
0.064	42.401	1.282	2.5157E ⁻¹⁰	5.0960E9
0.04	36.968	1.2823	3.6237E ⁻¹⁰	3.5386E9

APPENDIX 10

TABLE A9 QUANTITATIVE MICROSCOPY MODEL CALCULATIONS

RESULTS FOR T = 1200 °C							
TIME =	2	6	16	31	61	121	
X	0.0238	0.0276	0.1463	0.3369	0.7986	0.9115	
KT PB	0.0080	0.0093	0.0514	0.1280	0.4139	0.5543	
KT J	0.0001	0.0001	0.0026	0.0164	0.1713	0.3073	
KT GB	0.0001	0.0001	0.0025	0.0150	0.1240	0.1937	
KT VC	0.0001	0.0001	0.0041	0.0226	0.1627	0.2429	
KT ZLT	0.0001	0.0001	0.0029	0.0215	0.4986	1.5473	
KT DW	-0.4736	-0.4697	-0.3395	-0.0869	1.1049	1.9269	
KT NG	0.0145	0.0156	0.1037	0.2760	1.2470	1.9730	
KT VCS	1.10E8	1.30E8	8.60E8	3.11E9	2.64E10	4.72E10	

RESULTS FOR T = 1300 °C							
TIME =	3	7	17	32	62	122	
X	0.0599	0.1102	0.6600	0.7492	0.8684	0.8819	
KT PB	0.0204	0.0382	0.3020	0.3694	0.4914	0.5093	
KT J	0.0004	0.0015	0.0912	0.1365	0.2415	0.2594	
KT GB	0.0004	0.0014	0.0728	0.1029	0.1624	0.1713	
KT VC	0.0007	0.0023	0.1001	0.1372	0.2074	0.2176	
KT ZLT	0.0004	0.0016	0.1872	0.3432	0.9335	1.0775	
KT DW	-0.4360	-0.3810	0.5810	0.8856	1.5306	1.6383	
KT NG	0.0395	0.0523	0.7580	1.0740	1.8180	1.8350	
KT VCS	3.00E8	6.20E8	1.50E10	2.16E10	3.60E10	3.86E10	

RESULTS FOR T = 1400 °C							
TIME =	4	8	18	33	63	123	
X	0.1322	0.8106	0.8609	0.8505	0.8939	0.8827	
KT PB	0.0462	0.4258	0.4818	0.4692	0.5266	0.5105	
KT J	0.0021	0.1813	0.2322	0.2202	0.2774	0.2606	
KT GB	0.0021	0.1298	0.1576	0.1513	0.1800	0.1719	
KT VC	0.0033	0.1695	0.2019	0.1946	0.2274	0.2183	
KT ZLT	-0.0023	0.5497	0.8647	0.7815	1.2379	1.0874	
KT DW	-0.3559	1.1664	1.4747	1.4025	1.7460	1.6452	
KT NG	0.1070	1.2570	1.8940	1.9230	2.2520	2.2180	
KT VCS	7.60E8	2.75E10	3.46E10	3.28E10	4.16E10	3.88E10	

Appendix 10 - continued.

TABLE A9 CONTINUED
 RESULTS FOR $T = 1500 \text{ }^\circ\text{C}$

TIME =	5	9	19	34	64	124
<i>X</i>	0.6678	0.8794	0.9203	0.9108	0.9255	0.9000
<i>KT PB</i>	0.3074	0.5060	0.5697	0.5532	0.5792	0.5358
<i>KT J</i>	0.0945	0.2560	0.3246	0.3060	0.3355	0.2871
<i>KT GB</i>	0.0751	0.1697	0.2013	0.1932	0.2059	0.1845
<i>KT VC</i>	0.1030	0.2157	0.2513	0.2422	0.2564	0.2326
<i>KT ZLT</i>	0.1971	1.0489	1.7530	1.5331	1.8944	1.3323
<i>KT DW</i>	0.6044	1.6178	2.0322	1.9193	2.0990	1.8046
<i>KT NG</i>	0.7680	2.0150	2.5070	2.4250	2.6790	2.4280
<i>KT VCS</i>	1.52E10	3.82E10	5.2E10	4.71E10	5.64E10	4.36E10

APPENDIX 11

TABLE A10
QUANTITATIVE X-RAY MODEL CALCULATIONS

		RESULTS FOR T = 1100 °C					
TIME =		0	5	15	30	60	120
X		0.0800	0.0000	0.1860	0.2280	0.3680	0.4890
KT PB		0.0274	0.0000	0.0663	0.0826	0.1418	0.2005
KT J		0.0008	0.0000	0.0044	0.0068	0.0201	0.0402
KT GB		0.0007	0.0000	0.0042	0.0065	0.0182	0.0348
KT VC		0.0012	0.0000	0.0066	0.0101	0.0273	0.0504
KT ZLT		0.0008	0.0000	0.0050	0.0081	0.0273	0.0629
KT DW		-0.4143	0.0000	-0.2919	-0.2389	-0.0388	0.1737
KT NG		0.0800	0.0000	0.1860	0.2280	0.3680	0.4890
KT VCS		4.20E9		1.18E9	1.56E9	3.70E9	7.00E9

		RESULTS FOR T = 1200 °C					
TIME =		1	6	16	31	61	121
X		0.1300	0.2500	0.3610	0.5630	0.7360	0.8450
KT PB		0.0454	0.0914	0.1387	0.2411	0.3585	0.4628
KT J		0.0021	0.0084	0.0192	0.0581	0.1285	0.2142
KT GB		0.0020	0.0079	0.0175	0.0488	0.0978	0.1481
KT VC		0.0032	0.0122	0.0262	0.0691	0.1311	0.1909
KT ZLT		0.0023	0.0101	0.0259	0.1010	0.3123	0.7424
KT DW		-0.3584	-0.2100	-0.0498	0.3301	0.8341	1.3666
KT NG		0.1300	0.2500	0.3610	0.5630	0.7360	0.8450
KT VCS		7.60E8	1.80E9	3.58E9	9.80E9	2.04E10	3.2E10

		RESULTS FOR T = 1300 °C					
TIME =		2	7	17	32	62	122
X		0.3190	0.4550	0.6600	0.7620	0.8300	0.8480
KT PB		0.1202	0.1832	0.3020	0.3803	0.4460	0.4663
KT J		0.0144	0.0336	0.0912	0.1446	0.1989	0.2175
KT GB		0.0133	0.0295	0.0729	0.1080	0.1398	0.1499
KT VC		0.0202	0.0430	0.1001	0.1434	0.1812	0.1930
KT ZLT		0.0187	0.0503	0.1873	0.3766	0.6483	0.7635
KT DW		-0.1135	0.1093	0.5811	0.9378	1.2743	1.3862
KT NG		0.3190	0.4550	0.6600	0.7620	0.8300	0.8480
KT VCS		2.76E9	6.00E9	1.48E10	2.26E10	3.0E10	3.26E10

Appendix 11 - continued.

TABLE A10 CONTINUED
RESULTS FOR T = 1400 °C

<i>TIME =</i>	<i>3</i>	<i>8</i>	<i>18</i>	<i>33</i>	<i>63</i>	<i>123</i>
<i>X</i>	0.4890	0.7380	0.8480	0.8610	0.8710	0.8730
<i>KT PB</i>	0.2005	0.3601	0.4663	0.4820	0.4947	0.4973
<i>KT J</i>	0.0402	0.1297	0.2175	0.2323	0.2448	0.2474
<i>KT GB</i>	0.0348	0.0986	0.1499	0.1577	0.1640	0.1653
<i>KT VC</i>	0.0504	0.1320	0.1930	0.2020	0.2093	0.2108
<i>KT ZLT</i>	0.0629	0.3167	0.7635	0.8658	0.9587	0.9790
<i>KT DW</i>	0.1737	0.8417	1.3862	1.4756	1.5502	1.5659
<i>KT NG</i>	0.4890	0.7380	0.8480	0.8610	0.8710	0.8730
<i>KT VCS</i>	7.00E9	2.06E10	3.26E10	3.48E10	3.64E10	3.7E10

APPENDIX 12

TABLE A11
QUANTITATIVE MICROSCOPY SLOPE DATA: TIR2

TIME =	0	5	15	30	60	120
TEMP °C	<i>D VVB/DT</i>					
1200	7.58E ⁻³	5.77E ⁻³	3.91E ⁻³	2.62E ⁻³	1.55E ⁻³	7.04E ⁻⁴
1300	1.27E ⁻¹	1.29E ⁻²	2.64E ⁻³	1.66E ⁻³	6.72E ⁻⁴	0.00E0
1400	7.00E ⁻¹	4.61E ⁻³	8.40E ⁻⁴	6.00E ⁻⁴	0.00E0	0.00E0
1500	7.00E ⁻¹	4.17E ⁻³	4.00E ⁻⁴	0.00E0	0.00E0	0.00E0
	<i>D SVB/DT</i>					
1200	4.50E1	8.07E0	1.16E0	8.98E0	2.56E0	1.06E0
1300	4.00E2	2.08E1	8.75E0	6.25E0	2.30E0	0.00E0
1400	9.41E2	1.48E1	3.36E0	1.44E0	7.04E ⁻¹	0.00E0
1500	1.09E2	9.09E0	1.12E0	0.00E0	0.00E0	0.00E0
	<i>D SVBG/DT</i>					
1200	1.2E0	1.6E0	7.3E0	2.7E0	-2.3E0	0.0E0
1300	3.6E1	1.6E1	6.4E ⁻¹	-2.7E0	-1.0E0	0.0E0
1400	3.5E1	0.0E0	2.0E0	-1.3E0	-8.0E ⁻¹	0.0E0
1500	-7.2E1	-1.6E0	0.0E0	0.0E0	0.0E0	0.0E0
	<i>D MVB/DT</i>					
1200	1.23E11	5.40E9	1.00E3	1.03E10	5.27E9	8.00E8
1300	9.64E3	1.39E4	3.10E4	8.36E3	3.40E3	0.00E0
1400	4.17E5	3.54E3	1.80E3	1.40E3	0.00E0	0.00E0
1500	9.04E4	7.00E3	0.00E0	0.00E0	0.00E0	0.00E0

D VVB/DT, D SVB/DT, AND D MVB/DT ARE NEGATIVE
ABSOLUTE VALUES PRINTED FOR CLARITY

APPENDIX 13

TABLE A12
VELOCITY AND CURVATURE RESULTS

TIME =	0	5	15	30	60	120
<i>TEMP °C</i>						
<i>VBARS MICRONS/MIN.</i>						
1200	3.77E0	7.77E0	6.84E ⁻¹	8.42E ⁻²	7.17E ⁻²	4.38E ⁻²
1300	2.61E1	6.45E ⁻¹	9.22E ⁻²	7.12E ⁻²	4.89E ⁻²	0.00E0
1400	8.23E1	2.29E ⁻¹	7.08E ⁻²	3.92E ⁻²	0.00E0	0.00E0
1500	2.17E1	2.90E ⁻¹	3.45E ⁻²	0.00E0	0.00E0	0.00E0
<i>VBARS* MICRONS/MIN.</i>						
1200	3.04E0	2.06E0	5.90E ⁻²	7.18E ⁻²	6.77E ⁻²	3.13E ⁻²
1300	1.15E0	5.90E ⁻¹	1.57E ⁻¹	5.80E ⁻²	2.40E ⁻²	0.00E0
<i>VBARR MICRONS/MIN.</i>						
1200	1.82E ⁻¹	4.43E ⁻²	4.31E ⁻³	5.19E ⁻²	4.94E ⁻²	3.95E ⁻²
1300	2.20E0	1.15E ⁻¹	8.15E ⁻²	8.35E ⁻²	8.02E ⁻²	0.00E0
1400	5.39E0	3.44E ⁻¹	8.50E ⁻²	4.25E ⁻²	2.40E ⁻²	0.00E0
1500	1.21E0	2.71E ⁻¹	3.57E ⁻²	0.00E0	0.00E0	0.00E0
<i>HBARR CM⁻¹/MIN.</i>						
1200	2.97E3	6.99E2	1.48E2	1.71E3	8.26E2	7.50E2
1300	1.57E3	8.05E2	1.66E3	1.89E3	1.71E3	5.00E ⁻²
1400	6.72E2	1.61E3	2.00E3	1.20E3	3.52E9	5.00E ⁻²
1500	7.81E1	1.09E3	1.40E3	5.00E ⁻³	5.00E ⁻¹	5.00E ⁻¹

BIBLIOGRAPHY

1. G. C. Walther and E. D. Whitney, "Reaction Kinetics of $B_{12}C_3$ and Ti," presented at the 76th Annual Meeting, The American Ceramic Society, 1974.
2. L. Andrieux, "Making Metallic Powders by Electrolysis of Fused Salts," Comptes Rendue, 189 (1929) 1279-84.
3. C. Agte and K. Moers, "Methods for the Preparation of Pure High-Melting Carbides, Nitrides, and Borides and a Description of a few of Their Properties," Z. Anorg. Allgem. Chem., 198 (1931) 233-45.
4. P. Ehrlich, "The Binary Systems Ti-N, Ti-C, Ti-B, Ti-Be," Z. Anorg. Chem., 259 (1949) 1-41.
5. J. T. Norton, H. Blumenthal and S. J. Sindeband, "Structure of Diborides of Titanium, Zirconium, Columbium, Tantalum, and Vanadium," J. Metals, 1(10) (1949) 749-51.
6. W. H. Zachariasen, "Crystal Chemistry Studies of the 5 f-Series of Elements," Acta Cryst., 2 (1949) 94-99.
7. L. H. Andersson and R. Kiessling, "Binary Systems of Boron with Chromium, Columbium, Nickel, and Thorium, including a Discussion of the Phase 'TiB' in the Titanium-Boron System," Acta Chem. Scand., 4 (1950) 160-4.
8. L. Brewer, D. L. Sawyer, D. H. Templeton, and C. H. Dauben, "A Study of the Refractory Borides," J. Am. Ceram. Soc., 34 (1951) 173-9.
9. H. M. Greenhouse, O. E. Accountius, and H. H. Sisler, "High Temperature Reactions in the System Titanium Carbide-Boron Carbide," J. Am. Chem. Soc., 73 (1951) 5086-7.
10. H. R. Ogden and R. I. Jaffee, "Titanium-Boron Alloys," J. Metals, 3 (1951) 335-6.

11. M. Hansen, personal communication to R. I. Jaffee, 1951.
12. F. W. Glaser, "Metal-Carbon-Boron Systems," J. Metals, 4 (1952) 391-6.
13. B. Post and F. W. Glaser, "Borides of Some Transition Metals," J. Chem. Phys., 20 (1952) 1050-1.
14. B. Post, F. W. Glaser, and D. W. Moskowitz, "Transition Metal Diborides," Acta Met., 2 (1954) 20-25.
15. A. E. Palty, H. Margolin, and J. P. Nielsen, "Titanium-Nitrogen and Titanium-Boron Systems," Trans. ASM, 46 (1954) 312-28.
16. G. V. Samsonov and Ya. S. Umanskiy, "Hard Compounds of Refractory Metals," Tech. Trans. TT-F-102 NASA (June, 1962).
17. M. Hansen, Constitution of Binary Alloys, 2nd ed., McGraw-Hill, New York, 1958.
18. C. M. Craighead, O. W. Simmons, and L. W. Eastwood, "Titanium Binary Alloys," Trans. AIME, 188 (1950) 485-513.
19. B. F. Decker and J. S. Kasper, "The Crystal Structure of TiB," Acta Cryst., 7 (1954) 77-80.
20. B. Aronsson, "Borides and Silicides of the Transition Metals," Arkiv Kemi, 16(36) (1960) 379-423.
21. H. Nowotny, "Structural Investigations in Combined Silicide and Boride Cermets," U.S. Dept. Comm. Office Techn. Serv., PB Report 145949 (1961).
22. H. Nowotny, F. Benesovsky, C. Brukl, and O. Schob, "The Systems Ti-B-C and Ti-B-N," Monatsh. Chem., 92 (1961) 403-14.
23. A. Whitmann, H. Nowotny, and H. Boller, "A Contribution to the System Ti-Mo-B," Monatsh. Chem., 91 (1960) 608-15.

24. A. V. Seybolt, "An Exploration of High-Boron Alloys," Trans. ASM, 52 (1960) 971-89.
25. E. Rudy and R. St. Windisch, "Ternary Phase Equilibria in Transition Metal-Boron-Carbon-Silicon Systems: Part I. Related Binary Systems, Volume VII TiB System," AFML-TR-65-2, Part 1, Volume VII, January, 1966.
26. M. Garfinkle and H. M. Davis, "Reaction of Liquid Titanium with Some Refractory Compounds," Trans. ASM, 58 (1965) 520-30.
27. J. D. Latva, "Selection and Fabrication of Ceramics and Intermetallics," Metal Progress, 82(4) (1962) 139-44.
28. N. Engel, "Metallic Lattices Considered as Electron Concentration Phases," Trans. ASM, 57 (1964) 610-19.
29. R. G. Fenish, "A New Intermediate Compound in the Titanium-Boron System, Ti_3B_4 ," Trans. AIME, 236 (1966) 804.
30. R. G. Fenish, personal communication, 1974.
31. K. C. Antony and W. V. Cummings, "Metallurgical Stability of Several Boride Dispersion Systems," U.S. AEC GEAP 3530 (1960).
32. L. V. Strashinskaya and A. N. Stepanchuk, "Contact Interaction of Titanium Diboride with Titanium, Zirconium, and Vanadium in Vacuo," Soviet Materials Science, 6 (1970) 722-25.
33. G. N. Samsonov, "The Interaction of Titanium, Zirconium, and Tungsten Borides with Their Carbides," Voprosy Poroshkovo Met. i Prochnosti Materialov, Akad. Nauk. Ukr. SSR, 7 (1950) 72-98.
34. A. P. Epik, "The Boronization of Refractory Transition Metals," Soviet Powder Metallurgy, 3 (1963) 361-65.
35. G. V. Samsonov and A. P. Epik, "Reactive Diffusion of Boron and Carbon in Refractory Transition Metals," Dopovidi Akad. Nauk. RSR, 1 (1964) 67-70.

36. G. L. Zhunkovskii and G. V. Samsonov, "Vacuum Boronizing of Group IV, V and VI Transition Metals," Fiz. Khim. Obrab. Mater., (1968) 132-40.
37. G. L. Zhunkovskii, "Preparation and Investigation of Diffusion Coatings on Metals of Group IV of the Periodic System," Protective Coatings on Metals, 2 (1968) 202-7.
38. A. L. Burykina and T. M. Evtushok, "High-Temperature Coatings of Refractory Compounds on Graphite," Protective Coatings on Metals, 3 (1970) 178-84.
39. H. Kryzminski, "Boriding Refractory Metals," Z. Wirt. Fertigung, 68 (1973) 496-500.
40. A. L. Burykina, Yu. V. Dzyadykevich, and V. V. Gorskii, "Compatibility of Boron Fibers with a Tungsten Substrate and a Titanium Matrix," Soviet Powder Metallurgy, 12 (1972) 900-903.
41. K. P. Staudhammer, L. E. Murr, C. Marinoff, and V. Reineking, "Chemical Compatibility in Metal-Fiber Composites," Microstructures, 3(4) (1972) 17-21.
42. G. K. Schmitz and A. G. Metcalfe, "Evaluation of Compatible Titanium Alloys in Boron Filament Composites," USNTIS AD Rep. No. 758294 (1973).
43. G. V. Samsonov and V. P. Latysheva, "Boron, Carbon, and Nitrogen Diffusion into the Transition Elements of the Fourth, Fifth, and Sixth Groups of the Periodic System," Doklady Akad. Nauk. SSSR, 109 (1956) 582-5.
44. G. V. Samsonov and A. P. Epik, "Parameters of Reactive Diffusion of Boron and Carbon into Refractory Metals," Phys. Metals Metallog., 14(3) (1962) 144.
45. A. H. Silver and P. J. Bray, "NMR Study of Bonding in Some Solid Boron Compounds," J. Chem. Phys., 32 (1960) 288-92.
46. A. H. Silver and T. Kushida, "Nuclear Magnetic Resonance in Transition Metal Diborides," J. Chem. Phys., 38 (1963) 865-72.

47. Y. Tyan, L. E. Toth, and Y. A. Chang, "Low Temperature Specific Heat Study of the Electron Transfer Theory in Refractory Metal Borides," J. Phys. Chem., 30 (1969) 785-92.
48. D. C. Gillies and D. Lewis, "Bond Strength in Diborides of Some Group IV and V Metals," J. Less-Common Metals, 16(2) (1968) 162-3.
49. W. H. Philipp, "Chemical Reactions of Carbides, Nitrides, and Diborides of Titanium and Zirconium and Chemical Bonding in These Compounds," NASA-TN-D-3533 (1966).
50. R. T. DeHoff, "The Dynamics of Microstructural Change," Treatise on Materials Science, Vol. 1, Academic Press, New York, 1972.
51. Quantitative Microscopy, R. T. DeHoff and F. N. Rhines, eds., McGraw-Hill, New York, 1968.
52. R. T. DeHoff and S. M. Gehl, "Quantitative Microscopy of Lineal Features in Three Dimensions," submitted to J. Microscopy.
53. G. Dörfler, "Sequence-Analysis, A New Method for the Quantitative Determination of the Arrangement of Phases in Opaque Samples," Stereology, H. Elias, ed., Springer-Verlag, New York, 1967.
54. F. N. Rhines, "Origins of Quantitative Metallography," Met. Soc. Conf., 27 (1963) 417-34.
55. H. F. Fischmeister, "Applications of Quantitative Microscopy in Materials Engineering," J. Microscopy, 95(pt. 1) (1972) 119-43.
56. R. A. Vandermeer and P. Gorden, "Edge-Nucleated, Growth Controlled Recrystallization in Aluminum," Trans. AIME, 215 (1959) 577-88.
57. F. N. Rhines, R. T. DeHoff and J. Kronsbein, "A Topological Study of the Sintering Process," Final Report, AEC Contract No. AT-(40-1)-2581 (December, 1969).

58. N. R. Hirji, "Evolution of Microstructure During the Sintering of Boron Carbide," M.S. Thesis, University of Florida, 1973.
59. W. D. Tuohig, "The Evolution of Microstructure During Sintering of UO_2 and its Effect Upon Mechanical and Thermal Properties," Ph.D. Dissertation, University of Florida, 1972.
60. R. E. Shepler, "Influence of Microstructure on Friability of Alumina-Zirconia Abrasives," Ph.D. Dissertation, University of Florida, 1975.
61. P. F. Johnson, "Quantitative Relations Between Microstructure and Electrical Properties of TiO , UO_2 , and Ta_2O_5 ," presented at the 76th Annual Meeting, The American Ceramic Society, 1974.
62. R. A. Rege, W. D. Forgeng, D. H. Stone and J. V. Alger, "Microcleanliness of Steel - A New Quantitative TV Rating Method," ASTM STP-480 (1970).
63. S. F. Hulbert, "Models for Solid-State Reactions in Powdered Compacts: A Review," J. Brit. Cer. Soc., 6 (1969) 11-20.
64. W. Jander, "Reactions in Solid State at High Temperatures," Z. Anorg. Chem., 163 (1927) 1-30.
65. A. M. Ginstling and B. I. Brounshtein, "Concerning the Diffusion Kinetics of Reactions in Spherical Particles," J. Appl. Chem. USSR, 23 (1950) 1327-29.
66. G. Valensi, "Kinetics of the Oxidation of Metallic Spherules and Powders," Comptes Rendue, 202 (1936) 309.
67. R. E. Carter, "Kinetic Model for Solid-State Reactions," J. Chem. Phys., 34 (1961) 2010-15.
68. R. E. Carter, "Addendum: Kinetic Model for Solid-State Reactions," J. Chem. Phys., 35 (1961) 1137-38.
69. D. E. Clark, G. J. Scott and L. L. Hench, "Note on the Valensi-Carter Solid-State Kinetics Model," submitted for publication.

70. G. Tammann, "Chemical Reactions in Powdered Mixtures of Two Kinds of Crystals," Z. Anorg. Chem., 149 (1925) 21-43.
71. C. Kroger and G. Zeigler, "Reaction Rates of Glass Batch Melting," Glastech., 26 (1953) 346-50.
72. S. F. Hulbert, R. H. Smoak, and D. Brosnan, "Kinetics and Mechanism of the Reaction Between MgO and Cr₂O₃," International Symposium on the Reactivity of Solids, 6th, J. W. Michell, ed., Wiley-Interscience, New York, 1969.
73. V. F. Zhuravlev, I. G. Lesokhin, and R. G. Templ'man, "Kinetics of the Reactions for the Formation of Aluminates and the Role of Mineralizers in the Process," J. Appl. Chem. USSR, 21 (1948) 887-93.
74. B. Serin and R. T. Ellickson, "Determination of Diffusion Coefficients," J. Chem. Phys., 9 (1941) 742-43.
75. H. Dunwald and C. Wagner, "Measurement of Diffusion Rate in the Process of Dissolving Gases in Solid Phases," Z. Physik. Chem., B24 (1934) 53-58.
76. J. W. Cahn and W. C. Hagel, "Divergent Pearlite in a Manganese Eutectoid Steel," Acta Met., 11 (1963) 561-74.
77. J. W. Cahn, "The Significance of Average Mean Curvature and Its Determination by Quantitative Metallography," Trans. AIME, 239 (1967) 610-16.
78. R. T. DeHoff, "The Quantitative Estimation of Mean Surface Curvature," Trans. AIME, 239 (1967) 617-21.
79. G. A. Moore, "Is Quantitative Metallography Quantitative?," ASTM STP-480 (1970).
80. L. Alexander and H. P. Klug, "Basic Aspects of X-ray Absorption," Anal. Chem., 20 (1948) 886-89.
81. G. L. McCreery, "Improved Mount for Powdered Specimens Used on the Geiger-Counter X-ray Spectrometer," J. Am. Ceram. Soc., 32 (1949) 141-46.

82. J. W. Edwards, H. L. Johnston, and W. E. Ditmars, "Vapor Pressures of Inorganic Substances. XI Titanium Between 1587 and 1764 K and Copper Between 1143 and 1292 K," J. Am. Chem. Soc., 75 (1953) 2467-70.
83. L. Kaufman and E. V. Clougherty, "Investigation of Boride Compounds for High-Temperature Applications," Plansee Proc., Reutte/Tyrol, 5 (1964) 722-58.
84. P. O. Schissel and O. C. Trulson, "Mass Spectrometric Study of the Vaporization of the Titanium-Boron System," J. Phys. Chem., 66 (1962) 1492-6.
85. E. W. Hoyt and J. Chorne, "Preparation of Self-Bonded Borides," U.S. AEC GEAP-3332 (1960).
86. V. Mandorf, J. Hartwig and, E. J. Seldin, "High-Temperature Properties of Titanium Diboride," Met. Soc. Conf., 18 (1961) 455-67.
87. E. V. Clougherty and D. Kalish, "High-Pressure, High Temperature Ceramic Structures," Proc. Sagamore Army Mater. Res. Congr., Raquette Lake, New York, 12 (1966) 431-43.
88. R. Jenkins, An Introduction to X-ray Spectrometry, Heyden, New York, 1974.
89. B. D. Cullity, Elements of X-ray Diffraction, Addison-Wesley, Reading, Mass., 1956.
90. H. T. Clark, "The Lattice Parameters of High Purity Alpha Titanium; and the Effects of Oxygen and Nitrogen on Them," Trans. AIME, 185 (1949) 588-89.
91. W. B. Pearson, A Handbook of Lattice Spacings and Structure of Metals and Alloys, Pergamon Press, New York, Vol. 1, 1958; Vol. 2, 1967.
92. S. Miyagi, "A Criticism on Jander's Equation of Reaction Rate Considering the Statistical Distribution of Particle Size of Reacting Substance," J. Japan Ceram. Soc., 59 (1951) 132-35.
93. H. Sasaki, "Introduction of Particle Size Distribution into Kinetics of Solid State Reactions," J. Am. Ceram. Soc., 47 (1961) 512-16.

94. K. J. Gallagher, "The Effect of Particle Size Distribution on the Kinetics of Diffusion," International Symposium on the Reactivity of Solids, 5th, G. M. Schwab, ed., Elsevier, New York, 1965.
95. P. C. Kapur, "Kinetics of Solid-State Reactions of Particulate Ensembles with Size Distributions," J. Am. Ceram. Soc., 56 (1973) 79-81.

BIOGRAPHICAL SKETCH

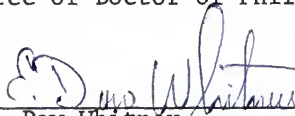
George C. Walther, Jr., was born September 22, 1947, in St. Louis, Missouri. He obtained a B.S. in Ceramic Engineering from the University of Missouri at Rolla in 1969. He then came to the University of Florida to pursue a Ph.D. program on semiconducting glasses. Subsequently inducted into the Army, he served in Germany as a red-eye gunner. After military service, he returned to the University of Florida and obtained a M.E.S. in Materials Science and Engineering in 1974. In 1976, he completed his Ph.D. dissertation on the Kinetics of TiB Formation. He is presently a member of The American Ceramic Society, Keramos, Tau Beta Pi, The National Institute of Ceramic Engineers, AIME-ASM, and The International Society for Stereology. He resides with his wife and dog in Gainesville, Florida.

I certify that I have read this study and that in my opinion it conforms to acceptable standards of scholarly presentation and is fully adequate, in scope and quality, as a dissertation for the degree of Doctor of Philosophy.



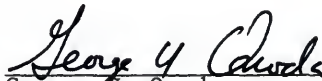
Ronald E. Loehman, Chairman
Associate Professor of Materials Science and Engineering

I certify that I have read this study and that in my opinion it conforms to acceptable standards of scholarly presentation and is fully adequate, in scope and quality, as a dissertation for the degree of Doctor of Philosophy.



E. Dow Whitney
Professor of Materials Science and Engineering

I certify that I have read this study and that in my opinion it conforms to acceptable standards of scholarly presentation and is fully adequate, in scope and quality, as a dissertation for the degree of Doctor of Philosophy.



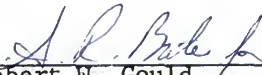
George Y. Onoda
Associate Professor of Materials Science and Engineering

I certify that I have read this study and that in my opinion it conforms to acceptable standards of scholarly presentation and is fully adequate, in scope and quality, as a dissertation for the degree of Doctor of Philosophy.



Robert T. DeHoff
Professor of Materials Science
and Engineering

I certify that I have read this study and that in my opinion it conforms to acceptable standards of scholarly presentation and is fully adequate, in scope and quality, as a dissertation for the degree of Doctor of Philosophy.



Robert W. Gould
Professor of Materials Science
and Engineering

I certify that I have read this study and that in my opinion it conforms to acceptable standards of scholarly presentation and is fully adequate, in scope and quality, as a dissertation for the degree of Doctor of Philosophy.



John W. Connolly
Associate Professor of Physics

This dissertation was submitted to the Graduate Faculty of the College of Engineering and to the Graduate Council, and was accepted as partial fulfillment of the requirements for the degree of Doctor of Philosophy.

August, 1976



Dean, College of Engineering

Dean, Graduate School

UNIVERSITY OF FLORIDA



3 1262 08553 3106